SHAPE VALIDATION AND RF PERFORMANCE OF INFLATABLE ANTENNAS

BRYAN WELCH

Bachelor of Electrical Engineering

Cleveland State University

May 2003

Master of Science in Electrical Engineering

Cleveland State University

December 2006

Submitted in partial fulfillment of requirements for the degree

DOCTOR OF PHILOSOPHY IN ENGINEERING

at the

CLEVELAND STATE UNIVERSITY

May 2020

We hereby approve this dissertation for

Bryan Welch

Candidate for the Doctor of Philosophy in Engineering degree for the

Department of Electrical Engineering and Computer Science

and the CLEVELAND STATE UNIVERSITY'S

College of Graduate Studies by

Committee Chairperson, Dr. Chansu Yu

Department of Electrical Engineering and Computer Science, February 6, 2020

Committee Member, Dr. Lili Dong

Department of Electrical Engineering and Computer Science, February 6, 2020

Committee Member, Dr. Nigamanth Sridhar

Department of Electrical Engineering and Computer Science, February 6, 2020

Committee Member, Dr. Eugenio Villaseca, Professor Emeritus

Department of Electrical Engineering and Computer Science, February 6, 2020

Committee Member, Dr. Ulrich Zurcher

Department of Physics, February 6, 2020

Student's Date of Defense: February 6, 2020

ACKNOWLEDGMENTS

I am grateful to my advisor, Dr. Murad Hizlan, for his guidance, encouragement, assistance, and support during the entirety of the period of my Doctoral studies. I would also like to thank Dr. Chansu Yu, Dr. Lili Dong, Dr. Robert Romanofsky, Dr. Nigamanth Sridhar, Dr. Eugenio Villaseca, and Dr. Ulrich Zurcher, who are on my dissertation committee, for reviewing this dissertation as well as for their suggestions to my research.

I am also grateful to the NASA Glenn Research Center Graduate Studies Program, for its financial support to enhance my education and technical expertise, while I pursue this degree. I would also like to thank my management at the NASA Glenn Research Center for their continued support of me completing this dissertation.

I am most grateful to my wife, Samantha Welch, for her unwavering support of me finishing this endeavor. Without her love, encouragement, and support, I would not have completed this dissertation. Finally, thank you to our “fur-kids”, Ellie, Elvis, Lyla, Rambo, and Smooch, who always made the writing of this dissertation an entertaining experience.

SHAPE VALIDATION AND RF PERFORMANCE OF INFLATABLE ANTENNAS

BRYAN WELCH

ABSTRACT

Inflatable aperture antennas are an emerging technology that is being investigated for potential use in science and exploration missions. In particular, for missions to Mars and beyond, large deployable aperture antennas can provide the antenna gain required for high data rate communications, where the necessary antenna diameter exceeds the available volume of typical launch vehicle platforms. As inflatable aperture antennas have not been proven fully qualified for space missions, the author's Master's Thesis assessed the Ruze equation in characterizing this antenna technology. Inflatable aperture antennas do not follow a parabolic shape, and so the Ruze equation is not applicable due to the macroscopic shape errors of this technology. Therefore, geometric evaluations of the surface profile cannot simply correlate antenna gain degradation with the root-mean-square shape error with a parabolic surface.

Consequently, the focus of this work was to derive an accurate mathematical model of an inflatable aperture antenna in order to characterize its Radio Frequency (RF) performance. Calculus of Variations methodologies were used to derive the surface profile shape of the inflatable aperture antenna. Physical Optics techniques were used to generate the antenna pattern profile. Validation testing of the predicted inflatable antenna shape model was performed through use of Laser Radar metrology measurements on an inflatable test article. Assessments of the RF performance of the inflatable aperture antenna, compared with nominally shaped solid paraboloidal antennas, were obtained through simulations of both technologies using a common diameter, depth, and arc

length. Assessments of the RF performance of the inflatable aperture antenna was also performed against itself for changes in distance of the antenna feed location in the axial direction. Whereas the Ruze equation is limited to assessing gain reduction, this effort will also assess beam spreading and first side lobe angle and magnitude. The ability to characterize the RF response of this antenna will provide for an improved understanding of this technology. The accurate representation of the shape of this type of antenna technology will help to identify the most appropriate ways in which this technology could be utilized in planning future communication architectures for NASA missions to Mars and beyond.

TABLE OF CONTENTS

Page

LIST OF TABLES

LIST OF FIGURES

CHAPTER I

INTRODUCTION

Inflatable aperture antennas are an emerging technology that National Aeronautics and Space Administration (NASA) is investigating for potential uses in science and exploration missions. In particular for missions to Mars and beyond, large aperture antennas are of interest as they can provide the antenna gain required for high data rate communications. In the Deep Space realm, the free space path loss becomes so large that the antenna diameter required to support the desired data rates exceeds the available volume of typical launch vehicle platforms required to launch the spacecraft to these locations [33, 39]. Inflatable aperture antennas also have advantages over solid parabolic reflector antennas in terms of reduced aerial density and stowage volume. In comparison, inflatable aperture antennas also have advantages over mesh-deployable reflector antennas in terms of ease of construction and the lack of a tuning process associated with all mesh joints. Inflatable aperture antennas can be manufactured on a pre-shaped mandrel through casting and curing polymer material and vapor depositing reflective silver flake coating [28], as opposed to wiring mesh reflector surfaces.

Inflatable aperture antennas also cannot suffer from the same type of deployment issues that precluded the use of the Galileo Spacecraft High Gain Antenna, which was a deployable mesh reflector in which three of eighteen stowed ribs did not deploy, due to additional stowage time due to the launch delay of the Galileo spacecraft due to the Challenger accident [18]. As inflatable aperture antennas have not been proven fully qualified for space missions, their performance must be characterized properly so that the behavior of the antennas is understood in advance.

1.1 Background on Antenna Surface Theory

Commonly, the surface errors that exist on an antenna are thought of as phase errors. However, when there are surface errors, there can be a change in the direction that the reflected ray will travel, which can also change the phase of the ray when the ray reaches the aperture plane. Snell's Law states that the incident and reflection angles from the surface normal will be equal [2, 9, 10, 31, 32]. Surface errors will cause a change in the direction that the surface normal vector will be pointing, and therefore change the direction that the reflected ray will travel. In perfect solid paraboloid antennas, the surface normal can be easily determined from the equation of the paraboloid and geometric optics states that rays originating from the feed of an antenna travel to the antenna surface and are reflected traveling parallel to the axial direction of the antenna [7]. All of the rays are thought of as being parallel when dealing with an ideal paraboloidal surface. Once these rays reach the aperture plane, they would have all traveled the same distance and the aperture would be a plane of constant phase [4, 9, 10].

However, when the antenna no longer maintains the ideal paraboloidal shape, the surface normal vector direction will vary from the ideal surface normal vector. If the errors in the antenna surface are such that the incident angle on the antenna surface is decreased from the ideal incident angle, the reflecting rays will be propagated in a direction that is non-parallel to the axial direction, and will have a smaller radial distance from the feed in the aperture plane. Similarly, if the errors in the antenna surface are such that the incident angle on the antenna surface is increased from the ideal incident angle, the reflection rays will have a larger radial distance from the feed in the aperture plane, and will also induce a change in the distance that the reflected ray must propagate. Phase errors are also introduced because of this reflection angle error [5, 6, 11, 31, 32]. An example of an ideal and non-ideal paraboloidal antenna surface reflection rays are illustrated in Figure 1.

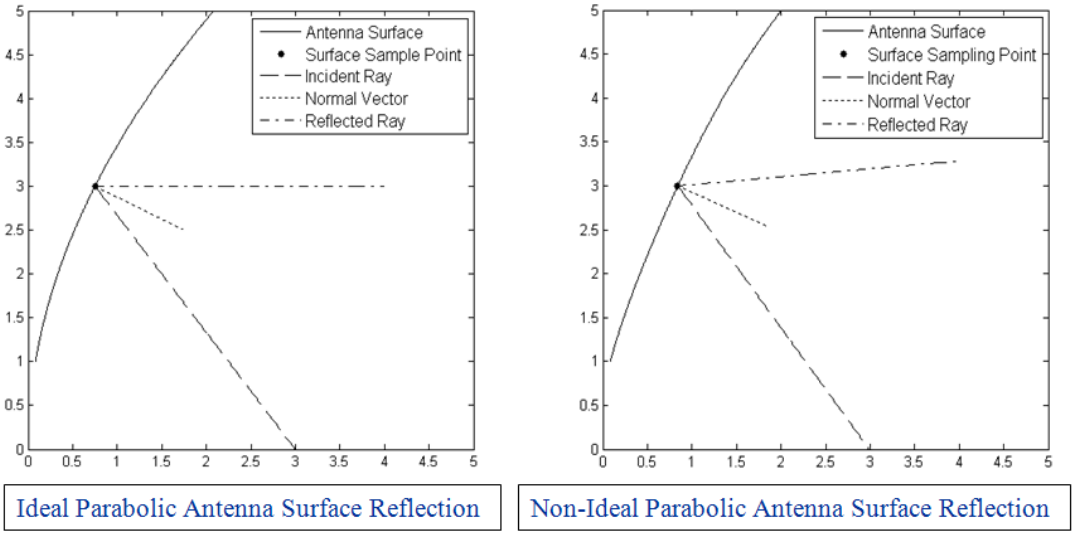

FIGURE 1: Ideal & Non-Ideal Paraboloidal Antenna Surface Reflections

In Figure 1, the dashed line shows the ray that originates from the feed, at the focal point location, travels to the antenna surface. The antenna surface is shown as the solid line, with the dotted line denotes the normal vector at the point of reflection on the antenna surface. Finally, the dashed-dotted line illustrates the ray reflecting off of the antenna surface and traveling parallel to the axial direction, defined as the x-axis of the plot. For the ideal surface, the reflected ray is parallel to the axial direction; for the non-ideal surface, the reflected ray is no longer parallel to the axial direction.

The Ruze equation attempts to characterize surface profile induced phase errors to determine the degradation of the directivity of the antenna based on the root-mean-square (RMS) surface error and the antenna operating frequency [34, 35]. The Ruze equation gain degradation formula is given by (1.1).

$$L_R = \mathrm{e}^{-\left(\frac{4\pi\epsilon}{\lambda_A}\right)^2} \tag{1.1}$$

In (1.1), the terms used are defined as follows:

- L_R is the loss in directivity due to surface errors
- ϵ is the RMS surface error of the antenna
- λ_A is the wavelength of operation of the antenna

The Ruze equation makes assumptions about the nature of the surface errors. These limitations are based on assumptions that were made during the derivation regarding the statistical estimates of the phase errors that are present for the antenna. Five distinct assumptions are noted by Ruze [34, 35].

1. The surface errors on the antenna are random in nature.

2. The surface errors are uniformly distributed over the aperture.
3. The surface errors are distributed in fixed, circular correlation regions.
4. The aperture of the antenna (Diameter D) is much larger compared to the diameter correlation region (c), $D >> 2c$
5. The surface errors have a Gaussian spatial phase correlation.

1.2 Application of Antenna Surface Theory to Inflatable Aperture Antenna

In the author's Master's Thesis [37], it was proven through laboratory testing that the Ruze equation, which relates Root Mean Square (RMS) surface error to a predicted gain degradation [34], is not applicable to inflatable antennas, as the error profile does not correlate to the requirements for use of the Ruze equation. Laboratory testing included Laser Radar metrology of an inflatable antenna surface under various pressurization levels, while concurrently performing Radio Frequency (RF) metrology in a Near-Field antenna facility. Antenna pattern response was obtained and gain degradation was obtained, and compared with predicted gain degradation using the RMS surface error. For all pressurization levels tested, the Ruze equation overstated gain degradation. The reason for the Ruze equation not being applicable to this antenna type is due to the surface profile error spatial distribution and profile type.

Inflatable aperture antennas have more than random surface errors present on the antenna surface. These errors create a non-paraboloidal shape at the edges of the inflatable antenna surface and a spherical aberration near the vertex [4, 19, 20]. This

causes many errors to be created near the edge of the antenna. Other errors that can exist on an inflatable antenna include those caused from improper inflation of the antenna. The inflatable antenna could be over-inflated and cause a change in the ideal focal point of the paraboloid, or the inflatable antenna could be under-inflated and wrinkles could form on the antenna surface, creating additional surface errors. All of these factors contribute to the inflatable aperture antenna not being able to utilize the Ruze equation methodology to estimate gain degradation.

The 0.3m inflatable offset antenna, tested at 8.4 GHz, in the author's Master's Thesis [37] is shown in Figure 2.

FIGURE 2: 0.3 Meter Antenna in GRC Planar Near-Field Antenna Test Facility

Using the ideal inflation pressurization, the raw photogrammetry data on the 0.3m inflatable offset antenna are shown in the top half of Figure 3, while that data are rotated and plotted against the ideal parabolic shape in the bottom half of Figure 3.

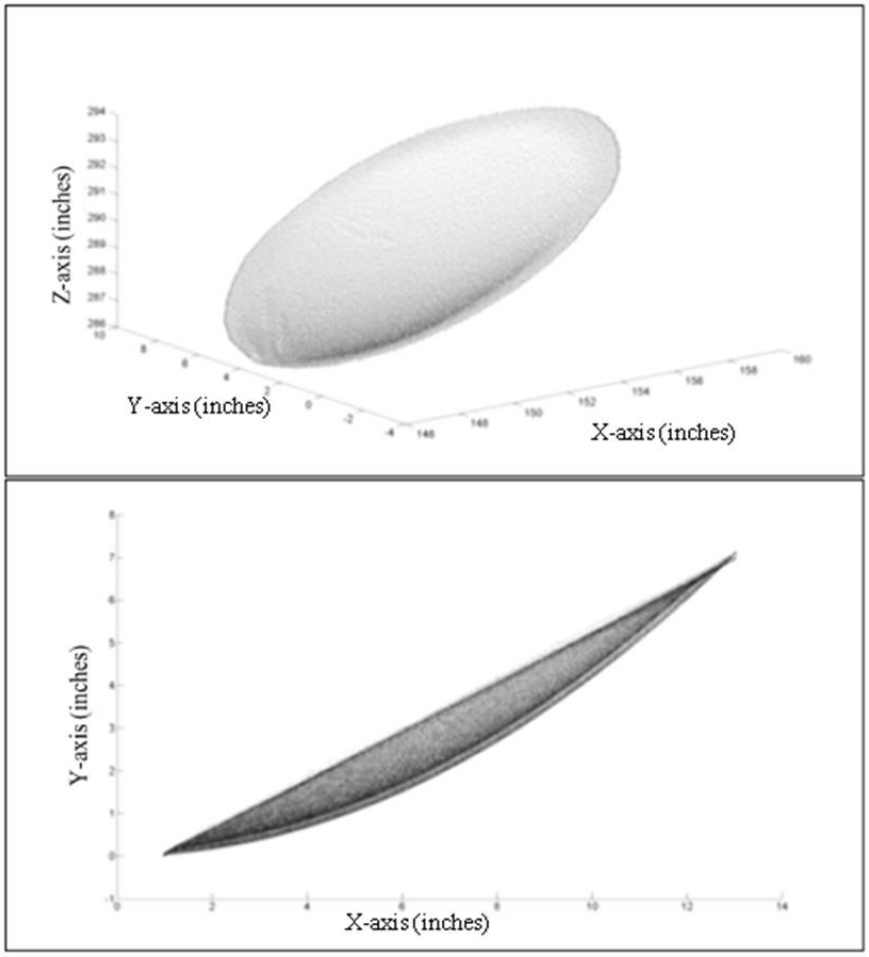

FIGURE 3: Raw Photogrammetry Data, Ideal Paraboloid Edge-View Profile

Table I provides the summary data of the measured gain, gain degradation from ideal paraboloid, as well as surface profile RMS error and Ruze-Equation-derived Gain Degradation at the various pressurization levels tested. The final column references the Difference in the Radio Frequency (RF) Derived gain degradation and the Ruze-derived

gain degradation, with a positive value meaning the Ruze-derived degradation overestimates the gain degradation [37].

TABLE I: RF & Ruze Equation Performance Comparisons

Pressurization Differential (inch H_2O)	**RF Gain (dBi)**	**RF-Derived Gain Degradation (dB)**	**RMS Surface Error (inch)**	**Ruze-Derived Gain Degradation (dB)**	**Difference (dB)**
0.00	14.42	−12.33	1.20	−402.02	389.69
0.03	23.14	−3.61	0.34	−32.21	28.60
0.04	24.37	−2.38	0.26	−19.05	16.67
0.05	24.52	−2.23	0.23	−15.12	12.89
0.06	24.47	−2.28	0.19	−9.86	7.58
0.07	24.45	−2.30	0.26	−19.47	17.17

The results of the testing summarized above are that the Ruze equation overestimates gain degradation for inflatable aperture antennas. The error profile of the inflatable antenna does not match the limitations specified by Ruze, and as such, the Ruze equation should not be used in conjunction with this particular antenna type.

1.3 History of Inflatable Aperture Antenna Technologies

This section will detail various efforts over the last 33 years relating to the development of inflatable aperture antennas and the understanding of their performance characteristics and capabilities. There are five referenced activities, ranging from a space experiment, to ground testing, to analytical derivations.

Inflatable Antenna Experiment

There has been only one inflatable aperture antenna flown in space to date. The antenna was the 14-meter offset-parabolic inflatable reflector antenna, dubbed the Inflatable Antenna Experiment (IAE), and was launched aboard the Space Shuttle Endeavor in 1996. The IAE was an effort managed by NASA Jet Propulsion Laboratory (JPL) and the antenna was constructed by L'Garde, Inc. The objectives of the experiment were to validate the deployment of the antenna, measure the reflector surface precision, which was expected to be on the order of 1mm RMS, and demonstrate that the structure could be build at low cost and be stowed in a small-size container [13, 14]. Figure 4 shows an image of the IAE as viewed from the Space Shuttle Endeavor [39].

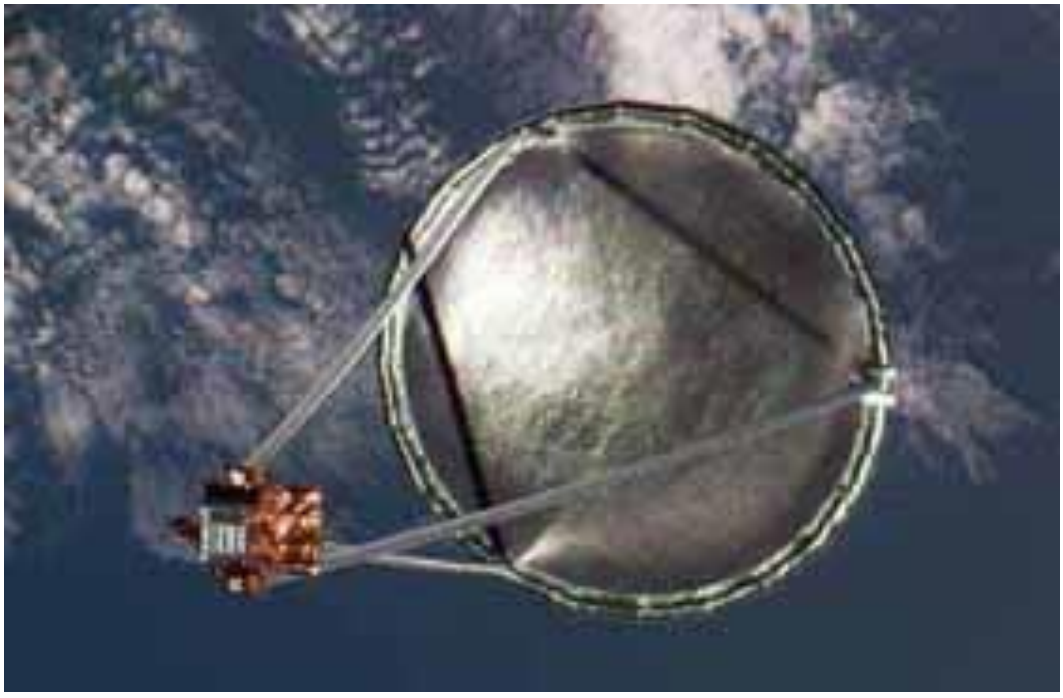

FIGURE 4: Inflatable Antenna Experiment

The experiment lasted 90 minutes, during which the antenna support structure was successfully deployed to the proper shape. However, the lens shaped reflector failed to

inflate due to an unexpected leak in the nitrogen gas inflation system [14]. This failure meant that there were no in-flight measurements regarding the surface accuracy of the inflatable aperture antenna [39].

NASA Small Business Innovative Research Efforts

Several inflatable aperture antennas have been under investigation at NASA GRC since 2004 as part of the NASA Small Business Innovative Research (SBIR) program. NASA GRC has overseen efforts with SRS Technologies, which has manufactured several inflatable aperture antennas, including a 0.3 meter offset inflatable antenna [15, 29, 30, 33, 39] and a 4 x 6 meter offset inflatable antenna [39]. The 0.3 meter offset inflatable antenna, which is shown in Figure 5, was tested at 8.4 GHz. The performance of the antenna was comparable to a similar size conventional rigid reflector antenna and also performed well compared to the theoretical predictions [15, 29, 30, 33, 39].

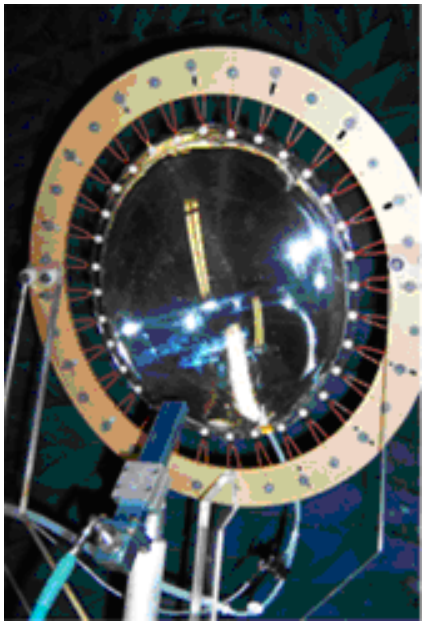

FIGURE 5: 0.3 Meter Offset Inflatable Antenna

A 4 x 6 meter offset inflatable antenna was also manufactured by SRS Technologies. This antenna is inflated in the aperture, as well as in a torus surrounding the diameter of the aperture antenna, with the purpose of the torus to provide structural support of the inflatable antenna. The 4 x 6 meter offset inflatable antenna, shown in Figure 6 inside the NASA GRC Near-Field test facility, was tested and characterized at 8.4 GHz and 32 GHz [39].

FIGURE 6: 4 x 6 Meter Offset Inflatable Antenna

Measured gains were 49.4 dBi with a 71% efficiency at 8.4 GHz and 51.6 dBi with an 8% efficiency at 32 GHz [28, 39]. An RMS surface error was measured for this antenna and was computed to be 3.5 mm. According to the Ruze equation, this amount of surface error would lead to much greater gain degradation at the Ka-band frequency of 32 GHz (i.e. 99 dB). Phase plots of the near field data show macroscopic surface errors,

which contribute to the gain degradation, but also show that some of the surface errors are dependent on each other.

Harbin Institute of Technology Photogrammetry Analysis

A non-NASA effort to characterize the surface accuracy of inflatable aperture antennas has been performed by the Key Laboratory of Science and Technology for National Defense, at the Harbin Institute of Technology, in Harbin, China. In this effort, the surface RMS was calculated by performing a photogrammetry analysis on a 3m parabolic reflector and canopy system, shown below in Figure 7 [36]. For the testing, 1170 round retro-reflective targets of 3mm diameter are attached on the reflective surface. The photogrammetry effort utilized the Geodetic Services V-STARS system.

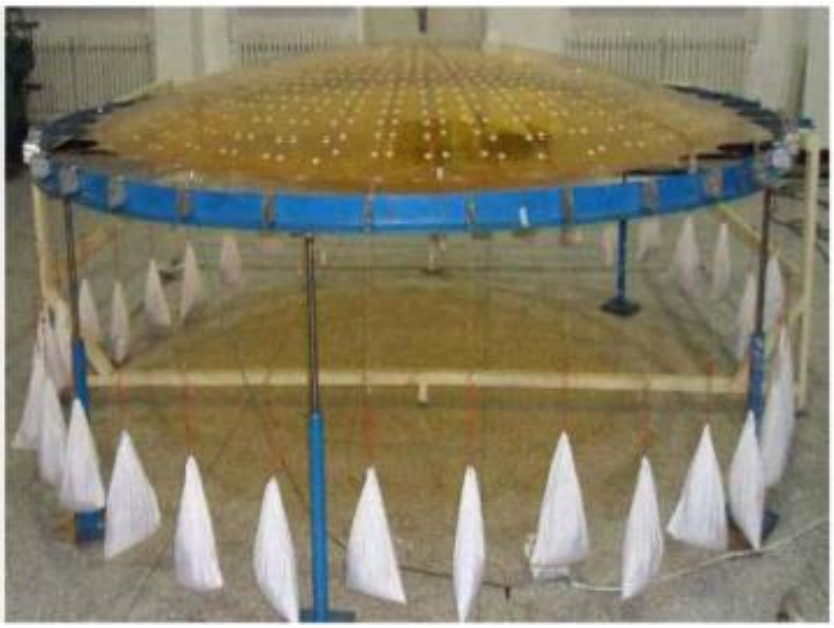

FIGURE 7: 3 Meter Inflatable Reflector Antenna with Canopy

The analysis looked to understand how the surface RMS changed on the antenna surface as a function of inflation pressurization, a similar technique to this author's Master's Thesis efforts [37], but without determining the Ruze equation predicted gain degradation. One interesting graphic that was obtained was using an internal pressurization of 20Pa, where the contour map of displacement of the antenna surface, compared to the ideal parabolic surface, showing large-scale macroscopic surface profile errors. This is shown below in Figure 8, while Figure 9 illustrates a cross-sectional displacement error plot [36].

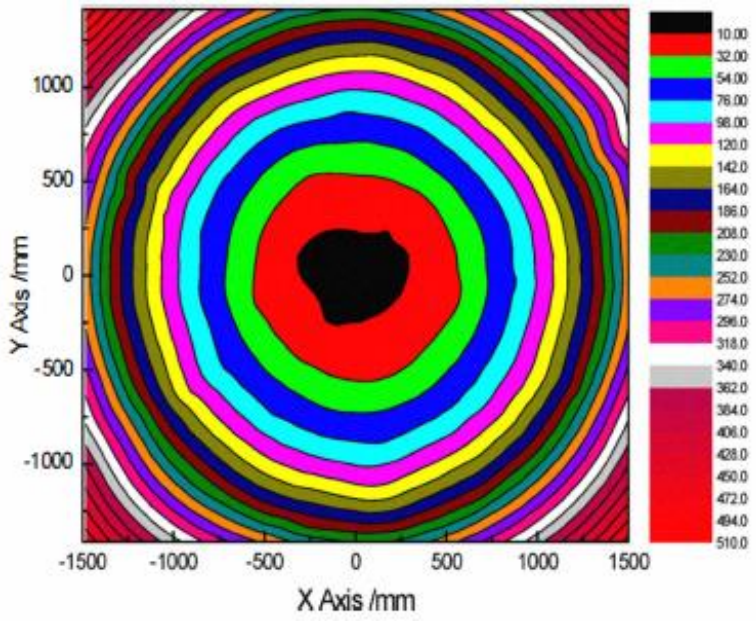

FIGURE 8: 3 Meter Inflatable Reflector Antenna Displacement Contour Map

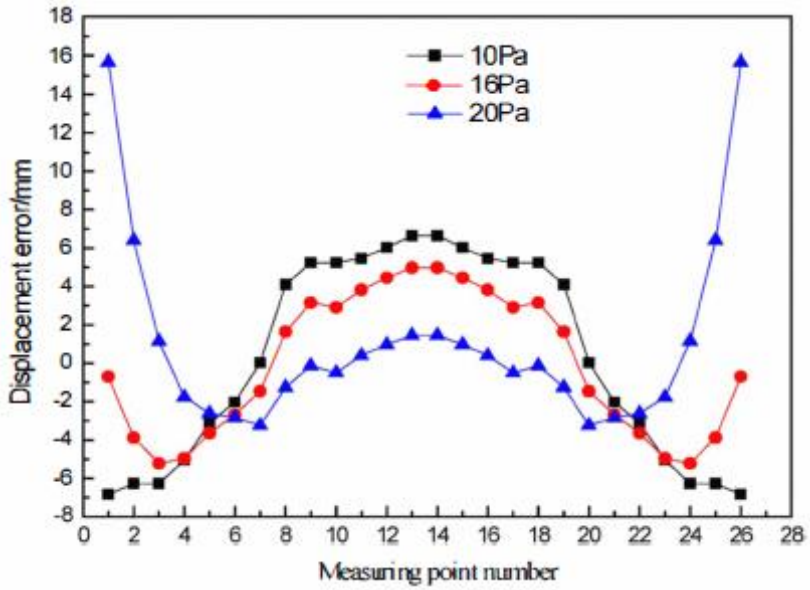

FIGURE 9: 3 Meter Inflatable Reflector Antenna Cross-Section Error

Soil Moisture Radiation Mission RF Modeling

The NASA Soil Moisture Radiation Mission proposed to use an inflatable offset reflector antenna as a novel radiometer system to collect global data of the Earth surface. The antenna was to use L-Band and S-Band and the proposed mission would need a reflector antenna with a diameter of 25m, which forces the use of a deployable antenna due to launch vehicle constraints. An effort was performed to characterize the RF performance of the inflatable parabolic reflector antenna design, such to be able to simulate accurate RF performance for the proposed science mission [17].

This effort utilized the Physical Optics (PO) RF prediction methodology while modeling the offset reflector antenna surface as being modified by an elevation distortion, as torus surface distortions have a strong functional dependency in elevation

due to azimuthal rotational symmetry [17]. Equation (1.2) is the radial distortion dependency model used in the effort.

$$\Delta r(\theta) = h\cos\left(2\pi N\frac{\theta}{\alpha}\right) \quad \text{[mm]} \tag{1.2}$$

In (1.2), the terms used are defined as follows:

- $\Delta r(\theta)$ is the radial distortion as a function of the elevation angle [mm]
- θ is the elevation angle
- h is the center-to-peak height [mm]
- N is the periodicity of the distortion
- α is the parabolic offset reflector tilt angle

Radiation parameters calculated by the PO model include directivity, cross polarization, beam tilt, beamwidth, and beam efficiency. Calculations were performed at both L-Band and S-Band, for undistorted surfaces, and distorted surface models with periodicity of 0.75 and 1.0, both with center to peak heights of 10mm. The RF characteristics are tabulated for these cases, but generalizations for functionals of periodicity are not calculated. First side-lobe peak increases were not of interest here.

Deployable Aperture Elastic Antenna Surface Accuracy Analysis

A Dissertation effort at The George Washington University was performed to calculate the equilibrium configuration of an inflatable elastic membrane, supported by elastic tendons subjected to constant hydrostatic pressure, with the concern being that the design may not maintain the ideal parabolic shape within tolerance due to elastic

deformation of the surface, particularly near the rim [8]. The equilibrium system modeled total system energy and determined an optimized solution of minimum energy. Analysis to determine the shape behavior of the elastic inflatable aperture antenna included factors such as internal pressure, film strain energy, tendon strain energy, and gravitational energy. Two principle findings of the effort was that 1) the support tendon system tends to flatten the parabolic reflector near the edge, and 2) large membranes can exhibit improved surface accuracy if the cutting pattern of the flat components were altered [8]. RF performance predictions utilized the PO methodology to determine antenna gain, and first side-lobe levels for a fixed-rim and tendon supported antenna models, with RF performance provided for specific test cases without generalizations of performance provided.

1.4 Dissertation Motivation and Contributions

Therefore, the focus of this work is to first derive a mathematical model of the inflatable antenna surface. This mathematical model of the inflatable antenna will be determined using the Calculus of Variations methodology, which looks to determine the maximum volume surface model, which is applicable for the basic inflation process of the inflatable aperture antenna. The mathematical model of the inflatable aperture antenna will be validated by performing surface mapping of an inflatable test article using Laser Radar metrology.

This inflatable antenna mathematical model will be used in conjunction with the PO approach to determine the antenna gain and pattern profile of the inflatable aperture

antenna. The RF performance predicted by the PO model will be compared with simulated radiation patterns of solid paraboloidal antennas of the same diameter, depth, or curved arc length using focal length over diameter ratios minimizing RMS error of the inflatable aperture antenna shape to an ideal paraboloidal shape. Finally, performance variations of the inflatable aperture antenna will be performed over a trade space of focal length over diameter ratio errors up to 10% of the nominal best-fit focal length over diameter ratio magnitude.

Finally, with the mathematical model and RF performance derived and verified for the inflatable aperture antenna, an RF performance degradation analysis will be performed. Included in this RF performance degradation analysis will be calculations for gain degradation at boresight (similar to what the Ruze equation predicts for solid parabolic antennas), as well as calculations for spreading of the main beam width, in terms of the 3dB beamwidth and first null beamwidth, as well as first side-lobe peak degradation and location. Here, side-lobe peak degradation refers to the magnitude of the difference in gain between the boresight peak response and the first side-lobe peak response. Similarly, side-lobe peak location refers to the shifting in angular space for where the side-lobe peak degradation is located.

The novel concepts derived in this effort are the mathematical derivation of the surface model of the inflatable aperture antenna, as well as the RF pattern variations expected for this type of communication antenna. The Ruze equation does not calculate beam spreading effects due to random Gaussian surface profile noise, nor does it determine the reduction in the side-lobe peak to boresight peak difference. This work builds on the author's work in his Master's Thesis [37] and culminates in answering the

questions posed in conclusion of that effort. This work will enable a better understanding of this type of antenna technology, which will then be used to identify the most appropriate ways in which this technology could be utilized in supporting future communication architectures for NASA missions to Mars and beyond [33, 39].

1.5 Dissertation Outline

Chapter Two will focus on the background relationship of the inflatable aperture antenna to the Mylar balloon, along with the background derivation of the shape of the Mylar balloon using the Calculus of Variations technique. That technique will then be extended to support the shape derivation of the inflatable aperture antenna. Validation testing data will be presented of the inflatable aperture antenna surface profile model against Laser Radar metrology based test data of an inflatable test article.

Chapter Three will focus on the background theory of the physical optics modeling of the solid parabolic reflector antenna. That technique will then be extended to support inflatable aperture antenna by modifying the surface profile, surface normal vector, and surface area calculations consistent with the physical optics modeling approach.

Chapter Four will focus on the RF performance metrics and RF performance comparison methodologies used to compare the RF performance of the inflatable aperture antenna against the solid parabolic reflector antenna. Simulated RF performance results of the inflatable aperture antenna will be presented. Additionally, RF performance comparisons against the solid parabolic reflector antenna will be presented using either a

common diameter, depth, or arc length. A discussion of the noted observations from these results will be provided.

Chapter Five will present the summarized conclusions observed in the Dissertation effort. Additionally, several possible future work activities will be briefly discussed that extend the efforts developed in this Dissertation to continue to advance this antenna technology field.

CHAPTER II

INFLATABLE APERTURE ANTENNA SURFACE SHAPE PROFILE DERIVATION

The inflatable aperture antenna is a structure that is made out of a Mylar-like material, such as polyimide [30], that does not stretch, similar to the properties of the Mylar balloon. Just as for the Mylar balloon, the inflatable aperture antenna is constructed from two circular sheets that are connected at the boundary and inflated with a gas. However, unlike the Mylar balloon, whose inflated radius is found upon maximizing the volume of the balloon, the inflatable antenna is held in place via an external structure, such as an inflatable torus or a tendon network [17, 29], which determines the diameter of the inflatable aperture antenna. Ideally, the inflatable antenna will have the shape of a paraboloid, due to the optimal reflective properties associated with this geometric structure, with the diameter set via the needs of the communication link [39]. Figure 10 illustrates differences in the surface profiles between the fully inflated Mylar balloon and the fully inflated inflatable aperture antenna, where the surface profile removes the axially symmetric geometry from the three dimensional shape

into a two dimensional curve. This chapter was also published as a journal article to fulfill Dissertation requirements [38].

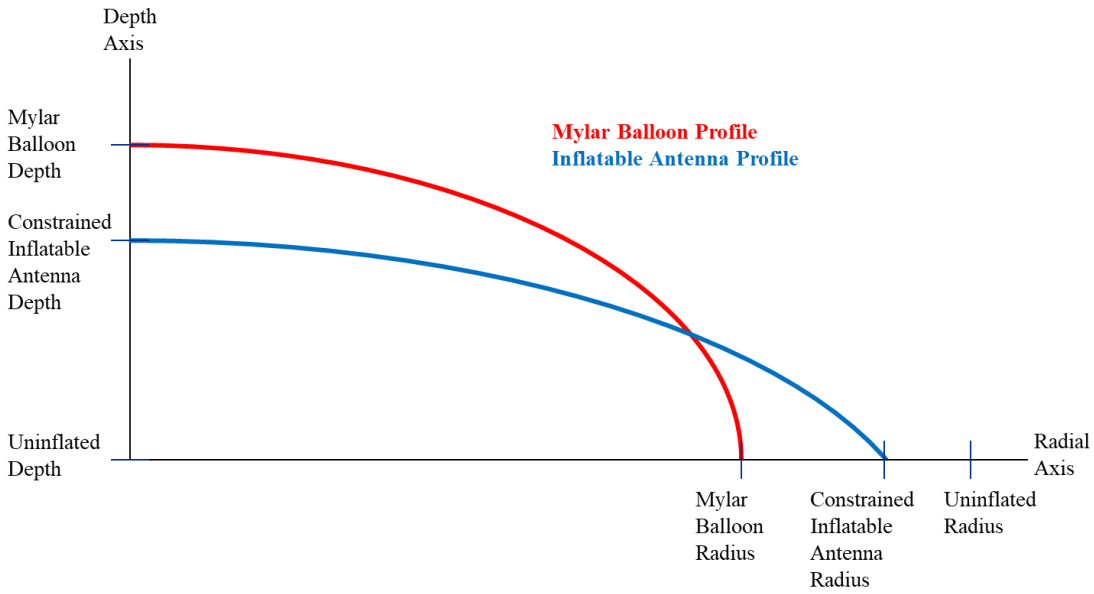

FIGURE 10: Surface Profile Shapes: Inflatable Antenna and Inflated Mylar Balloon

The important observations of the fully inflated Mylar balloon surface profile are the following:

- Arc length of fully inflated profile is equal to the uninflated radius
- Depth reaches a maximum upon full inflation of Mylar balloon
- Radius reaches a minimum upon full inflation of Mylar balloon
- Derivative of slope of surface profile is increasingly negative as the radial direction magnitude increases, from a value of zero to negative infinity

In regards to the inflatable aperture antenna, here are the important observations:

- Arc length of fully inflated profile is equal to the uninflated radius
- Depth is less than that of fully inflated structure
- Radius is larger than that of fully inflated structure
- Derivative of slope of surface profile is increasingly negative as the radial direction magnitude increases, from a value of zero to a negative non-infinite value

Figure 11 illustrates the importance of slope at the depth location, as well as the radius location.

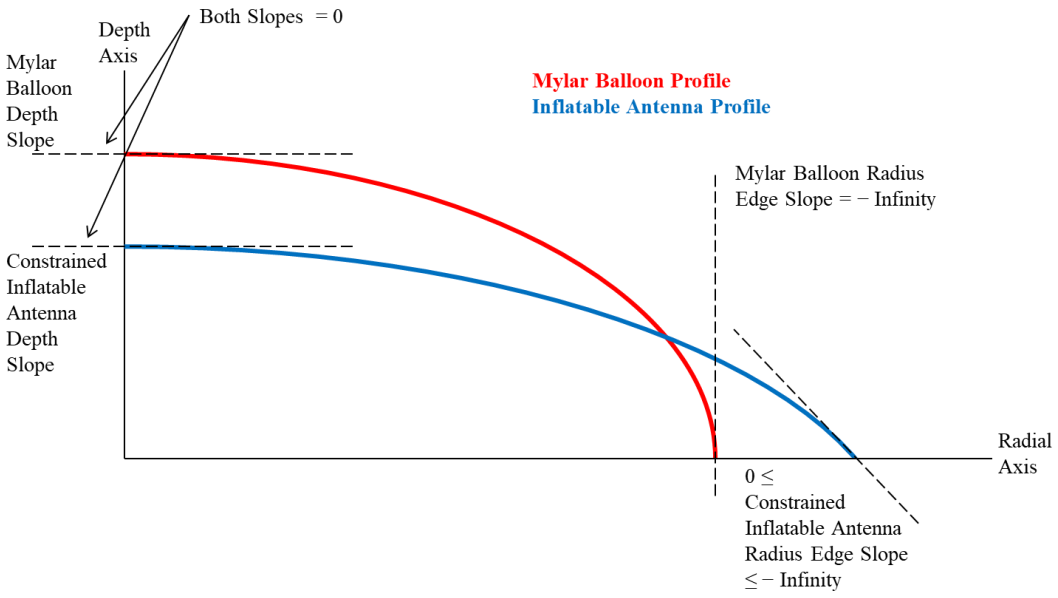

FIGURE 11: Surface Profile Slopes: Inflatable Antenna and Inflated Mylar Balloon

The remaining content of this chapter provides the background and reference of the Mylar balloon surface shape model in Section 2.1, from which the author's personal contributions towards the development of the shape model of the Inflatable Antenna are provided in Section 2.2. Section 2.3 continues the shape model development by

discussing the author's methodology for how the edge slope was derived. Section 2.4 completes the shape model derivation with the utilized edge slope model, while Section 2.5 provides validation assessments of that shape model against measured photogrammetry data. Finally, Section 2.6 summarizes the author's contributions towards the shape model, provided in Sections 2.2 through 2.5 against the reference contributions from Section 2.1.

2.1 Background and Derivation of Mylar Balloon Surface Shape Model

The surface model of the inflated Mylar balloon has been investigated and developed using the Maple software development package [24, 26]. Here, a closed-form solution has been found for the shape profile which utilizes elliptic integrals as a parameterization of the surface model, as opposed to the use of the gamma function [27]. This closed-form solution was obtained through the approach of calculus of variations, which is a field of mathematics that involves functionals of integrals of unknown functions and their derivatives. Calculus of variations allows one to solve for a maximum or minimum of a functional, where the unknown function that provides this optimization is called an extremal function. Equation (2.1) provides a generic example of this concept [16, 26].

$$J = \int_{t_0}^{t_1} f\big(t, x(t), x'(t)\big)dt \tag{2.1}$$

In (2.1), the terms used are defined as follows:

- J is the functional

- t_0 is the lower integration limit of variable t
- t_1 is the upper integration limit of variable t
- $f(\,)$ is the unknown extremal function
- t is the integration variable
- $x(t)$ is the variable function with respect to variable t
- $x'(t)$ is the derivative of the variable function with respect to variable t

The process of finding the function $x(\,)$ that optimizes J involves solving the Euler-Lagrange equation for the function $x(t)$. The Euler-Lagrange equation for a single variable function $x(t)$ is given below in (2.2).

$$\frac{\partial f}{\partial x} - \frac{d}{dt}\left(\frac{\partial f}{\partial x'}\right) = 0 \tag{2.2}$$

One class of problem that is typically solved using the Calculus of variations methodology is the fixed-endpoint problem, such that in (2.1) for functional J, $x(t_0)$, and $x(t_1)$ are defined. However, it is also possible that one of the endpoints is not defined, in which case the problem is called an endpoint-curve problem. The endpoint-curve problem is solved using a transversality condition. The analytical solution to the shape definition of the Mylar balloon is obtained through the use of a transversality condition. Equation (2.3) provides the relationship of the slope of the functional curve with the uninflated and inflated radii of the Mylar balloon [21, 22, 23, 24, 26].

$$\int_0^{r_B} \sqrt{1 + z'(x)^2}\,dx = a \tag{2.3}$$

In (2.3), the terms used are defined as follows:

- r_B is the inflated radius of the Mylar balloon
- $z'(x)$ is the slope of the Mylar balloon functional curve
- a is the uninflated radius of the Mylar balloon
- x is the Mylar balloon radial direction axis variable

(2.3) provides the constraint of the shape of the balloon, which is used in conjunction with a Lagrange multiplier in solving the Euler-Lagrange Equation. The curve is reflected over the x-axis, and the overall curve is rotated around the x-y plane using a typical circle-to-sphere rotation methodology. It is also useful here to note two properties of the slope of the curve $z(x)$, given in (2.4) and (2.5). These properties hold at the intersection of the curve with the z-axis and with the x-axis [26].

$$z'(x = 0) = 0 \tag{2.4}$$

$$\lim_{x \to r_B^-} z' = -\infty \tag{2.5}$$

The functional that is maximized using the methodology described in (2.1), is the volume of the balloon, given by the Shell method below in (2.6) [26].

$$V = 4\pi \int_0^{r_B} xz(x)dx \tag{2.6}$$

In (2.6), the additional terms used are defined as follows:

- V is the volume of the Mylar balloon
- $z(x)$ is the depth of the Mylar balloon with respect to radial direction axis variable x

Therefore, the process of solving the Euler-Lagrange equation begins with the use of the volume functional, which is maximized in (2.7). The volume functional is utilized in the Euler-Lagrange (2.2), in (2.8).

$$f(x, z, z') = 4\pi x z(x) + \lambda\sqrt{1 + z'(x)^2} \tag{2.7}$$

$$\frac{\partial}{\partial z}\left(4\pi x z(x) + \lambda\sqrt{1 + z'(x)^2}\right) - \frac{d}{dx}\left(\frac{\partial}{\partial z'}\left[4\pi x z(x) + \lambda\sqrt{1 + z'(x)^2}\right]\right) = 0 \tag{2.8}$$

In (2.7), the additional term used is defined as follows:

- λ is the Lagrange multiplier

The four partial derivative elements of (2.8) are provided as (2.9) through (2.12), with aggregation of those elements being (2.13).

$$\frac{\partial}{\partial z}\left(4\pi x z(x)\right) = 4\pi x \tag{2.9}$$

$$\frac{\partial}{\partial z}\left(\lambda\sqrt{1 + z'(x)^2}\right) = 0 \tag{2.10}$$

$$\frac{\partial}{\partial z'}\left(4\pi x z(x)\right) = 0 \tag{2.11}$$

$$\frac{\partial}{\partial z'}\left(\lambda\sqrt{1 + z'(x)^2}\right) = \frac{\lambda z'(x)}{\sqrt{1+z'(x)^2}} \tag{2.12}$$

$$4\pi x - \frac{d}{dx}\frac{\lambda z'(x)}{\sqrt{1+z'(x)^2}} = 0 \tag{2.13}$$

(2.14) rearranges (2.13) to enable an integration to be performed, and (2.15) shows the result of that integration.

$$\frac{\lambda z'(x)}{\sqrt{1+z'(x)^2}} = \int 4\pi x dx \tag{2.14}$$

$$\frac{\lambda z'(x)}{\sqrt{1+z'(x)^2}} = 2\pi x^2 + C \tag{2.15}$$

In (2.15), the additional term used is defined as follows:

- C is the integration constant

Implementing the constraint given in (2.4) with (2.15) provides the following solution of the integration constant in (2.16) and (2.17).

$$\frac{\lambda z'(x=0)}{\sqrt{1+z'(x=0)^2}} = 2\pi(x=0)^2 + C \Rightarrow C = 0 \tag{2.16}$$

$$\frac{z'(x)}{\sqrt{1+z'(x)^2}} = \frac{2\pi}{\lambda}x^2 \tag{2.17}$$

Next, a variable substitution using the Lagrange multiplier is formed in (2.18) and then is substituted into (2.17) as (2.19). Equation (2.20) contains the solution of (2.19) for $z'(x)$.

$$\frac{\lambda}{2\pi} = -m^2 \tag{2.18}$$

In (2.18), the additional term used is defined as follows:

- m is the substitution variable

$$\frac{z'(x)}{\sqrt{1+z'(x)^2}} = -\frac{x^2}{m^2} \tag{2.19}$$

$$z'(x) = \sqrt{1+z'(x)^2}\left(-\frac{x^2}{m^2}\right)$$

$$z'(x)^2 = (1+z'(x)^2)\left(-\frac{x^2}{m^2}\right)^2$$

$$z'(x)^2 = \left(-\frac{x^2}{m^2}\right)^2 + z'(x)^2\left(-\frac{x^2}{m^2}\right)^2$$

$$z'(x)^2\left(1-\left(-\frac{x^2}{m^2}\right)^2\right) = \left(-\frac{x^2}{m^2}\right)^2$$

$$z'(x)^2 = \frac{\left(-\frac{x^2}{m^2}\right)^2}{\left(1-\left(-\frac{x^2}{m^2}\right)^2\right)}$$

$$z'(x) = \pm\frac{-\frac{x^2}{m^2}}{\sqrt{1-\left(-\frac{x^2}{m^2}\right)^2}}$$

$$z'(x) = \pm \frac{-x^2}{\sqrt{m^4\left(1-\frac{x^4}{m^4}\right)}}$$

$$z'(x) = \frac{-x^2}{\sqrt{m^4-x^4}} \tag{2.20}$$

Next, the constraint provided in (2.5) is used to determine the substitution variable in (2.20), provided as (2.21), where the solution for that substitution variable provided in (2.22) and the fully inflated Mylar balloon curve slope defined in (2.23).

$$z'(x = r_B) = \frac{-(x=r_B)^2}{\sqrt{m^4-(x=r_B)^4}} = -\infty \tag{2.21}$$

$$z'(r_B) = \frac{-(r_B)^2}{\sqrt{m^4-(r_B)^4}} = -\infty \Rightarrow m = r_B \tag{2.22}$$

$$z'(x) = \frac{-x^2}{\sqrt{r_B^4-x^4}} \tag{2.23}$$

Finally, the curve slope in (2.23) is integrated to form the curve equation, defined in (2.24).

$$z(x) = \int_x^{r_B} \frac{t^2}{\sqrt{r_B^4-t^4}} dt \tag{2.24}$$

In (2.24), the additional term used is defined as follows:

- t is the substitution integration variable

Note that this integral in (2.24) is the elliptic integral, and thus, further simplifications can be made using additional elliptic and Jacobi functions, [21, 24, 26], as follows in (2.25) and (2.26), through the use of a parameterization variable.

$$x(u) = r_B \mathrm{cn}\left(u, \frac{1}{\sqrt{2}}\right) \tag{2.25}$$

$$z(u) = r_B\sqrt{2}\left[\mathrm{E}\left(\mathrm{sn}\left(u, \frac{1}{\sqrt{2}}\right), \frac{1}{\sqrt{2}}\right) - \frac{1}{2}\mathrm{F}\left(\mathrm{sn}\left(u, \frac{1}{\sqrt{2}}\right), \frac{1}{\sqrt{2}}\right)\right] \tag{2.26}$$

In (2.25) and (2.26), the additional functions and terms used are defined as follows:

- E( ) is the elliptic E function
- F( ) is the elliptic F function
- sn( ) is the Jacobi sine function
- cn( ) is the Jacobi cosine function
- $x(u)$ is the parameterization of the variable x, with parameterization variable u
- $z(u)$ is the parameterization of the variable z, with parameterization variable u
- u is the parameterization variable

The overall parameterization of the Mylar balloon utilizes a similar technique that is seen in the sphere of using nominal sine and cosine trigonometric functions to parameterize the circle from the x-z plane around the z axis in the x-y plane to form the sphere. This final parameterization of the Mylar balloon is given by (2.27) through (2.29), and illustrated in Figure 12. Additionally, the relationship between the fully inflated radius and the arc length, which is also the uninflated radius, is provided in (2.30) [24, 26] with four digits of numerical accuracy.

$$x(u,v) = r_B \mathrm{cn}\left(u, \tfrac{1}{\sqrt{2}}\right)\cos(v) \tag{2.27}$$

$$y(u,v) = r_B \mathrm{cn}\left(u, \tfrac{1}{\sqrt{2}}\right)\sin(v) \tag{2.28}$$

$$z(u) = r_B\sqrt{2}\left[\mathrm{E}\left(\mathrm{sn}\left(u, \tfrac{1}{\sqrt{2}}\right), \tfrac{1}{\sqrt{2}}\right) - \tfrac{1}{2}\mathrm{F}\left(\mathrm{sn}\left(u, \tfrac{1}{\sqrt{2}}\right), \tfrac{1}{\sqrt{2}}\right)\right] \tag{2.29}$$

In (2.27) through (2.29), the additional functions and terms used are defined as follows:

- sin( ) is the sine function

- $\cos(\,)$ is the cosine function
- v is the parameterization variable

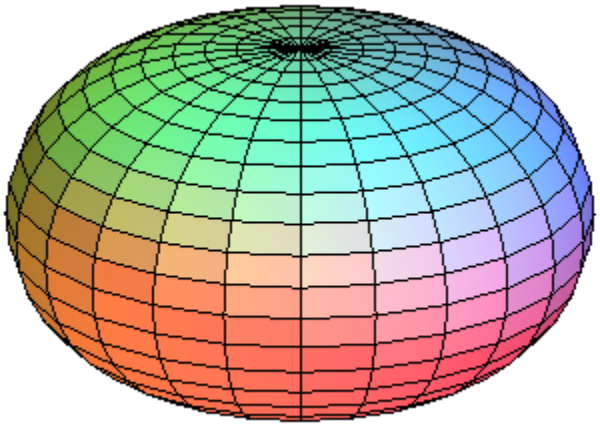

FIGURE 12: Parameterized Mylar Balloon Profile

$$r_B = 0.7627a \tag{2.30}$$

2.2 Derivation of Inflatable Aperture Antenna Surface Profile Shape Model

Figure 11 has illustrated the similarities and differences between the surface shape model of the inflated Mylar balloon and that of a diametrically constrained inflatable aperture antenna. Given that such similarities exist, it was hypothesized that following a similar calculus of variations approach to deriving the surface shape model of the inflatable aperture antenna could be possible. Starting from the previously defined (2.20), the inflated radius of inflatable aperture antenna is used in place of the fully inflated Mylar balloon radius. Therefore, the edge slope of the inflatable aperture

antenna at radius r_A is used instead of the edge slope of the Mylar balloon, which was negative infinity. This is shown below in (2.31).

$$z'(x)|_{x=r_A} = \frac{-{r_A}^2}{\sqrt{m^4-{r_A}^4}} = -A \tag{2.31}$$

In (2.31), the additional terms used are defined as follows:

- r_A is the inflated radius of the inflatable aperture antenna
- A is the edge slope of the inflatable aperture antenna at radius r_A

(2.31) is then simplified and with terms rearranged to solve for variable substitution, m, so that the surface slope equation can be derived in a manner similar to the derivation in (2.23). The final simplified form is provided in (2.32).

$$\frac{r_A^4}{m^4-r_A^4} = A^2$$

$$r_A^4 = (m^4 - r_A^4)A^2$$

$$m^4A^2 = r_A^4(1 + A^2)$$

$$m^4 = \frac{r_A^4(1+A^2)}{A^2} \tag{2.32}$$

(2.33) then uses (2.32) solution for the variable substitution, m^4, to solve the surface slope equation, where the factor m^4 is used from (2.20).

$$z'(x) = \frac{-x^2}{\sqrt{\frac{r_A^4(1+A^2)}{A^2}-x^4}} \tag{2.33}$$

Note that in the derivation above, the edge slope, A, and the radius of the inflatable aperture antenna, r_A, are used to derive the surface slope shown in (2.33); however, that radius can take on a range of values, depending on allowable constrained diameter. As seen in Figure 11, the radius can range from the arc length, where the edge

slope is zero when the surface is uninflated, to the fully inflated radius, where the edge slope is negative infinity when the surface is fully inflated. It can be deduced that as that radius changes across those two boundary conditions, the edge slope will also change monotonically. As such, a new term called the Inflation Ratio, is created to aid in the discussion of the shape of the inflatable aperture antenna, as a function of the constrained diameter to that of the allowable minimum diameter if the antenna were allowed to be fully inflated, where this is provided in (2.34). Alternately, the Inflation Ratio is defined in (2.35), using the relationship provided in (2.30) between the arc length, a, and the fully inflated radius, r_B.

$$I = \frac{a - r_A}{a - r_B} \tag{2.34}$$

$$I = \frac{a - r_A}{0.2373a} \tag{2.35}$$

In (2.34) and (2.35), the additional term used is defined as follows:

- I is the Inflation Ratio of the inflatable aperture antenna

When examining the functionality of the I parameter, it can be noted that if the inflatable aperture antenna were uninflated, where $r_A = a$, then $I = 0$. This is consistent with the notion that the inflatable aperture antenna is uninflated and this is actually a flat disc. If the inflatable aperture antenna were fully inflated without restriction from a support structure, where $r_A = r_B$, then $I = 1$. Again, this is consistent with the notion that the inflatable aperture antenna is fully inflated, and the shape would be like that of the Mylar balloon.

2.3 Inflatable Antenna Edge Slope Derivation

The surface slope given in (2.33) does not provide sufficient information for one to be able to integrate to obtain the inflatable antenna surface curvature similar to what is provided in (2.24). To be able to obtain such derivations, the edge slope of the inflatable aperture antenna at radius r_A, A, would need to be understood at all possible values of radius r_A, and therefore across the full range of possible Inflation Ratio values. As such, experimental testing was performed on an inflatable test article across the full range of Inflation Ratio values to obtain the edge slope value as a function of Inflation Ratio. Note that the testing across the full range of Inflation Ratio will allow for an understanding of any antenna, as the Inflation Ratio can be defined for any inflatable aperture diameter.

A testing structure was created that would allow for the acquisition of multiple edge slope measurements across multiple Inflation Ratio values on a given inflatable test article. For the sake of consistency, the test structure was created in a way that would allow for the inflatable test article to have its diameter modified so that a common test article could be utilized throughout the entire experimental test collection activity. The test structure can be described as a wood-aluminum hybrid frame that utilizes 36 diametrically adjustable support brackets which have a fixed attachment to a Mylar balloon test article. The outer frame was constructed from aluminum bracketing, while a wood sheet interior was used so that the diametrically adjustable support brackets could be easily mountable. The diameter of the diametrically constrained test article can be physically controlled to test various Inflation Ratio values of interest. A Laser Radar

surface metrology technique was utilized to measure the edge slope around the perimeter of the inflatable test article, in relation to the outer seam of the Mylar balloon, which is parallel to the test structure frame's reference tooling balls, used to act as control points of reference across different Inflation Ratio data collection experiments. The test structure is shown in Figure 13.

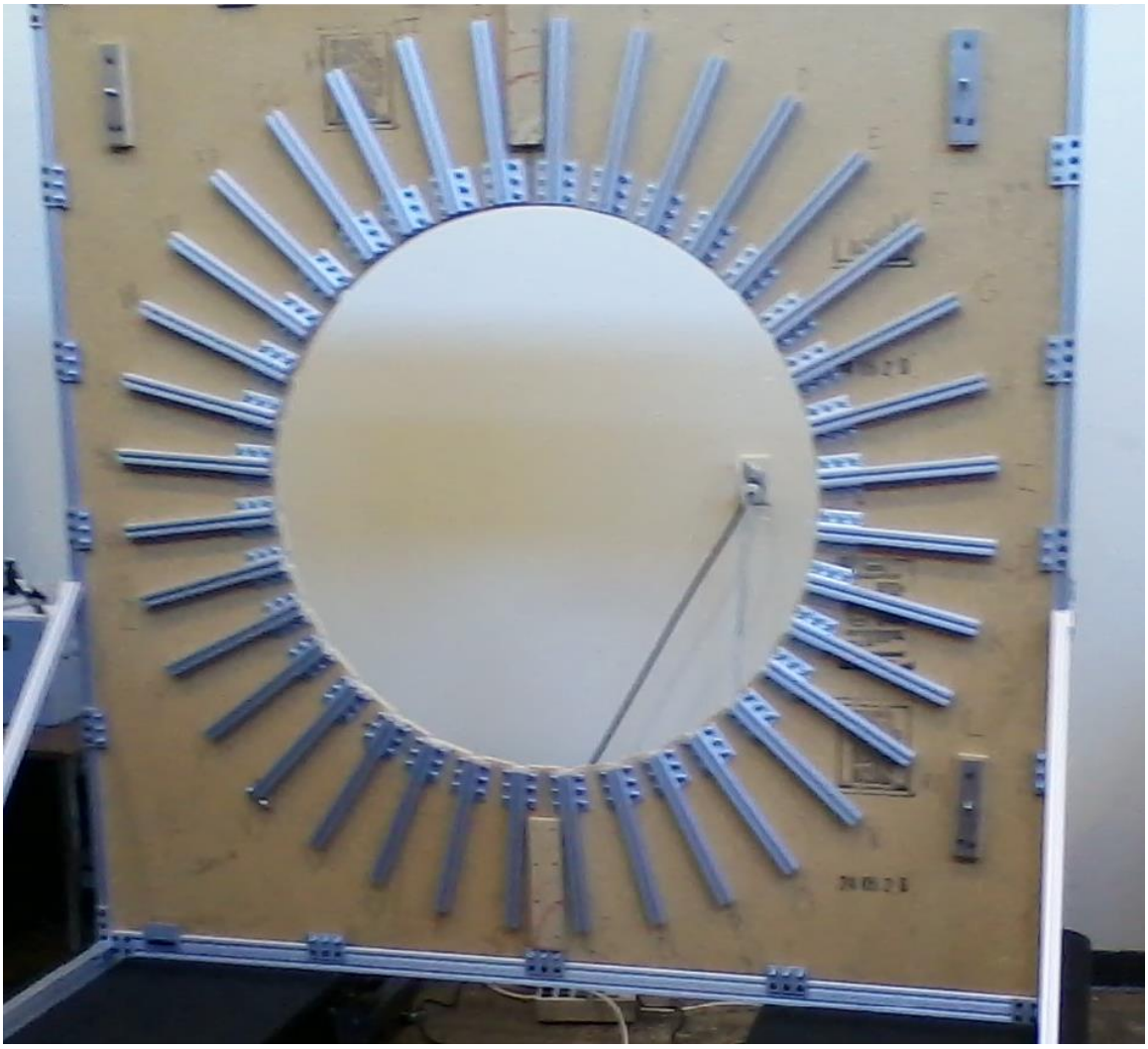

FIGURE 13: Inflation Ratio Test Structure

The inflatable test article utilized in the experiment was a 34.5 inch diameter Mylar balloon, where the diameter measurement was made along the surface to the

maximum width where the outer seam joining the two discs was located. As mentioned, 36 attachment points were utilized on the inflatable test article, such that a good representation of measurement points around the perimeter were obtained. Figure 14 shows the inflatable test article before being mounted to the test structure.

FIGURE 14: Pre-Mounted Inflatable Test Article

The test article was attached to the test structure along the 36 support brackets, as shown below in Figure 15. The test article underwent initial Laser Radar surface metrology with the goal of maximizing tautness between the test article and the attached support brackets, and minimizing rim planar variations across the test article's surface. The final initial test setup Laser Radar surface metrology measured the test article's rim planar with the test structure to have a root mean square error of 0.002497 inches.

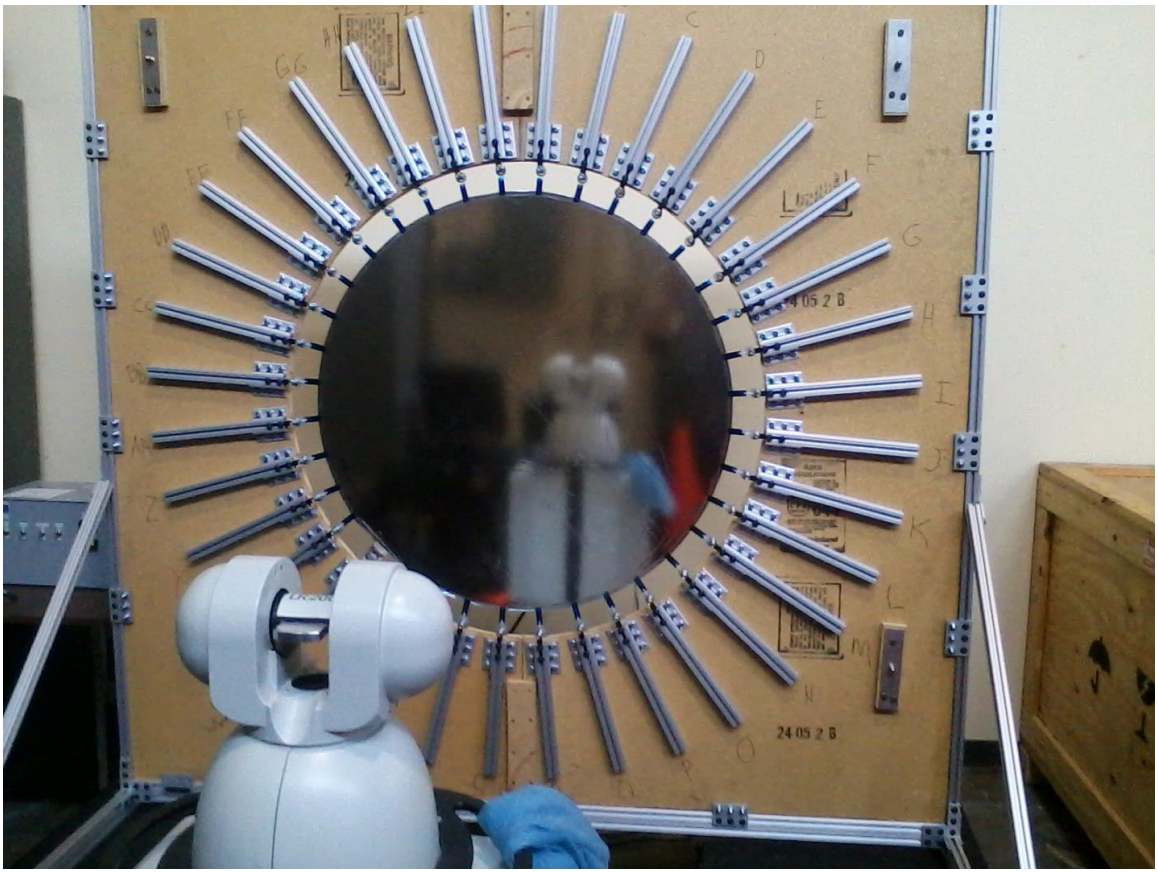

FIGURE 15: Post-Mounted Inflatable Test Article

The Laser Radar surface metrology was performed under various test article diameters using a surface metrology data sampling of 0.1 inch spacing. This sample spacing allows for a maximum Nyquist sampling-based frequency of 53.6 GHz [1, 3]. The maximum diameter for the test article was 34.5 inches, which corresponds to a fully inflated test diameter of 26.31 inches, per (2.30). Thus, the testing was performed using nominal test diameters ranging from 34.375 inches down to 26.75 inches, at increments of 0.25 inches for diameters below 34.25 inches. Testing at these diameters allowed for Inflation Ratio experimental data collections to be made between 0.015 and 0.946. All testing was performed under constant pressurization, as a closed-loop pressurization control system regulated internal pressurization of the test article at all times. Figure 16

shows the test article at the constrained diameter of 34.375 inches. Figure 17 shows the test article at the constrained diameter of 32.0 inches. Figure 18 shows the test article at the constrained diameter of 29. 75 inches. Figure 19 shows the test article at the constrained diameter of 26.75 inches.

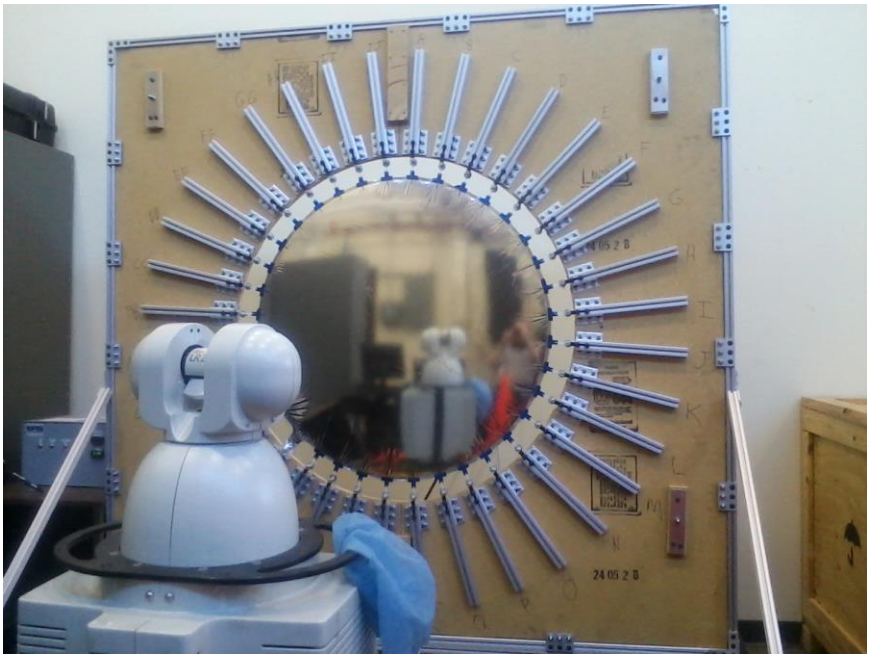

FIGURE 16: Test Article at Diameter of 34.375 Inches

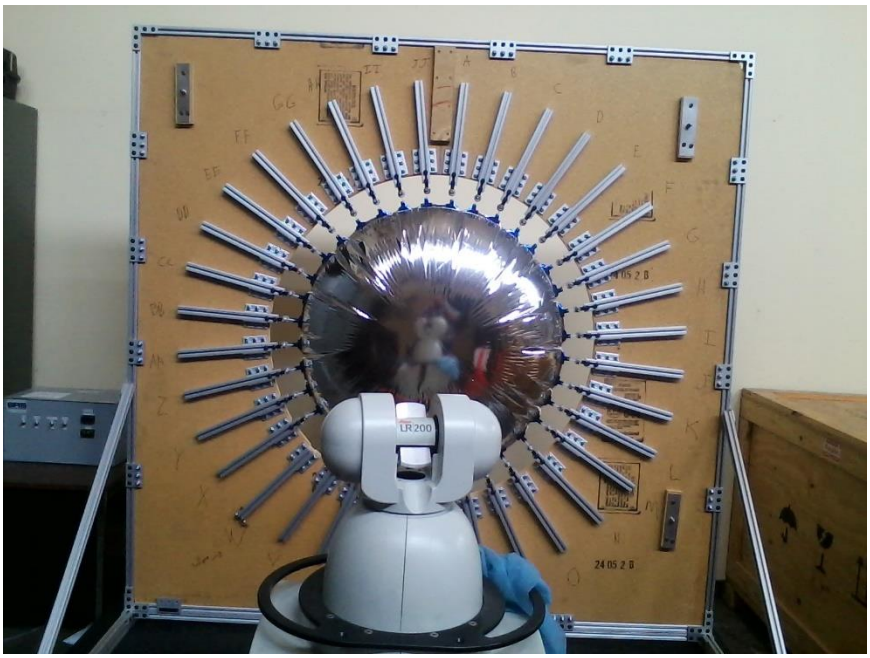

FIGURE 17: Test Article at Diameter of 32.0 Inches

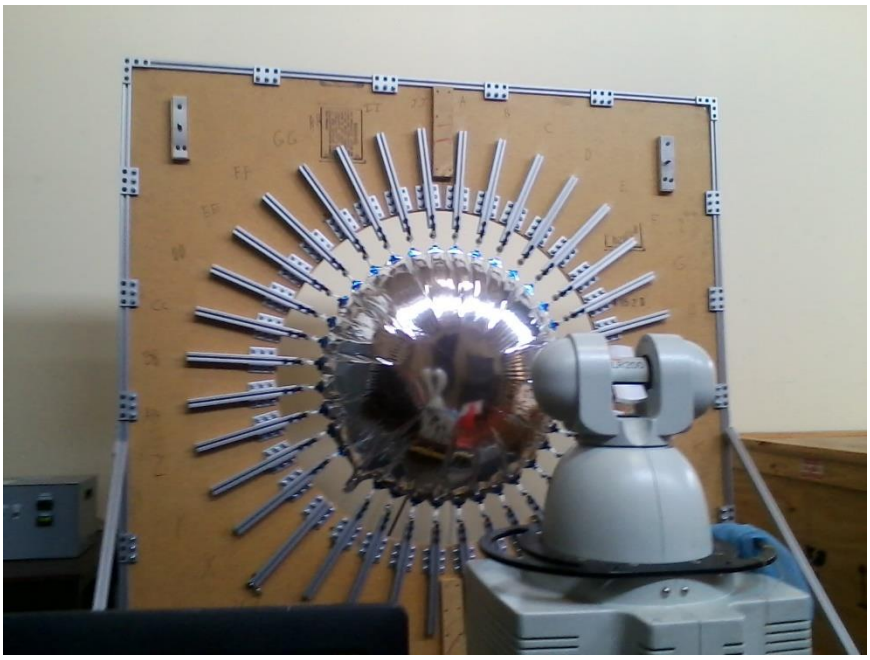

FIGURE 18: Test Article at Diameter of 29.75 Inches

FIGURE 19: Test Article at Diameter of 26.75 Inches

At each diametrically constrained test activity, data were obtained for a large portion of the perimeter of the test article, as well as over the entire surface of the test article, using the Laser Radar metrology technique. Data over the perimeter was analyzed at each of test support locations to derive the average edge slope angle at the particular Inflation Ratio under test. Previously, it was stated that the edge slope was the desired value, however, the edge slope angle is a geometric function of the edge slope, and given that the edge slope angle is easier to comprehend, it was used for the following derivation. Figure 20 illustrates the data and relationship across the data measured.

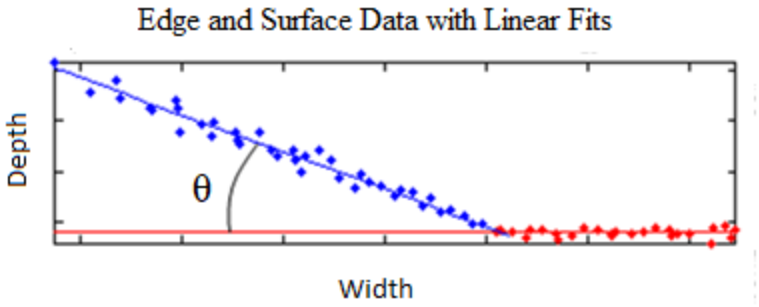

FIGURE 20: Edge and Surface Data with Linear Fits

Figure 20 illustrates the data split into edge and surface groups, where the edge group is colored red and the inflatable surface group is colored blue. Data in each group is combined into a linear fit, and the edge slope angle, θ, is computed from the dot product of these two linear fits. This process is repeated for all 32 test article diameters, each utilizing the 36 test article support attachment edge surface data investigations.

Using the Inflation Ratio constraints previously discussed, the edge slope angle at an Inflation Ratio of zero would have an edge slope angle of zero degrees, since the slope at that edge is zero. Likewise, the edge slope angle at an Inflation Ratio of one would have an edge slope angle of 90 degrees, since the slope at that edge is negative infinity. These constraints limit the curve fit options, as those points must appear on the optimal curve fit. Five curve fit options were investigated that meet these boundary constraints. The equations for these five curve fit options are provided next in (2.36) through (2.40). The tabulated correlations of these five curve fit models is provided in Table II. Plots visualizing these five curve fit options are shown next in Figures 21 through 25, in the same sequence of (2.36) through (2.40).

$$\theta = 90\sqrt{I} \tag{2.36}$$

$$\theta = 90 \sin\left(I \frac{\pi}{2}\right) \tag{2.37}$$

$$\theta = \frac{360}{\pi} \tan^{-1}(I) \tag{2.38}$$

$$\theta = 90 \sqrt[3]{I} \tag{2.39}$$

$$\theta = 90(1 - (I - 1)^2) \tag{2.40}$$

In (2.36) through (2.40), the additional term and function used are defined as follows:

- θ is the edge slope angle of the inflatable aperture antenna
- $\tan^{-1}(\,)$ is the inverse tangent function

TABLE II: Correlation Model Performance of Inflation Ratio versus Edge Slope Angle

Curve Fit Model Description	**Curve Fit Model Equation**	**Correlation with Test Article Data**
Square Root	(2.36)	0.99963
Sine	(2.37)	0.99487
Arc-Tangent	(2.38)	0.99248
Cubic Root	(2.39)	0.99513
Polynomial	(2.40)	0.99592

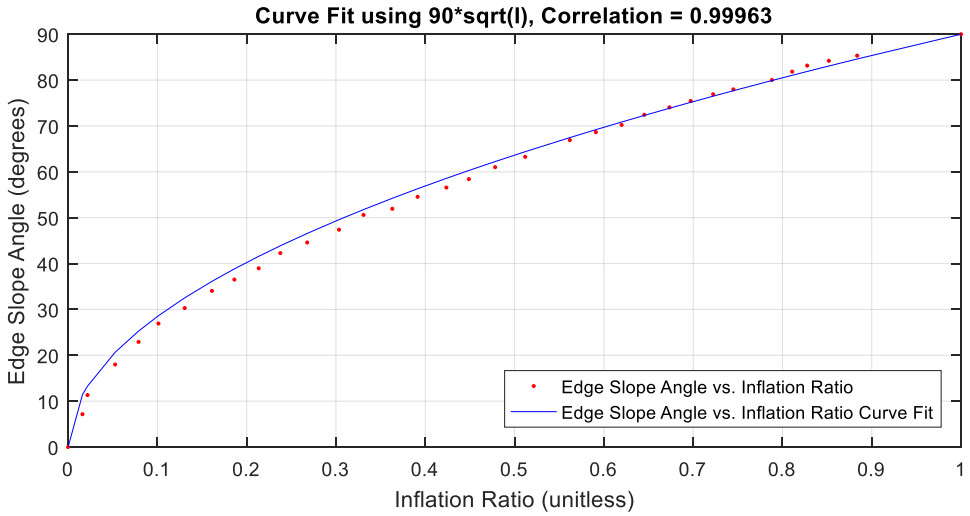

FIGURE 21: Square Root Curve Fit Model with Edge Slope Angle Measurements

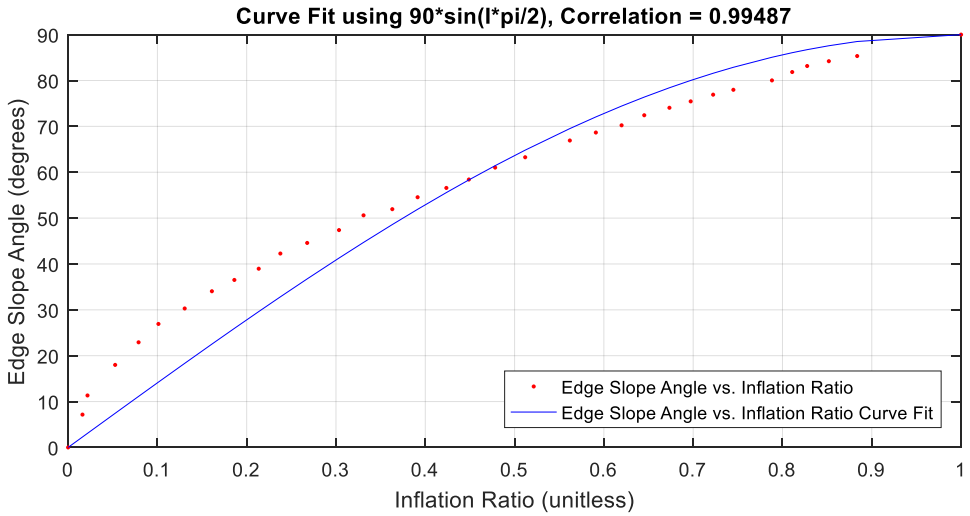

FIGURE 22: Sine Curve Fit Model with Edge Slope Angle Measurements

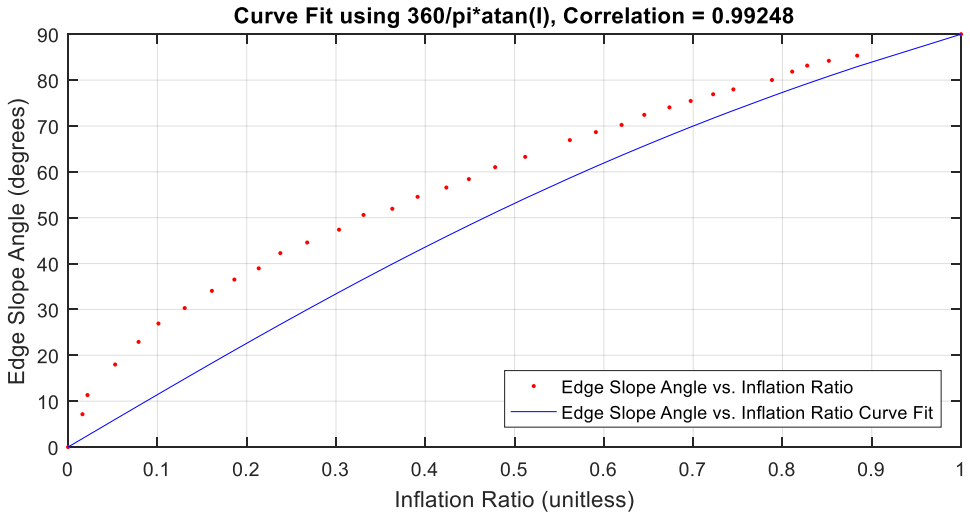

FIGURE 23: Arc-Tangent Curve Fit Model with Edge Slope Angle Measurements

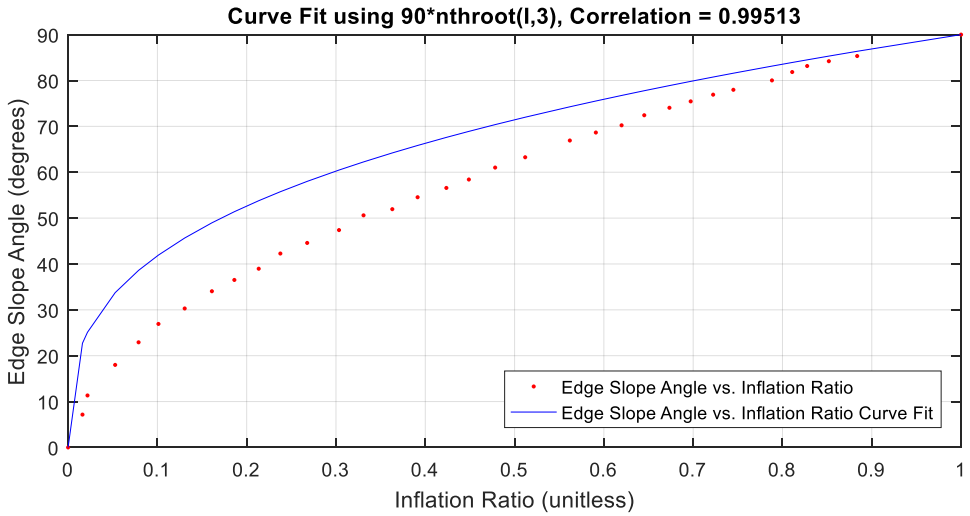

FIGURE 24: Cubic Root Curve Fit Model with Edge Slope Angle Measurements

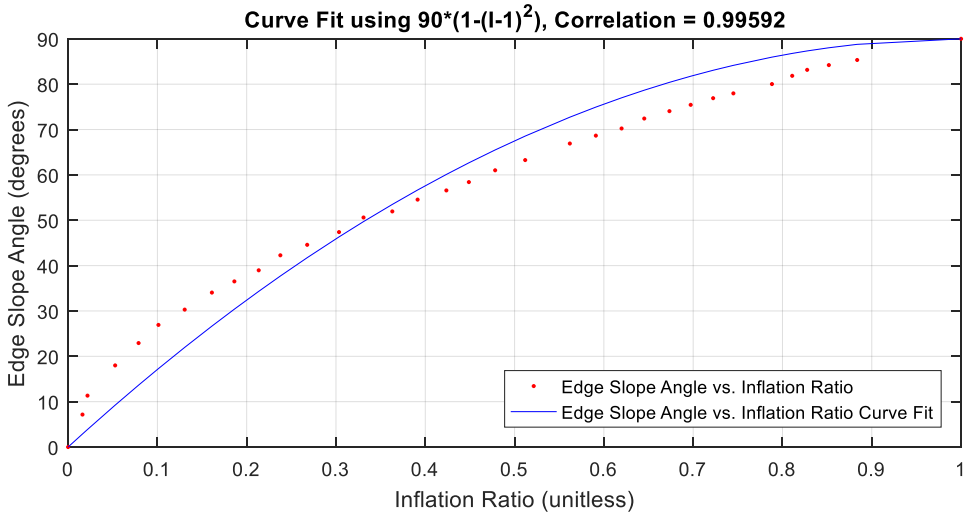

FIGURE 25: Polynomial Curve Fit Model with Edge Slope Angle Measurements

(2.36) has the strongest correlation to the test article measurements, with a correlation of 0.99963, as illustrated in Figure 21. As such, that correlation model was chosen for use to complete the model development of the inflatable aperture antenna. Equation (2.41) converts (2.36) into the form needed for the edge slope. Equation (2.42) then represents (2.41), but eliminating the form of Inflation Ratio term introduced in (2.34).

$$A = \tan\left(\frac{\pi}{2}\sqrt{I}\right) \tag{2.41}$$

$$A = \tan\left(\frac{\pi}{2}\sqrt{\frac{a-r_A}{a-r_B}}\right) \tag{2.42}$$

In (2.41) and (2.42), the additional function used is defined as follows:

- tan( ) is the tangent function

2.4 Inflatable Aperture Antenna Surface Profile Derivation

With the necessary edge slope equation derived in (2.42), the inflatable aperture antenna surface slope derivation, (2.33), can now be completed. Equation (2.43) replaces the edge slope angle, from (2.33), with its derivation from (2.42), while also expanding the denominator.

$$z'(x) = \frac{-x^2}{\sqrt{\frac{r_A^4}{\tan^2\left(\frac{\pi}{2}\sqrt{\frac{a-r_A}{a-r_B}}\right)} + r_A^4 - x^4}} \tag{2.43}$$

Next, a radius substitute variable defined in (2.44), is substituted into (2.43) as (2.45). Equation (2.46) is the integration of (2.45).

$$r_C^4 = \frac{r_A^4}{\tan^2\left(\frac{\pi}{2}\sqrt{\frac{a-r_A}{a-r_B}}\right)} + r_A^4 \tag{2.44}$$

$$z'(x) = \frac{-x^2}{\sqrt{r_C^4 - x^4}} \tag{2.45}$$

$$z(x) = \int_x^{r_C} \frac{t^2}{\sqrt{r_C^4 - t^4}}\, dt \tag{2.46}$$

In (2.44) through (2.46), the additional term used is defined as follows:

- r_C^4 is the radius substitution variable

(2.46) follows the exact same form as (2.24), which was the elliptic Integral, and thus the same simplifications made previously for the Mylar balloon can now be made for the diametrically constrained inflatable aperture antenna, through the use of the parameterization variable u, in (2.47) and (2.48).

$$x(u) = r_C \mathrm{cn}\left(u, \frac{1}{\sqrt{2}}\right) \tag{2.47}$$

$$z(u) = r_C\sqrt{2}\left[\mathrm{E}\left(\mathrm{sn}\left(u, \frac{1}{\sqrt{2}}\right), \frac{1}{\sqrt{2}}\right) - \frac{1}{2}\mathrm{F}\left(\mathrm{sn}\left(u, \frac{1}{\sqrt{2}}\right), \frac{1}{\sqrt{2}}\right)\right] \tag{2.48}$$

Finally, the radius substitution variable, r_C, is simplified in (2.49).

$$r_C = r_A \sqrt[4]{1 + \cot^2\left(\frac{\pi}{2}\sqrt{\frac{a - r_A}{a - r_B}}\right)} \tag{2.49}$$

In (2.49), the additional function used is defined as follows:

- $\cot(\,)$ is the co-tangent function

As (2.47) and (2.48) are still parameterized, the limits on the parameterization variable, u, must be understood so that its representation is valid in this form of the problem. For this problem, the limits of $x(u)$ need to be maintained between zero and r_A, as shown next in (2.50).

$$0 \le x(u) \le r_A \tag{2.50}$$

One natural maximum limit of elliptic Integrals comes from the elliptic Integral of the first kind. The value of $x(u)$ at this maximum value of parameterization variable u is given in (2.51).

$$x\left(\mathrm{K}\left(\frac{1}{\sqrt{2}}\right)\right) = 0 \tag{2.51}$$

In (2.51), the additional function used is defined as follows:

- $\mathrm{K}\left(\frac{1}{\sqrt{2}}\right)$ is the elliptic Integral of the first kind

Therefore, the limits of the parameterization variable u is shown in (2.52).

$$u_0 \le u \le \mathrm{K}\left(\frac{1}{\sqrt{2}}\right) \tag{2.52}$$

In (2.52), the additional term used is defined as follows:

- u_0 is the minimum value of the parameterization variable u

Here, u_0 corresponds to the minimum value of the parameterization variable, and since the maximum value corresponds to the minimum value of $x(u)$, this minimum value corresponds to the maximum value of $x(u)$, which is already known to be r_A from (2.50). Therefore, this minimum parameterization value is derived from (2.47) at this point on the range of (2.50), as shown in (2.53), with the inverse Jacobi cosine function, $arccn(\,)$.

$$r_A = r_C \operatorname{cn}\left(u_0, \frac{1}{\sqrt{2}}\right)$$

$$r_A = r_A \sqrt[4]{1 + \cot^2\left(\frac{\pi}{2}\sqrt{\frac{a-r_A}{a-r_B}}\right)} \operatorname{cn}\left(u_0, \frac{1}{\sqrt{2}}\right)$$

$$\operatorname{cn}\left(u_0, \frac{1}{\sqrt{2}}\right) = \frac{1}{\sqrt[4]{1+\cot^2\left(\frac{\pi}{2}\sqrt{\frac{a-r_A}{a-r_B}}\right)}}$$

$$u_0 = \operatorname{arccn}\left(\frac{1}{\sqrt[4]{1+\cot^2\left(\frac{\pi}{2}\sqrt{\frac{a-r_A}{a-r_B}}\right)}}, \frac{1}{\sqrt{2}}\right) \tag{2.53}$$

This range of parameterization variable u also applies to $z(u)$, but visual inspection of performance shows that this new non-zero limit on u means the limits of $z(u)$ need to be maintained between zero and depth of the surface off of the axis, as stated in (2.54).

$$0 \leq z(u) \leq Depth \tag{2.54}$$

Therefore, (2.48) needs to be shifted by a constant factor to maintain the lower limit of (2.54), as shown next in (2.55).

$$z(u) = r_C\sqrt{2}\left[\mathrm{E}\left(\mathrm{sn}\left(u,\frac{1}{\sqrt{2}}\right),\frac{1}{\sqrt{2}}\right) - \frac{1}{2}\mathrm{F}\left(\mathrm{sn}\left(u,\frac{1}{\sqrt{2}}\right),\frac{1}{\sqrt{2}}\right)\right] + C \tag{2.55}$$

In (2.55), the additional term used is defined as follows:

- C is the constant offset factor

The solution to this constant offset factor goes back to lower limit on $z(u)$, as expressed in (2.56).

$$0 = r_C\sqrt{2}\left[\mathrm{E}\left(\mathrm{sn}\left(u,\frac{1}{\sqrt{2}}\right),\frac{1}{\sqrt{2}}\right) - \frac{1}{2}\mathrm{F}\left(\mathrm{sn}\left(u,\frac{1}{\sqrt{2}}\right),\frac{1}{\sqrt{2}}\right)\right] + C \tag{2.56}$$

When the shift is applied correctly, the value of $x(u) = r_A$, which means the parameterization variable takes on the form expressed in (2.53). Therefore, the solution to the constant offset factor is provided in (2.57), and the final form of the $z(u)$ expression is given in (2.58), both using the limits of the parameterization variable in (2.59).

$$C = -r_C\sqrt{2}\left[\mathrm{E}\left(\mathrm{sn}\left(u_0,\frac{1}{\sqrt{2}}\right),\frac{1}{\sqrt{2}}\right) - \frac{1}{2}\mathrm{F}\left(\mathrm{sn}\left(u_0,\frac{1}{\sqrt{2}}\right),\frac{1}{\sqrt{2}}\right)\right] \tag{2.57}$$

$$z(u) = \begin{matrix} r_C\sqrt{2}\left[\mathrm{E}\left(\mathrm{sn}\left(u,\frac{1}{\sqrt{2}}\right),\frac{1}{\sqrt{2}}\right) - \frac{1}{2}\mathrm{F}\left(\mathrm{sn}\left(u,\frac{1}{\sqrt{2}}\right),\frac{1}{\sqrt{2}}\right)\right] \\ -r_C\sqrt{2}\left[\mathrm{E}\left(\mathrm{sn}\left(u_0,\frac{1}{\sqrt{2}}\right),\frac{1}{\sqrt{2}}\right) - \frac{1}{2}\mathrm{F}\left(\mathrm{sn}\left(u_0,\frac{1}{\sqrt{2}}\right),\frac{1}{\sqrt{2}}\right)\right] \end{matrix} \tag{2.58}$$

$$\mathrm{arccn}\left(\frac{1}{\sqrt[4]{1+\cot^2\left(\frac{\pi}{2}\sqrt{\frac{a-r_A}{a-r_B}}\right)}},\frac{1}{\sqrt{2}}\right) \leq u \leq \mathrm{K}\left(\frac{1}{\sqrt{2}}\right) \tag{2.59}$$

In (2.59), the additional function used is defined as follows:

- arccn( ) is the inverse Jacobi cosine function

This derivation in (2.47) and (2.58) still relies on parameterization variable u, using the limits in (2.59). While this is useful in mathematical applications, it is not useful for engineering analysis performed in similar manners as that of paraboloidal antennas, which take the form of (2.60).

$$Z(X,Y) = \frac{(X^2+Y^2)}{4f} \tag{2.60}$$

In (2.60), the additional terms used are defined as follows:

- $Z(X,Y)$ is the depth of the parabolic antenna as a function of radial direction axis variables X and Y
- X is the paraboloidal antenna radial direction axis variable
- Y is the paraboloidal antenna radial direction axis variable
- f is the paraboloidal antenna focal length

Therefore, it is desired to eliminate the parameterization variables and solve the inflatable aperture antenna surface in the form of $z(x,y)$. This is accomplished in (2.61) through the inverse Jacobi cosine function, as a way to solve the parameterization variable u in (2.47). Equation (2.61) is then substituted in (2.57) to obtain the non-parameterized definition of the inflatable aperture antenna surface, in (2.62), using the same definition before for variables u_0 and r_C.

$$u(x) = \operatorname{arccn}\left(\frac{x}{r_C}, \frac{1}{\sqrt{2}}\right) \tag{2.61}$$

$$z(x) = \begin{matrix} r_C\sqrt{2}\left[\mathrm{E}\left(\operatorname{sn}\left(\operatorname{arccn}\left(\frac{x}{r_C},\frac{1}{\sqrt{2}}\right),\frac{1}{\sqrt{2}}\right),\frac{1}{\sqrt{2}}\right)-\frac{1}{2}\mathrm{F}\left(\operatorname{sn}\left(\operatorname{arccn}\left(\frac{x}{r_C},\frac{1}{\sqrt{2}}\right),\frac{1}{\sqrt{2}}\right),\frac{1}{\sqrt{2}}\right)\right] \\ -r_C\sqrt{2}\left[\mathrm{E}\left(\operatorname{sn}\left(u_0,\frac{1}{\sqrt{2}}\right),\frac{1}{\sqrt{2}}\right)-\frac{1}{2}\mathrm{F}\left(\operatorname{sn}\left(u_0,\frac{1}{\sqrt{2}}\right),\frac{1}{\sqrt{2}}\right)\right] \end{matrix} \tag{2.62}$$

The expansion of the surface into the third dimension will now follow the same framework as for the Mylar balloon into (2.27) through (2.29), since this is not a parameterized definition. Instead, the length of x in (2.62) will be replaced by the length of the combination of x and y, shown in (2.63), with (2.64) showing the final form of the inflatable antenna surface.

$$w = \sqrt{x^2 + y^2} \tag{2.63}$$

$$z(x,y) = \begin{matrix} r_C\sqrt{2}\left[\mathrm{E}\left(\mathrm{sn}\left(\mathrm{arccn}\left(\frac{\sqrt{x^2+y^2}}{r_C},\frac{1}{\sqrt{2}}\right),\frac{1}{\sqrt{2}}\right),\frac{1}{\sqrt{2}}\right)-\frac{1}{2}\mathrm{F}\left(\mathrm{sn}\left(\mathrm{arccn}\left(\frac{\sqrt{x^2+y^2}}{r_C},\frac{1}{\sqrt{2}}\right),\frac{1}{\sqrt{2}}\right),\frac{1}{\sqrt{2}}\right)\right] \\ -r_C\sqrt{2}\left[\mathrm{E}\left(\mathrm{sn}\left(u_0,\frac{1}{\sqrt{2}}\right),\frac{1}{\sqrt{2}}\right)-\frac{1}{2}\mathrm{F}\left(\mathrm{sn}\left(u_0,\frac{1}{\sqrt{2}}\right),\frac{1}{\sqrt{2}}\right)\right] \end{matrix} \tag{2.64}$$

In (2.63), the additional term used is defined as follows:

- w is the magnitude of the radial direction axis variables

2.5 Inflatable Aperture Antenna Surface Profile Validation

Laser Radar metrology testing was performed over the entire surface of the test article at each Inflation Ratio test point, as described in Section III.B Edge Slope Derivation. This testing involved the laser scan measuring the entire surface of the inflatable test article's surface within its diametrically constrained perimeter. This measured surface data was processed to determine the average measured depth from the vertex of the surface. This data was then compared to the predicted surface model, which was derived in (2.64). Correlation assessments of the average measured depth from the vertex of the surface against the predicted surface model are provided in Table III for all of the Inflation Ratio test points, while Table IV provides the RMS assessments between

the same datasets. Plots of these datasets that underwent the correlation assessments are shown in Figures 26 through 57 for the 32 Inflation Ratio test points.

TABLE III: Correlation of Off-Vertex Depth Performance

Inflation Ratio	Correlation	Inflation Ratio	Correlation	Inflation Ratio	Correlation
0.01610	0.99405	0.30339	0.99972	0.64521	0.99972
0.02172	0.99773	0.33085	0.99984	0.67341	0.99971
0.05269	0.99919	0.36306	0.99984	0.69722	0.99947
0.07892	0.99953	0.39141	0.99985	0.72235	0.99958
0.10117	0.99951	0.42359	0.99978	0.74501	0.99936
0.13056	0.99964	0.44881	0.99971	0.78822	0.99912
0.16104	0.99965	0.47824	0.99975	0.81090	0.99892
0.18619	0.99969	0.51188	0.99983	0.82766	0.99705
0.21346	0.99987	0.56186	0.99961	0.85193	0.99743
0.23770	0.99976	0.59101	0.99960	0.88366	0.99591
0.26773	0.99973	0.61984	0.99946		

TABLE IV: Root-Mean-Square of Off-Vertex Depth Performance

Inflation Ratio	RMS (inches)	Inflation Ratio	RMS (inches)	Inflation Ratio	RMS (inches)
0.01610	8.0241e-2	0.30339	9.2262e-2	0.64521	8.8610e-2
0.02172	5.4313e-2	0.33085	8.8614e-2	0.67341	1.0560e-1
0.05269	4.3107e-2	0.36306	1.0324e-1	0.69722	1.1557e-1
0.07892	4.3663e-2	0.39141	9.9497e-2	0.72235	9.1278e-2
0.10117	4.3136e-2	0.42359	9.6326e-2	0.74501	1.3076e-1
0.13056	4.2488e-2	0.44881	1.0257e-1	0.78822	8.3695e-2
0.16104	5.6605e-2	0.47824	1.0310e-1	0.81090	9.2674e-2
0.18619	6.5102e-2	0.51188	9.8272e-2	0.82766	1.3623e-1
0.21346	5.6469e-2	0.56186	8.4268e-2	0.85193	1.2088e-1
0.23770	8.7152e-2	0.59101	8.8070e-2	0.88366	1.8325e-1
0.26773	9.3182e-2	0.61984	1.1383e-1		

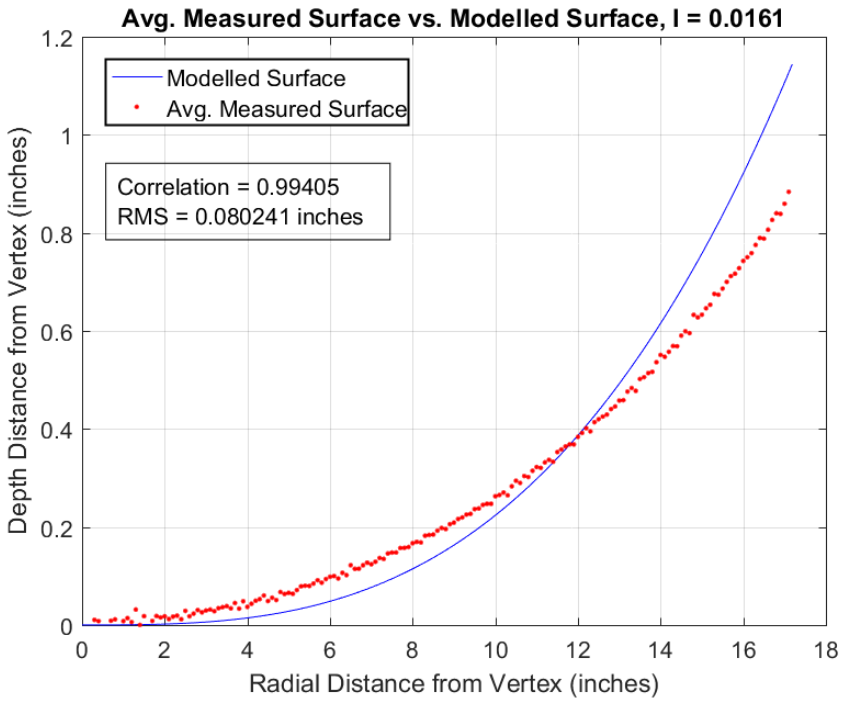

FIGURE 26: Surface Shape Validation Data Comparison at Inflation Ratio of 0.01610

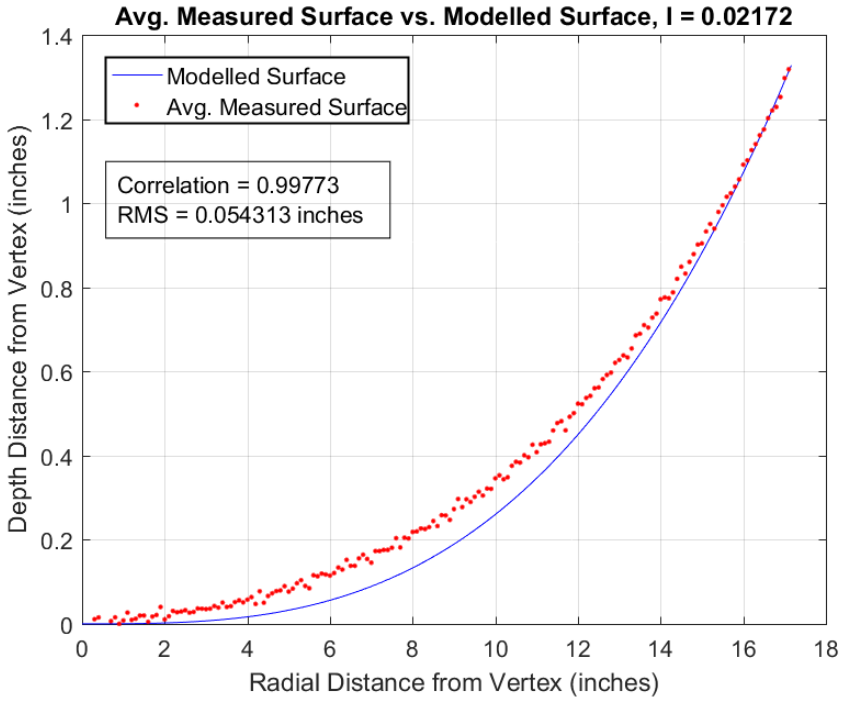

FIGURE 27: Surface Shape Validation Data Comparison at Inflation Ratio of 0.02172

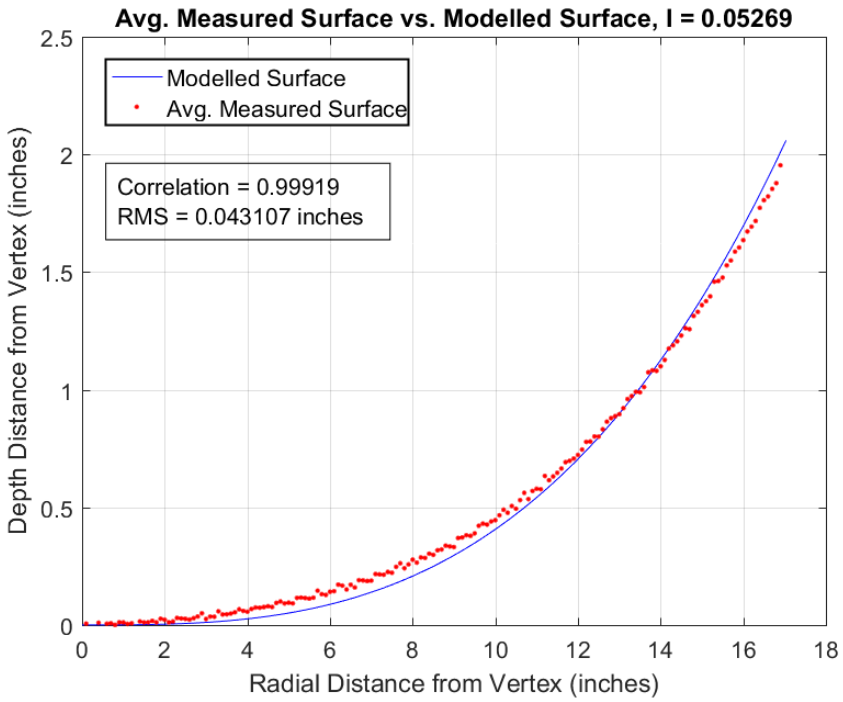

FIGURE 28: Surface Shape Validation Data Comparison at Inflation Ratio of 0.05269

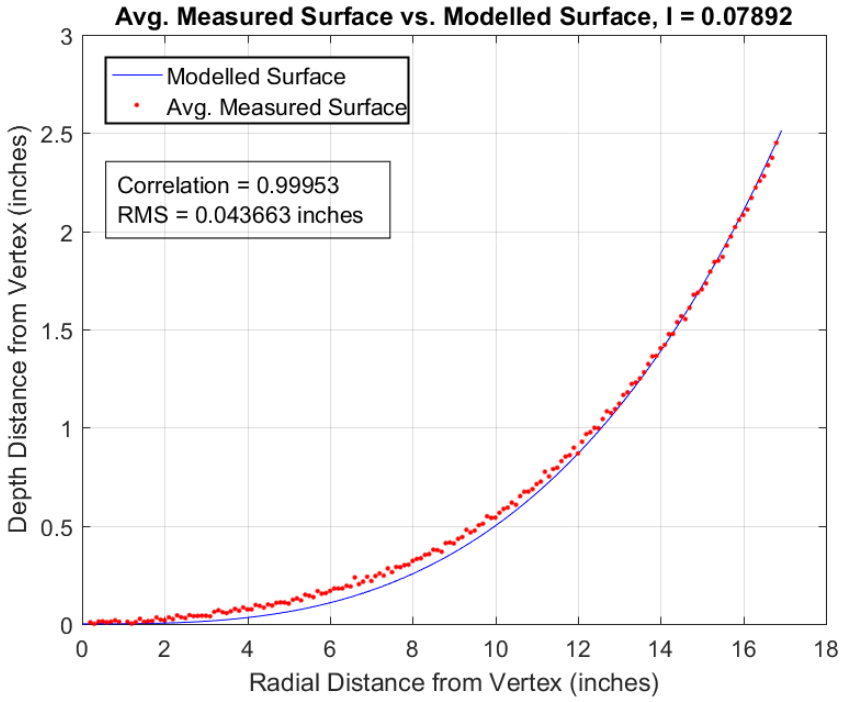

FIGURE 29: Surface Shape Validation Data Comparison at Inflation Ratio of 0.07892

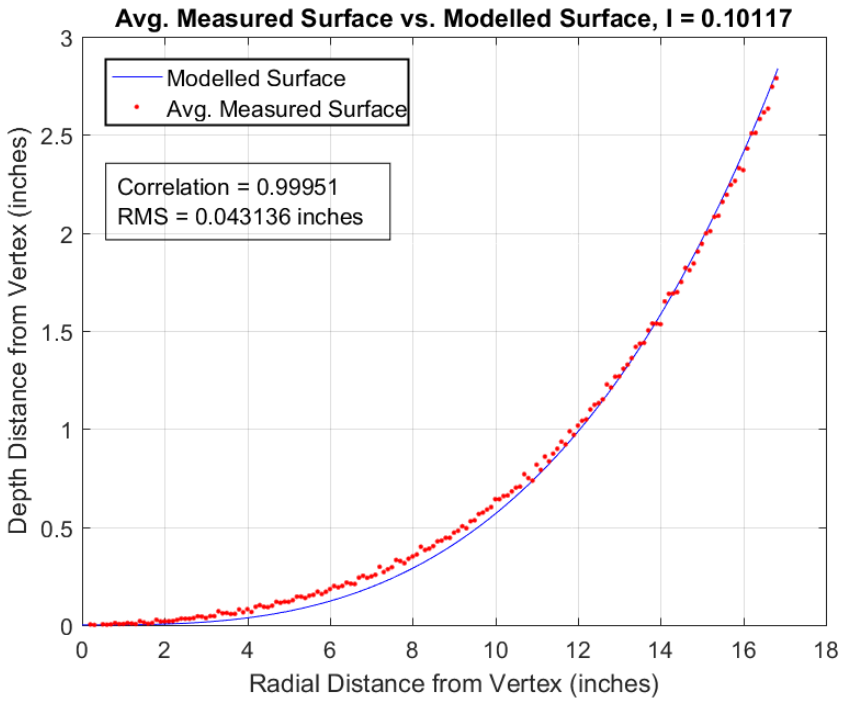

FIGURE 30: Surface Shape Validation Data Comparison at Inflation Ratio of 0.10117

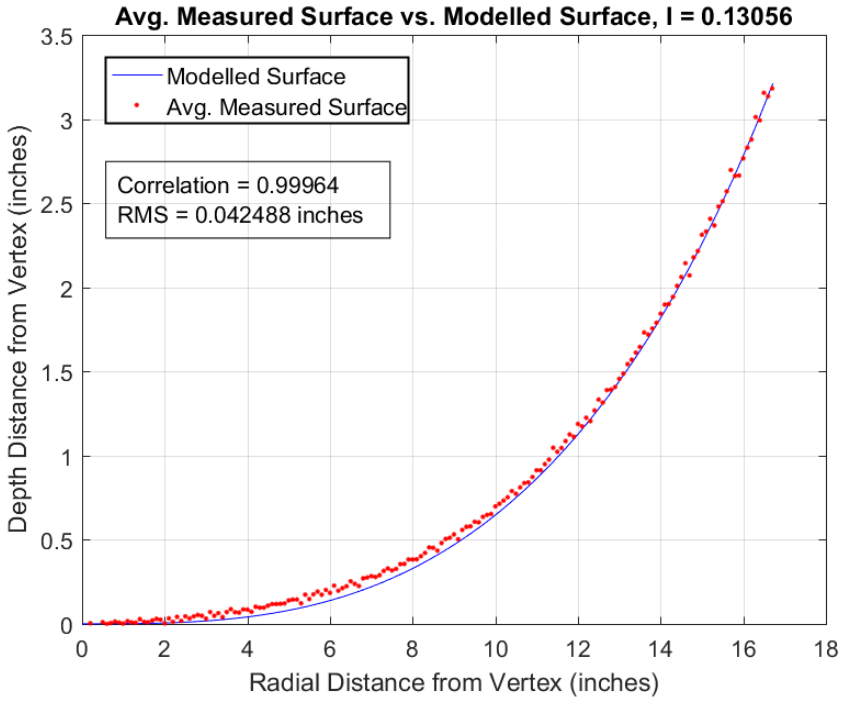

FIGURE 31: Surface Shape Validation Data Comparison at Inflation Ratio of 0.13056

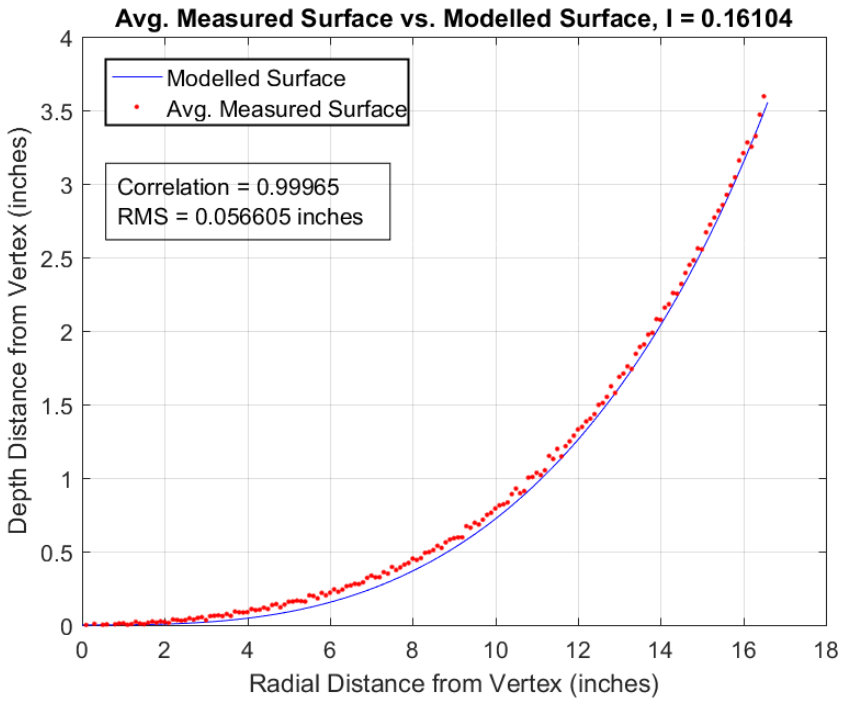

FIGURE 32: Surface Shape Validation Data Comparison at Inflation Ratio of 0.16104

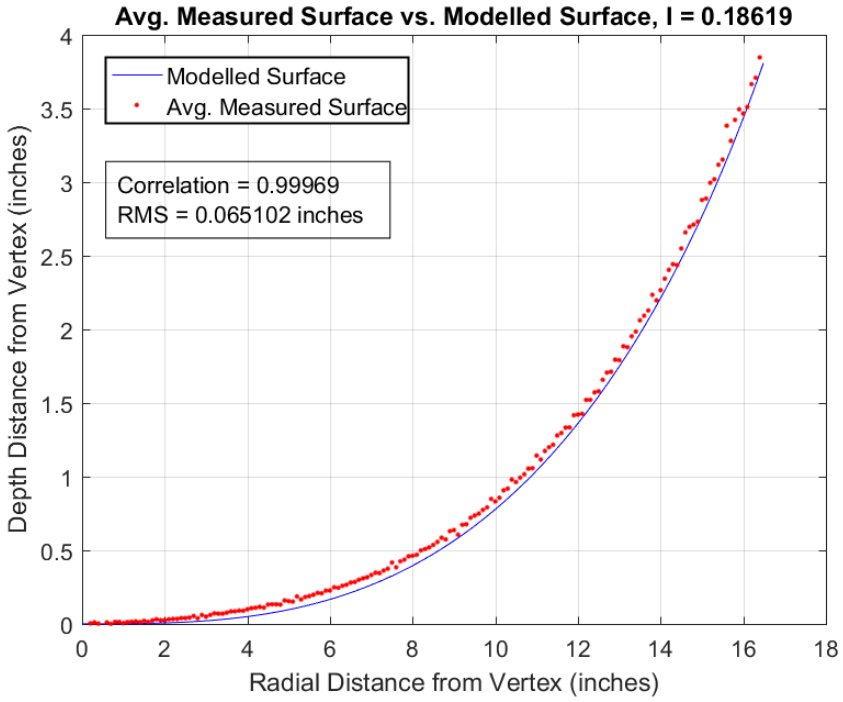

FIGURE 33: Surface Shape Validation Data Comparison at Inflation Ratio of 0.18619

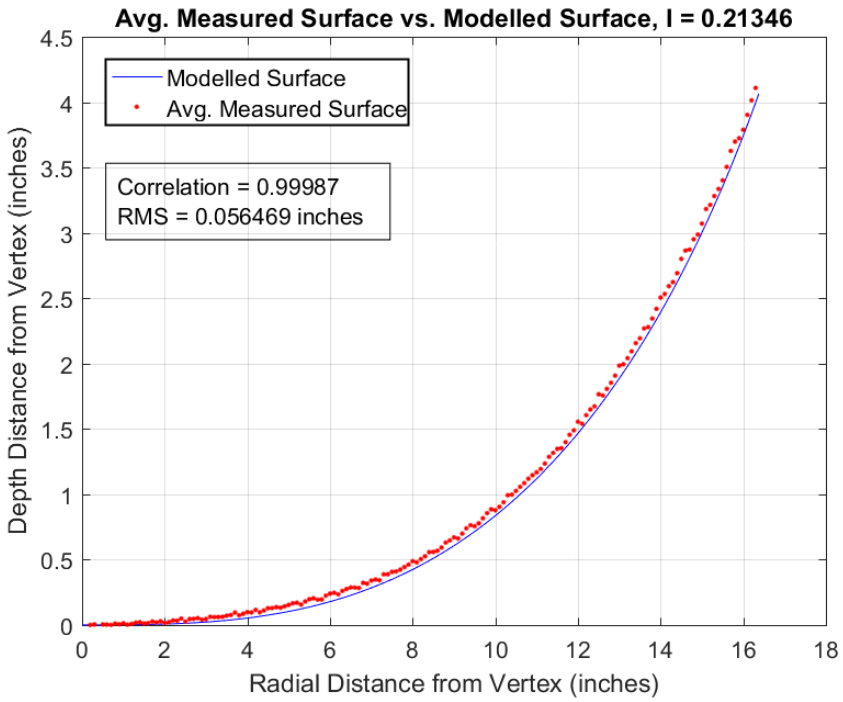

FIGURE 34: Surface Shape Validation Data Comparison at Inflation Ratio of 0.21346

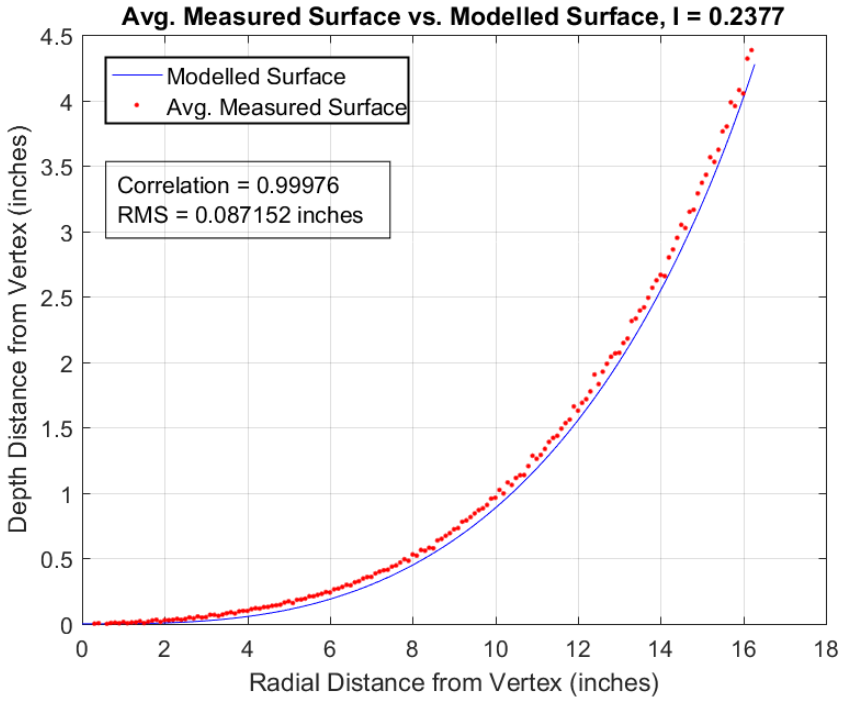

FIGURE 35: Surface Shape Validation Data Comparison at Inflation Ratio of 0.23770

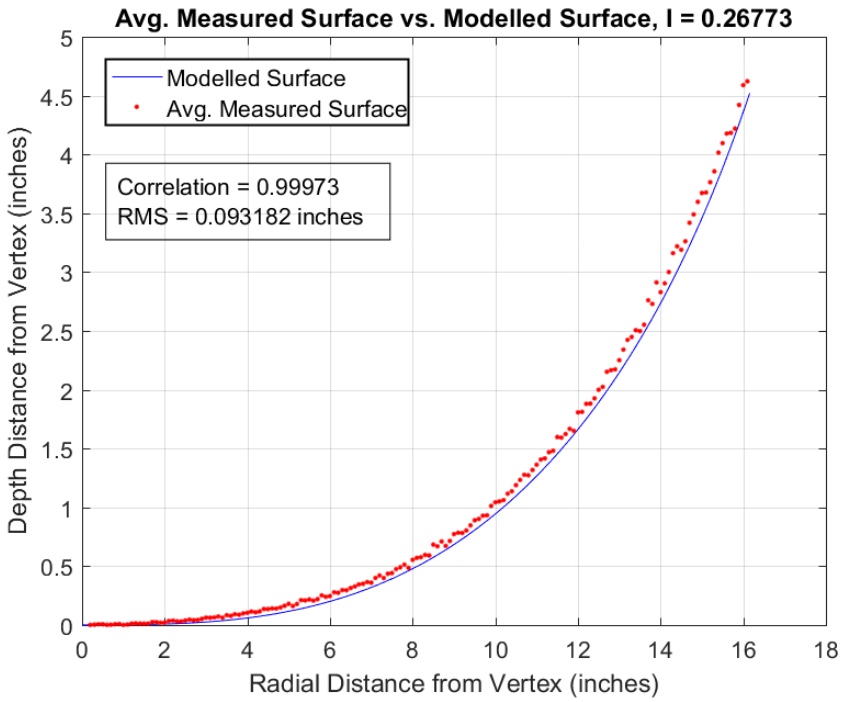

FIGURE 36: Surface Shape Validation Data Comparison at Inflation Ratio of 0.26773

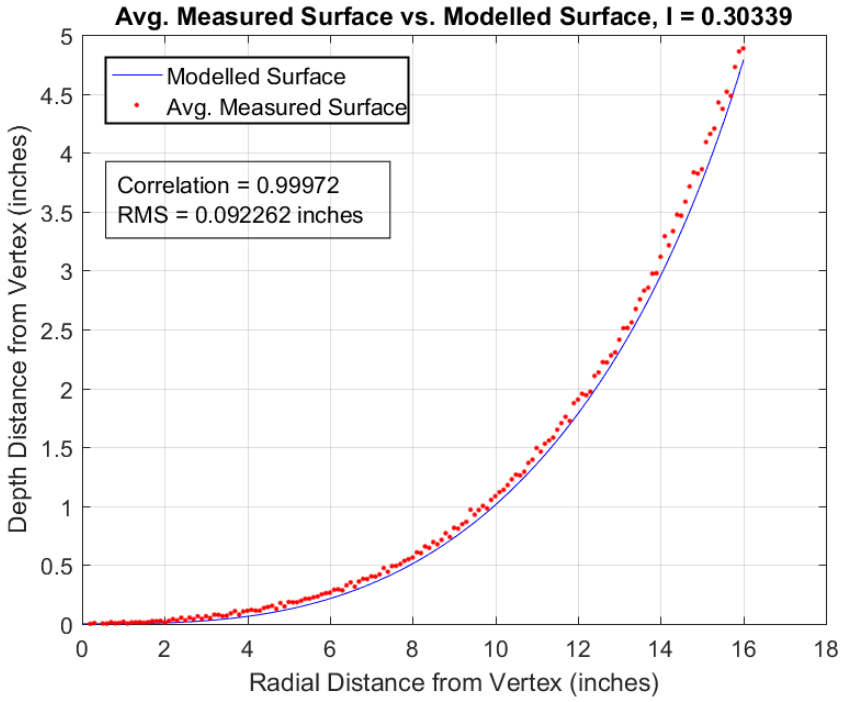

FIGURE 37: Surface Shape Validation Data Comparison at Inflation Ratio of 0.30339

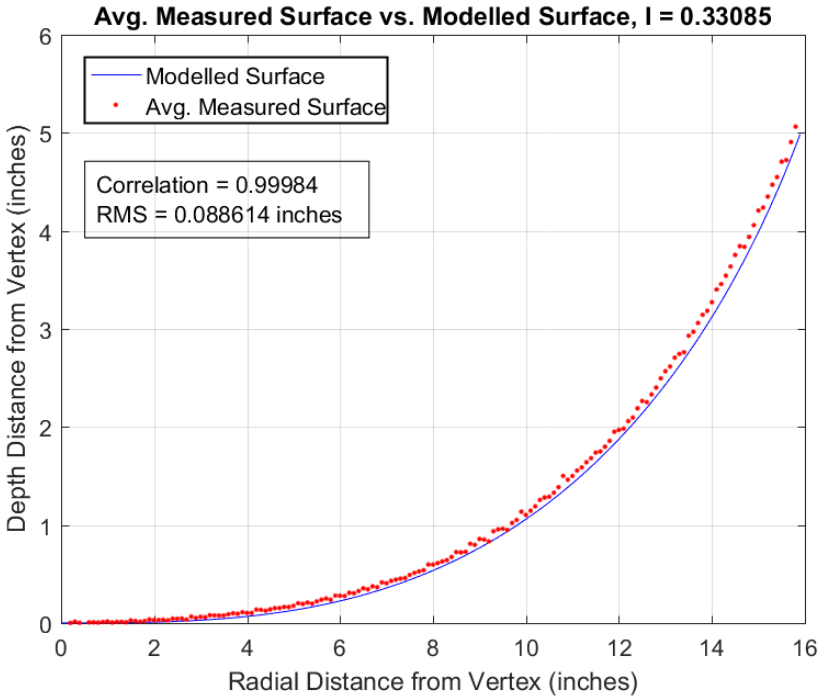

FIGURE 38: Surface Shape Validation Data Comparison at Inflation Ratio of 0.33085

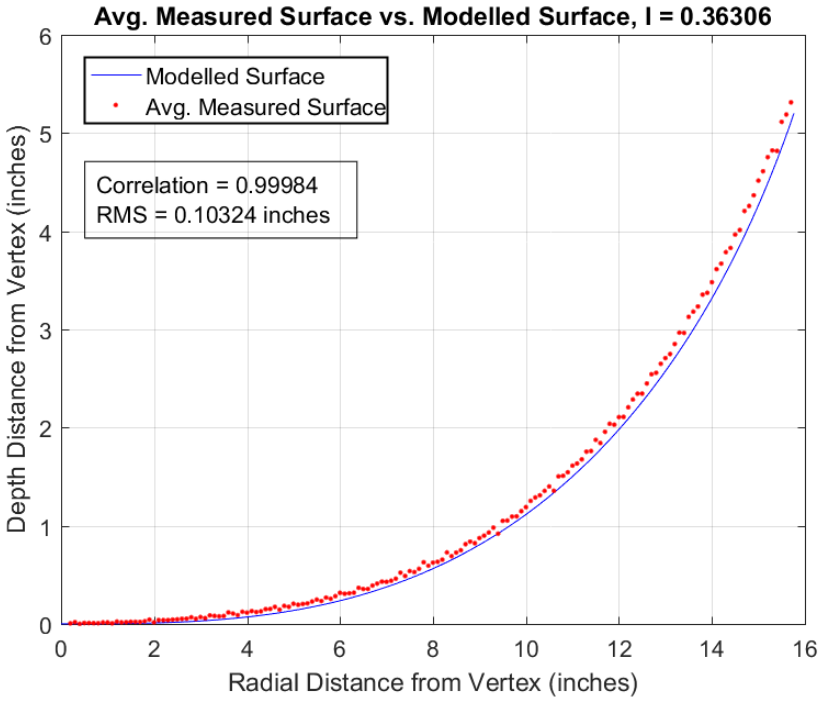

FIGURE 39: Surface Shape Validation Data Comparison at Inflation Ratio of 0.36306

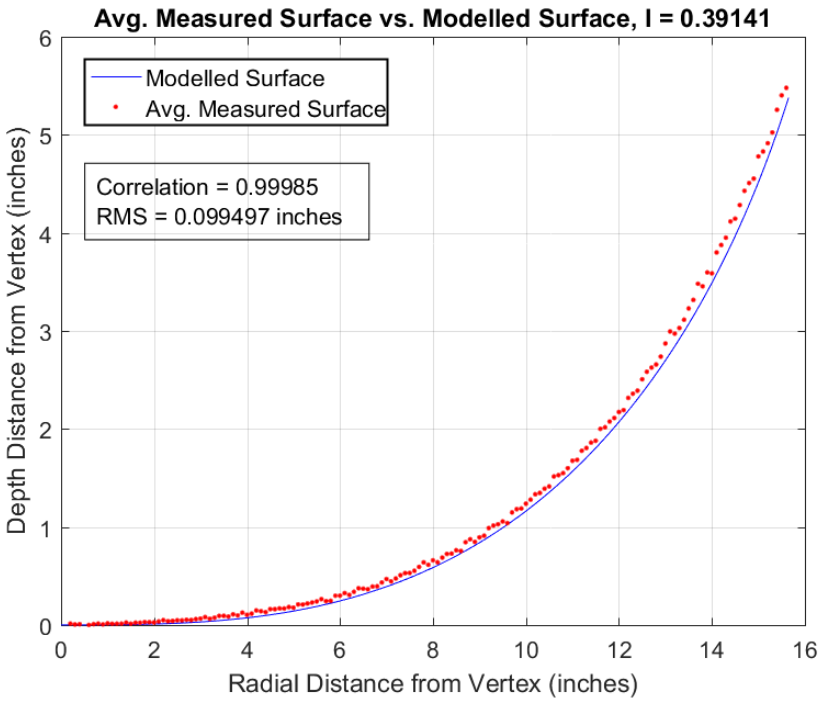

FIGURE 40: Surface Shape Validation Data Comparison at Inflation Ratio of 0.39141

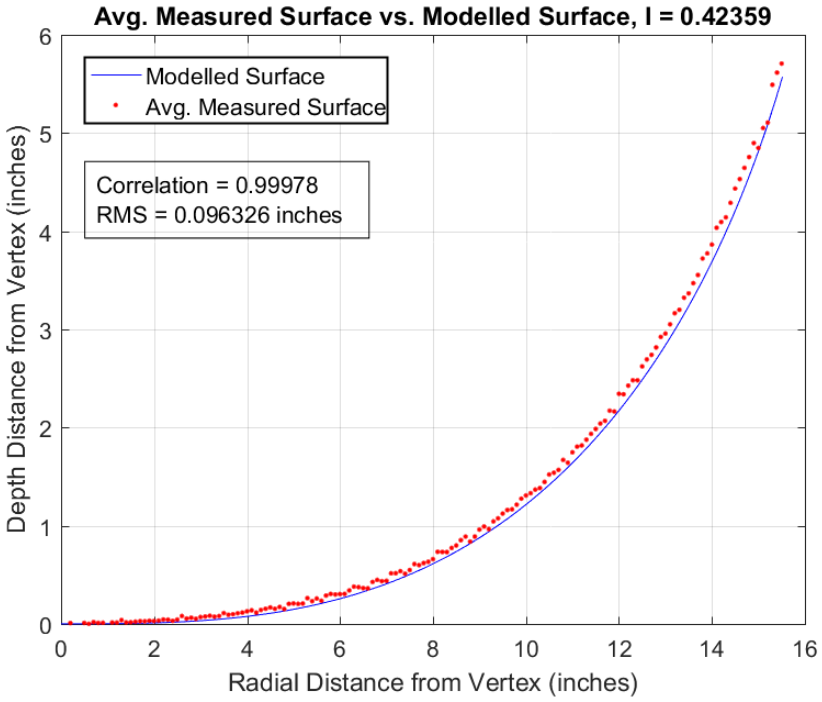

FIGURE 41: Surface Shape Validation Data Comparison at Inflation Ratio of 0.42359

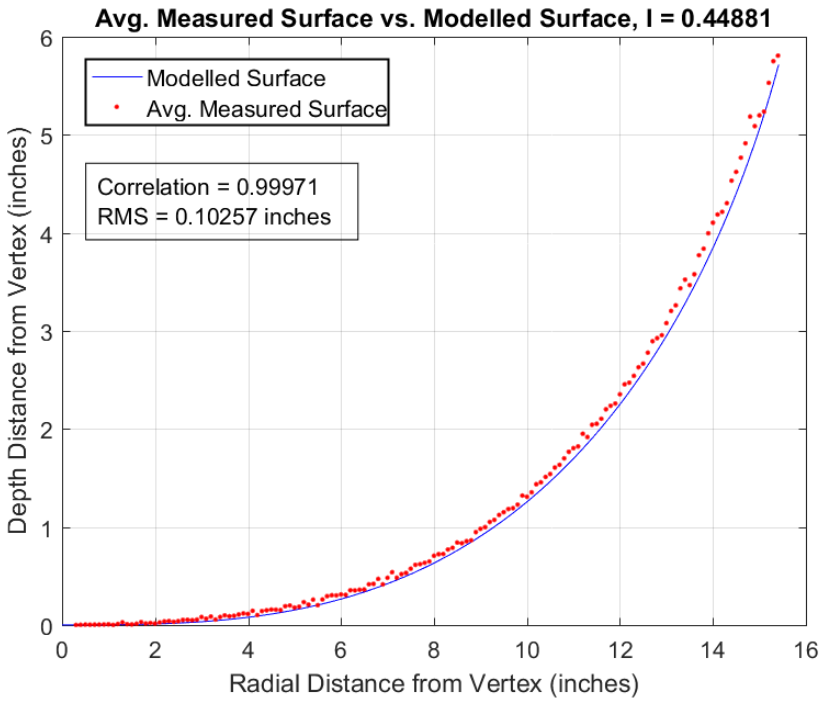

FIGURE 42: Surface Shape Validation Data Comparison at Inflation Ratio of 0.44881

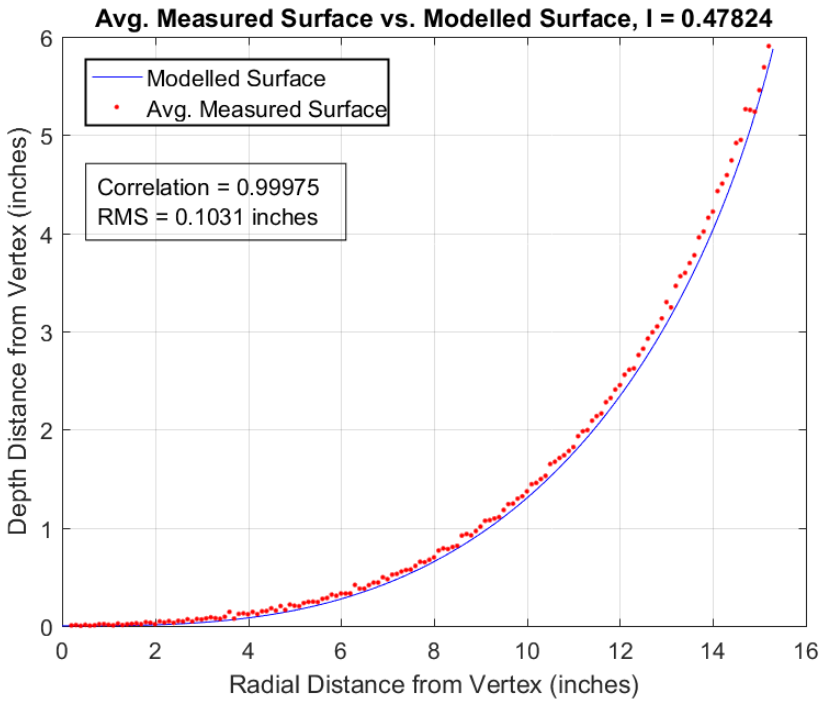

FIGURE 43: Surface Shape Validation Data Comparison at Inflation Ratio of 0.47824

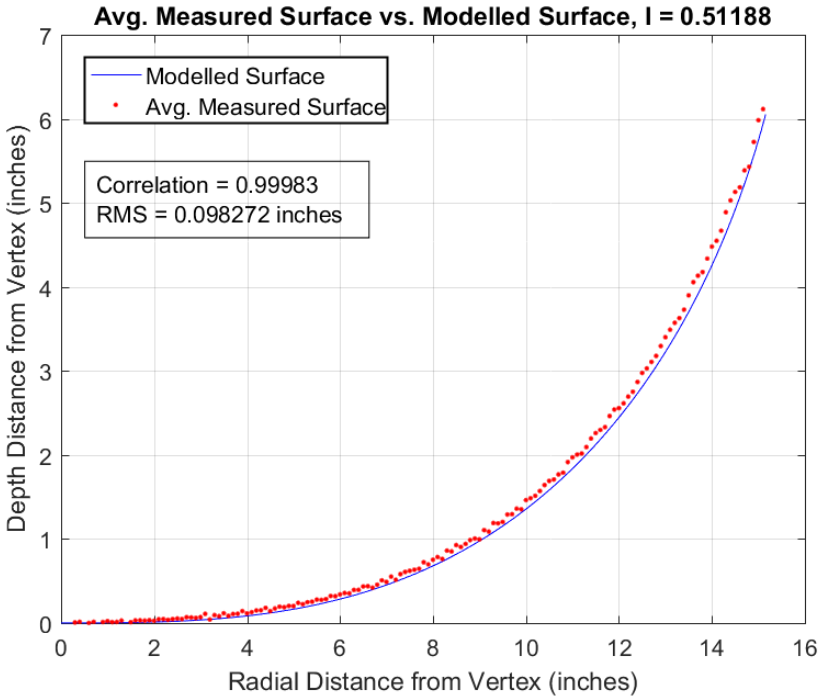

FIGURE 44: Surface Shape Validation Data Comparison at Inflation Ratio of 0.51188

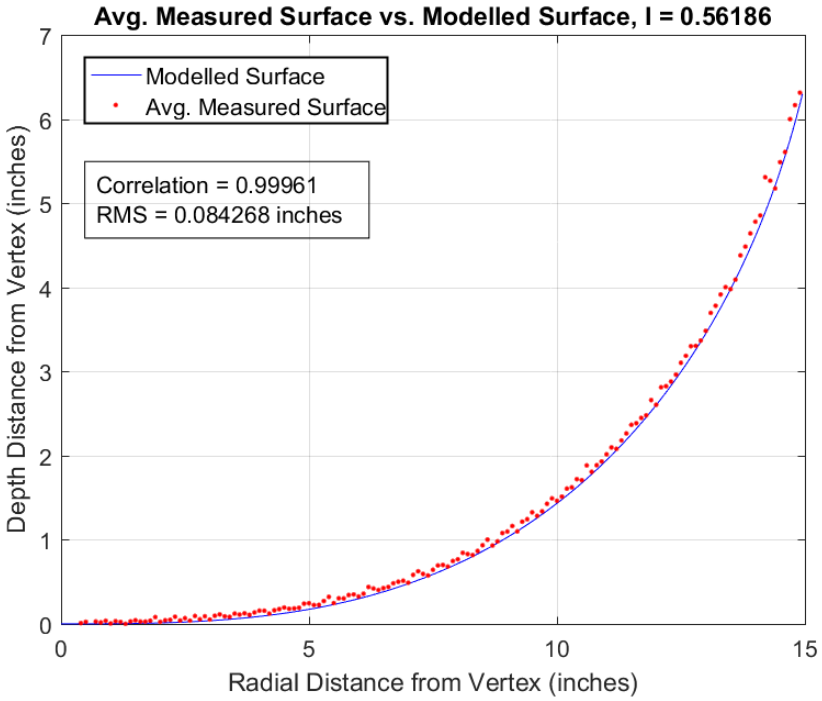

FIGURE 45: Surface Shape Validation Data Comparison at Inflation Ratio of 0.56186

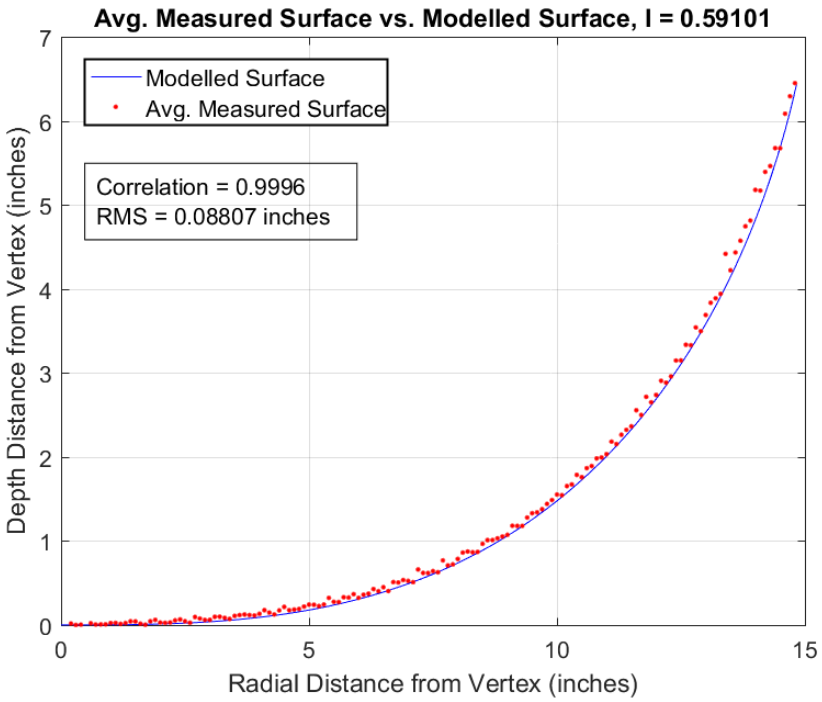

FIGURE 46: Surface Shape Validation Data Comparison at Inflation Ratio of 0.59101

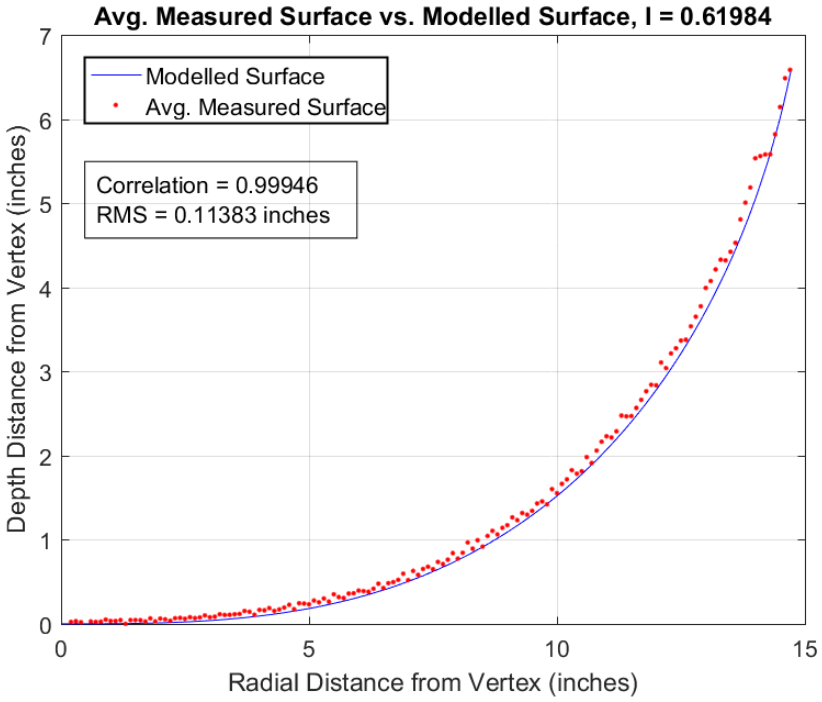

FIGURE 47: Surface Shape Validation Data Comparison at Inflation Ratio of 0.61984

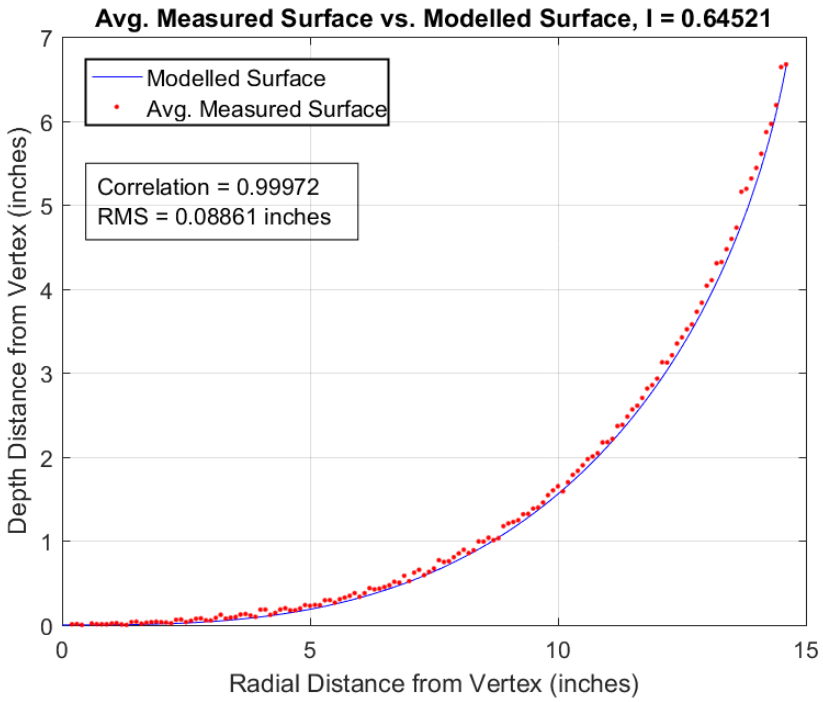

FIGURE 48: Surface Shape Validation Data Comparison at Inflation Ratio of 0.64521

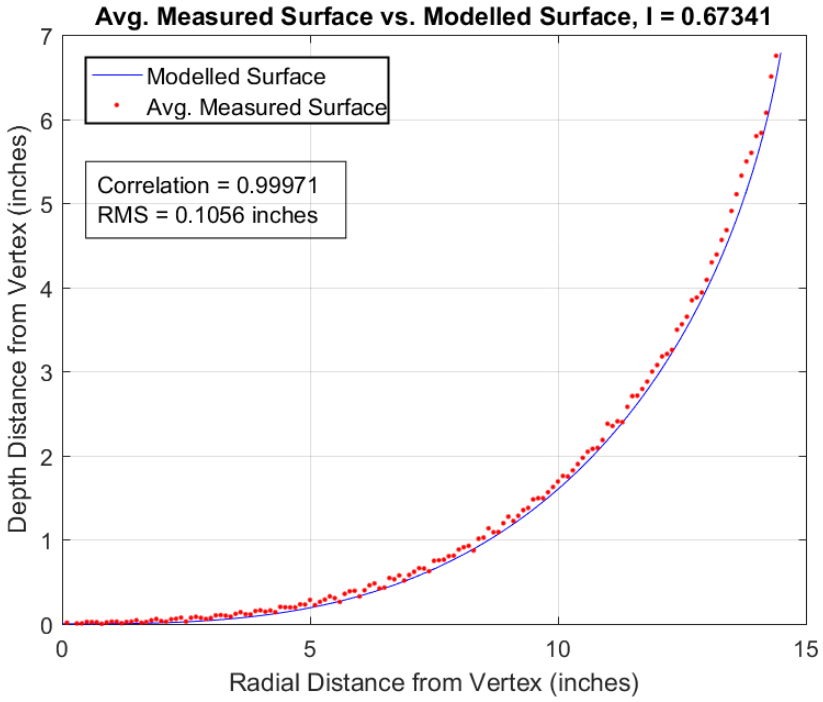

FIGURE 49: Surface Shape Validation Data Comparison at Inflation Ratio of 0.67341

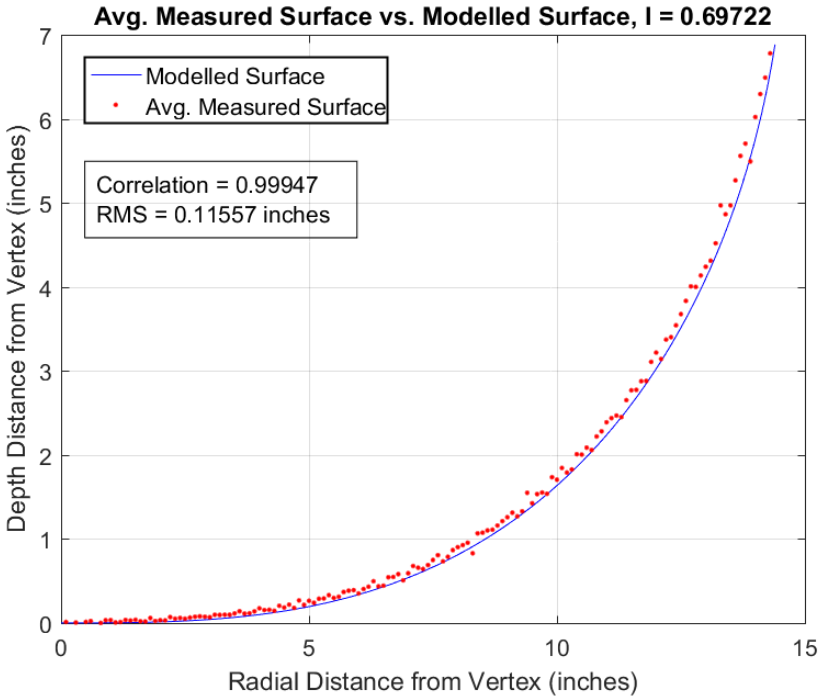

FIGURE 50: Surface Shape Validation Data Comparison at Inflation Ratio of 0.69722

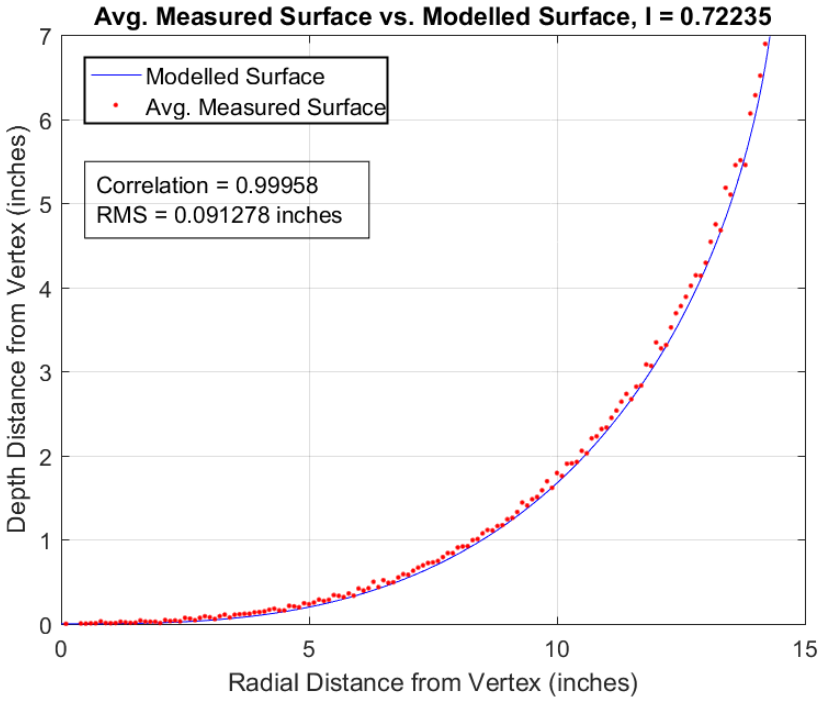

FIGURE 51: Surface Shape Validation Data Comparison at Inflation Ratio of 0.72235

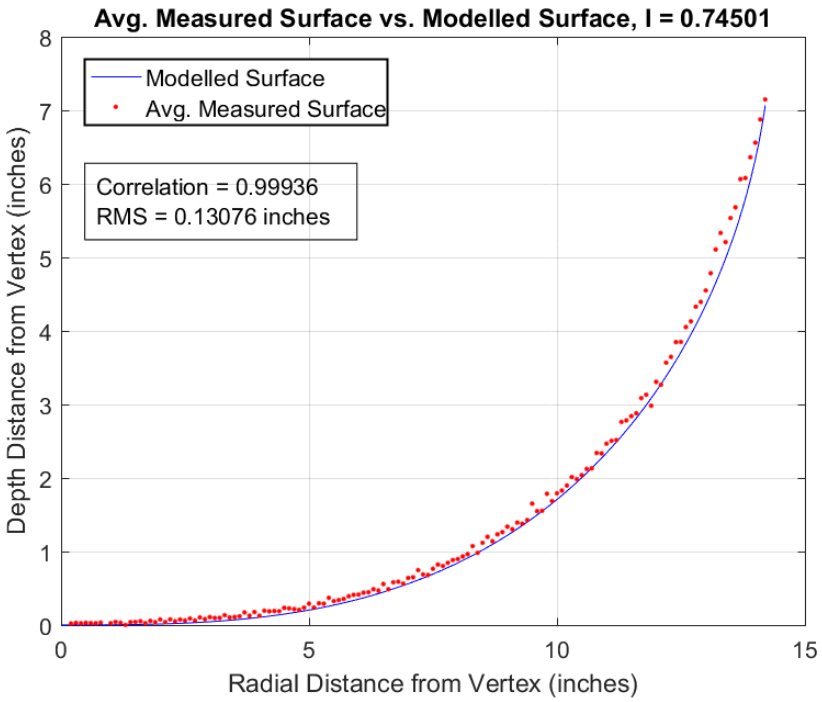

FIGURE 52: Surface Shape Validation Data Comparison at Inflation Ratio of 0.74501

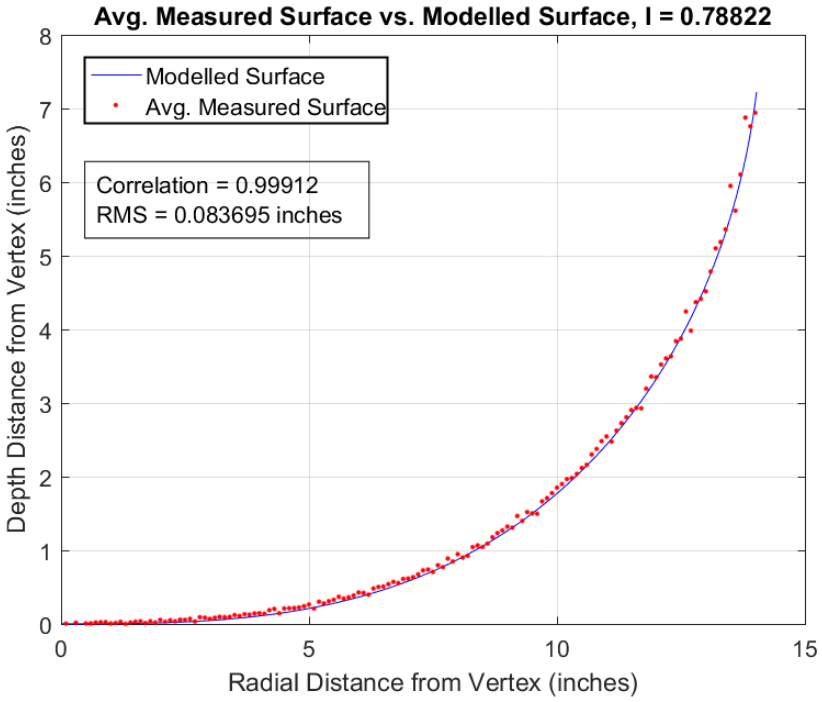

FIGURE 53: Surface Shape Validation Data Comparison at Inflation Ratio of 0.78822

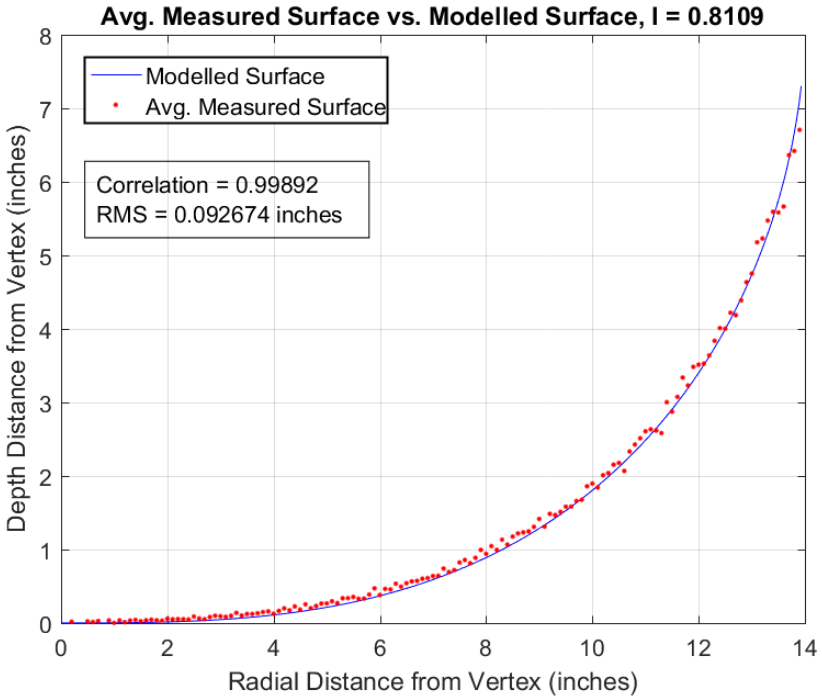

FIGURE 54: Surface Shape Validation Data Comparison at Inflation Ratio of 0.81090

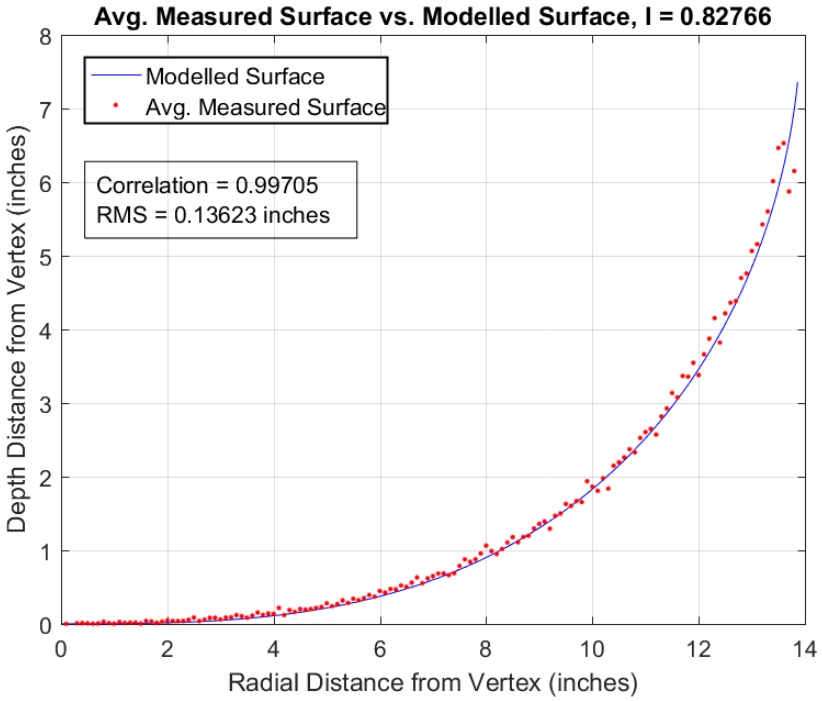

FIGURE 55: Surface Shape Validation Data Comparison at Inflation Ratio of 0.82766

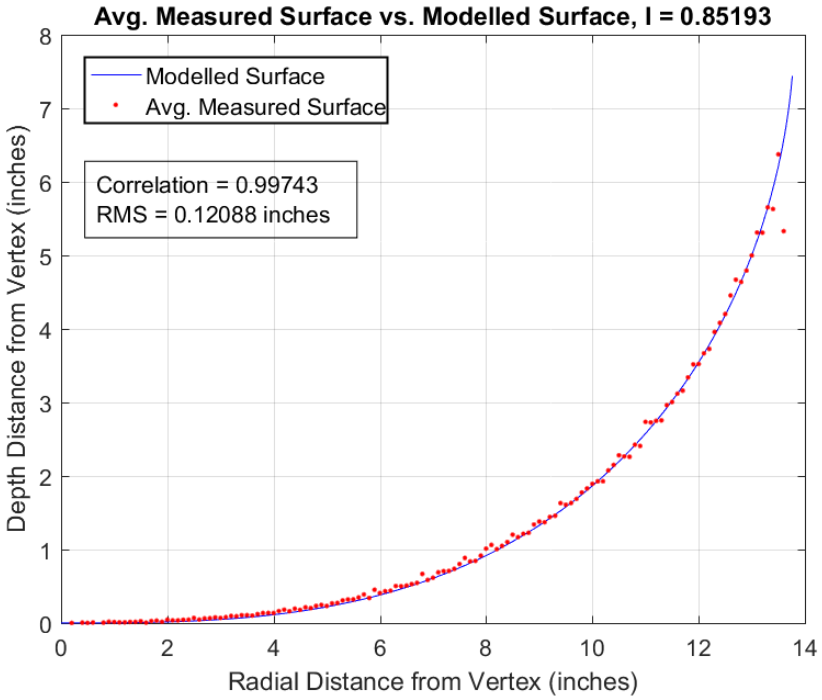

FIGURE 56: Surface Shape Validation Data Comparison at Inflation Ratio of 0.85193

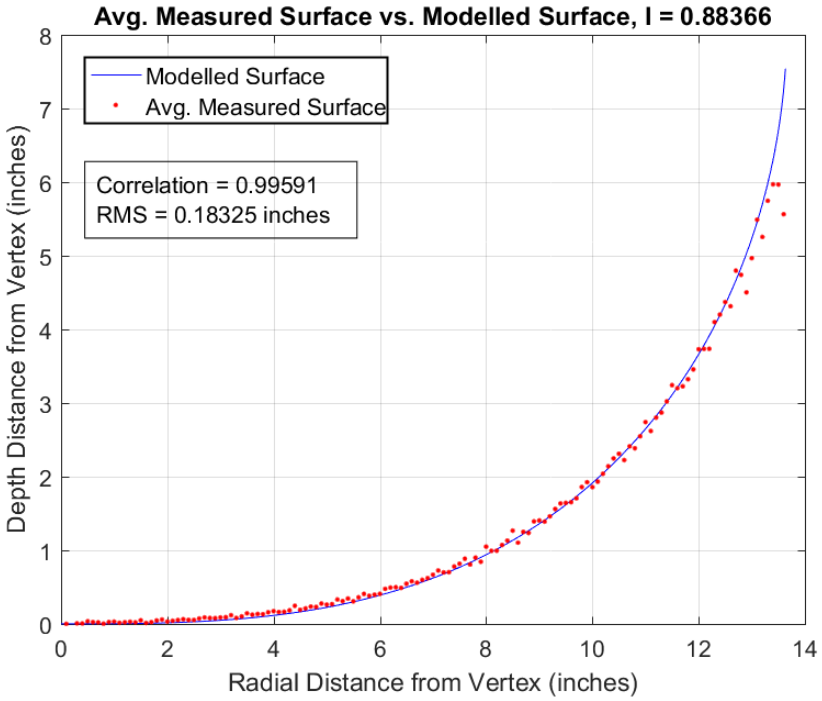

FIGURE 57: Surface Shape Validation Data Comparison at Inflation Ratio of 0.88366

As a further attempt to validate the derived model against the measurements, the calculated depth of the inflatable aperture antenna surface was compared against the simulated depth. The depth is defined at the point on the vertex of the surface, the x and y axes are zero. Therefore, (2.64) is solved for the depth in (2.65), using two elliptic Integral function identities in (2.66) and (2.67) in the final form as (2.68).

$$z(0,0) = \begin{matrix} r_C\sqrt{2}\left[\mathrm{E}\left(\mathrm{sn}\left(\mathrm{arccn}\left(\frac{\sqrt{0^2+0^2}}{r_C},\frac{1}{\sqrt{2}}\right),\frac{1}{\sqrt{2}}\right),\frac{1}{\sqrt{2}}\right)-\frac{1}{2}\mathrm{F}\left(\mathrm{sn}\left(\mathrm{arccn}\left(\frac{\sqrt{0^2+0^2}}{r_C},\frac{1}{\sqrt{2}}\right),\frac{1}{\sqrt{2}}\right),\frac{1}{\sqrt{2}}\right)\right] \\ -r_C\sqrt{2}\left[\mathrm{E}\left(\mathrm{sn}\left(u_0,\frac{1}{\sqrt{2}}\right),\frac{1}{\sqrt{2}}\right)-\frac{1}{2}\mathrm{F}\left(\mathrm{sn}\left(u_0,\frac{1}{\sqrt{2}}\right),\frac{1}{\sqrt{2}}\right)\right] \end{matrix} \quad (2.65)$$

$$\mathrm{arccn}\left(\frac{\sqrt{0^2+0^2}}{r_C},\frac{1}{\sqrt{2}}\right) = \mathrm{K}\left(\frac{1}{\sqrt{2}}\right) \quad (2.66)$$

$$\mathrm{sn}\left(\mathrm{K}\left(\frac{1}{\sqrt{2}}\right),\frac{1}{\sqrt{2}}\right) = 1 \quad (2.67)$$

$$z_0 = r_C\sqrt{2}\left(\mathrm{E}\left(1,\frac{1}{\sqrt{2}}\right)-\frac{1}{2}\mathrm{F}\left(1,\frac{1}{\sqrt{2}}\right)-\mathrm{E}\left(\mathrm{sn}\left(u_0,\frac{1}{\sqrt{2}}\right),\frac{1}{\sqrt{2}}\right)+\frac{1}{2}\mathrm{F}\left(\mathrm{sn}\left(u_0,\frac{1}{\sqrt{2}}\right),\frac{1}{\sqrt{2}}\right)\right) \quad (2.68)$$

Using all of the measured Inflation Ratio data collections, the ratio of the measured depth to measured diameter was compared to the simulated ratio of depth over diameter. The plot of this comparison is shown in Figure 58, where the correlation between the predicted model and measured models was 0.99925.

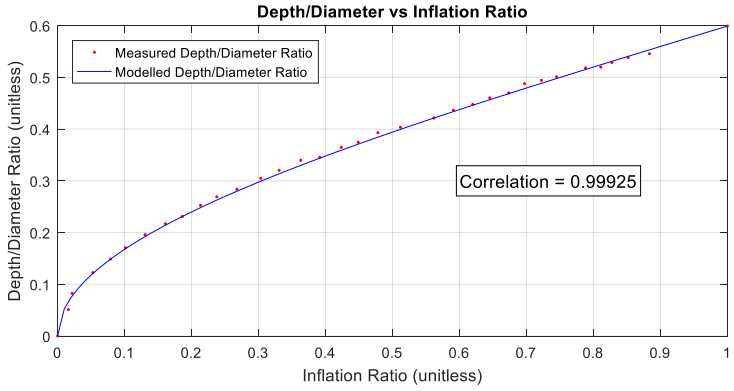

FIGURE 58: Depth to Diameter Shape Validation Data Comparison

With the surface profile validated against test data, it is useful in order to visualize the surface profile as a function of the Inflation Ratio parameter. The three-dimensional surface profile is illustrated in Figures 59 through 68 for Inflation Ratio values of 0.09, 0.19, 0.29, 0.39, 0.49, 0.59, 0.69, 0.79, 0.89, and 0.99 respectively, all while using a constant diameter. Each plot is color-coded individually to represent the depth of the surface illustrated in that particular figure.

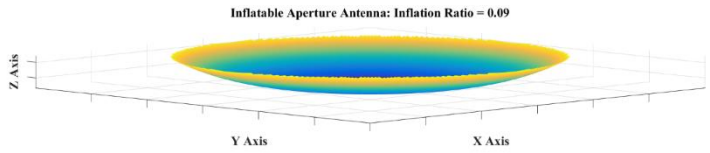

FIGURE 59: Inflatable Aperture Antenna Surface Profile: Inflation Ratio = 0.09

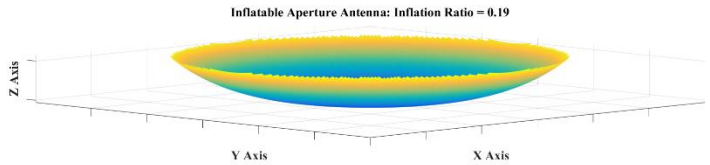

FIGURE 60: Inflatable Aperture Antenna Surface Profile: Inflation Ratio = 0.19

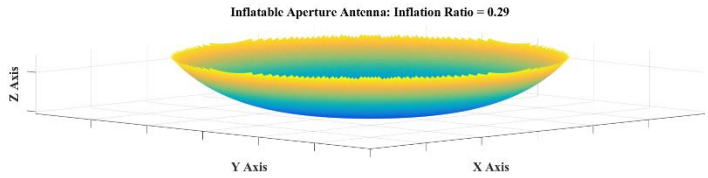

FIGURE 61: Inflatable Aperture Antenna Surface Profile: Inflation Ratio = 0.29

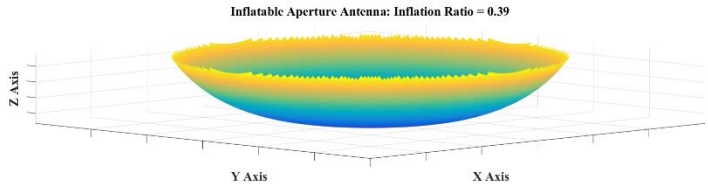

FIGURE 62: Inflatable Aperture Antenna Surface Profile: Inflation Ratio = 0.39

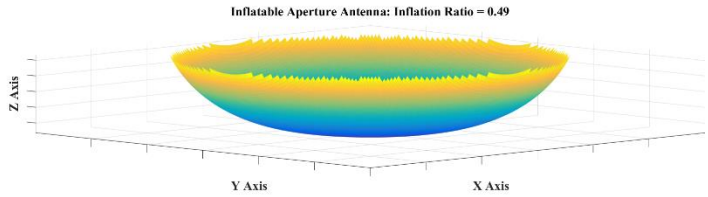

FIGURE 63: Inflatable Aperture Antenna Surface Profile: Inflation Ratio = 0.49

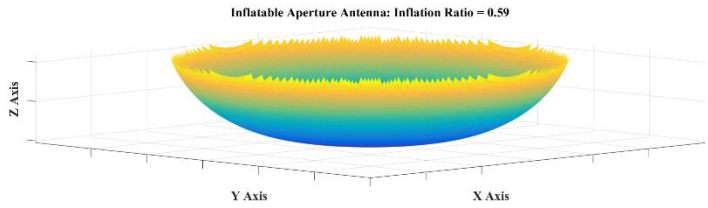

FIGURE 64: Inflatable Aperture Antenna Surface Profile: Inflation Ratio = 0.59

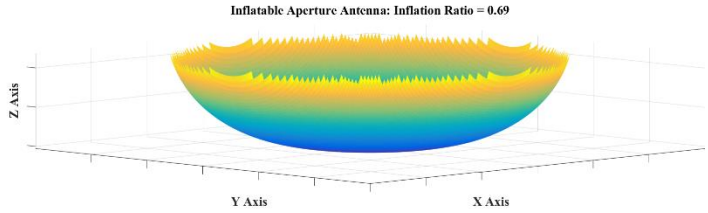

FIGURE 65: Inflatable Aperture Antenna Surface Profile: Inflation Ratio = 0.69

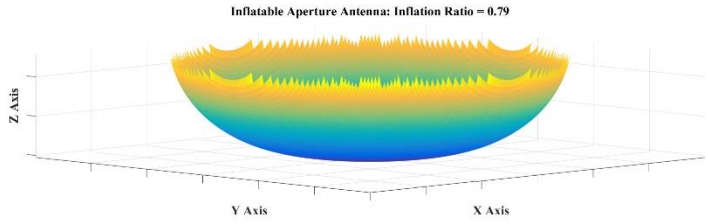

FIGURE 66: Inflatable Aperture Antenna Surface Profile: Inflation Ratio = 0.79

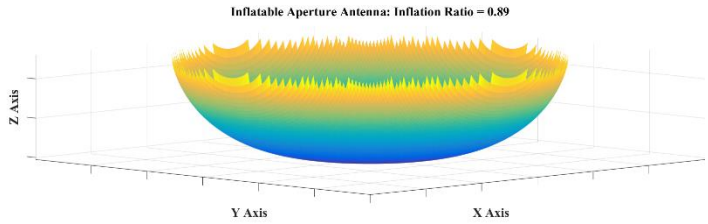

FIGURE 67: Inflatable Aperture Antenna Surface Profile: Inflation Ratio = 0.89

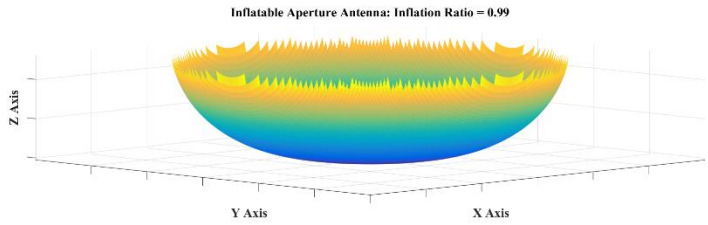

FIGURE 68: Inflatable Aperture Antenna Surface Profile: Inflation Ratio = 0.99

2.6 Summary

The author's contributions derived the mathematical model of the inflatable aperture antenna surface using the Calculus of Variations technique in Sections 2.2 through 2.5, following a similar, referenced derivation approach to previous efforts using Mylar balloons in Section 2.1. The inflatable aperture antenna surface shape is highly consistent with the form of the Mylar balloon surface shape, with the primary differences

being with an offset factor such that the edge of the surface resides on the axis. For the Mylar balloon, that edge does reside on the axis, as illustrated in Figure 10; however, it is at that point, where the slope is negative infinity, as illustrated in Figure 11. Experimental data collection activities were necessary to derive the edge slope as a function of the Inflation Ratio, and that data collection was performed using Laser Radar metrology. That same data collection activity provided validation data for measuring the entire inflatable test article surface. The validation data correlated with over 0.999 relationship to the predicted model of the surface.

It is important to note that the derivation of the surface of the Mylar balloon does not factor in wrinkles, which appear when the balloon is inflated, based on the material of the balloon manufactured from two flat discs. The Mylar balloon model is derived in two dimensions, and extrapolated around an axis, to create the third dimension. The derivation of the inflatable aperture antenna follows a similar approach, however, it is expected that an application of the development of the large aperture antenna surface model is that such a technology would not utilize two flat discs as utilized in a Mylar balloon. It is expected that manufacturing of this technology would be performed on a shaped mandrel, where the desired shape would be used as a mold of the surface, and the surfaces created on the mandrel would then be joined together to form the inflatable aperture antenna. Mandrels are typically predistorted to compensate for shape changes after curing and/or releasing film. The surface created from such a technique would therefore be free of wrinkles when deployed and have the nominal predistortion aspects of the films handled.

CHAPTER III

INFLATABLE APERTURE ANTENNA RF PERFORMANCE MODEL DERIVATION

Optics is the study of light, in which geometric optics (GO), in particular, is the part of optics that deals with light rays or "beams" of light. This is the phenomena of reflection and refraction, such as in prisms, lenses, mirrors, microscopes, telescopes, or cameras. A consequence of geometric optics is that obstructions create a 1-to-1 mapping with a shadow produced, and that the beam of light can propagate without diverging. Now, as seen via Huygen's analysis of diffraction, the theory of geometric optics does not predict the measured response, as diffraction shows that shadows do not exhibit sharp edges, and that beams of light diverge, or spread, as a function of transmitted distance [9, 10, 12].

However, the above response does not match the natural response of light when light is viewed as a wave and not a ray. Physical optics (PO) deals with the wave nature of light, in which the phenomena of diffraction, interference, polarization, color, diffraction gratings, spectroscopy, and diffraction patterns are examined [12]. It is

important to state that although these theories discuss the nature and effect of light, light is only different from RF energy when examining the frequency and corresponding wavelength of the spectrum of interest. As such, it is completely correct to apply optical theories to determine RF performance for antennas, as a corollary for assessing the performance of a telescope in the optics domain.

The remaining content of this chapter provides the background and reference of the PO methodology for solid parabolic antennas in Section 3.1. Sections 3.2 through 3.6 provide further referenced explanations of the five step analysis process highlighted in Section 3.1, in order to allow Section 3.7 to discuss the author's contributions in modifying the PO methodology of a solid parabolic reflector antenna to support the analysis of the inflatable aperture antenna. Finally, Section 3.8 summarizes the author's contributions towards the PO methodology of the inflatable aperture antenna provided in Section 3.7 against the reference contributions from Sections 3.1 through 3.6.

3.1 Background of Physical Optics Model

It is also important to state that while geometric optics does have limitations in terms of its accuracies; some aspects of the approach are still valid and appropriate to utilize. For example, in the general theory of geometric optics for antenna theory, one has RF rays emanating from the focal point of the antenna, which are reflected by the antenna surface towards the axial direction, due to the reflective properties and shape of parabolic antennas. The geometric optics theory is valid when determining the direction of which the rays will travel once reflected by the antenna surface. However, the

limitation of the geometrical optics result is that the RF energy has to be converted from within the near-field of the antenna to the far-field to determine realistic antenna patterns. According to geometric optics, the beam would exhibit no divergence, and the RF energy would be transmitted in a collimated beam that is the size of the diameter of the antenna with constant in-plane phase. To overcome this, the geometrical optics approach typically determines the far-field antenna response with a two-dimensional Fast Fourier Transform (FFT) [1]. This is the same as how the Fraunhofer diffraction is calculated in the optics realm.

To implement the physical optics approach, one must understand that the field at any point is considered the sum of contributions of the fields at all other points in space [12]. As such, for example, the feed element in an antenna system does not have a point source origin, as that is not the manner in which feed elements operate. One must also understand the differences in the electric field and the magnetic field, and how the two fields interact to produce the overall electromagnetic field. First, it is clear in Maxwell's equations, provided in (3.1) and (3.2), that the Electric Field Intensity **E** and the Magnetic Field Intensity **H** jointly interact.

$$j\omega\varepsilon_0\mathbf{E} - \nabla \times \mathbf{H} = -\mathbf{J} \tag{3.1}$$

$$j\omega\mu_0\mathbf{H} - \nabla \times \mathbf{E} = -\mathbf{M} \tag{3.2}$$

In (3.1) and (3.2), the terms and functions used are defined as follows:

- ω is the frequency of the wave, in rad/s
- ε_0 is the permittivity of free space
- **E** is the Electric Field Intensity of the wave

- $\nabla \times$ is the curl operator of the variable that follows
- $\mathbf{H}$ is the Magnetizing Field Intensity of the wave
- $\mathbf{J}$ is the Electric Current Density of the wave
- μ_0 is the permeability of free space
- $\mathbf{M}$ is the Magnetic Current Density of the wave

If an arbitrary vector source current distribution pair were $\mathbf{J}(\mathbf{r}')$ and $\mathbf{M}(\mathbf{r}')$ with $\mathbf{r}'$ defined in (3.3), then the radiated fields are given in (3.4) and (3.5).

$$\mathbf{r}' = \hat{\mathbf{x}}x' + \hat{\mathbf{y}}y' + \hat{\mathbf{z}}z' \tag{3.3}$$

$$\mathbf{E}(\mathbf{r}) = \int \left[\mathbf{E}_{le}\left(\mathbf{r}, \mathbf{r}', \mathbf{J}(\mathbf{r}')\right) + \mathbf{E}_{lm}\left(\mathbf{r}, \mathbf{r}', \mathbf{M}(\mathbf{r}')\right)\right] dV' \tag{3.4}$$

$$\mathbf{H}(\mathbf{r}) = \int \left[\mathbf{H}_{le}\left(\mathbf{r}, \mathbf{r}', \mathbf{J}(\mathbf{r}')\right) + \mathbf{H}_{lm}\left(\mathbf{r}, \mathbf{r}', \mathbf{M}(\mathbf{r}')\right)\right] dV' \tag{3.5}$$

In (3.3) through (3.5), the additional terms used are defined as follows:

- $\mathbf{r}'$ is the position vector of the source current sample coordinate system, $[\hat{\mathbf{x}}, \hat{\mathbf{y}}, \hat{\mathbf{z}}]$
- $\mathbf{E}(\mathbf{r})$ is the radiated Electric Field Intensity of the wave at position $\mathbf{r}$
- $\mathbf{H}(\mathbf{r})$ is the Magnetizing Field Intensity of the wave at position $\mathbf{r}$
- $\mathbf{J}(\mathbf{r}')$ is the arbitrary vector source Electric Current Density of the wave at position $\mathbf{r}'$
- $\mathbf{M}(\mathbf{r}')$ is the arbitrary vector source Magnetic Current Density of the wave at position $\mathbf{r}'$
- $\mathbf{E}_{le}\left(\mathbf{r}, \mathbf{r}', \mathbf{J}(\mathbf{r}')\right)$ is the vector Electric Field Intensity at position $\mathbf{r}$ radiated by the vector Electric Current Density at position $\mathbf{r}'$

- $\mathbf{E}_{lm}(\mathbf{r}, \mathbf{r}', \mathbf{M}(\mathbf{r}'))$ is the vector Electric Field Intensity at position $\mathbf{r}$ radiated by the vector Magnetic Current Density at position $\mathbf{r}'$
- $\mathbf{H}_{le}(\mathbf{r}, \mathbf{r}', \mathbf{J}(\mathbf{r}'))$ is the vector Magnetic Field Intensity at position $\mathbf{r}$ radiated by the vector Electric Current Density at position $\mathbf{r}'$
- $\mathbf{H}_{lm}(\mathbf{r}, \mathbf{r}', \mathbf{M}(\mathbf{r}'))$ is the vector Magnetic Field Intensity at position $\mathbf{r}$ radiated by the vector Magnetic Current Density at position $\mathbf{r}'$
- V' is the volume of space from which position $\mathbf{r}'$ exists

When using the PO methodology with a reflector antenna, one must understand the fields and currents that are incident on the reflector surface. Included in this is the direction in which the fields have propagated to reach the surface, the tangential plane to the reflector surface at the location of incidence, and the magnitude of the field on the reflector surface at the location of incidence [12]. The theories utilized in GO to determine the direction of arrival, and therefore, the direction of reflection apply in this aspect. However, in terms of the reflector surface currents, the following two equations apply in understanding the variation between the incident current and reflected current, given below in (3.6) and (3.7).

$$\mathbf{J}_R = -\mathbf{J}_I \tag{3.6}$$

$$\mathbf{M}_R = \mathbf{M}_I \tag{3.7}$$

In (3.6) and (3.7), the additional terms used are defined as follows:

- $\mathbf{J}_R$ is the reflected Electric Current Density of the wave
- $\mathbf{J}_I$ is the incident Electric Current Density of the wave

- $\mathbf{M}_R$ is the reflected Magnetic Current Density of the wave
- $\mathbf{M}_I$ is the incident Magnetic Current Density of the wave

It is important to note that the types of RF waves that are being utilized in reflector antenna systems are those designated Transverse Electro-Magnetic waves (TEM) [9, 10, 12]. As such, the Electric and Magnetic fields remain orthogonal to each other, and to the direction of propagation. Thus, the end result is that if both current densities were to be negated upon reflection, then the direction of propagation would not change, and reflection on the surface would not occur.

The PO methodology for a prime focus antenna is written using scripts and follows a straightforward five step process [12], as illustrated in Figure 69. Note that this process can also be later modified to include effects such as spillover and blockages.

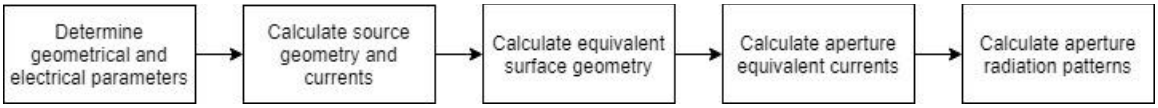

FIGURE 69: Physical Optics Calculation Workflow

3.2 Derivation of RF Geometrical and Electrical Parameters

In the first step of Figure 69, parameters such as the operating frequency, TEM mode numbers, focal length, focal position, aperture size, aperture sampling, radiation pattern angle limits, and radiation pattern angle sampling, are provided as inputs to the problem. Free space constants of impedance and the speed of light are defined based on the free space permittivity and permeability [12], in (3.8) and (3.9).

$$Z_0 = \sqrt{\frac{\mu_0}{\varepsilon_0}} \tag{3.8}$$

$$c = \frac{1}{\sqrt{\varepsilon_0 \mu_0}} \tag{3.9}$$

In (3.8) and (3.9), the additional terms used are defined as follows:

- Z_0 is the impedance of free space
- c is the speed of light in free space

Given a specific operating frequency of an antenna, the operating wavelength of the antenna, the radian-based frequency of the antenna, and the wavenumber of the antenna [12] are defined in (3.10) through (3.12) respectively.

$$\lambda = \frac{c}{f} \tag{3.10}$$

$$\omega = 2\pi f \tag{3.11}$$

$$k_0 = \omega\sqrt{\varepsilon_0 \mu_0} \tag{3.12}$$

In (3.10) through (3.12), the additional terms used are defined as follows:

- λ is the operating wavelength of the antenna
- f is the operating frequency of the antenna
- k_0 is the operating wavenumber of the antenna

Given a specific size of the prime-focus parabolic antenna and its $\frac{F}{D}$ ratio, the focal length, paraboloidal surface shape, and minimum far-field distance [12] are defined in (3.13) through (3.15) respectively.

$$F = \frac{F}{D} D \tag{3.13}$$

$$z = \frac{(x^2+y^2)}{4F} - F \tag{3.14}$$

$$R_{FF} = \frac{2D^2}{\lambda} \tag{3.15}$$

In (3.13) through (3.15), the additional terms used are defined as follows:

- F is the focal length between the antenna focus and the antenna vertex
- $\frac{F}{D}$ is the focal length to diameter ratio
- D is the antenna diameter
- $[x, y, z]$ are coordinates on the antenna's surface
- R_{FF} is the antenna's minimum far-field distance

The surface profile equation given in (3.14) has the antenna feed located at the focus, nominally at the origin of the coordinate system, which has the antenna vertex located along the negative z-axis at a distance of the focal length from the coordinate system origin. The far-field distance is based on the distance from the antenna vertex, where the nominal coordinate system of the antenna's far-field response being in spherical θ-φ coordinates at the distance of R_{FF}. Additional inputs are nominally specified to determine the desired angular antenna response, defined in (3.16) and (3.17).

$$\boldsymbol{\theta} = \theta_{min}{:}\,\Delta\theta{:}\,\theta_{max} \tag{3.16}$$

$$\boldsymbol{\varphi} = \varphi_{min}{:}\,\Delta\varphi{:}\,\varphi_{max} \tag{3.17}$$

In (3.16) and (3.17), the additional terms used are defined as follows:

- $\boldsymbol{\theta}$ is the set of far-field angles off of the axial axis
- θ_{min} is the minimum off-axial far-field angle

- $\Delta\theta$ is the increment of the off-axial far-field angle
- θ_{max} is the maximum off-axial far-field angle
- **φ** is the set of far-field angles rotated around the axial axis
- φ_{min} is the minimum axial-rotated far-field angle
- $\Delta\varphi$ is the increment of the axial-rotated far-field angle
- φ_{max} is the maximum axial-rotated far-field angle

For circularly symmetric antenna patterns, **φ** may usually take the form of a single value. Additionally, **θ** may usually take the form of a set of angles from zero to the user-specified maximum off-axial angle. For an antenna pattern that is not circularly symmetric, the **φ** set should not be a single value, as that set of far-field antenna angles would not provide a sufficient set of angular data to have the antenna pattern properly characterized.

3.3 Derivation of Antenna Source Geometry and Currents

In the second step of Figure 69, the reflector feed element geometry and aperture incident currents are determined, which are dependent on the nature of the feed element geometry and the distance between the feed and the aperture surface. The feed of an antenna pattern can typically take the form of a hardware-specific feed profile given the size and shape of the antenna feed, or can take the form of a user-specified feed-taper utilizing a cosinusoidal response to achieve the feed taper at the edge of the aperture [2, 12]. This second style of antenna feed is used in this derivation effort, with the subtended

angle of the paraboloid given in (3.18) and the cosinusoidal powers associated with the antenna feed response in terms of Electric and Magnetizing Fields of the wave in (3.19) and (3.20).

$$\theta_{subtended} = 2\tan^{-1}\left(\frac{D}{4F}\right) \tag{3.18}$$

$$q_E = \frac{1}{2}\frac{T}{10\log_{10}(\cos(\theta_{subtended}))} \tag{3.19}$$

$$q_H = \frac{1}{2}\frac{T}{10\log_{10}(\cos(\theta_{subtended}))} \tag{3.20}$$

In (3.18) through (3.20), the additional terms used are defined as follows:

- $\theta_{subtended}$ is the subtended angle of the paraboloid
- q_E is the cosinusoidal power of the feed Electric Field Intensity
- T is the feed taper of the antenna
- q_H is the cosinusoidal power of the feed Magnetizing Field Intensity

For a y-axis axially polarized field incident on the antenna surface, the cosinusoidal powers are used with the polarization axis angle to provide the form of the reflector feed incident fields across the reflector surface [12], utilizing polar axes, in (3.21) for the Electric Field Intensity. Equation (3.22) defines the relationship for the Magnetizing Field Intensity incident on the reflector surface, with (3.23) providing the final form.

$$\mathbf{E}_{inc}(\mathbf{r}_s) = \left[((\cos(\boldsymbol{\theta}_s))^{q_E}\sin(\boldsymbol{\varphi}_s))\hat{\boldsymbol{\theta}}_s + ((\cos(\boldsymbol{\theta}_s))^{q_H}\cos(\boldsymbol{\varphi}_s))\hat{\boldsymbol{\varphi}}_s\right]\frac{e^{-jk_0 r_s}}{r_s} \tag{3.21}$$

$$\mathbf{H}_{inc}(\mathbf{r}_s) = \frac{1}{Z_0}\mathbf{r}_s \times \mathbf{E}_{inc}(\mathbf{r}_s) \tag{3.22}$$

$$\mathbf{H}_{inc}(\mathbf{r}_s) = \left[(-(\cos(\boldsymbol{\theta}_s))^{q_H}\cos(\boldsymbol{\varphi}_s))\hat{\boldsymbol{\theta}}_s + ((\cos(\boldsymbol{\theta}_s))^{q_E}\sin(\boldsymbol{\varphi}_s))\hat{\boldsymbol{\varphi}}_s\right]\frac{e^{-jk_0 r_s}}{Z_0 r_s} \tag{3.23}$$

In (3.21) through (3.23), the additional terms used are defined as follows:

- $\mathbf{r}_s$ is the radial element on the reflector surface, in the reflector polar coordinate system, $[\hat{\mathbf{r}}_s, \hat{\boldsymbol{\theta}}_s, \hat{\boldsymbol{\varphi}}_s]$
- $\boldsymbol{\theta}_s$ is the theta angle element on the reflector surface, in the reflector polar coordinate system, $[\hat{\mathbf{r}}_s, \hat{\boldsymbol{\theta}}_s, \hat{\boldsymbol{\varphi}}_s]$
- $\boldsymbol{\varphi}_s$ is the phi angle element on the reflector surface, in the reflector polar coordinate system, $[\hat{\mathbf{r}}_s, \hat{\boldsymbol{\theta}}_s, \hat{\boldsymbol{\varphi}}_s]$
- $\mathbf{E}_{inc}(\mathbf{r}_s)$ is the incident Electric Field Intensity of the wave at position $\mathbf{r}_s$ on the reflector surface
- j is the imaginary unit number, defined by $\sqrt{-1}$
- r_s is the distance to the reflector surface for position vector $\mathbf{r}_s$
- $\mathbf{H}_{inc}(\mathbf{r}_s)$ is the incident Magnetizing Field Intensity of the wave at position $\mathbf{r}_s$ on the reflector surface

Given that polar coordinates are an inconvenient form to describe interactions on the reflector surface, commonly understood in Cartesian form [12], (3.21) is defined in Cartesian form in (3.24) through (3.26) and (3.23) is defined in Cartesian form in (3.27) through (3.29).

$$\mathbf{E}_{inc}(\mathrm{r}_{s,x}) = \left(\left((\cos(\theta_s))^{(q_E+1)} - (\cos(\theta_s))^{q_H}\right)\cos(\varphi_s)\sin(\varphi_s)\right)\frac{\mathrm{e}^{-jk_0 r_s}}{r_s} \tag{3.24}$$

$$\mathbf{E}_{inc}(\mathrm{r}_{s,y}) = \left((\cos(\theta_s))^{(q_E+1)}(\sin(\varphi_s))^2 + (\cos(\theta_s))^{q_H}(\cos(\varphi_s))^2\right)\frac{\mathrm{e}^{-jk_0 r_s}}{r_s} \tag{3.25}$$

$$\mathbf{E}_{inc}(\mathrm{r}_{s,z}) = (-(\cos(\theta_s))^{q_E}\sin(\theta_s)\sin(\varphi_s))\frac{\mathrm{e}^{-jk_0 r_s}}{r_s} \tag{3.26}$$

$$\mathbf{H}_{inc}(\mathrm{r}_{s,x}) = \left(-(\cos(\theta_s))^{(q_H+1)}(\cos(\varphi_s))^2 - (\cos(\theta_s))^{q_E}(\sin(\varphi_s))^2\right)\frac{\mathrm{e}^{-jk_0r_s}}{Z_0r_s} \tag{3.27}$$

$$\mathbf{H}_{inc}(\mathrm{r}_{s,y}) = \left(\left(-(\cos(\theta_s))^{(q_H+1)} + (\cos(\theta_s))^{q_E}\right)\sin(\varphi_s)\cos(\varphi_s)\right)\frac{\mathrm{e}^{-jk_0r_s}}{Z_0r_s} \tag{3.28}$$

$$\mathbf{H}_{inc}(\mathrm{r}_{s,z}) = ((\cos(\theta_s))^{q_H}\sin(\theta_s)\cos(\varphi_s))\frac{\mathrm{e}^{-jk_0r_s}}{Z_0r_s} \tag{3.29}$$

In (3.24) through (3.29), the additional terms used are defined as follows:

- $[\mathrm{r}_{s,x}, \mathrm{r}_{s,y}, \mathrm{r}_{s,z}]$ is the position vector on the reflector surface, in Cartesian coordinates
- θ_s is the theta angle on the reflector surface toward the position vector $\mathbf{r}_s$
- φ_s is the phi angle on the reflector surface toward the position vector $\mathbf{r}_s$
- $\mathbf{E}_{inc}(\mathrm{r}_{s,x})$ is the incident Electric Field Intensity of the wave at position $\mathbf{r}_s$ on the reflector surface in the x-axis Cartesian coordinate
- $\mathbf{E}_{inc}(\mathrm{r}_{s,y})$ is the incident Electric Field Intensity of the wave at position $\mathbf{r}_s$ on the reflector surface in the y-axis Cartesian coordinate
- $\mathbf{E}_{inc}(\mathrm{r}_{s,z})$ is the incident Electric Field Intensity of the wave at position $\mathbf{r}_s$ on the reflector surface in the z-axis Cartesian coordinate
- $\mathbf{H}_{inc}(\mathrm{r}_{s,x})$ is the incident Magnetizing Field Intensity of the wave at position $\mathbf{r}_s$ on the reflector surface in the x-axis Cartesian coordinate
- $\mathbf{H}_{inc}(\mathrm{r}_{s,y})$ is the incident Magnetizing Field Intensity of the wave at position $\mathbf{r}_s$ on the reflector surface in the y-axis Cartesian coordinate

- $\mathbf{H}_{inc}(\mathrm{r}_{s,z})$ is the incident Magnetizing Field Intensity of the wave at position $\mathbf{r}_s$ on the reflector surface in the z-axis Cartesian coordinate

3.4 Derivation of Antenna Surface Geometry

In the third step of Figure 69, the aperture is divided into sampled surface points. These sampled surface points are based on the surface profile of the aperture. Integration areas corresponding to the sampled surface points, based on the curvature of the aperture at those sampled surface points, are also calculated in this third step. The specific reflector surface points and angles to those points, in which the incident Electric and Magnetizing Field Intensities of the wave was defined in (3.24) through (3.29) are defined by this process. Given the reflector surface defined by (3.14), the vertex and center of the reflector in the z-axis is defined by (3.30).

$$z(x = 0, y = 0) = -F \tag{3.30}$$

As the reflector surface is defined by the antenna diameter, D, the minimum number of points on a single axis is defined by the Nyquist sampling process in (3.31) [1, 3].

$$N = \text{floor}\left(\frac{D}{2\lambda}\right) + 1 \tag{3.31}$$

In (3.31), the terms and functions used are defined as follows:

- N is the minimum number of sample points across a single axis for the reflector antenna
- $\text{floor}(\,)$ is the floor operator process of the argument

Given the number of sample points, the set of x-axis and y-axis points that could comprise the reflector surface are given by (3.32) and (3.33).

$$\mathrm{r}_{s,x,all} = -\frac{D}{2} : \frac{\mathrm{D}}{(N-1)} : \frac{D}{2} \tag{3.32}$$

$$\mathrm{r}_{s,y,all} = -\frac{D}{2} : \frac{\mathrm{D}}{(N-1)} : \frac{D}{2} \tag{3.33}$$

In (3.32) and (3.33), the additional terms used are defined as follows:

- $[\mathrm{r}_{s,x,all}, \mathrm{r}_{s,y,all}]$ are the x-axis and y-axis potential reflector grid points defined by the gridding process

An illustration of all the possible x-axis and y-axis grid points associated with the parabolic reflector, as defined by (3.32) and (3.33) is shown below in Figure 70.

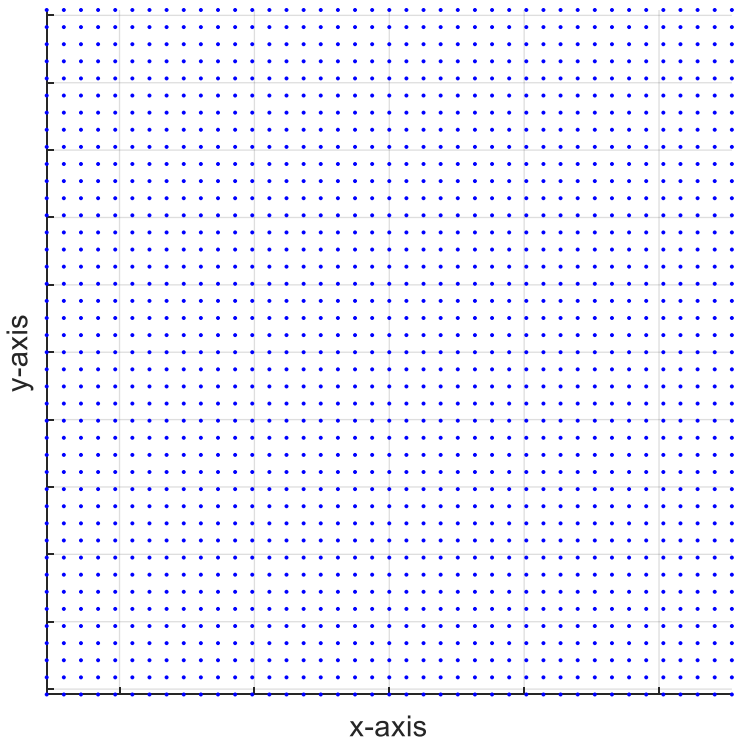

FIGURE 70: Potential X- & Y-Axis Reflector Grid Points

However, this format of the reflector surface points defined in (3.32) and (3.33) define a pure grid, which is inconsistent with the outer circle defined by the prime focus reflector surface, and so that set of points must be limited to the subset of points that meet the condition [12] provided in (3.34), in that the points must be within the radius of the reflector. The constrained version of the grid points that are defined in (3.34) is illustrated in Figure 71.

$$\left[r_{s,x}, r_{s,y}\right] := \sqrt{r_{s,x,all}{}^2 + r_{s,y,all}{}^2} \leq \frac{D}{2} \tag{3.34}$$

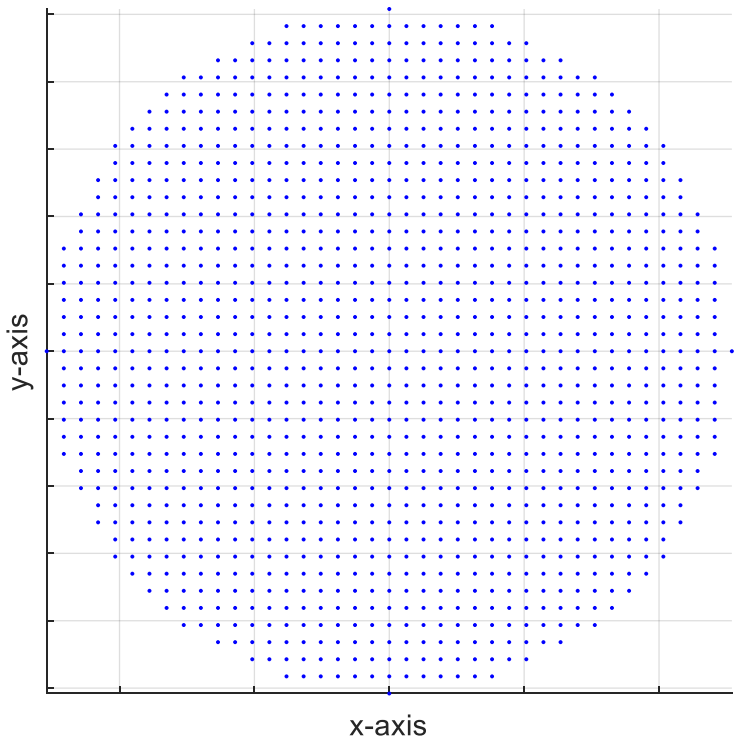

FIGURE 71: Sampled X- & Y-Axis Reflector Grid Points

Given the set of sampled x-axis and y-axis reflector points, the sampled z-axis point is again defined by (3.14), and provided in (3.35) for the specific x-axis and y-axis sampled

points. Figure 72 illustrates the three-dimensional form of the constrained reflector grid points using an $\frac{F}{D}$ ratio of 0.25.

$$f(r_{s,x}, r_{s,y}, r_{s,z}) = r_{s,z} - \frac{(r_{s,x}^2 + r_{s,y}^2)}{4F} + F \tag{3.35}$$

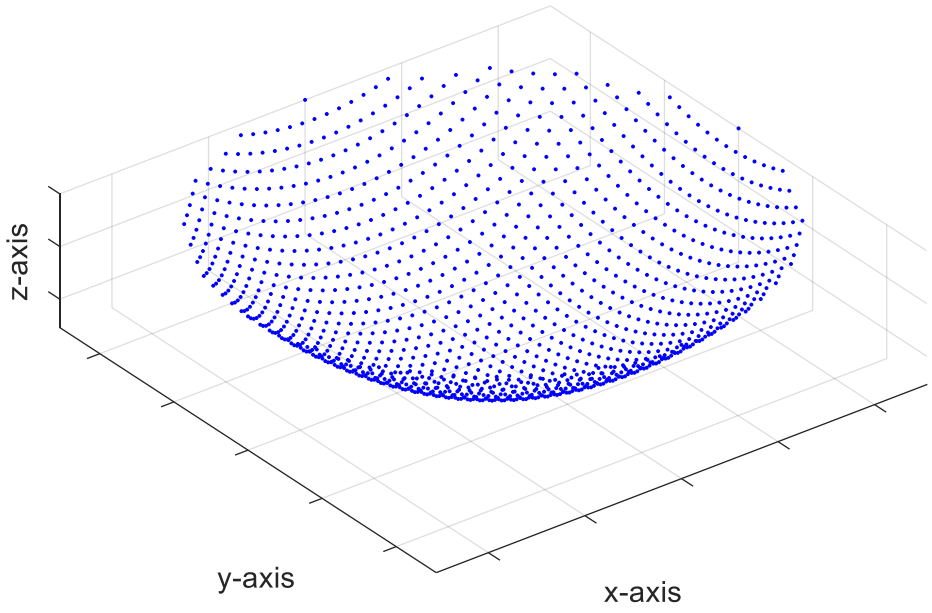

FIGURE 72: Sampled Reflector Grid Points

The theta and phi angles to these sampled reflector surface points are defined by (3.36) and (3.37), with the plots of the theta and phi angles to these sampled reflector grid points shown in Figures 73 and 74, respectively, using the same $\frac{F}{D}$ ratio of 0.25.

$$\theta_s = \cos^{-1}\left(\frac{Fr_{s,z}}{r_s\sqrt{r_{s,x}^2 + r_{s,y}^2 + r_{s,z}^2}}\right) \tag{3.36}$$

$$\varphi_s = \tan^{-1}\left(\frac{r_{s,y}}{r_{s,x}}\right) \tag{3.37}$$

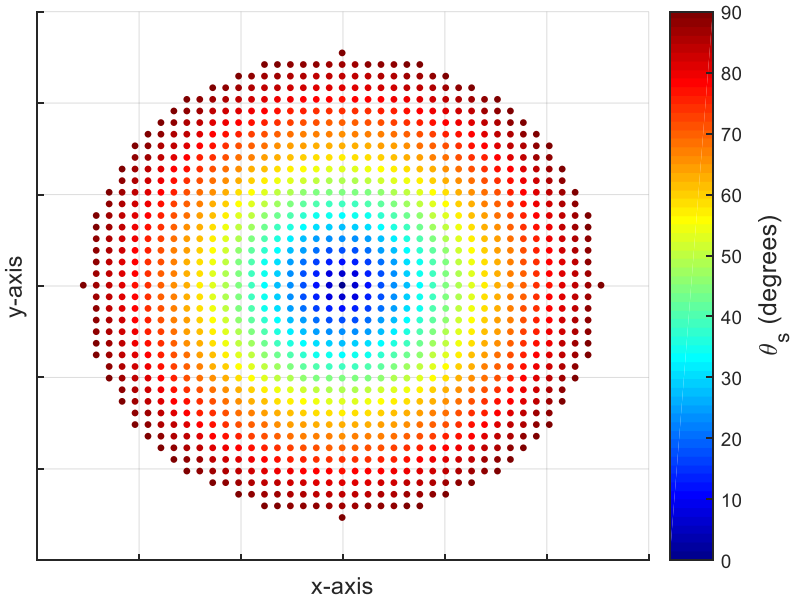

FIGURE 73: Sampled Reflector Grid Point Theta Angles

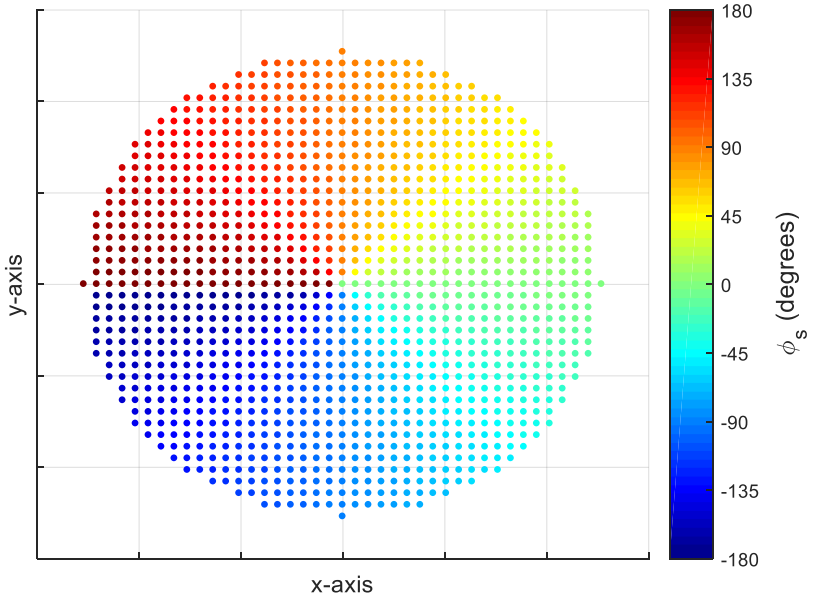

FIGURE 74: Sampled Reflector Grid Point Phi Angles

Next, the axial components of the normal vector to the reflector surface, based on the shape of the reflector surface [12], are provided in (3.38) through (3.40). The normal vector to the reflector surface is based on the derivative of the reflector shape (3.35). The magnitude of this normal vector is given in (3.41), and the unit normal components are provided in (3.42) through (3.44).

$$\mathrm{n}_x = \frac{\partial}{\partial x} f\left(\mathrm{r}_{s,x}, \mathrm{r}_{s,y}, \mathrm{r}_{s,z}\right) \tag{3.38}$$

$$\mathrm{n}_x = -\frac{\mathrm{r}_{s,x}}{2F}$$

$$\mathrm{n}_y = \frac{\partial}{\partial y} f\left(\mathrm{r}_{s,x}, \mathrm{r}_{s,y}, \mathrm{r}_{s,z}\right) \tag{3.39}$$

$$\mathrm{n}_y = -\frac{\mathrm{r}_{s,y}}{2F}$$

$$\mathrm{n}_z = \frac{\partial}{\partial z} f\left(\mathrm{r}_{s,x}, \mathrm{r}_{s,y}, \mathrm{r}_{s,z}\right) \tag{3.40}$$

$$\mathrm{n}_z = 1$$

$$\|\mathrm{n}\| = \sqrt{\left(-\frac{\mathrm{r}_{s,x}}{2F}\right)^2 + \left(-\frac{\mathrm{r}_{s,y}}{2F}\right)^2 + (1)^2} \tag{3.41}$$

$$\mathrm{n}'_x = \frac{-\frac{\mathrm{r}_{s,x}}{2F}}{\sqrt{\left(-\frac{\mathrm{r}_{s,x}}{2F}\right)^2 + \left(-\frac{\mathrm{r}_{s,y}}{2F}\right)^2 + (1)^2}} \tag{3.42}$$

$$\mathrm{n}'_y = \frac{-\frac{\mathrm{r}_{s,y}}{2F}}{\sqrt{\left(-\frac{\mathrm{r}_{s,x}}{2F}\right)^2 + \left(-\frac{\mathrm{r}_{s,y}}{2F}\right)^2 + (1)^2}} \tag{3.43}$$

$$\mathrm{n}'_z = \frac{1}{\sqrt{\left(-\frac{\mathrm{r}_{s,x}}{2F}\right)^2 + \left(-\frac{\mathrm{r}_{s,y}}{2F}\right)^2 + (1)^2}} \tag{3.44}$$

In (3.38) through (3.44), the additional terms used are defined as follows:

- $\left[\mathrm{n}_x, \mathrm{n}_y, \mathrm{n}_z\right]$ are the reflector surface normal vector components at the sampled grid points $\left[\mathrm{r}_{s,x}, \mathrm{r}_{s,y}, \mathrm{r}_{s,z}\right]$

- $\|\mathrm{n}\|$ is the magnitude of the reflector surface normal vector
- $[\mathrm{n}'_x, \mathrm{n}'_y, \mathrm{n}'_z]$ are the reflector surface unit normal vector components at the sampled grid points $[\mathrm{r}_{s,x}, \mathrm{r}_{s,y}, \mathrm{r}_{s,z}]$

Figure 75 illustrates the surface normal vectors from the sampled reflector grid points of Figure 72, where the normal vector is in the direction leaving each sampled reflector grid point. These normal vectors will be utilized in the fourth step of the analysis process.

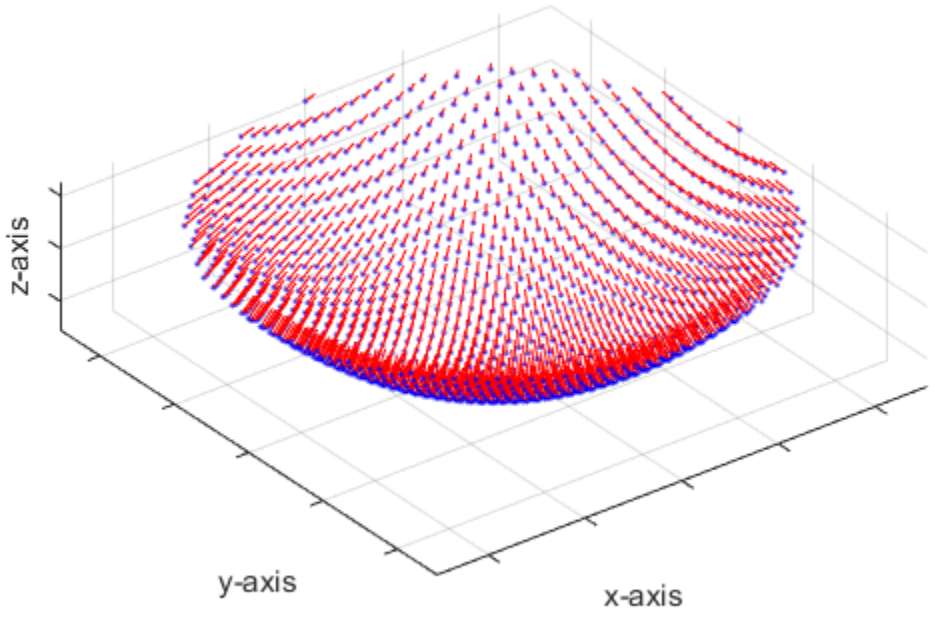

FIGURE 75: Sampled Reflector Grid Points with Normal Vectors

Finally, the surface area is defined based on the two-dimensional integration of the surface [12], similar to how (2.3) defines the arc-length of a curve as the integration

of along the curvature in one dimension. This is defined in (3.45) and expanded on for the parabolic antenna using its shape from (3.35) in (3.46) through (3.49).

$$\Delta S = \int_{x-\Delta x/2}^{x+\Delta x/2} \int_{y-\Delta y/2}^{y+\Delta y/2} \sqrt{1 + \left(\frac{\partial z(x,y)}{\partial x}\right)^2} \sqrt{1 + \left(\frac{\partial z(x,y)}{\partial y}\right)^2}\, dS \tag{3.45}$$

$$dS = \Delta x \Delta y \sqrt{1 + \left(-\frac{x}{2F}\right)^2} \sqrt{1 + \left(-\frac{y}{2F}\right)^2} \tag{3.46}$$

$$\Delta S = dS_x dS_y \tag{3.47}$$

$$dS_x = F\left[\ln\left(\frac{x}{2F} + \sqrt{\left(\frac{x}{2F}\right)^2 + 1}\right) + \frac{x}{2F}\sqrt{\left(\frac{x}{2F}\right)^2 + 1}\right]_{x-\Delta x/2}^{x+\Delta x/2} \tag{3.48}$$

$$dS_y = F\left[\ln\left(\frac{y}{2F} + \sqrt{\left(\frac{y}{2F}\right)^2 + 1}\right) + \frac{y}{2F}\sqrt{\left(\frac{y}{2F}\right)^2 + 1}\right]_{y-\Delta y/2}^{y+\Delta y/2} \tag{3.49}$$

In (3.45) through (3.49), the additional terms and functions used are defined as follows:

- ΔS is the sampled surface area of the reflector surface at the sampled grid point $[x, \mathrm{y}, z]$
- Δx is the sampling interval in the x-axis
- Δy is the sampling interval in the y-axis
- $\ln(\,)$ is the natural logarithm function

The implementation of this process is performed around each of the sampled reflector grid points, at equally spaced points defining a box around the sampled reflector grid point, in the X and Y axes, as observed in (3.48) and (3.49). These box points around the sampled reflector grid point are defined in (3.50) through (3.53).

$$T_{+,+} = \left[\mathrm{r}_{s,x} + \frac{\mathrm{D}}{(N-1)}, \mathrm{r}_{s,y} + \frac{\mathrm{D}}{(N-1)}\right] \tag{3.50}$$

$$T_{+,-} = \left[\mathrm{r}_{s,x} + \frac{\mathrm{D}}{(N-1)}, \mathrm{r}_{s,y} - \frac{\mathrm{D}}{(N-1)}\right] \tag{3.51}$$

$$T_{-,+} = \left[\mathrm{r}_{s,x} - \frac{\mathrm{D}}{(N-1)}, \mathrm{r}_{s,y} + \frac{\mathrm{D}}{(N-1)}\right] \tag{3.52}$$

$$T_{-,-} = \left[\mathrm{r}_{s,x} - \frac{\mathrm{D}}{(N-1)}, \mathrm{r}_{s,y} - \frac{\mathrm{D}}{(N-1)}\right] \tag{3.53}$$

In (3.50) through (3.53), the additional terms used are defined as follows:

- $T_{+,+}$ consists of the positive adjusted x-axis component and positive adjusted y-axis component, $\left[\mathrm{T}_{x,+}, \mathrm{T}_{y,+}\right]$, around the sampled grid point $\left[\mathrm{r}_{s,x}, \mathrm{r}_{s,y}\right]$
- $T_{+,-}$ consists of the positive adjusted x-axis component and negative adjusted y-axis component, $\left[\mathrm{T}_{x,+}, \mathrm{T}_{y,-}\right]$, around the sampled grid point $\left[\mathrm{r}_{s,x}, \mathrm{r}_{s,y}\right]$
- $T_{-,+}$ consists of the negative adjusted x-axis component and positive adjusted y-axis component, $\left[\mathrm{T}_{x,-}, \mathrm{T}_{y,+}\right]$, around the sampled grid point $\left[\mathrm{r}_{s,x}, \mathrm{r}_{s,y}\right]$
- $T_{-,-}$ consists of the negative adjusted x-axis component and negative adjusted y-axis component, $\left[\mathrm{T}_{x,-}, \mathrm{T}_{y,-}\right]$, around the sampled grid point $\left[\mathrm{r}_{s,x}, \mathrm{r}_{s,y}\right]$

This set of box points around each sampled reflector grid point are utilized in the calculation of the sampled surface point surface area, using three intermediate steps [12] which utilize the two evaluation point criteria from (3.48) and (3.49), where these intermediate steps are defined (3.54) through (3.65), to derive the full surface area equation in (3.66).

$$T_{x,+,1} = \frac{T_{x,+}}{2F} \tag{3.54}$$

$$T_{x,+,2} = \sqrt{{T_{x,+,1}}^2 + 1} \tag{3.55}$$

$$T_{x,+,3} = F\left(T_{x,+,1}T_{x,+,2} + \log\left(T_{x,+,1} + T_{x,+,2}\right)\right) \tag{3.56}$$

$$T_{x,-,1} = \frac{T_{x,-}}{2F} \tag{3.57}$$

$$T_{x,-,2} = \sqrt{{T_{x,-,1}}^2 + 1} \tag{3.58}$$

$$T_{x,-,3} = F\left(T_{x,-,1}T_{x,-,2} + \log\left(T_{x,-,1} + T_{x,-,2}\right)\right) \tag{3.59}$$

$$T_{y,+,1} = \frac{T_{y,+}}{2F} \tag{3.60}$$

$$T_{y,+,2} = \sqrt{{T_{y,+,1}}^2 + 1} \tag{3.61}$$

$$T_{y,+,3} = F\left(T_{y,+,1}T_{y,+,2} + \log\left(T_{y,+,1} + T_{y,+,2}\right)\right) \tag{3.62}$$

$$T_{y,-,1} = \frac{T_{y,-}}{2F} \tag{3.63}$$

$$T_{y,-,2} = \sqrt{{T_{y,-,1}}^2 + 1} \tag{3.64}$$

$$T_{y,-,3} = F\left(T_{y,-,1}T_{y,-,2} + \log\left(T_{y,-,1} + T_{y,-,2}\right)\right) \tag{3.65}$$

$$\mathrm{A}_s = \left(T_{x,+,3} - T_{x,-,3}\right)\left(T_{y,+,3} - T_{y,-,3}\right) \tag{3.66}$$

In (3.54) through (3.66), the additional terms used are defined as follows:

- $T_{x,+,1}$ is the first intermediate calculation of the positive adjusted x-axis component, around the sampled grid point $\left[\mathrm{r}_{s,x}, \mathrm{r}_{s,y}\right]$
- $T_{x,+,2}$ is the second intermediate calculation of the positive adjusted x-axis component, around the sampled grid point $\left[\mathrm{r}_{s,x}, \mathrm{r}_{s,y}\right]$
- $T_{x,+,3}$ is the third intermediate calculation of the positive adjusted x-axis component, around the sampled grid point $\left[\mathrm{r}_{s,x}, \mathrm{r}_{s,y}\right]$

- $T_{x,-,1}$ is the first intermediate calculation of the negative adjusted x-axis component, around the sampled grid point $[\mathrm{r}_{s,x}, \mathrm{r}_{s,y}]$
- $T_{x,-,2}$ is the second intermediate calculation of the negative adjusted x-axis component, around the sampled grid point $[\mathrm{r}_{s,x}, \mathrm{r}_{s,y}]$
- $T_{x,-,3}$ is the third intermediate calculation of the negative adjusted x-axis component, around the sampled grid point $[\mathrm{r}_{s,x}, \mathrm{r}_{s,y}]$
- $T_{y,+,1}$ is the first intermediate calculation of the positive adjusted y-axis component, around the sampled grid point $[\mathrm{r}_{s,x}, \mathrm{r}_{s,y}]$
- $T_{y,+,2}$ is the second intermediate calculation of the positive adjusted y-axis component, around the sampled grid point $[\mathrm{r}_{s,x}, \mathrm{r}_{s,y}]$
- $T_{y,+,3}$ is the third intermediate calculation of the positive adjusted y-axis component, around the sampled grid point $[\mathrm{r}_{s,x}, \mathrm{r}_{s,y}]$
- $T_{y,-,1}$ is the first intermediate calculation of the negative adjusted y-axis component, around the sampled grid point $[\mathrm{r}_{s,x}, \mathrm{r}_{s,y}]$
- $T_{y,-,2}$ is the second intermediate calculation of the negative adjusted y-axis component, around the sampled grid point $[\mathrm{r}_{s,x}, \mathrm{r}_{s,y}]$
- $T_{y,-,3}$ is the third intermediate calculation of the negative adjusted y-axis component, around the sampled grid point $[\mathrm{r}_{s,x}, \mathrm{r}_{s,y}]$
- A_s is the sampled surface area of the reflector surface at the sampled grid point $[\mathrm{r}_{s,x}, \mathrm{r}_{s,y}, \mathrm{r}_{s,z}]$

Evaluation of (3.66) shows that each grid point does not have equal curvature surface area throughout the surface. However, for grid points that are located near the edge of the reflector, their surface area may be too large based on this approach, as this nominal approach utilizes potential area beyond the sampled grid point, since the evaluation criteria in (3.48) and (3.49) extend into regions beyond the actual surface of the antenna. As such, a process is enabled to reduce the surface area of grid points that meet the any of the criteria specified in (3.67) through (3.70).

$$Condition_{x,+} := \sqrt{\left(\mathrm{r}_{s,x} + \frac{\mathrm{D}}{(N-1)}\right)^2 + \mathrm{r}_{s,y}{}^2} > \frac{D}{2} \tag{3.67}$$

$$Condition_{x,-} := \sqrt{\left(\mathrm{r}_{s,x} - \frac{\mathrm{D}}{(N-1)}\right)^2 + \mathrm{r}_{s,y}{}^2} > \frac{D}{2} \tag{3.68}$$

$$Condition_{y,+} := \sqrt{\mathrm{r}_{s,x}{}^2 + \left(\mathrm{r}_{s,y} + \frac{\mathrm{D}}{(N-1)}\right)^2} > \frac{D}{2} \tag{3.69}$$

$$Condition_{y,-} := \sqrt{\mathrm{r}_{s,x}{}^2 + \left(\mathrm{r}_{s,y} - \frac{\mathrm{D}}{(N-1)}\right)^2} > \frac{D}{2} \tag{3.70}$$

As stated, if any of the criteria from (3.67) through (3.70) are found to be true, then the box defined in (3.50) through (3.53) is subdivided in the X and Y axes by a factor of $\frac{\mathrm{D}}{10(N-1)}$ to produce 100 sub-boxes. Those sub-boxes are then evaluated to see if they are found to be within the radius of the reflector. If they are within the radius of the reflector, then the process of deriving the surface area for each grid point is performed around the center of each sub-box, replicating the process of (3.48) and (3.49) but with different sub-box centers per sub-box and the reduced sub-box spacing of $\frac{\mathrm{D}}{10(N-1)}$. The surface area of each of these grid points with any of the conditions met in (3.67) through

(3.70) are then found as the sum of the sub-box surface areas that are within the reflector radius.

A visualization of the reflector surface area, using this criteria approach in (3.67) through (3.70) to accurately reduce the surface area for grid points near the reflector edge, is illustrated in Figure 76. This information will be utilized later in the fifth step of this analysis process defined in Figure 69.

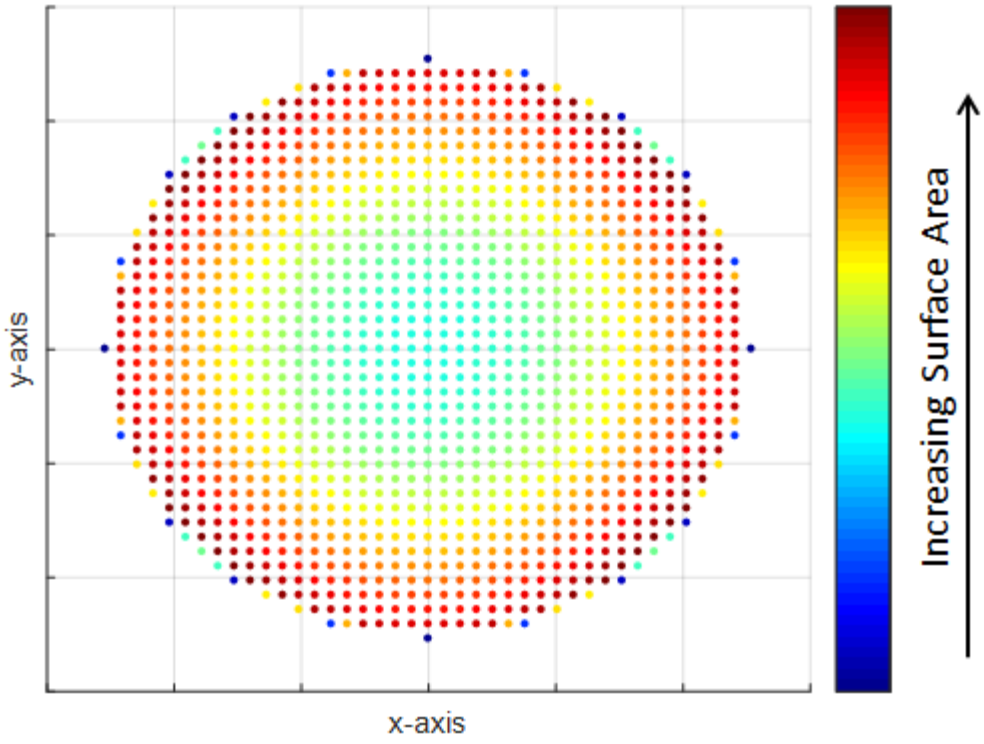

FIGURE 76: Sampled Reflector Grid Point Surface Area

3.5 Derivation of Antenna Aperture Incident Equivalent Currents

In the fourth step of Figure 69, the incident fields from the second step are converted to incident Electric and Magnetic Current Densities, using the methodology provided in (3.4) and (3.5). Additionally, the reflected Electric and Magnetic Current Densities are determined from the incident field direction of travel and the reflector curvature normal vector directions, using the methodology provided in (3.6) and (3.7). Equations (3.71) and (3.72) are the driving equations to convert between the incident fields on the reflector surface and the incident current densities. The use of (3.71) and (3.72) enable the Cartesian field components, from (3.24) through (3.29), to be converted into incident current densities. Equations (3.73) through (3.75) provide the normalized Electric Current Densities, while (3.76) through (3.78) provide the normalized Magnetic Current Densities, all in Cartesian form at the same reflector surface grid points as in (3.24) through (3.29).

$$\mathbf{J}_{inc}(\mathbf{r}_s) = \mathbf{n}(\mathbf{r}_s) \times \mathbf{H}_{inc}(\mathbf{r}_s) \tag{3.71}$$

$$\mathbf{M}_{inc}(\mathbf{r}_s) = -\mathbf{n}(\mathbf{r}_s) \times \mathbf{E}_{inc}(\mathbf{r}_s) \tag{3.72}$$

$$\mathbf{J}_{inc}(\mathrm{r}_{s,x}) = \left(\mathrm{n}'_y \mathbf{H}_{inc}(\mathrm{r}_{s,z}) - \mathrm{n}'_z \mathbf{H}_{inc}(\mathrm{r}_{s,y})\right) \mathrm{A}_s \tag{3.73}$$

$$\mathbf{J}_{inc}(\mathrm{r}_{s,y}) = \left(\mathrm{n}'_z \mathbf{H}_{inc}(\mathrm{r}_{s,x}) - \mathrm{n}'_x \mathbf{H}_{inc}(\mathrm{r}_{s,z})\right) \mathrm{A}_s \tag{3.74}$$

$$\mathbf{J}_{inc}(\mathrm{r}_{s,z}) = \left(\mathrm{n}'_x \mathbf{H}_{inc}(\mathrm{r}_{s,y}) - \mathrm{n}'_y \mathbf{H}_{inc}(\mathrm{r}_{s,x})\right) \mathrm{A}_s \tag{3.75}$$

$$\mathbf{M}_{inc}(\mathrm{r}_{s,x}) = -\left(\mathrm{n}'_y \mathbf{E}_{inc}(\mathrm{r}_{s,z}) - \mathrm{n}'_z \mathbf{E}_{inc}(\mathrm{r}_{s,y})\right) \mathrm{A}_s \tag{3.76}$$

$$\mathbf{M}_{inc}(\mathrm{r}_{s,y}) = -\left(\mathrm{n}'_z \mathbf{E}_{inc}(\mathrm{r}_{s,x}) - \mathrm{n}'_x \mathbf{E}_{inc}(\mathrm{r}_{s,z})\right) \mathrm{A}_s \tag{3.77}$$

$$\mathbf{M}_{inc}(\mathrm{r}_{s,z}) = -\left(\mathrm{n}'_x\mathbf{E}_{inc}(\mathrm{r}_{s,y}) - \mathrm{n}'_y\mathbf{E}_{inc}(\mathrm{r}_{s,x})\right)\mathrm{A}_s \tag{3.78}$$

In (3.71) through (3.78), the additional terms used are defined as follows:

- $\mathbf{n}(\mathbf{r}_s)$ is the normal vector of the wave at position $\mathbf{r}_s$ on the reflector surface
- $\mathbf{J}_{inc}(\mathrm{r}_{s,x})$ is the incident Electric Current Density of the wave at position $\mathbf{r}_s$ on the reflector surface in the x-axis Cartesian coordinate
- $\mathbf{J}_{inc}(\mathrm{r}_{s,y})$ is the incident Electric Current Density of the wave at position $\mathbf{r}_s$ on the reflector surface in the y-axis Cartesian coordinate
- $\mathbf{J}_{inc}(\mathrm{r}_{s,z})$ is the incident Electric Current Density of the wave at position $\mathbf{r}_s$ on the reflector surface in the z-axis Cartesian coordinate
- $\mathbf{M}_{inc}(\mathrm{r}_{s,x})$ is the incident Magnetic Current Density of the wave at position $\mathbf{r}_s$ on the reflector surface in the x-axis Cartesian coordinate
- $\mathbf{M}_{inc}(\mathrm{r}_{s,y})$ is the incident Magnetic Current Density of the wave at position $\mathbf{r}_s$ on the reflector surface in the y-axis Cartesian coordinate
- $\mathbf{M}_{inc}(\mathrm{r}_{s,z})$ is the incident Magnetic Current Density of the wave at position $\mathbf{r}_s$ on the reflector surface in the z-axis Cartesian coordinate

The reflected Electric and Magnetic current densities are derived using (3.6) and (3.7), and are provided in (3.79) through (3.84) for the reflected Electric and Magnetic current densities, respectively.

$$\mathbf{J}_{refl}(\mathrm{r}_{s,x}) = -\left(\mathrm{n}'_y\mathbf{H}_{inc}(\mathrm{r}_{s,z}) - \mathrm{n}'_z\mathbf{H}_{inc}(\mathrm{r}_{s,y})\right)\mathrm{A}_s \tag{3.79}$$

$$\mathbf{J}_{refl}(\mathrm{r}_{s,y}) = -\left(\mathrm{n}'_z\mathbf{H}_{inc}(\mathrm{r}_{s,x}) - \mathrm{n}'_x\mathbf{H}_{inc}(\mathrm{r}_{s,z})\right)\mathrm{A}_s \tag{3.80}$$

$$\mathbf{J}_{refl}(\mathrm{r}_{s,z}) = -\left(\mathrm{n}'_x\mathbf{H}_{inc}(\mathrm{r}_{s,y}) - \mathrm{n}'_y\mathbf{H}_{inc}(\mathrm{r}_{s,x})\right)\mathrm{A}_s \tag{3.81}$$

$$\mathbf{M}_{refl}(\mathrm{r}_{s,x}) = \left(\mathrm{n}'_y\mathbf{E}_{inc}(\mathrm{r}_{s,z}) - \mathrm{n}'_z\mathbf{E}_{inc}(\mathrm{r}_{s,y})\right)\mathrm{A}_s \tag{3.82}$$

$$\mathbf{M}_{refl}(\mathrm{r}_{s,y}) = \left(\mathrm{n}'_z\mathbf{E}_{inc}(\mathrm{r}_{s,x}) - \mathrm{n}'_x\mathbf{E}_{inc}(\mathrm{r}_{s,z})\right)\mathrm{A}_s \tag{3.83}$$

$$\mathbf{M}_{refl}(\mathrm{r}_{s,z}) = \left(\mathrm{n}'_x\mathbf{E}_{inc}(\mathrm{r}_{s,y}) - \mathrm{n}'_y\mathbf{E}_{inc}(\mathrm{r}_{s,x})\right)\mathrm{A}_s \tag{3.84}$$

In (3.79) through (3.84), the additional terms used are defined as follows:

- $\mathbf{J}_{refl}(\mathrm{r}_{s,x})$ is the reflected Electric Current Density of the wave at position $\mathbf{r}_s$ on the reflector surface in the x-axis Cartesian coordinate
- $\mathbf{J}_{refl}(\mathrm{r}_{s,y})$ is the reflected Electric Current Density of the wave at position $\mathbf{r}_s$ on the reflector surface in the y-axis Cartesian coordinate
- $\mathbf{J}_{refl}(\mathrm{r}_{s,z})$ is the reflected Electric Current Density of the wave at position $\mathbf{r}_s$ on the reflector surface in the z-axis Cartesian coordinate
- $\mathbf{M}_{refl}(\mathrm{r}_{s,x})$ is the reflected Magnetic Current Density of the wave at position $\mathbf{r}_s$ on the reflector surface in the x-axis Cartesian coordinate
- $\mathbf{M}_{refl}(\mathrm{r}_{s,y})$ is the reflected Magnetic Current Density of the wave at position $\mathbf{r}_s$ on the reflector surface in the y-axis Cartesian coordinate
- $\mathbf{M}_{refl}(\mathrm{r}_{s,z})$ is the reflected Magnetic Current Density of the wave at position $\mathbf{r}_s$ on the reflector surface in the z-axis Cartesian coordinate

3.6 Derivation of Antenna Aperture Radiation Patterns

Finally, in the fifth step of Figure 69, the far-field polarized field profiles of the antenna pattern are determined from the reflected Electric and Magnetic current densities using the methodology provided in (3.4) and (3.5). The driving equations to determine the far-field polarized fields [12] are provided in (3.85) and (3.86) using the far-field angles defined previously in (3.16) and (3.17). Equations (3.87) and (3.88) provide the combined theta-polarized and combined phi-polarized fields [2, 12] from the far-field Electric and Magnetizing Field Intensity components in (3.85) and (3.86) for a given polarization.

$$\mathbf{H}_{FF}(\boldsymbol{\theta},\boldsymbol{\varphi}) = -\frac{jk}{4\pi}\hat{\mathbf{r}}\int \mathbf{M}_{refl}(\mathbf{r}_s)\mathrm{e}^{-jk\hat{\mathbf{r}}R_{FF}}\,dS_{FF} \tag{3.85}$$

$$\mathbf{E}_{FF}(\boldsymbol{\theta},\boldsymbol{\varphi}) = \frac{jk}{4\pi}\hat{\mathbf{r}}\int \mathbf{J}_{refl}(\mathbf{r}_s)\mathrm{e}^{-jk\hat{\mathbf{r}}R_{FF}}\,dS_{FF} \tag{3.86}$$

$$\mathbf{F}_{\theta}(\boldsymbol{\theta},\boldsymbol{\varphi}) = \left(\mathbf{E}_{FF}(\boldsymbol{\theta},\boldsymbol{\varphi}) + Z_0\mathbf{H}_{FF}(\boldsymbol{\theta},\boldsymbol{\varphi})\right)\hat{\boldsymbol{\theta}} \tag{3.87}$$

$$\mathbf{F}_{\varphi}(\boldsymbol{\theta},\boldsymbol{\varphi}) = \left(\mathbf{E}_{FF}(\boldsymbol{\theta},\boldsymbol{\varphi}) + Z_0\mathbf{H}_{FF}(\boldsymbol{\theta},\boldsymbol{\varphi})\right)\hat{\boldsymbol{\varphi}} \tag{3.88}$$

In (3.85) through (3.88), the additional terms used are defined as follows:

- $\mathbf{H}_{FF}(\boldsymbol{\theta},\boldsymbol{\varphi})$ is the far-field Magnetizing Field Intensity of the wave at far-field angles $[\boldsymbol{\theta},\boldsymbol{\varphi}]$
- $\mathbf{E}_{FF}(\boldsymbol{\theta},\boldsymbol{\varphi})$ is the far-field Electric Field Intensity of the wave at far-field angles $[\boldsymbol{\theta},\boldsymbol{\varphi}]$
- dS_{FF} is the far-field region of interest to integrate the reflected current densities from the reflector surface

- $\mathbf{F}_{\theta}(\boldsymbol{\theta}, \boldsymbol{\varphi})$ is the combined theta-polarized far-field antenna pattern at far-field angles $[\boldsymbol{\theta}, \boldsymbol{\varphi}]$
- $\mathbf{F}_{\varphi}(\boldsymbol{\theta}, \boldsymbol{\varphi})$ is the combined phi-polarized far-field antenna pattern at far-field angles $[\boldsymbol{\theta}, \boldsymbol{\varphi}]$

3.7 Modification of Physical Optics Modeling for Inflatable Aperture Antenna

The modifications necessary to augment the physical optics modeling of reflector aperture antennas to support modeling inflatable aperture antennas is focused on the calculations performed in the third step of Figure 69 to derive the surface geometry. Three unique modification activities are necessary in order to perform physical optics modeling of inflatable aperture antennas. First, the inflatable aperture antenna surface profile needs to be modified to be in the form of the reflector surface profile provided in (3.35). Second, the surface normal vector needs to be redefined using derivatives of the inflatable aperture antenna equation. Third, the surface area of each grid point on the inflatable aperture antenna needs to be redefined using the arc length of the inflatable aperture antenna surface profile.

Efforts to define the inflatable aperture surface profile antenna in the form of (3.35) are based on the inflatable aperture surface profile (2.64) and (2.68). In (3.35), the z-axis of the surface profile when x and y components are zero is the negative focal length, and it is desired that the inflatable aperture antenna surface profile is shown in this same manner. Equation (2.68) provides the z-axis when the x and y components are zero, and so that equation is used with the nominal surface profile provided in (2.65), where

the z-axis is zero at the edge of the inflated surface, where the x and/or y-axis values are maximized. The combination of these equations to mimic (3.35) is provided next in (3.89) and simplified in (3.90).

$$z(x,y) = \begin{matrix} r_C\sqrt{2}\left[\mathrm{E}\left(\mathrm{sn}\left(\mathrm{arccn}\left(\frac{\sqrt{x^2+y^2}}{r_C},\frac{1}{\sqrt{2}}\right),\frac{1}{\sqrt{2}}\right),\frac{1}{\sqrt{2}}\right)-\frac{1}{2}\mathrm{F}\left(\mathrm{sn}\left(\mathrm{arccn}\left(\frac{\sqrt{x^2+y^2}}{r_C},\frac{1}{\sqrt{2}}\right),\frac{1}{\sqrt{2}}\right),\frac{1}{\sqrt{2}}\right)\right] \\ -r_C\sqrt{2}\left[\mathrm{E}\left(\mathrm{sn}\left(u_0,\frac{1}{\sqrt{2}}\right),\frac{1}{\sqrt{2}}\right)-\frac{1}{2}\mathrm{F}\left(\mathrm{sn}\left(u_0,\frac{1}{\sqrt{2}}\right),\frac{1}{\sqrt{2}}\right)\right] \\ -r_C\sqrt{2}\left(\mathrm{E}\left(1,\frac{1}{\sqrt{2}}\right)-\frac{1}{2}\mathrm{F}\left(1,\frac{1}{\sqrt{2}}\right)-\mathrm{E}\left(\mathrm{sn}\left(u_0,\frac{1}{\sqrt{2}}\right),\frac{1}{\sqrt{2}}\right)+\frac{1}{2}\mathrm{F}\left(\mathrm{sn}\left(u_0,\frac{1}{\sqrt{2}}\right),\frac{1}{\sqrt{2}}\right)\right)-F \end{matrix} \tag{3.89}$$

$$z(\mathrm{x},\mathrm{y}) = \begin{matrix} r_C\sqrt{2}\left[\mathrm{E}\left(\mathrm{sn}\left(\mathrm{arccn}\left(\frac{\sqrt{x^2+y^2}}{r_C},\frac{1}{\sqrt{2}}\right),\frac{1}{\sqrt{2}}\right),\frac{1}{\sqrt{2}}\right)-\frac{1}{2}\mathrm{F}\left(\mathrm{sn}\left(\mathrm{arccn}\left(\frac{\sqrt{x^2+y^2}}{r_C},\frac{1}{\sqrt{2}}\right),\frac{1}{\sqrt{2}}\right),\frac{1}{\sqrt{2}}\right)\right] \\ -r_C\sqrt{2}\left(\mathrm{E}\left(1,\frac{1}{\sqrt{2}}\right)-\frac{1}{2}\mathrm{F}\left(1,\frac{1}{\sqrt{2}}\right)\right)-F \end{matrix} \tag{3.90}$$

With the surface profile equation defined in the proper format by (3.90), the second step of the necessary modifications to redefine the surface normal vector can be performed. Previously, (3.38) and (3.39) defined the partial derivatives of the x and y-axis components of (3.35), and the final normal vector was defined in (3.42) through (3.44). The modification of that process is started in (3.91) and (3.92), as the modification of (3.38) and (3.39), utilizing the inflatable antenna surface profile given in (3.90).

$$\mathrm{n}_x = \frac{\partial}{\partial x} z(x,y) \tag{3.91}$$

$$\mathrm{n}_x = \frac{\partial}{\partial x}\left(\begin{matrix} r_C\sqrt{2}\left[\mathrm{E}\left(\mathrm{sn}\left(\mathrm{arccn}\left(\frac{\sqrt{x^2+y^2}}{r_C},\frac{1}{\sqrt{2}}\right),\frac{1}{\sqrt{2}}\right),\frac{1}{\sqrt{2}}\right)-\frac{1}{2}\mathrm{F}\left(\mathrm{sn}\left(\mathrm{arccn}\left(\frac{\sqrt{x^2+y^2}}{r_C},\frac{1}{\sqrt{2}}\right),\frac{1}{\sqrt{2}}\right),\frac{1}{\sqrt{2}}\right)\right] \\ -r_C\sqrt{2}\left(\mathrm{E}\left(1,\frac{1}{\sqrt{2}}\right)-\frac{1}{2}\mathrm{F}\left(1,\frac{1}{\sqrt{2}}\right)\right)-F \end{matrix}\right)$$

$$\mathrm{n}_x = \frac{\partial}{\partial x}\left(r_C\sqrt{2}\left[\mathrm{E}\left(\mathrm{sn}\left(\mathrm{arccn}\left(\frac{\sqrt{x^2+y^2}}{r_C},\frac{1}{\sqrt{2}}\right),\frac{1}{\sqrt{2}}\right),\frac{1}{\sqrt{2}}\right)-\frac{1}{2}\mathrm{F}\left(\mathrm{sn}\left(\mathrm{arccn}\left(\frac{\sqrt{x^2+y^2}}{r_C},\frac{1}{\sqrt{2}}\right),\frac{1}{\sqrt{2}}\right),\frac{1}{\sqrt{2}}\right)\right]\right)$$

$$\mathrm{n}_y = \frac{\partial}{\partial y} z(x,y) \tag{3.92}$$

$$\mathrm{n}_y = \frac{\partial}{\partial y}\begin{pmatrix} r_C\sqrt{2}\left[\mathrm{E}\left(\mathrm{sn}\left(\mathrm{arccn}\left(\frac{\sqrt{x^2+y^2}}{r_C},\frac{1}{\sqrt{2}}\right),\frac{1}{\sqrt{2}}\right),\frac{1}{\sqrt{2}}\right)-\frac{1}{2}\mathrm{F}\left(\mathrm{sn}\left(\mathrm{arccn}\left(\frac{\sqrt{x^2+y^2}}{r_C},\frac{1}{\sqrt{2}}\right),\frac{1}{\sqrt{2}}\right),\frac{1}{\sqrt{2}}\right)\right] \\ -r_C\sqrt{2}\left(\mathrm{E}\left(1,\frac{1}{\sqrt{2}}\right)-\frac{1}{2}\mathrm{F}\left(1,\frac{1}{\sqrt{2}}\right)\right)-F \end{pmatrix}$$

$$\mathrm{n}_y = \frac{\partial}{\partial y}\left(r_C\sqrt{2}\left[\mathrm{E}\left(\mathrm{sn}\left(\mathrm{arccn}\left(\frac{\sqrt{x^2+y^2}}{r_C},\frac{1}{\sqrt{2}}\right),\frac{1}{\sqrt{2}}\right),\frac{1}{\sqrt{2}}\right)-\frac{1}{2}\mathrm{F}\left(\mathrm{sn}\left(\mathrm{arccn}\left(\frac{\sqrt{x^2+y^2}}{r_C},\frac{1}{\sqrt{2}}\right),\frac{1}{\sqrt{2}}\right),\frac{1}{\sqrt{2}}\right)\right]\right)$$

Initial examination of (3.91) and (3.92) show that they are both functions of the elliptic E, elliptic F, Jacobi sine, and Jacobi cosine functions. In order to complete these partial derivatives, the chain rule will be required to evaluate to the inner-most variable arguments. Several important partial derivative identities of these elliptic E, elliptic F, Jacobi sine, and Jacobi cosine functions [25] are provided for reference in (3.93) through (3.96).

$$\frac{\partial}{\partial u}\mathrm{E}(u,k) = \sqrt{1-k^2\sin^2(u)} \tag{3.93}$$

$$\frac{\partial}{\partial u}\mathrm{F}(u,k) = \frac{1}{\sqrt{1-k^2\sin^2(u)}} \tag{3.94}$$

$$\frac{\partial}{\partial u}\mathrm{sn}(u,k) = \mathrm{cn}(u,k)\mathrm{dn}(u,k) \tag{3.95}$$

$$\frac{\partial}{\partial u}\mathrm{cn}(u,k) = -\mathrm{sn}(u,k)\mathrm{dn}(u,k) \tag{3.96}$$

In (3.93) through (3.96), the additional function used is defined as follows:

- dn( ) is the Jacobi delta amplitude function

The use of a quadruple function chain rule process to solve the partial derivative of (3.91) is shown next in (3.97) and simplified in (3.98).

$$\mathrm{n}_x = \begin{matrix} r_C\sqrt{2}\frac{\partial}{\partial x}\left(\mathrm{E}\left(\mathrm{sn}\left(\mathrm{arccn}\left(\frac{\sqrt{x^2+y^2}}{r_C},\frac{1}{\sqrt{2}}\right),\frac{1}{\sqrt{2}}\right),\frac{1}{\sqrt{2}}\right)\right)\frac{\partial}{\partial x}\left(\mathrm{sn}\left(\mathrm{arccn}\left(\frac{\sqrt{x^2+y^2}}{r_C},\frac{1}{\sqrt{2}}\right),\frac{1}{\sqrt{2}}\right)\right)\frac{\partial}{\partial x}\left(\mathrm{arccn}\left(\frac{\sqrt{x^2+y^2}}{r_C},\frac{1}{\sqrt{2}}\right)\right)\frac{\partial}{\partial x}\left(\frac{\sqrt{x^2+y^2}}{r_C}\right) \\ -\frac{r_C\sqrt{2}}{2}\frac{\partial}{\partial x}\left(\mathrm{F}\left(\mathrm{sn}\left(\mathrm{arccn}\left(\frac{\sqrt{x^2+y^2}}{r_C},\frac{1}{\sqrt{2}}\right),\frac{1}{\sqrt{2}}\right),\frac{1}{\sqrt{2}}\right)\right)\frac{\partial}{\partial x}\left(\mathrm{sn}\left(\mathrm{arccn}\left(\frac{\sqrt{x^2+y^2}}{r_C},\frac{1}{\sqrt{2}}\right),\frac{1}{\sqrt{2}}\right)\right)\frac{\partial}{\partial x}\left(\mathrm{arccn}\left(\frac{\sqrt{x^2+y^2}}{r_C},\frac{1}{\sqrt{2}}\right)\right)\frac{\partial}{\partial x}\left(\frac{\sqrt{x^2+y^2}}{r_C}\right) \end{matrix} \tag{3.97}$$

$$\mathrm{n}_x = r_C\sqrt{2}\frac{\partial}{\partial x}\left(\mathrm{sn}\left(\mathrm{arccn}\left(\frac{\sqrt{x^2+y^2}}{r_C},\frac{1}{\sqrt{2}}\right),\frac{1}{\sqrt{2}}\right)\right)\frac{\partial}{\partial x}\left(\mathrm{arccn}\left(\frac{\sqrt{x^2+y^2}}{r_C},\frac{1}{\sqrt{2}}\right)\right)\frac{\partial}{\partial x}\left(\frac{\sqrt{x^2+y^2}}{r_C}\right)\begin{pmatrix}\frac{\partial}{\partial x}\left(\mathrm{E}\left(\mathrm{sn}\left(\mathrm{arccn}\left(\frac{\sqrt{x^2+y^2}}{r_C},\frac{1}{\sqrt{2}}\right),\frac{1}{\sqrt{2}}\right),\frac{1}{\sqrt{2}}\right)\right)\\ -\frac{1}{2}\frac{\partial}{\partial x}\left(\mathrm{F}\left(\mathrm{sn}\left(\mathrm{arccn}\left(\frac{\sqrt{x^2+y^2}}{r_C},\frac{1}{\sqrt{2}}\right),\frac{1}{\sqrt{2}}\right),\frac{1}{\sqrt{2}}\right)\right)\end{pmatrix} \tag{3.98}$$

(3.93) and (3.94) provided the reference partial derivatives of the elliptic E and elliptic F functions, respectively, while (3.95) provided the reference partial derivative of the Jacobi sine function. Using a variable substitution shown in (3.99), (3.100) through (3.103) provide an augmentation of (3.93) and (3.94) that eliminates the asin( ) function component in the evaluations of those partial derivatives [25].

$$u = \mathrm{asin}(x) \tag{3.99}$$

$$\frac{\delta}{\delta x}\mathrm{E}(x,k) = \sqrt{1-k^2\sin^2(\mathrm{asin}(x))}\frac{\partial}{\partial x}(\mathrm{asin}(x)) \tag{3.100}$$

$$\frac{\delta}{\delta x}\mathrm{E}(x,k) = \sqrt{\frac{1-k^2x^2}{1-x^2}} \tag{3.101}$$

$$\frac{\delta}{\delta x}\mathrm{F}(x,k) = \frac{1}{\sqrt{1-k^2\sin^2(\mathrm{asin}(x))}}\frac{\partial}{\partial x}(\mathrm{asin}(x)) \tag{3.102}$$

$$\frac{\delta}{\delta x}\mathrm{F}(x,k) = \frac{1}{\sqrt{(1-k^2x^2)(1-x^2)}} \tag{3.103}$$

(3.98) contains five distinct partial derivative expressions that need evaluation to be fully simplified. Those partial derivative expressions are therefore simplified using (3.101), (3.103), and (3.95) in their evaluations. Equation (3.104) provides the inner-most partial derivative expression of the argument of the inverse Jacobi cosine function.

$$\frac{\partial}{\partial x}\left(\frac{\sqrt{x^2+y^2}}{r_C}\right) = \frac{x}{r_C\sqrt{x^2+y^2}} \tag{3.104}$$

(3.105) provides the nominal definition of the inverse Jacobi cosine function using definite integrals, so that the derivative of the inverse Jacobi cosine function can be provided in (3.106) and simplified in (3.107).

$$\operatorname{arccn}(x,k)=\int_x^1 \frac{dt}{\sqrt{(1-t^2)(1-k^2+k^2t^2)}} \tag{3.105}$$

$$\frac{\partial}{\partial x}\left(\operatorname{arccn}\left(\frac{\sqrt{x^2+y^2}}{r_C},\frac{1}{\sqrt{2}}\right)\right)=-\frac{1}{\sqrt{\frac{1}{2}\left(1-\frac{x^2+y^2}{{r_C}^2}\right)\left(1+\frac{x^2+y^2}{{r_C}^2}\right)}} \tag{3.106}$$

$$\frac{\partial}{\partial x}\left(\operatorname{arccn}\left(\frac{\sqrt{x^2+y^2}}{r_C},\frac{1}{\sqrt{2}}\right)\right)=-\frac{{r_C}^2\sqrt{2}}{\sqrt{{r_C}^4-(x^2+y^2)^2}} \tag{3.107}$$

(3.108) evaluates the partial derivative of the Jacobi sine function. Equations (3.109) through (3.111) provide reference identities of the Jacobi sine, cosine, and delta amplitude functions, and then (3.112) simplifies the partial derivative evaluation of (3.108) using the identities from (3.110) and (3.111).

$$\frac{\partial}{\partial x}\left(\operatorname{sn}\left(\operatorname{arccn}\left(\frac{\sqrt{x^2+y^2}}{r_C},\frac{1}{\sqrt{2}}\right),\frac{1}{\sqrt{2}}\right)\right)=\operatorname{cn}\left(\operatorname{arccn}\left(\frac{\sqrt{x^2+y^2}}{r_C},\frac{1}{\sqrt{2}}\right),\frac{1}{\sqrt{2}}\right)\operatorname{dn}\left(\operatorname{arccn}\left(\frac{\sqrt{x^2+y^2}}{r_C},\frac{1}{\sqrt{2}}\right),\frac{1}{\sqrt{2}}\right) \tag{3.108}$$

$$\operatorname{sn}\left(\operatorname{arccn}\left(x,\frac{1}{\sqrt{2}}\right),\frac{1}{\sqrt{2}}\right)=\sqrt{1-x^2} \tag{3.109}$$

$$\operatorname{cn}\left(\operatorname{arccn}\left(x,\frac{1}{\sqrt{2}}\right),\frac{1}{\sqrt{2}}\right)=x \tag{3.110}$$

$$\operatorname{dn}\left(\operatorname{arccn}\left(x,\frac{1}{\sqrt{2}}\right),\frac{1}{\sqrt{2}}\right)=\frac{1}{\sqrt{2}}\sqrt{x^2+1} \tag{3.111}$$

$$\frac{\partial}{\partial x}\left(\operatorname{sn}\left(\operatorname{arccn}\left(\frac{\sqrt{x^2+y^2}}{r_C},\frac{1}{\sqrt{2}}\right),\frac{1}{\sqrt{2}}\right)\right)=\frac{1}{{r_C}^2\sqrt{2}}\left(\sqrt{x^2+y^2}\right)\sqrt{x^2+y^2+{r_C}^2} \tag{3.112}$$

(3.113) evaluates the partial derivative of the elliptic E function, and then simplifies that using the identity from (3.109) in (3.114) and (3.115).

$$\frac{\partial}{\partial x}\left(\operatorname{E}\left(\operatorname{sn}\left(\operatorname{arccn}\left(\frac{\sqrt{x^2+y^2}}{r_C},\frac{1}{\sqrt{2}}\right),\frac{1}{\sqrt{2}}\right),\frac{1}{\sqrt{2}}\right)\right)=\sqrt{\frac{1-\frac{1}{2}\left(\operatorname{sn}\left(\operatorname{arccn}\left(\frac{\sqrt{x^2+y^2}}{r_C},\frac{1}{\sqrt{2}}\right),\frac{1}{\sqrt{2}}\right)\right)^2}{1-\left(\operatorname{sn}\left(\operatorname{arccn}\left(\frac{\sqrt{x^2+y^2}}{r_C},\frac{1}{\sqrt{2}}\right),\frac{1}{\sqrt{2}}\right)\right)^2}} \tag{3.113}$$

$$\frac{\partial}{\partial x}\left(\operatorname{E}\left(\operatorname{sn}\left(\operatorname{arccn}\left(\frac{\sqrt{x^2+y^2}}{r_C},\frac{1}{\sqrt{2}}\right),\frac{1}{\sqrt{2}}\right),\frac{1}{\sqrt{2}}\right)\right)=\sqrt{\frac{\frac{1}{2}\left(1+\left(\frac{\sqrt{x^2+y^2}}{r_C}\right)^2\right)}{\left(\frac{\sqrt{x^2+y^2}}{r_C}\right)^2}} \tag{3.114}$$

$$\frac{\partial}{\partial x}\left(\mathrm{E}\left(\mathrm{sn}\left(\mathrm{arccn}\left(\frac{\sqrt{x^2+y^2}}{r_C},\frac{1}{\sqrt{2}}\right),\frac{1}{\sqrt{2}}\right),\frac{1}{\sqrt{2}}\right)\right)=\frac{\sqrt{{r_C}^2+x^2+y^2}}{\sqrt{2}\sqrt{x^2+y^2}} \tag{3.115}$$

(3.116) evaluates the partial derivative of the elliptic F function, and then simplifies that using the identity from (3.109) in (3.117) and (3.118).

$$\frac{\partial}{\partial x}\left(\mathrm{F}\left(\mathrm{sn}\left(\mathrm{arccn}\left(\frac{\sqrt{x^2+y^2}}{r_C},\frac{1}{\sqrt{2}}\right),\frac{1}{\sqrt{2}}\right),\frac{1}{\sqrt{2}}\right)\right)=\frac{1}{\sqrt{\left(1-\frac{1}{2}\left(\mathrm{sn}\left(\mathrm{arccn}\left(\frac{\sqrt{x^2+y^2}}{r_C},\frac{1}{\sqrt{2}}\right),\frac{1}{\sqrt{2}}\right)\right)^2\right)\left(1-\left(\mathrm{sn}\left(\mathrm{arccn}\left(\frac{\sqrt{x^2+y^2}}{r_C},\frac{1}{\sqrt{2}}\right),\frac{1}{\sqrt{2}}\right)\right)^2\right)}} \tag{3.116}$$

$$\frac{\partial}{\partial x}\left(\mathrm{F}\left(\mathrm{sn}\left(\mathrm{arccn}\left(\frac{\sqrt{x^2+y^2}}{r_C},\frac{1}{\sqrt{2}}\right),\frac{1}{\sqrt{2}}\right),\frac{1}{\sqrt{2}}\right)\right)=\frac{1}{\sqrt{\frac{1}{2}\left(1+\left(\frac{\sqrt{x^2+y^2}}{r_C}\right)^2\right)\left(\frac{\sqrt{x^2+y^2}}{r_C}\right)^2}} \tag{3.117}$$

$$\frac{\partial}{\partial x}\left(\mathrm{F}\left(\mathrm{sn}\left(\mathrm{arccn}\left(\frac{\sqrt{x^2+y^2}}{r_C},\frac{1}{\sqrt{2}}\right),\frac{1}{\sqrt{2}}\right),\frac{1}{\sqrt{2}}\right)\right)=\frac{{r_C}^2\sqrt{2}}{\sqrt{x^2+y^2}\sqrt{{r_C}^2+x^2+y^2}} \tag{3.118}$$

With the five partial derivative expressions from (3.98) now defined in (3.112), (3.107), (3.104), (3.115) and (3.118) respectively, (3.98) is now evaluated using these five expressions, which is shown next in (3.119) and then simplified in (3.120).

$$\mathrm{n}_x = r_C\sqrt{2}\left(\frac{1}{{r_C}^2\sqrt{2}}\left(\sqrt{x^2+y^2}\right)\sqrt{x^2+y^2+{r_C}^2}\right)\left(-\frac{{r_C}^2\sqrt{2}}{\sqrt{{r_C}^4-(x^2+y^2)^2}}\right)\left(\frac{x}{r_C\sqrt{x^2+y^2}}\right)\begin{pmatrix}\frac{\sqrt{{r_C}^2+x^2+y^2}}{\sqrt{2}\sqrt{x^2+y^2}}\\ -\frac{1}{2}\frac{{r_C}^2\sqrt{2}}{\sqrt{x^2+y^2}\sqrt{{r_C}^2+x^2+y^2}}\end{pmatrix} \tag{3.119}$$

$$\mathrm{n}_x = \frac{-x\sqrt{x^2+y^2}}{\sqrt{{r_C}^4-(x^2+y^2)^2}} \tag{3.120}$$

The derivation of the normal component with respect to the y-axis follows the same process as for the x-axis, but with the change of the inner-most component partial derivative, from (3.104), being taken with respect to the y-axis, which is provided below in (3.121). The solution to (3.92) will utilize (3.121) in its final form in (3.122).

$$\frac{\partial}{\partial y}\left(\frac{\sqrt{x^2+y^2}}{r_C}\right)=\frac{y}{r_C\sqrt{x^2+y^2}} \tag{3.121}$$

$$\mathrm{n}_y = \frac{-y\sqrt{x^2+y^2}}{\sqrt{{r_C}^4-(x^2+y^2)^2}} \tag{3.122}$$

The unit normal vector for the inflatable reflector antenna is given in (3.123) through (3.125), which is based on the form of (3.42) through (3.44), utilizing instead (3.120) and (3.122).

$$\mathrm{n}'_x = \frac{\frac{-x\sqrt{x^2+y^2}}{\sqrt{{r_C}^4-(x^2+y^2)^2}}}{\sqrt{\left(\frac{-x\sqrt{x^2+y^2}}{\sqrt{{r_C}^4-(x^2+y^2)^2}}\right)^2+\left(\frac{-y\sqrt{x^2+y^2}}{\sqrt{{r_C}^4-(x^2+y^2)^2}}\right)^2+(1)^2}} \tag{3.123}$$

$$\mathrm{n}'_y = \frac{\frac{-y\sqrt{x^2+y^2}}{\sqrt{{r_C}^4-(x^2+y^2)^2}}}{\sqrt{\left(\frac{-x\sqrt{x^2+y^2}}{\sqrt{{r_C}^4-(x^2+y^2)^2}}\right)^2+\left(\frac{-y\sqrt{x^2+y^2}}{\sqrt{{r_C}^4-(x^2+y^2)^2}}\right)^2+(1)^2}} \tag{3.124}$$

$$\mathrm{n}'_z = \frac{1}{\sqrt{\left(\frac{-x\sqrt{x^2+y^2}}{\sqrt{{r_C}^4-(x^2+y^2)^2}}\right)^2+\left(\frac{-y\sqrt{x^2+y^2}}{\sqrt{{r_C}^4-(x^2+y^2)^2}}\right)^2+(1)^2}} \tag{3.125}$$

The surface area of each grid point on the inflatable aperture antenna needs to be redefined using the partial derivative expressions from (3.120) and (3.122), based on the surface area (3.45). The use of those partial derivative expressions, substituted into (3.45) is shown in (3.126), and simplified in (3.127).

$$\Delta S = \int_{x-\Delta x/2}^{x+\Delta x/2}\int_{y-\Delta y/2}^{y+\Delta y/2}\sqrt{1+\left(\frac{-x\sqrt{x^2+y^2}}{\sqrt{{r_C}^4-(x^2+y^2)^2}}\right)^2}\sqrt{1+\left(\frac{-y\sqrt{x^2+y^2}}{\sqrt{{r_C}^4-(x^2+y^2)^2}}\right)^2}\,dS \tag{3.126}$$

$$\Delta S = \int_{x-\Delta x/2}^{x+\Delta x/2}\int_{y-\Delta y/2}^{y+\Delta y/2}\frac{\sqrt{({r_C}^4-x^2y^2-y^4)({r_C}^4-x^2y^2-x^4)}}{{r_C}^4-(x^2+y^2)^2}\,dS \tag{3.127}$$

As can be seen in (3.120) and (3.122), as well as the combined and simplified (3.127), the x-axis and y-axis components are not separable, as was possible for the

parabolic reflector antenna. In order for the surface area of each grid point to utilize the approach of (3.54) through (3.66), the partial derivatives would need to not be a function of both the x-axis and y-axis variables, and so the approach to solving the surface area at each grid point must be done via numerical calculations performing a double integration analytically.

3.8 Summary

This work provided the full referenced, derivation of the physical optics modeling for solid parabolic reflector antennas in Sections 3.1 through 3.6, and provided the author's contributions of the necessary augmentation to that modeling approach to implement physical optics modeling of inflatable aperture antennas in Section 3.7. The augmentation for inflatable aperture antennas introduced changes to the derivation of the normal vector along the inflatable aperture antenna surface, as well as the derivation of the surface area of each analyzed grid point along the inflatable aperture antenna surface. Both of these modifications utilized the inflatable aperture antenna surface profile derivations from Chapter II, as well as other identities associated with the utilized elliptic E, elliptic F, Jacobi sine, and Jacobi cosine functions, along with the derivatives of those functions.

Of particular note, one can observe a commonality in the form of the normal vector components, as provided for the solid parabolic reflector antenna in (3.38), and for the inflatable aperture antenna in (3.120). Regarding the partial derivative of the shape equation with respect to the x-axis, both equations contain the x-component term in the

numerator. For the solid parabolic reflector, the denominator is twice the focal length. For the inflatable aperture antenna, the denominator is a set of square-root functions of the x-component, y-component, and the radius substitution variable, which was a function of the uninflated radius and inflated radius. Both of these denominator terms describe the shape of the two structures, but the solid parabolic antenna is a simple relationship of only the focal length. The nature of the inflatable aperture antenna shape term being a function of the uninflated radius, inflated radius, and the x- and y-axis components also illustrates why the surface area cannot be separated out into piecewise axis calculations, and must be performed via numerical integration.

CHAPTER IV

RF PERFORMANCE MODEL COMPARISON OF INFLATABLE APERTURE ANTENNA WITH SOLID PARABOLIC APERTURE ANTENNA

The RF performance of an antenna depends on several factors, ranging from, but not limited to, the size of the aperture, the frequency of transmission and/or reception, the focal length to diameter ratio, and the feed taper. The RF performance is measured in terms of the gain pattern of the antenna, which is the far-field response of the antenna with respect to the far-field angles. When comparing different antennas, one typically examines the difference in the gain, efficiency, beamwidth, first-null beamwidth, first side-lobe level, or the first side-lobe angles. No single metric can accurately assess the RF performance of the antenna, as the RF performance is not defined by a single value. It is with this understanding that this chapter will discuss the RF performance testing of the inflatable aperture antenna against the solid parabolic reflector antenna.

The remaining content of this chapter provides the author's implementation results and comparisons of the PO methodologies of analyzing a solid parabolic antenna against an inflatable aperture antenna. Section 4.1 provides an analysis of the

performance of a solid parabolic antenna as a function of sample spacing, while Section 4.2 provides brief background explanations of the performance metrics that will be used to assess the inflatable aperture antenna. Section 4.3 discusses the author's RF performance comparison methodologies, used in Sections 4.4 through 4.7 to illustrate the performance of the inflatable aperture antenna. Finally, Section 4.8 summarizes the author's contributions towards the performance assessments using the methodology described in Sections 4.1 through 4.3 from results provided in Sections 4.4 through 4.7.

4.1 Performance Assessment of Solid Parabolic Reflector Antenna Physical Optics Modeling

The processes described in Chapter III to model the physical optics-based RF performance of a solid parabolic reflector antenna and an inflatable aperture antenna were developed into two unique calculation scripts using Matlab®. The scripts only differed where necessary, as described in Section 3.7, such that the surface profile, surface normal, and surface area calculations for the inflatable aperture antenna. The scripts were setup to require a minimal set of input parameters to describe the antenna diameter (units of number wavelengths), focal length to diameter ratio (unitless), and input feed taper (dB). The inflatable aperture antenna script required one additional parameter referring to the Inflation Ratio of the inflatable aperture antenna, so that the proper shape can be modelled. The approach to setup the scripts in this manner removed the direct dependence on the antenna performance as functions of operating frequency and diameter size, where one common antenna operating at two unique frequencies would have unique

antenna patterns and RF performance. This approach simplified the process to only require one input parameter.

(3.31) had stated that the minimum number of sampling points was based on a ratio of one-half the aperture size divided by the wavelength, but other references state that higher sampling provides higher fidelity in the simulation, where the one-half ratio is a pure minimum to obtain proper results. A test case was ran on the solid parabolic reflector antenna script where the sample spacing was set to fractional values of one-half, one-fourth, and one-eighth. The test case utilized an antenna diameter of 20 wavelengths, a focal length to diameter ratio of 0.8, and a feed taper of -11 dB. The antenna pattern of these test cases are shown for the max far-field theta angle of 10° in Figure 77, while Figure 78 zooms into the main beam region of the pattern out to roughly 1°, and Figure 79 zooms onto the first side-lobe of the pattern between roughly 4.95° and 5.9°.

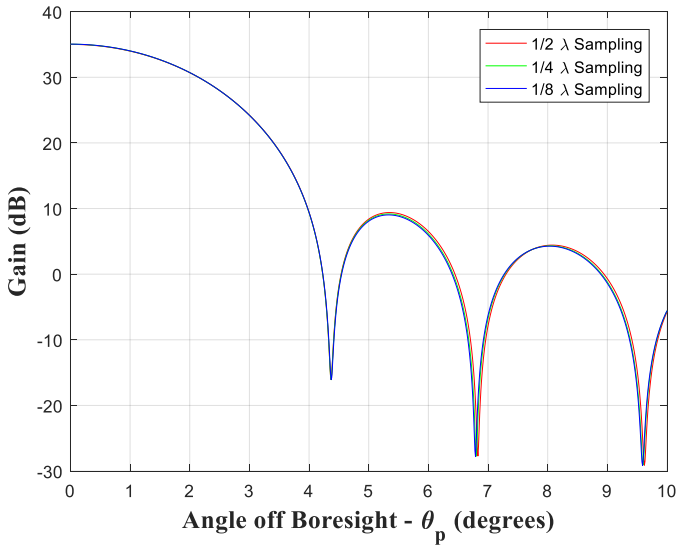

FIGURE 77: Parabolic Reflector Far-Field Patterns Against Sample Spacing

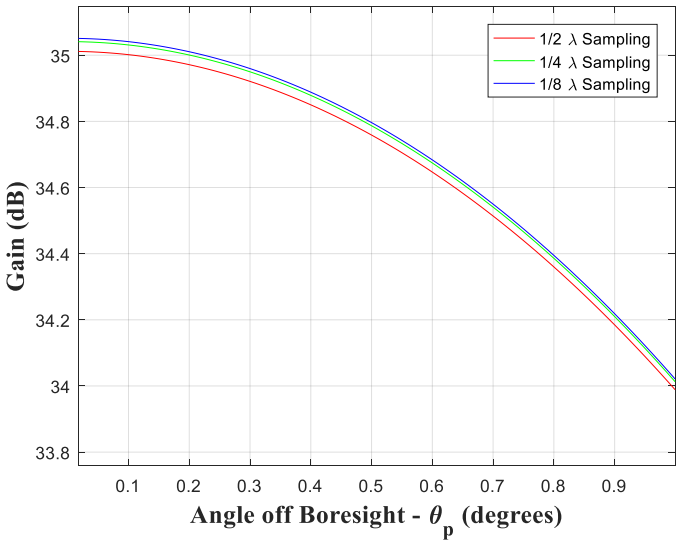

FIGURE 78: Main-Lobe Parabolic Reflector Far-Field Patterns Against Sample Spacing

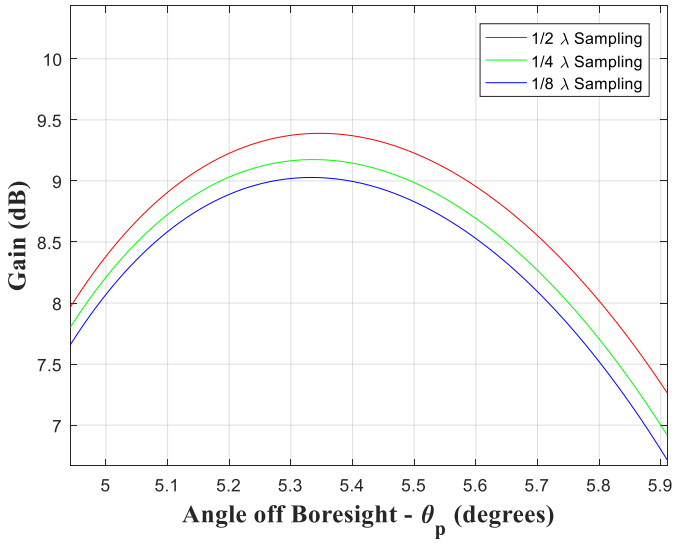

FIGURE 79: Side-Lobe Parabolic Reflector Far-Field Patterns Against Sample Spacing

A few key artifacts can be deduced from these three figures. First, at a glance from Figure 77, the pattern responses look very close, but when examining the zoomed in pattern responses in Figure 78 and Figure 79, one can observe minor differences in the responses. Figure 78 shows the peak gain at an angle of 0° increases slightly with

smaller sampling spacing. Figure 79 shows that the first side-lobe peak reduces slightly with smaller sampling spacing, while the first side-lobe peak location shifts slightly closer to the boresight vector direction. Therefore, for implementation, the utilized sample spacing equation will be (4.1), instead of (3.31) which provides the minimal sample spacing from the Nyquist sampling theorem.

$$N = \text{floor}\left(\frac{D}{8\lambda}\right) + 1 \tag{4.1}$$

4.2 Metrics of RF Performance Model Comparisons

Section 4.1 briefly introduced some antenna pattern metrics in assessing the utilized sample spacing for all of the RF comparison assessments that will be provided in this work, but did not formally introduce the full set of antenna pattern metrics that will be used for the RF comparison assessments. The full set of antenna pattern metrics includes: peak gain, half-power beamwidth, first-null beamwidth, first side-lobe level degradation, and the first side-lobe level angle.

The first metric is that of the peak gain of the response, which occurs at an angle of zero. Equation (4.2) shall formally describe this peak gain, referring back to the theta-aligned polarization from (3.87). Note that these efforts do not account for any polarization mismatch loss.

$$\mathrm{G}_{\max} = \mathbf{F}_{\theta}(0,0) \tag{4.2}$$

In (4.2), the additional term used is defined as follows:

- $\mathbf{G}_{\max}$ is the peak gain of the antenna pattern

The second metric is that of the half-power beamwidth, which is what represents when the antenna response is 3dB below the peak gain, which is half the power at the peak gain. This is formalized in (4.3).

$$3 = \mathrm{G}_{\max} - \mathbf{F}_{\theta}(\theta_{3dB}, 0) \tag{4.3}$$

In (4.3), the additional term used is defined as follows:

- θ_{3dB} is the theta angle where the antenna gain is 3dB below the peak gain

The third metric is that of the first-null beamwidth, which represents when the antenna pattern reduces down to a null response, lack of any energy, for the first time. This is formalized in (4.4) however, it should be noted that the definition can provide multiple values, and so a minimum function is utilized to guarantee that the lowest angle, or first, is returned.

$$-\infty = \mathbf{F}_{\theta}(\min(\theta_{Null}), 0) \tag{4.4}$$

In (4.4), the additional term and function used are defined as follows:

- θ_{Null} is the theta angle where the antenna gain is null for the first time
- $\min()$ is the minimum function to guarantee that the first null theta angle is returned

The fourth and fifth metrics are that of the first side-lobe level degradation and the first side-lobe level angle. The first side-lobe level degradation represents the difference in the magnitude of the antenna peak gain from the peak gain at the first side-lobe level angle. The first side-lobe level angle represents the location where the first side-lobe level peaks, and can be represented at the minimum angle location where the partial derivative of the antenna gain response is zero, given that it is observed at a starting angle

greater than that of the first null beamwidth. These two metrics are formalized in (4.5) and (4.6).

$$\Delta G_{SLL} = \mathbf{F}_{\theta}(\theta_{SLL}, 0) - G_{\max} \tag{4.5}$$

$$0 = \frac{\partial}{\partial \theta}\mathbf{F}_{\theta}(\min(\theta_{SLL} > \theta_{Null}), 0) \tag{4.6}$$

In (4.5) and (4.6), the additional terms used are defined as follows:

- ΔG_{SLL} is the first side lobe level degradation
- θ_{SLL} is the theta angle where the first side lobe of the antenna gain occurs

Figure 80 provides a graphic of an antenna pattern overlaid with labels and identifiers to aid in the understanding of this set of antenna pattern metrics that will be used to ascertain antenna pattern performance [2].

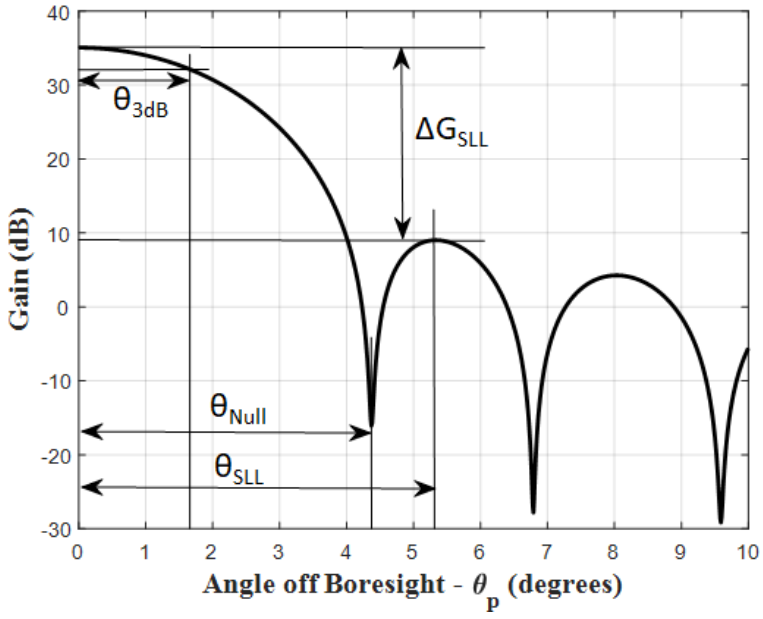

FIGURE 80: Metrics for RF Performance Model Comparisons

These metrics will be the set used to describe the RF performance comparisons of the solid parabolic reflector antenna and the inflatable aperture reflector antenna. Additionally, there will be terms used that describe the differences in these metrics between the two antenna types, which will be taken as differences with respect to the solid parabolic reflector antenna.

4.3 Methodologies of RF Performance Model Comparisons

With the RF performance metrics used to assess the performance variations between the solid parabolic reflector antenna and the inflatable aperture antenna described, the description of how the two antenna technologies compared is provided next. It is now known from the derivations in Chapter II that the inflatable aperture antenna has a fundamentally different shape profile than that of the solid parabolic reflector antenna. It is also known that there is not a single shape of the inflatable aperture antenna, as it is a function of the Inflation Ratio, which can range from zero to one. It will be of interest to analyze the performance of the inflatable aperture antenna within this range. Three distinct shape parameters will be used to perform the comparison testing between the solid parabolic reflector antenna and the inflatable aperture antenna, which include common diameters, common depths, and common arc-lengths. These comparison techniques are illustrated in Figures 81, 82, and 83, respectively.

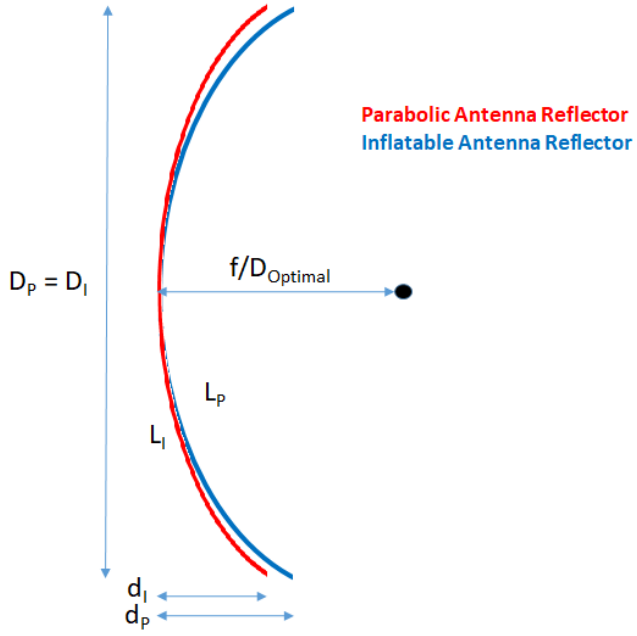

FIGURE 81: RF Performance Model Comparisons: Constant Diameter

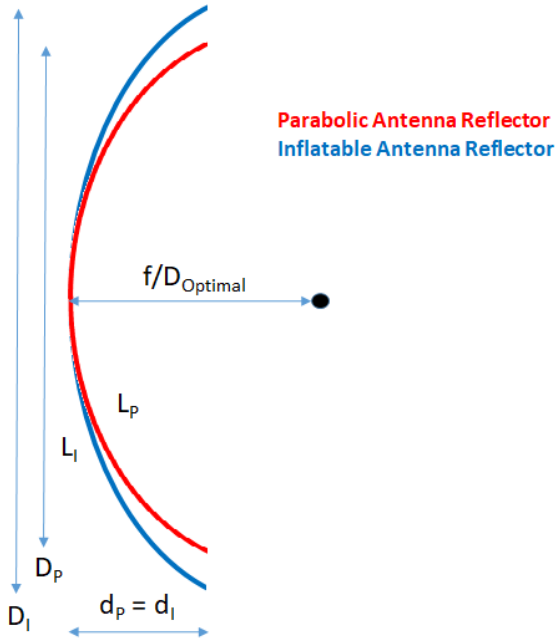

FIGURE 82: RF Performance Model Comparisons: Constant Depth

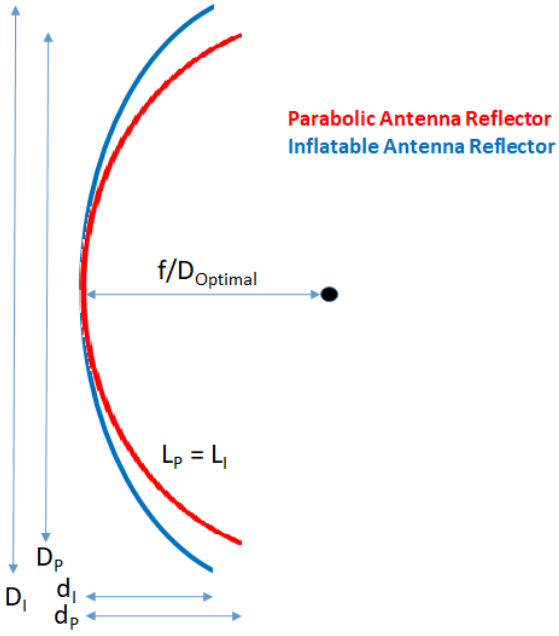

FIGURE 83: RF Performance Model Comparisons: Constant Arc Length

In Figures 81 through 83, the additional terms used are defined as follows:

- D_P is the diameter of the solid parabolic reflector antenna
- D_I is the diameter of the inflatable aperture antenna
- d_P is the depth of the solid parabolic reflector antenna
- d_I is the depth of the inflatable aperture antenna
- L_P is the arc-length of the solid parabolic reflector antenna
- L_I is the arc-length of the inflatable aperture antenna

Throughout all of the comparisons, the inflatable aperture antenna diameter will be the baseline. Therefore, for the constant depth and arc-length comparisons over the Inflation Ratio range, an example aperture size of 20 wavelengths with an Inflation Ratio of 0.01 will have a different depth or arc-length than the same size aperture with an Inflation Ratio of 0.99. As a common depth or arc-length is desired, the solid parabolic reflector

antenna will have unique diameters from that of the inflatable aperture antenna, while maintaining the desired depth or arc-length for the given Inflation Ratio of the inflatable aperture antenna.

4.4 RF Performance Assessment of Inflatable Aperture Antenna

This section will provide the RF performance assessment of the inflatable aperture antenna, independent of the solid parabolic antenna. As mentioned in Section 4.3, the solid parabolic reflector antenna size will be augmented to match the common size property of the inflatable aperture antenna, and so by implementing such a technique, the RF performance of the inflatable aperture antenna only needs to be calculated once. As mentioned in Section 4.1, the script to analyze the performance of the inflatable aperture antenna was a function of the antenna diameter (units of number wavelengths), Inflation Ratio (unitless), focal length to diameter ratio (unitless), and input feed taper (dB). For the inflatable aperture antenna, the focal length no longer represents the shape of the antenna, but rather only the distance between the antenna vertex and the antenna feed. Therefore, an optimal focal length to diameter ratio was necessary to be found, and a minimization on the RMS error technique was selected, with the error taken against a parabolic curve, due to the nature of the parabolic curve aggregating energy at the focal point. For the inflatable aperture antenna, this created a focal length to diameter curve as a function of Inflation Ratio, which is shown next in Figure 84.

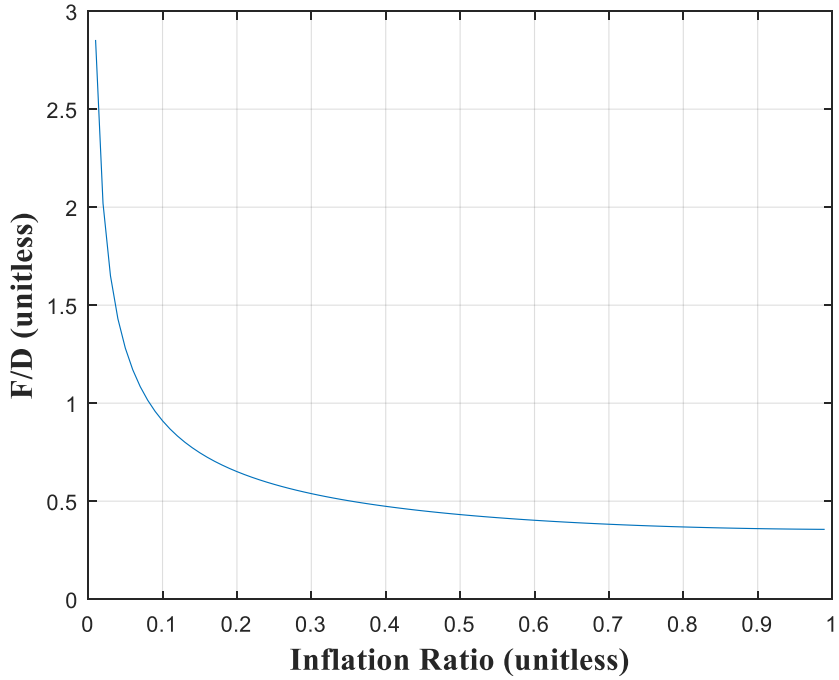

FIGURE 84: Utilized Focal Length to Diameter Curve as a Function of Inflation Ratio

As expected in Figure 84, the focal length to diameter ratio goes to infinity as the Inflation Ratio goes towards zero, as an Inflation Ratio of exactly zero means that the inflatable aperture antenna has no curvature. Interestingly, while a solid parabolic reflector antenna can have a minimum focal length to diameter ratio of 0.25, the minimum focal length to diameter ratio for the inflatable aperture antenna goes to a value near 0.386.

The RF performance of the inflatable aperture antenna will be illustrated next in Figures 85 through 94 for Inflation Ratio values of 0.05 through 0.95 in increments of 0.1. Each plot will illustrate the pattern using feed tapers values between -11dB and 0dB, in increments of 1dB, while maintaining a constant diameter of 20 wavelengths, while

using the focal length to diameter ratio value for a given Inflation Ratio value from Figure 84.

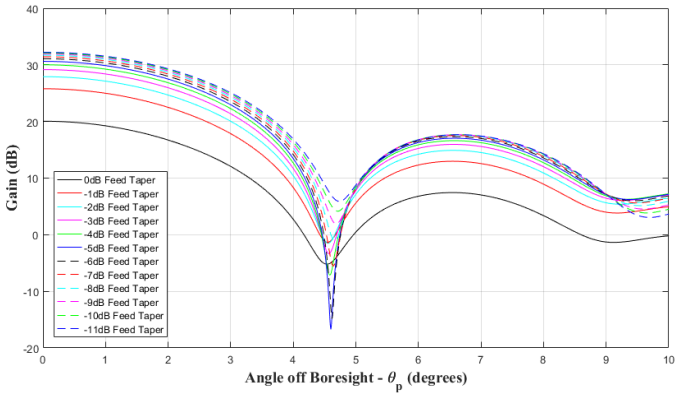

FIGURE 85: Inflatable Aperture Antenna Far-Field Patterns: Inflation Ratio = 0.05

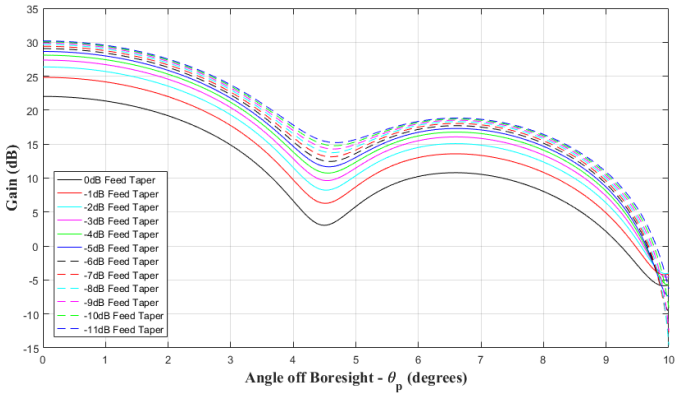

FIGURE 86: Inflatable Aperture Antenna Far-Field Patterns: Inflation Ratio = 0.15

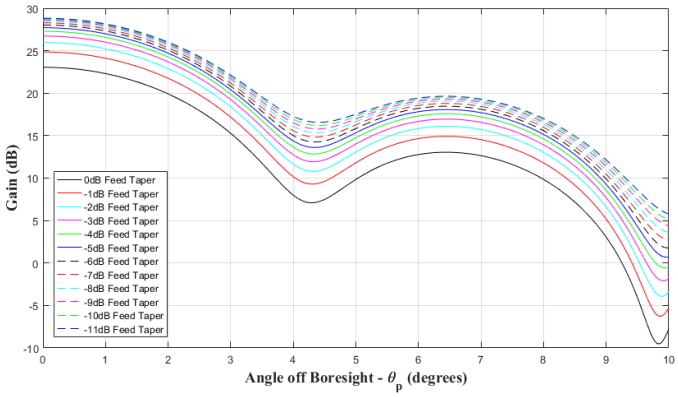

FIGURE 87: Inflatable Aperture Antenna Far-Field Patterns: Inflation Ratio = 0.25

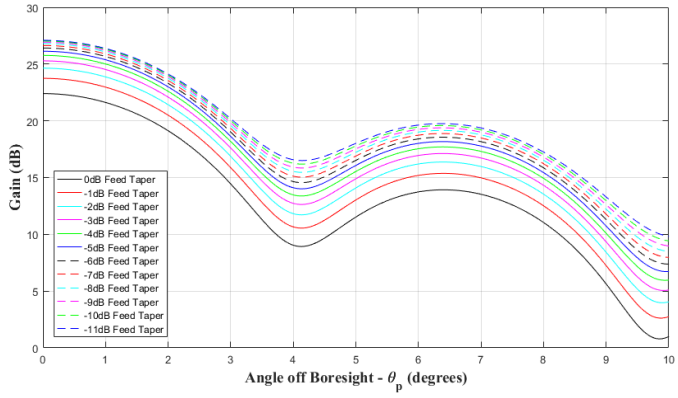

FIGURE 88: Inflatable Aperture Antenna Far-Field Patterns: Inflation Ratio = 0.35

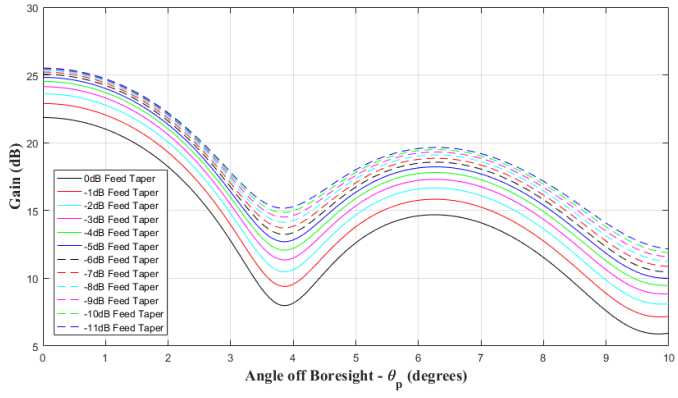

FIGURE 89: Inflatable Aperture Antenna Far-Field Patterns: Inflation Ratio = 0.45

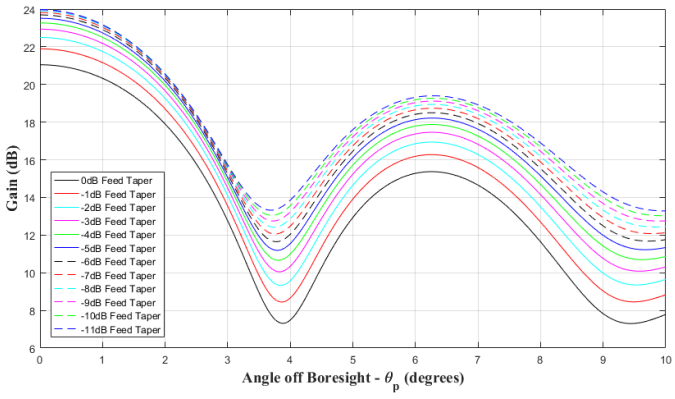

FIGURE 90: Inflatable Aperture Antenna Far-Field Patterns: Inflation Ratio = 0.55

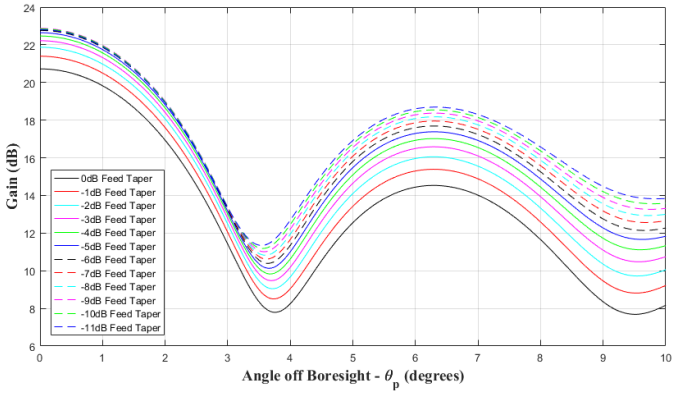

FIGURE 91: Inflatable Aperture Antenna Far-Field Patterns: Inflation Ratio = 0.65

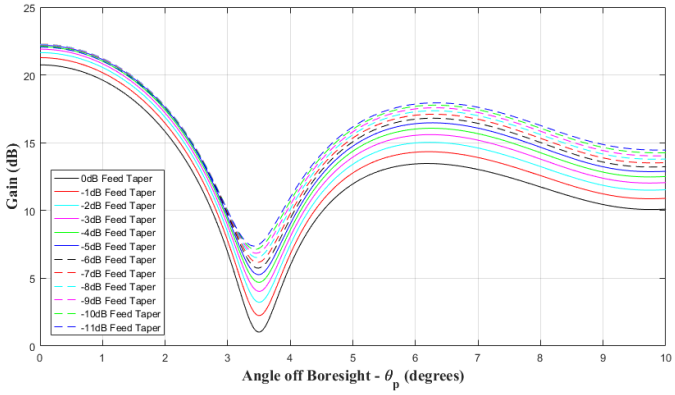

FIGURE 92: Inflatable Aperture Antenna Far-Field Patterns: Inflation Ratio = 0.75

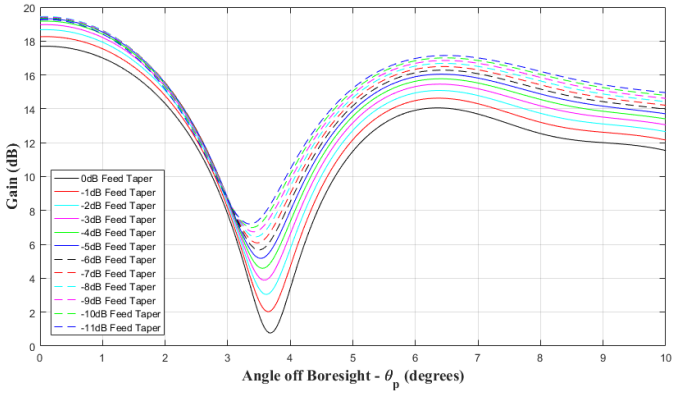

FIGURE 93: Inflatable Aperture Antenna Far-Field Patterns: Inflation Ratio = 0.85

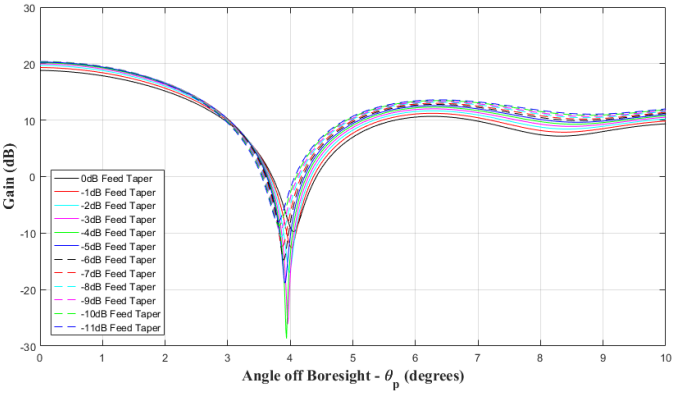

FIGURE 94: Inflatable Aperture Antenna Far-Field Patterns: Inflation Ratio = 0.95

There are several trends that can be observed across the pattern responses presented in Figures 85 through 94. The peak gain of the inflatable aperture antenna does decrease with an increase in the Inflation Ratio. The first null angle oscillates as the Inflation Ratio increases. The first side-lobe level degradation decreases as the Inflation Ratio increases, meaning that the energy is not as focused in the main beam. Finally, the disparity in the pattern responses across the feed taper range decreases as the Inflation

Ratio increases, showing how the focused feed energy cannot improve the overall antenna response in the peak gain.

With the nominal focal length to diameter ratio value defined as a function of the Inflation Ratio, the RF performance will be assessed using the focal length to diameter ratio value for a given Inflation Ratio value from Figure 84. The RF performance of the inflatable aperture antenna was calculated at antenna diameters ranging from 20 wavelengths to 100 wavelengths, in steps of 10 wavelengths. The RF performance was calculated across Inflation Ratio values ranging from 0.01 to 0.99 in increments of 0.01. The RF performance was calculated using feed taper values between -11dB and 0dB, in increments of 1dB. Figures 95 through 103 will illustrate the RF performance calculated with the inflatable aperture antenna. Each figure will contain five plots, corresponding to the peak gain in the first row, half-power beamwidth and first null beamwidth in the second row, and first side lobe level degradation and first side lobe level angle in the third row. Each figure is color coded against its colorbar to represent the numeric value of interest for each of the metrics.

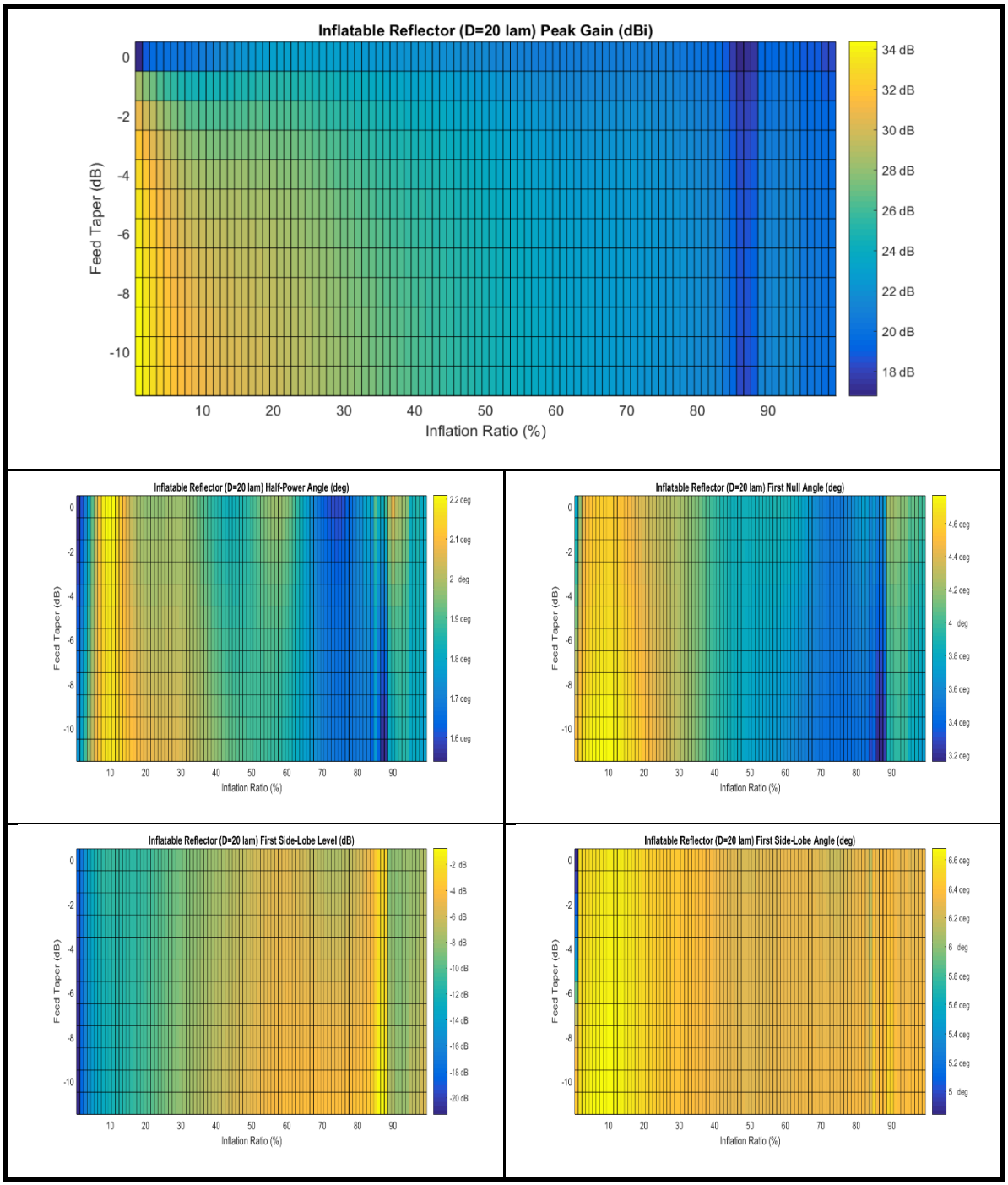

FIGURE 95: Inflatable Aperture Antenna Performance: Diameter = 20 Wavelengths

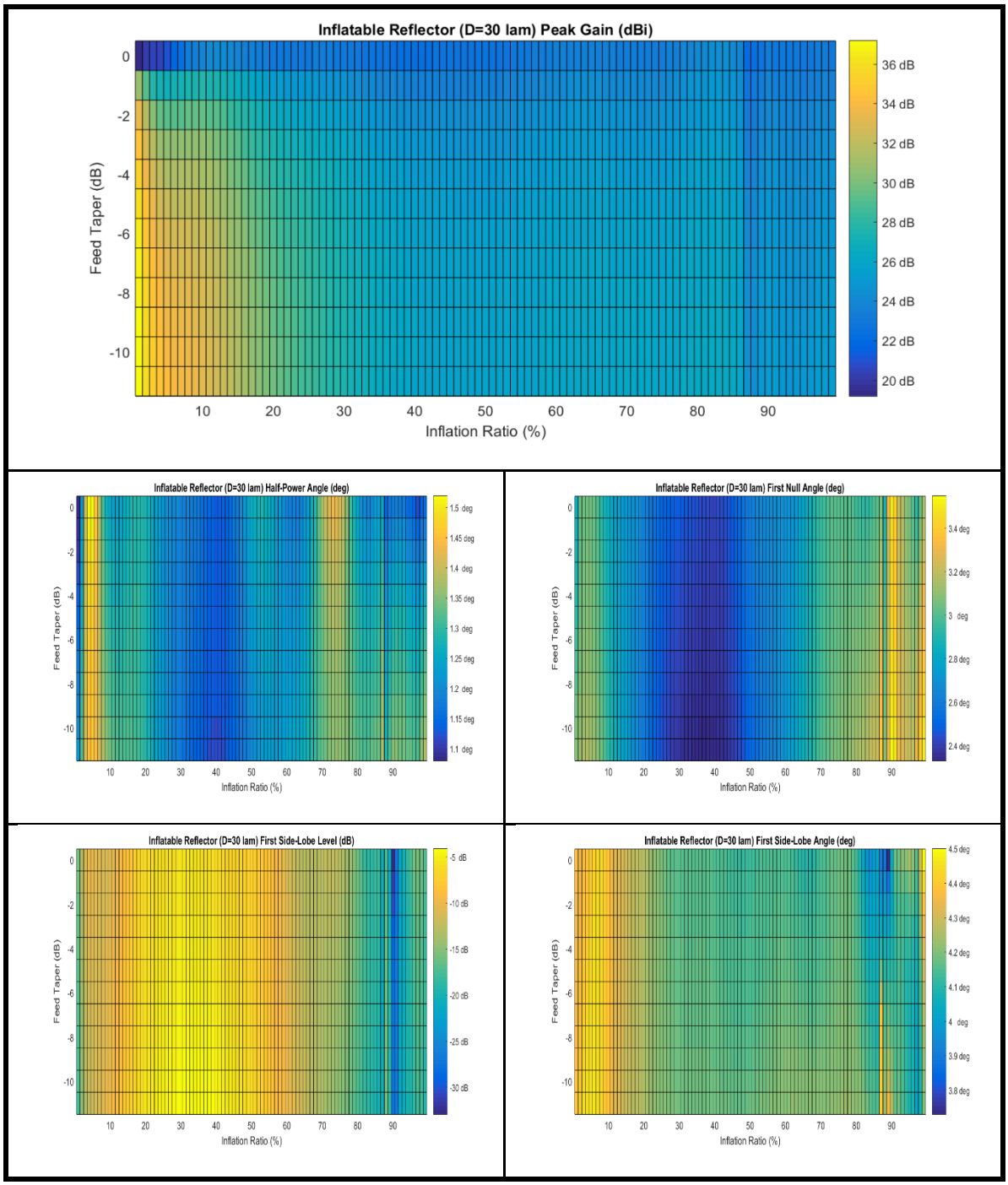

FIGURE 96: Inflatable Aperture Antenna Performance: Diameter = 30 Wavelengths

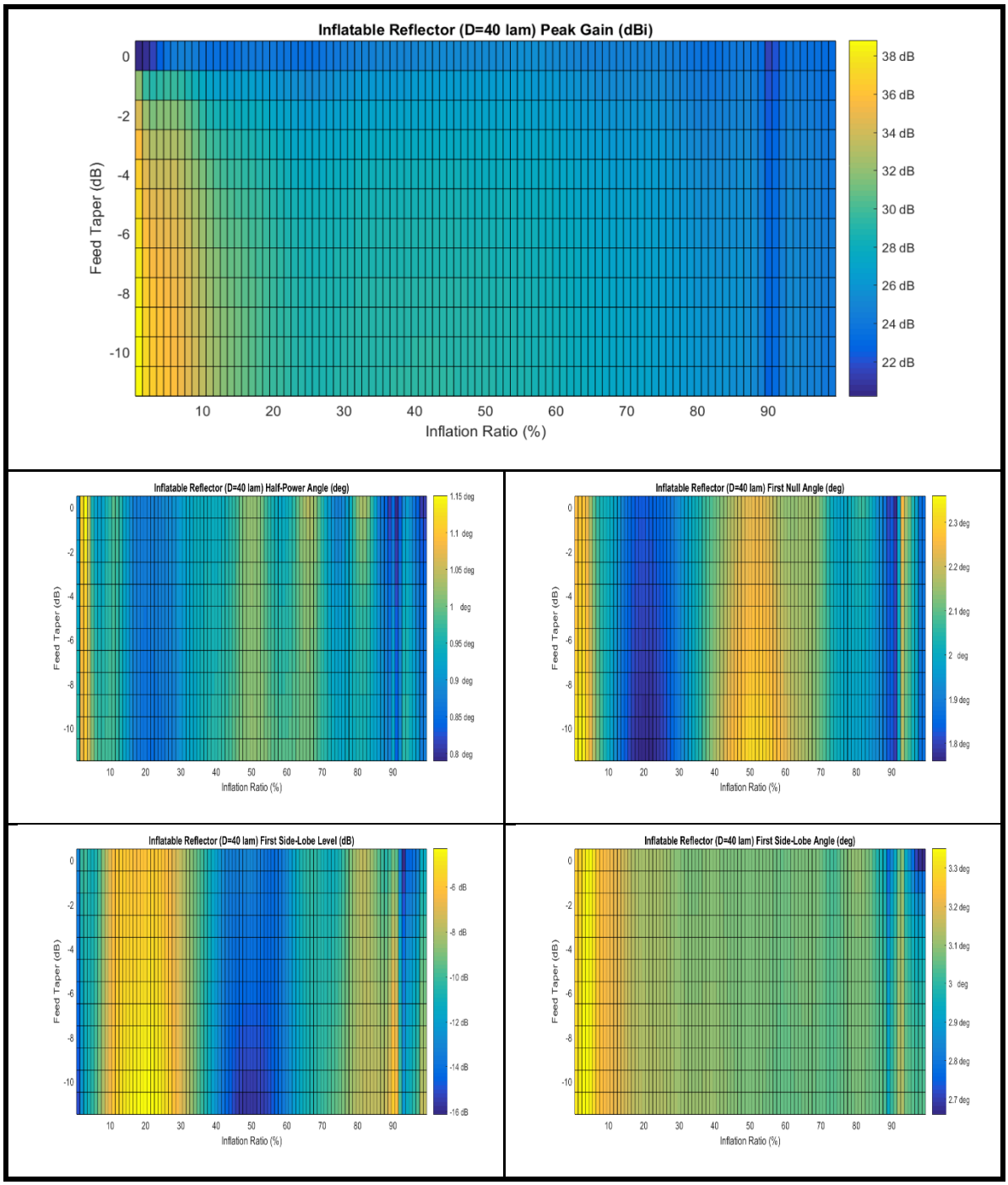

FIGURE 97: Inflatable Aperture Antenna Performance: Diameter = 40 Wavelengths

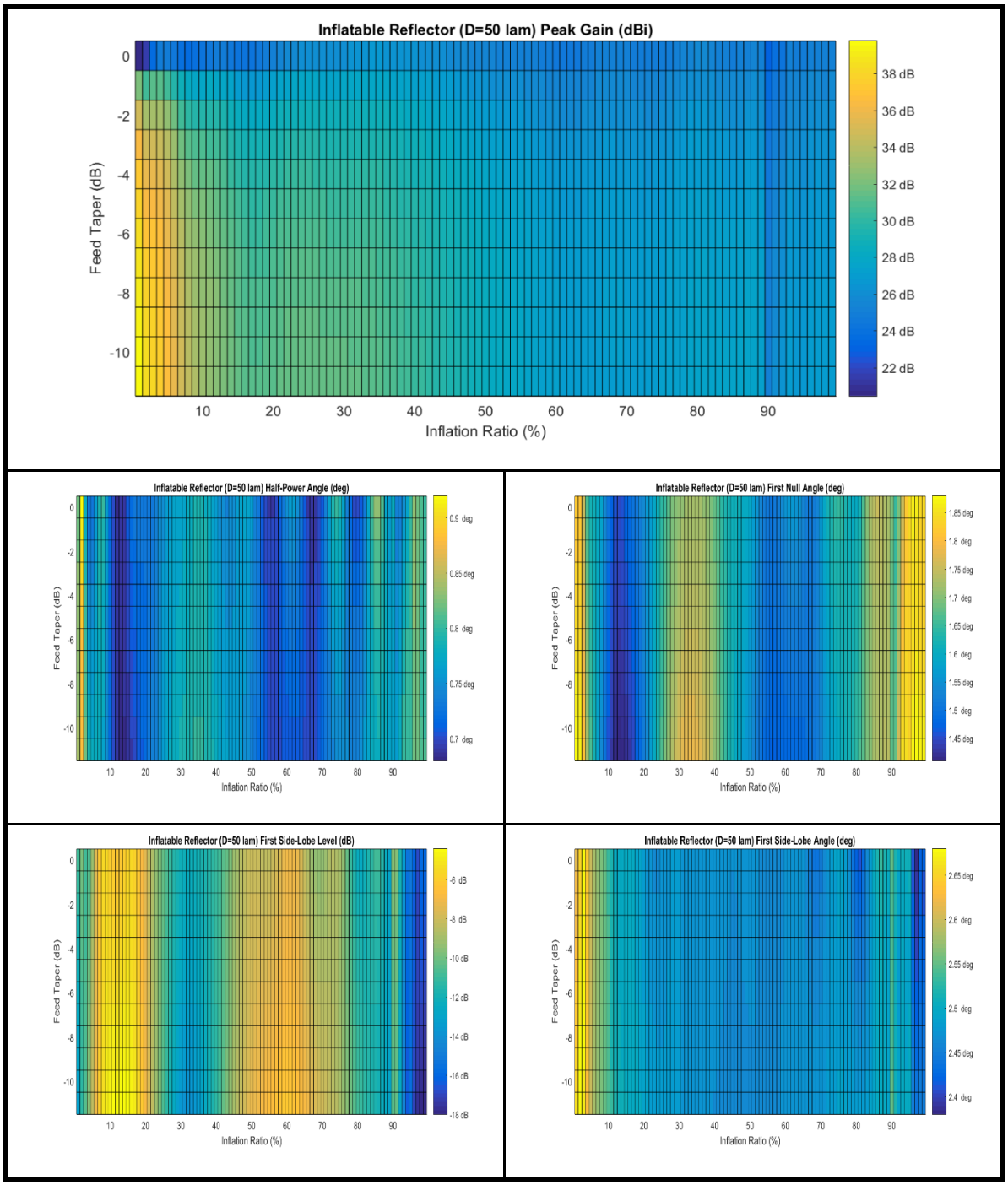

FIGURE 98: Inflatable Aperture Antenna Performance: Diameter = 50 Wavelengths

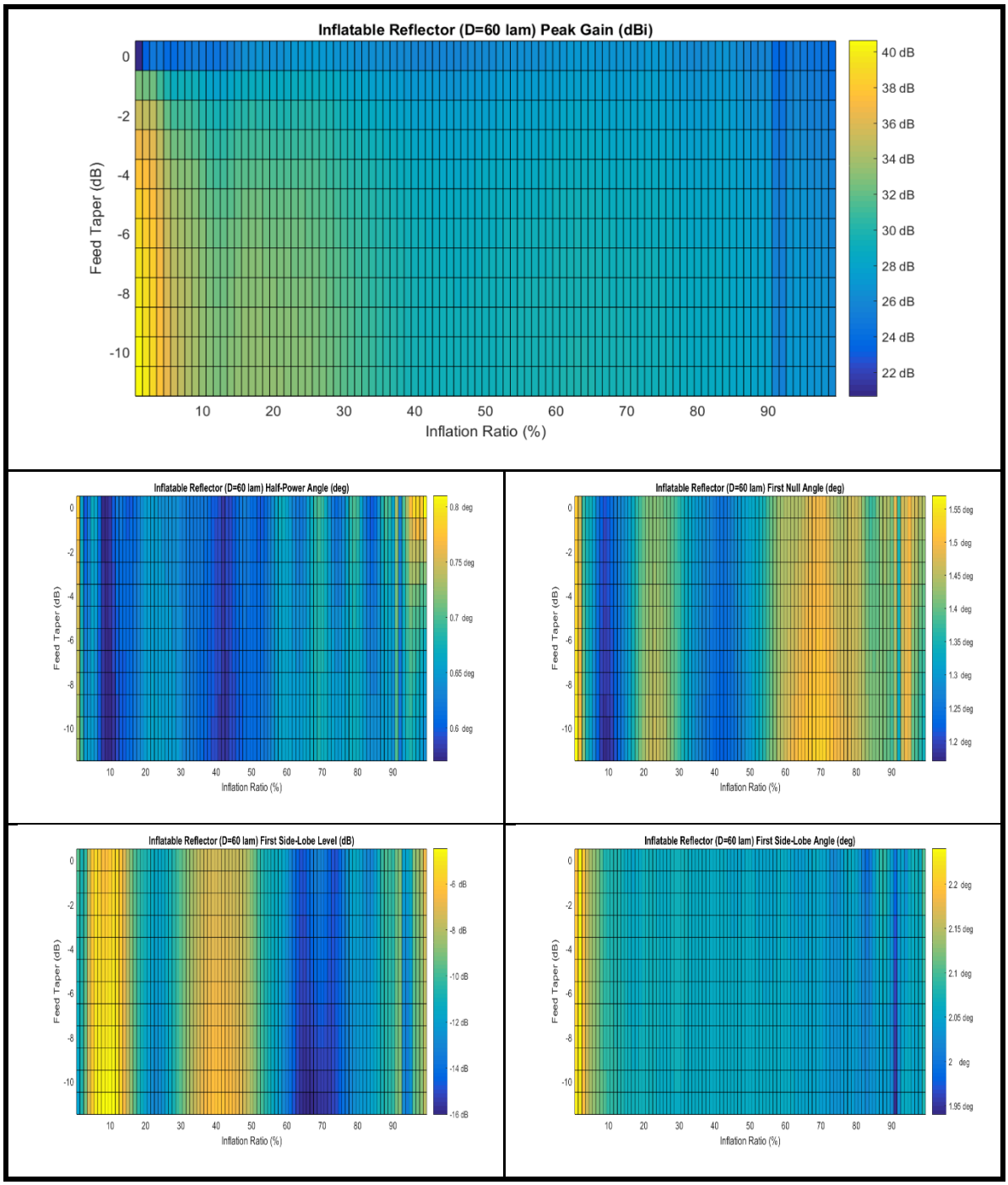

FIGURE 99: Inflatable Aperture Antenna Performance: Diameter = 60 Wavelengths

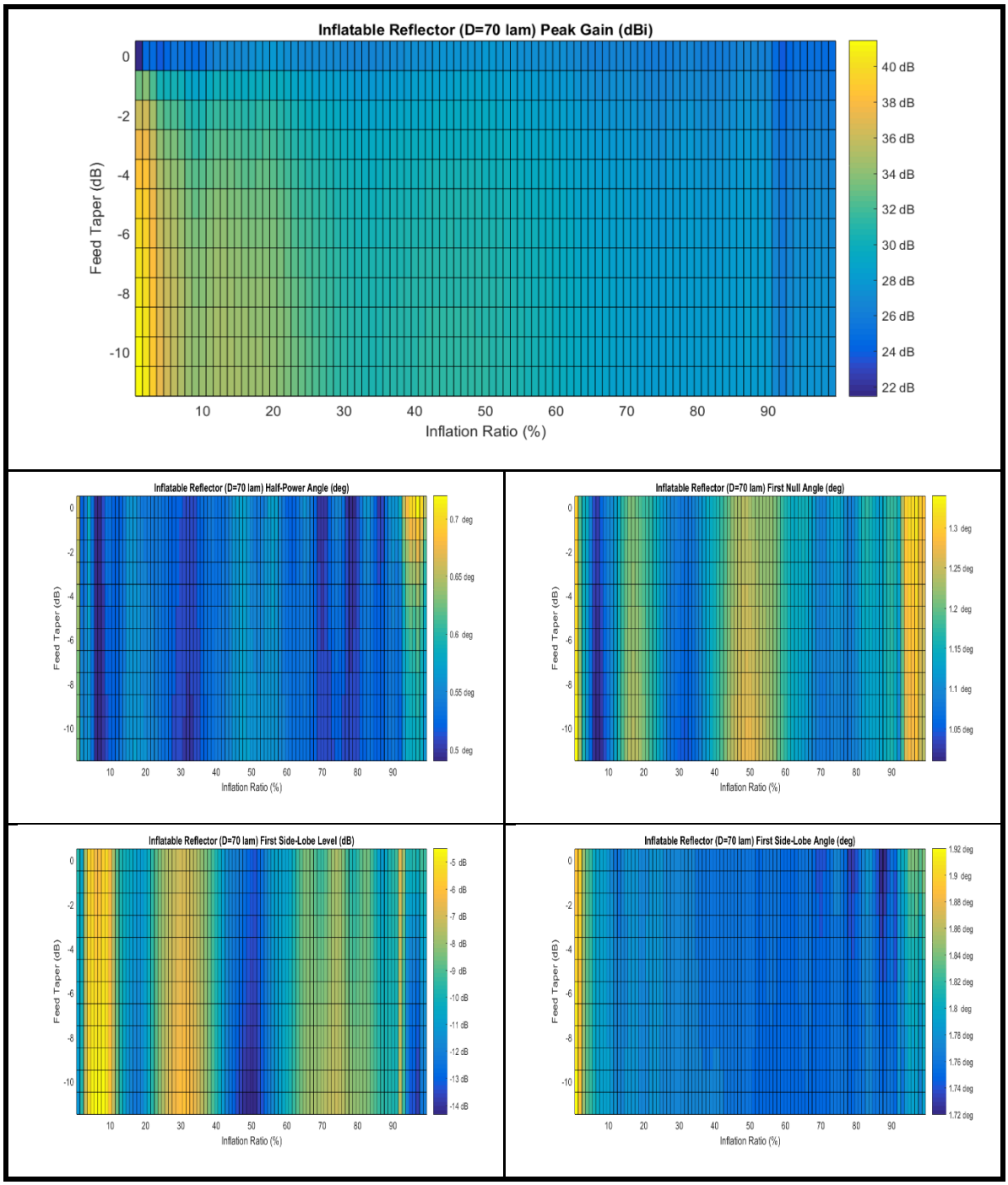

FIGURE 100: Inflatable Aperture Antenna Performance: Diameter = 70 Wavelengths

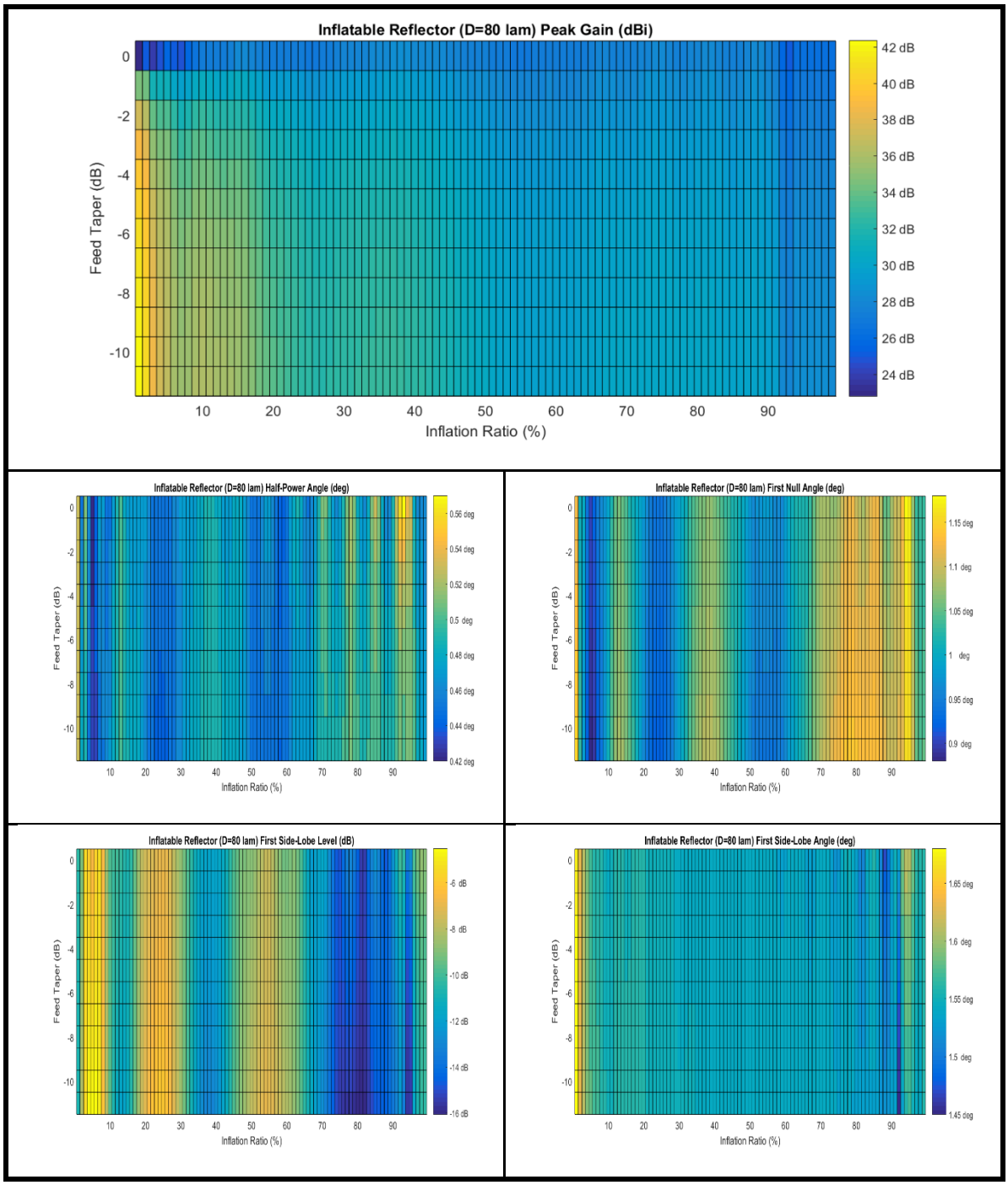

FIGURE 101: Inflatable Aperture Antenna Performance: Diameter = 80 Wavelengths

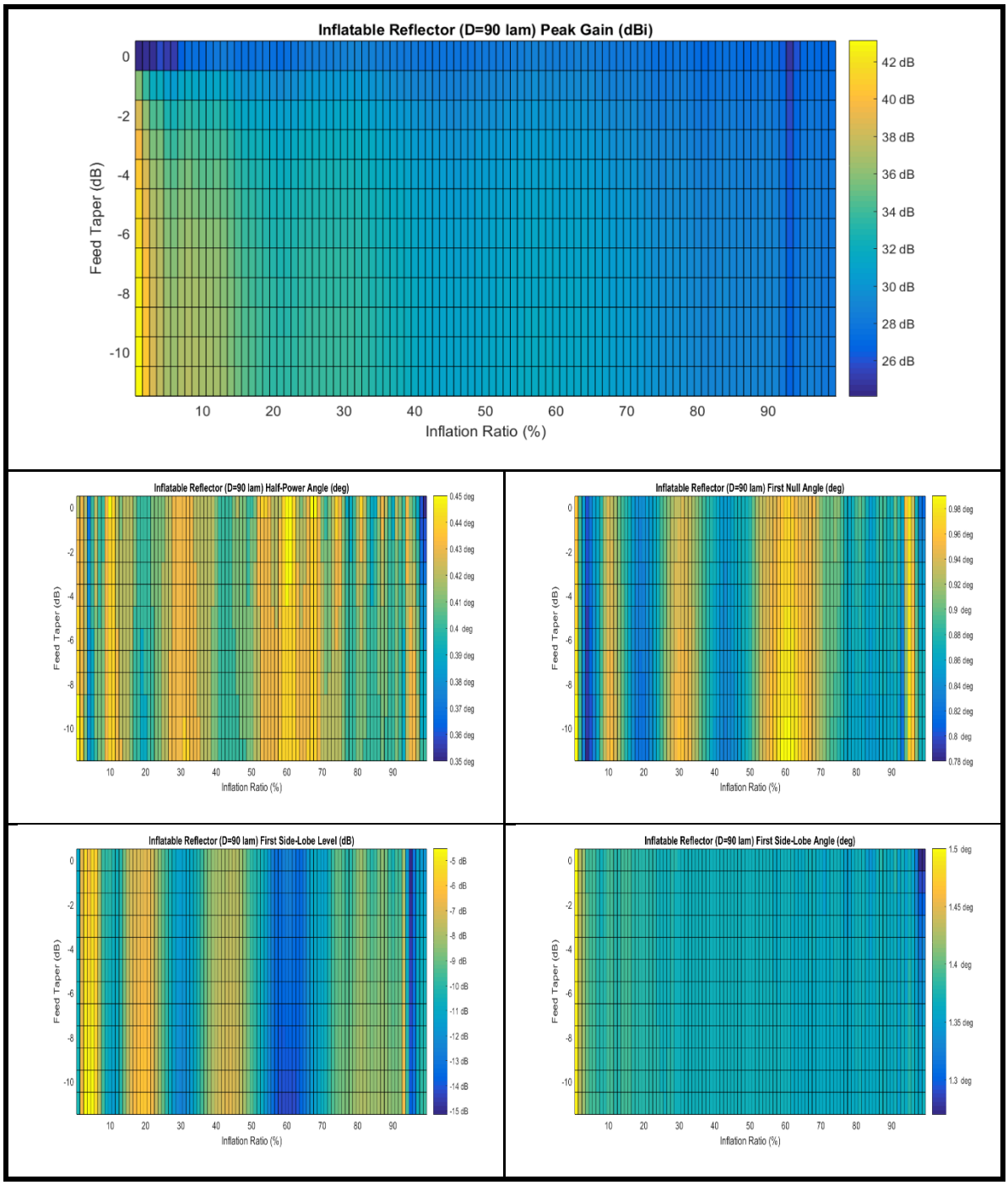

FIGURE 102: Inflatable Aperture Antenna Performance: Diameter = 90 Wavelengths

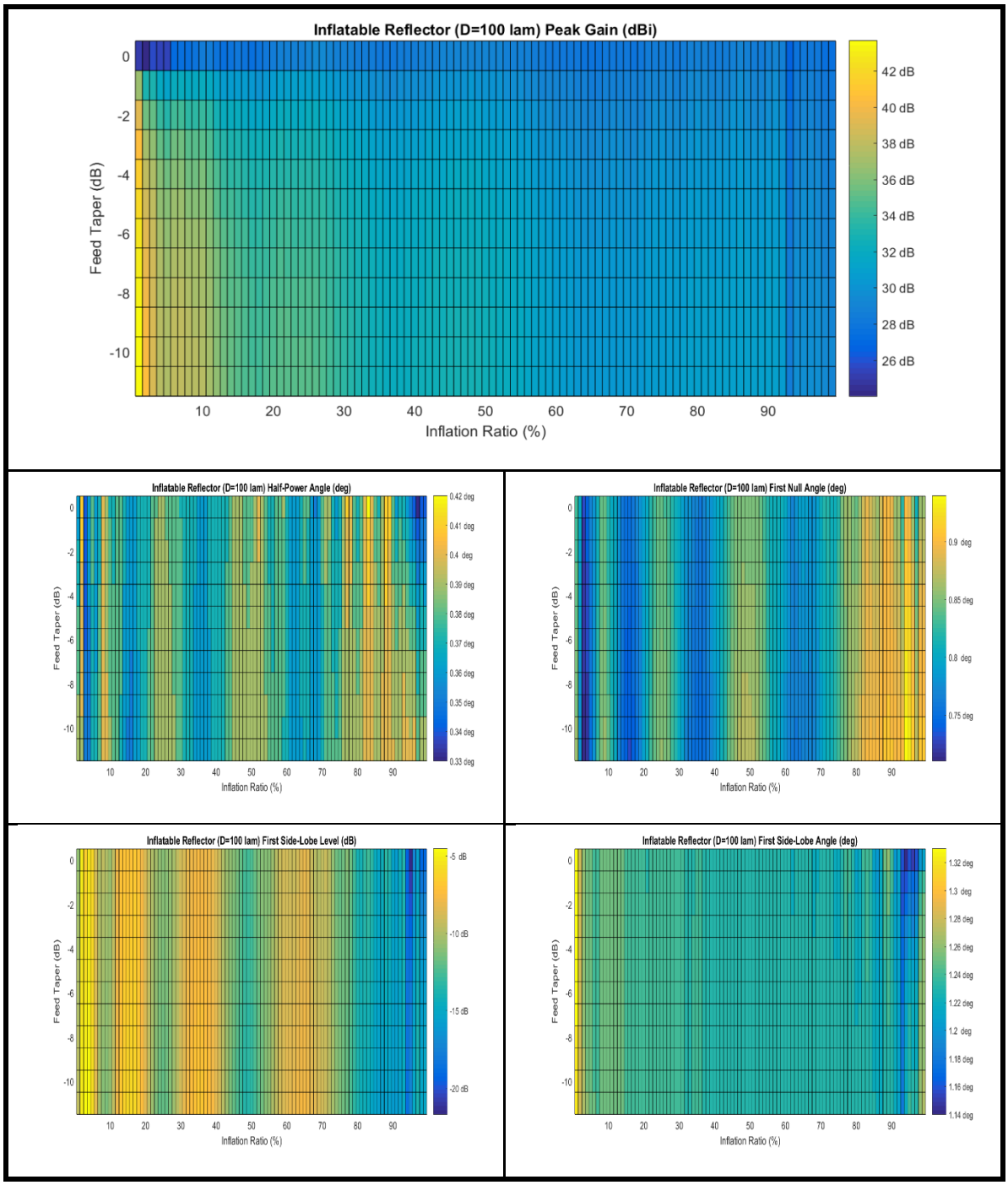

FIGURE 103: Inflatable Aperture Antenna Performance: Diameter = 100 Wavelengths

There are many common trends that can be gathered across the data presented in Figures 95 through 103. The peak gain of the inflatable aperture antenna does increase with the antenna diameter, and for a given antenna diameter, the peak gain increases as

the feed taper varies from -11dB through 0dB. These are consistent with the performance of solid parabolic reflector antennas. Also of note for the inflatable aperture antenna, the peak gain does vary with the Inflation Ratio, though not in terms of oscillating in value like the half-power beamwidth, first null beamwidth, or first side-lobe level degradation. The first side-lobe level degradation typically oscillates to larger negative values as the half-power beamwidth oscillates to larger angles. This shows that there is no single optimal configuration of the inflatable aperture antenna.

The previous analysis illustrated the calculated RF performance of the inflatable aperture antenna using the best-fit focal length for a given Inflation Ratio. This next set of analysis addresses the question of whether that best-fit focal length provides the optimal RF performance. To analyze this problem, the previous best-fit focal length was varied for a given Inflation Ratio by percent variations between -10% to +10% in 1% increments. This does mean that a change in focal length to diameter ratio of 0.1 has different meaning at lower Inflation Ratios, where the best-fit focal length was larger, than it would at higher Inflation Ratios, where the best-fit focal length is smaller. This issue was avoided by the use of the percent variation approach. The RF performance was again calculated at diameters ranging from 20 wavelengths to 100 wavelengths, in steps of 10 wavelengths. The RF performance was calculated across Inflation Ratio values ranging from 0.01 to 0.99 in increments of 0.01. The RF performance was calculated using a fixed feed taper value of 0dB. Figures 104 through 112 will illustrate the percent variation focal length-based RF performance calculated with the inflatable aperture antenna against the performance with the best-fit focal length. Each of these figures will follow the same format used in Figures 95 through 103.

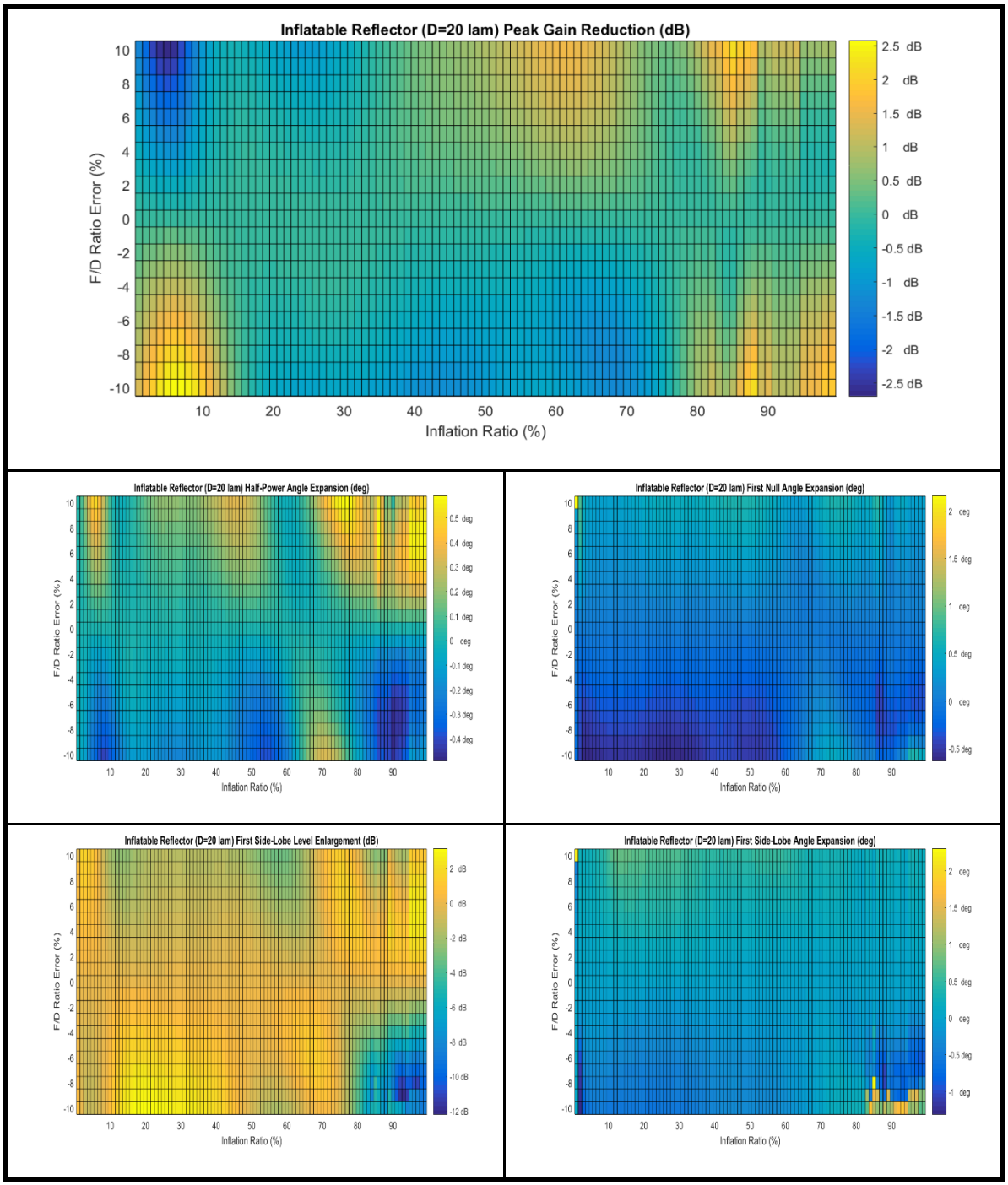

FIGURE 104: Focal Length Variation Comparisons: Diameter = 20 Wavelengths

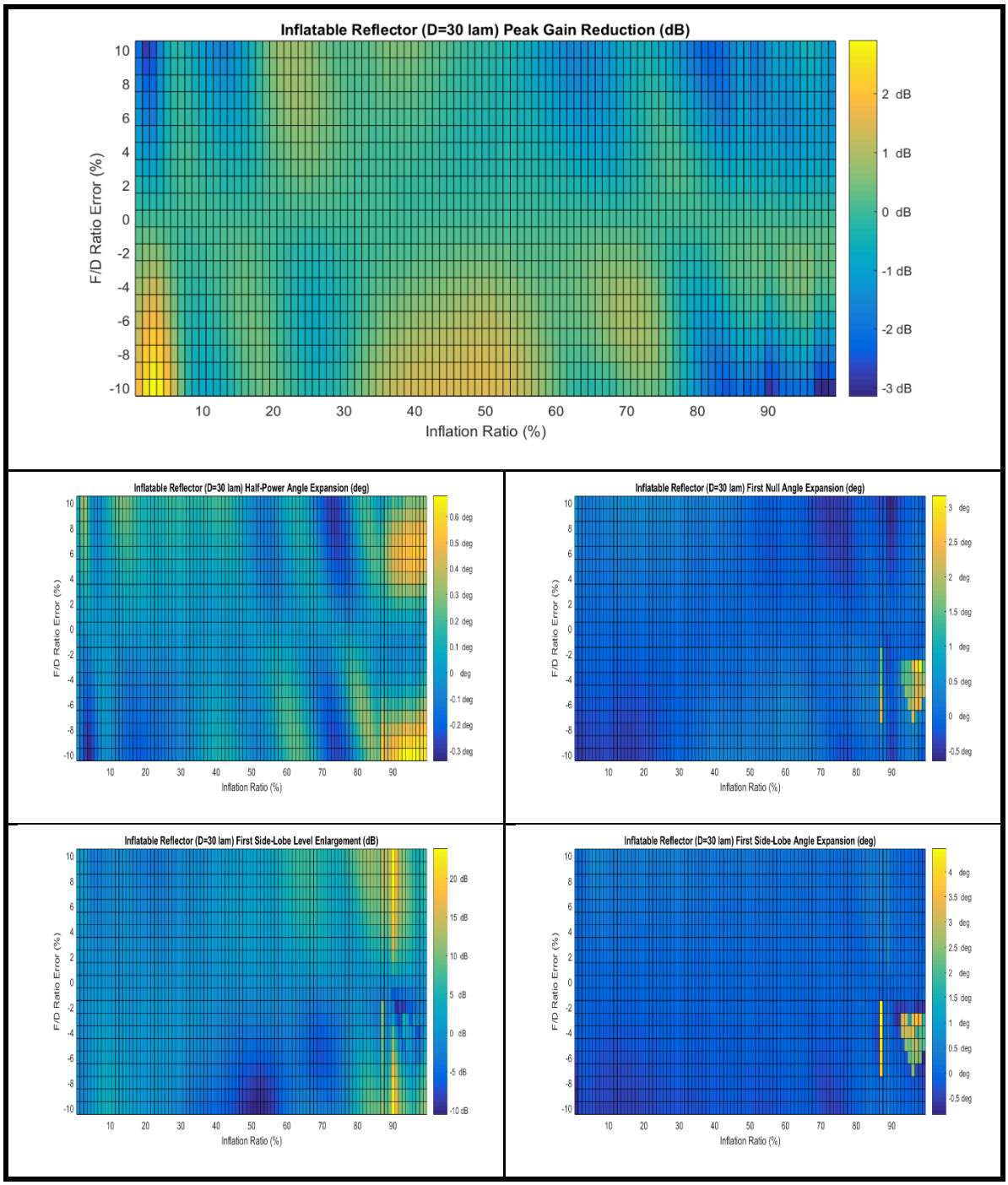

FIGURE 105: Focal Length Variation Comparisons: Diameter = 30 Wavelengths

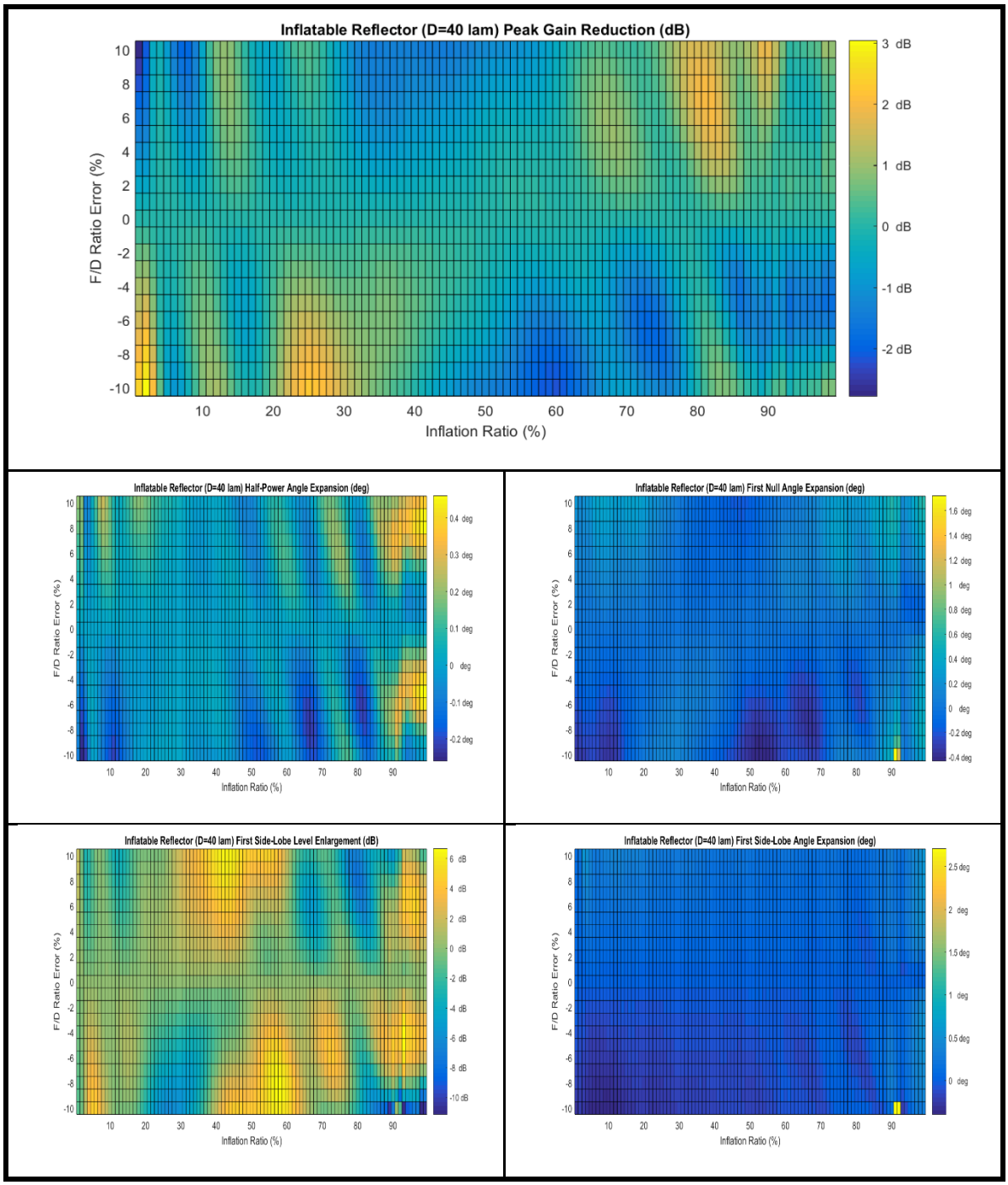

FIGURE 106: Focal Length Variation Comparisons: Diameter = 40 Wavelengths

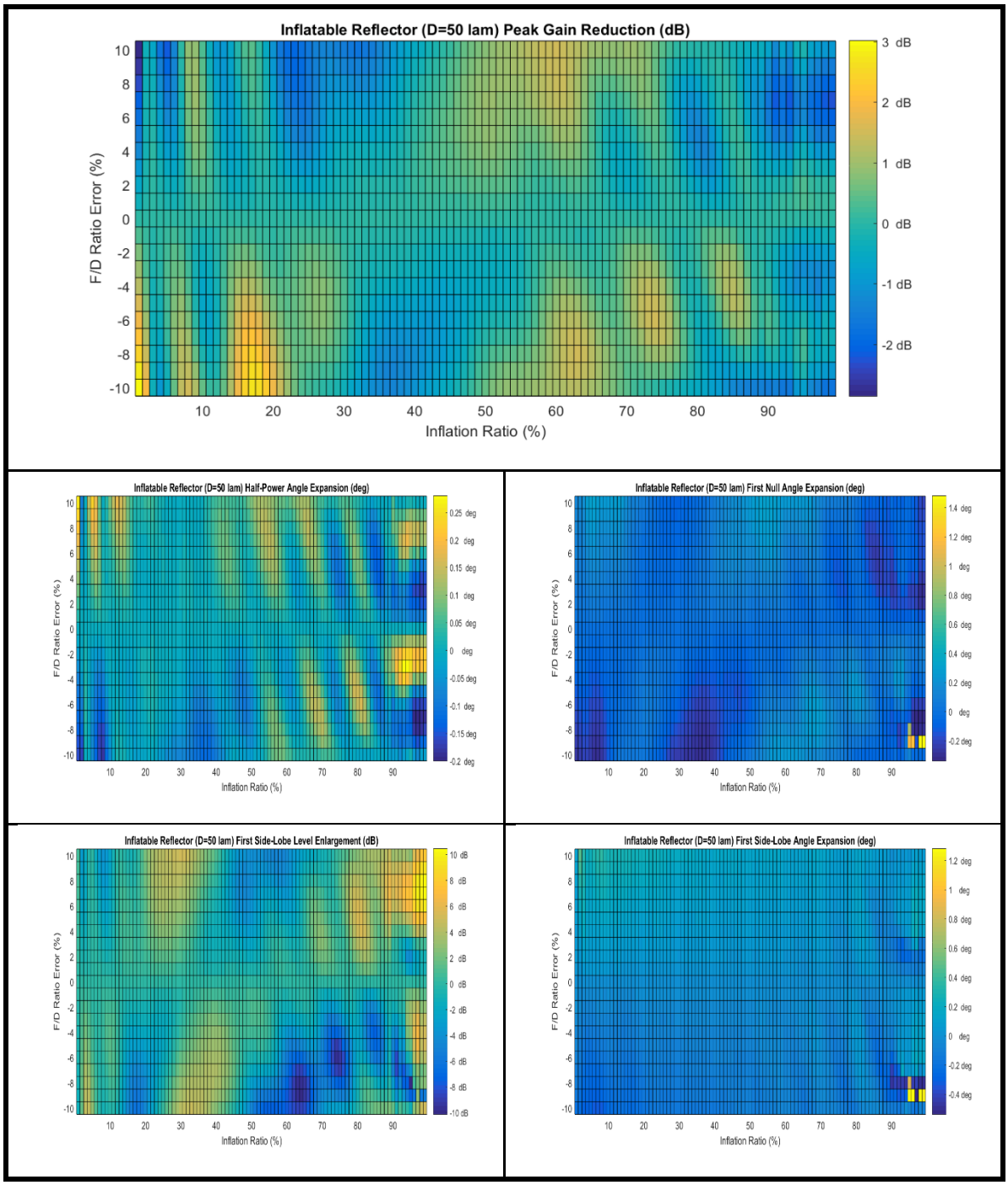

FIGURE 107: Focal Length Variation Comparisons: Diameter = 50 Wavelengths

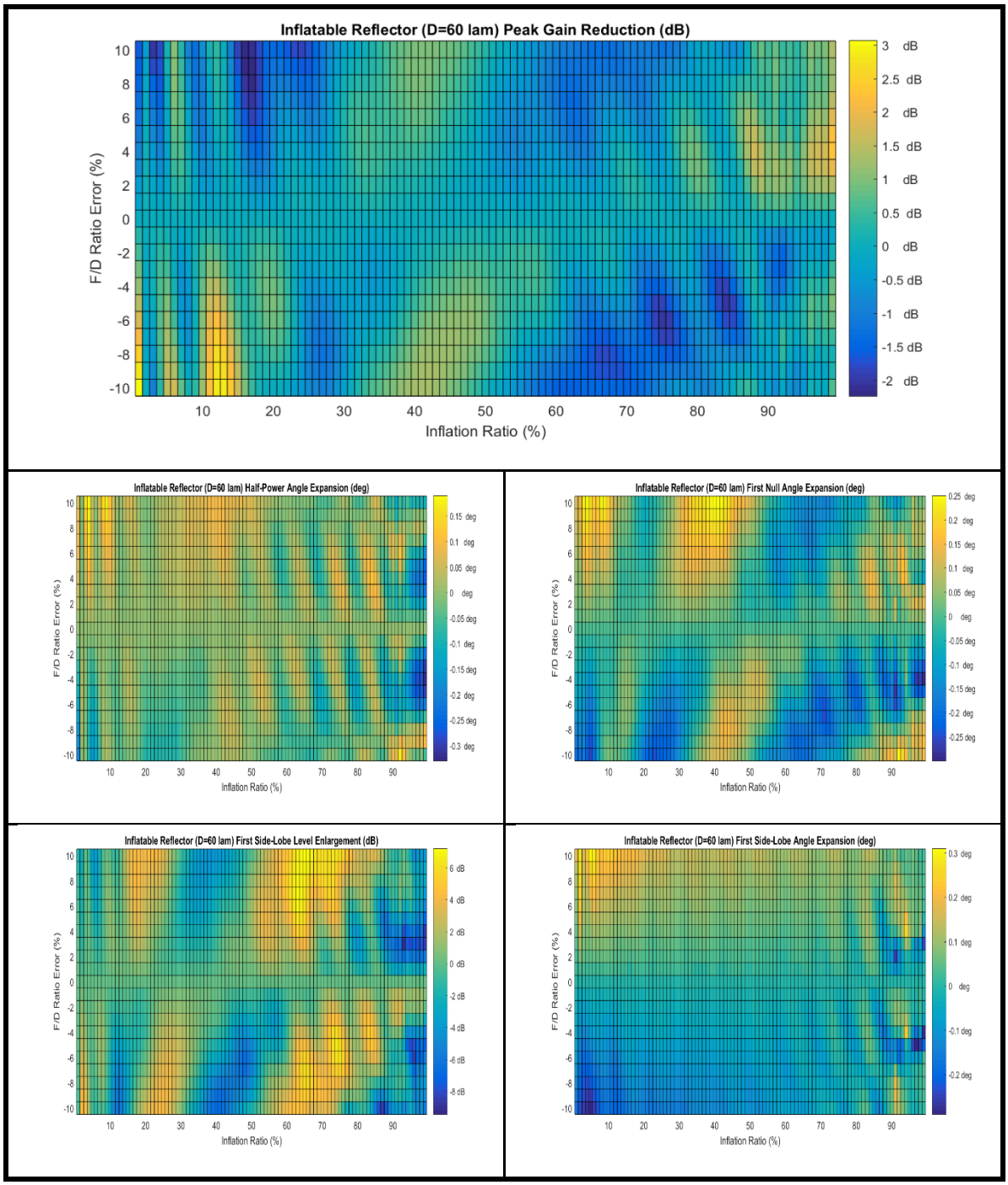

FIGURE 108: Focal Length Variation Comparisons: Diameter = 60 Wavelengths

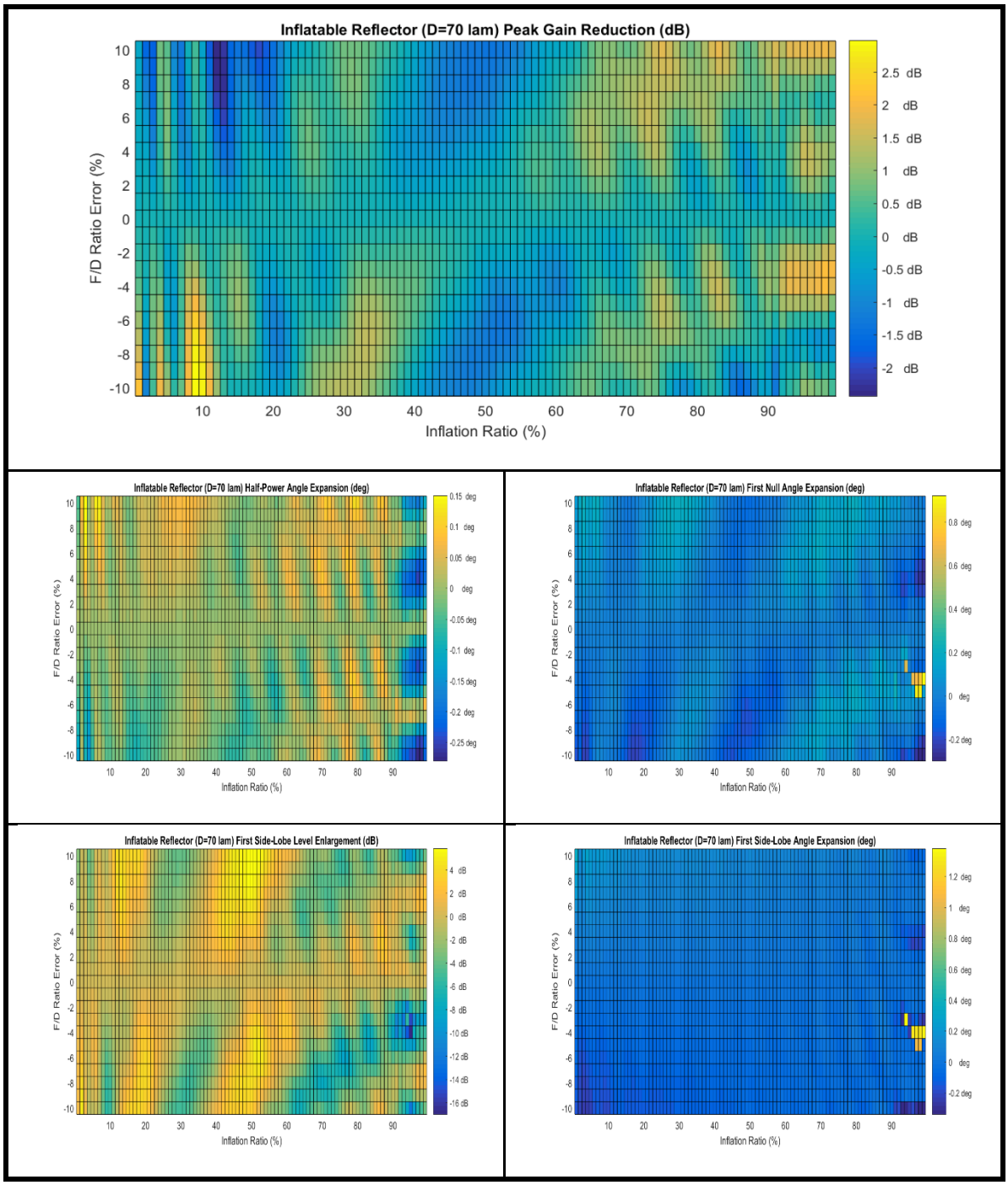

FIGURE 109: Focal Length Variation Comparisons: Diameter = 70 Wavelengths

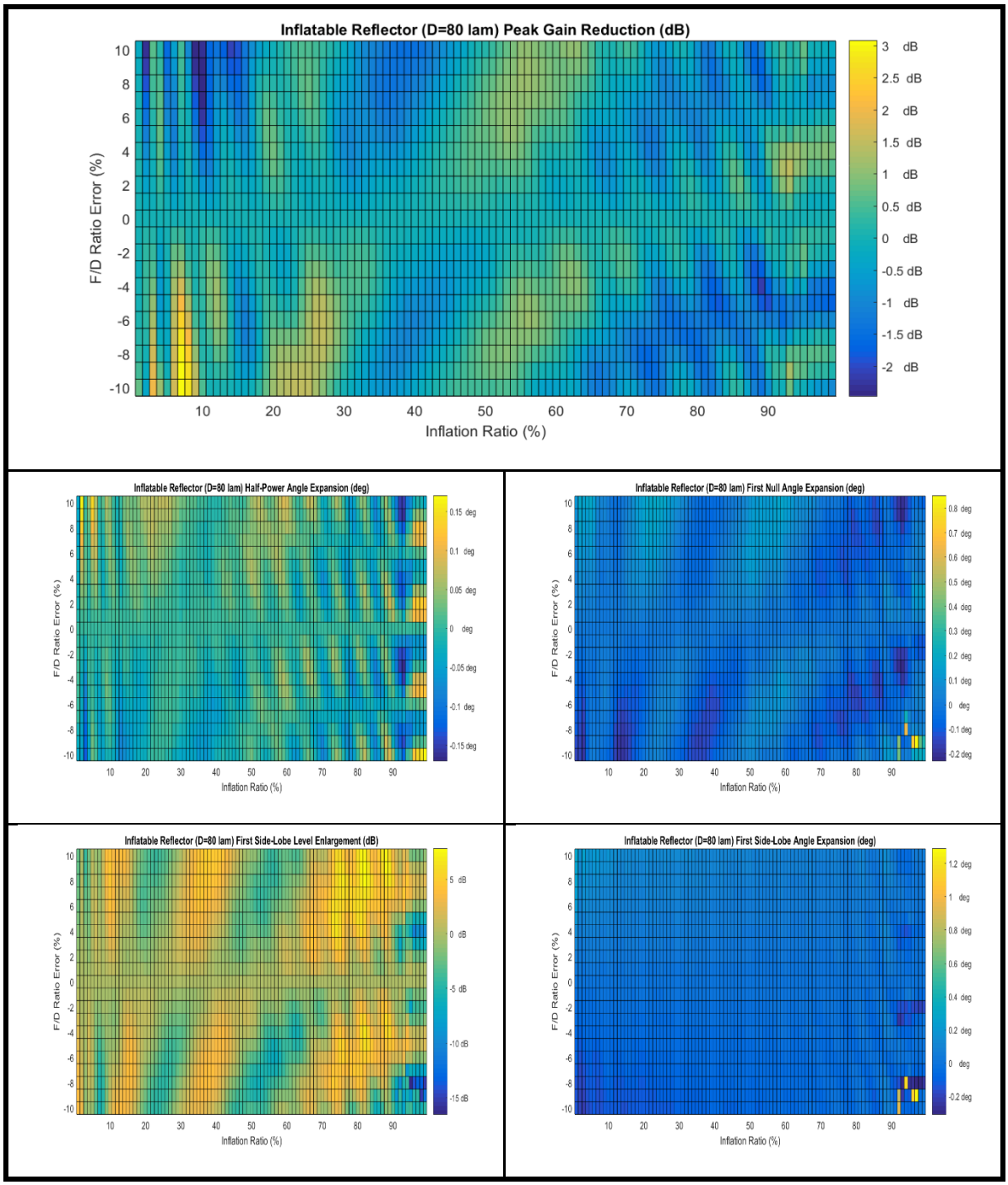

FIGURE 110: Focal Length Variation Comparisons: Diameter = 80 Wavelengths

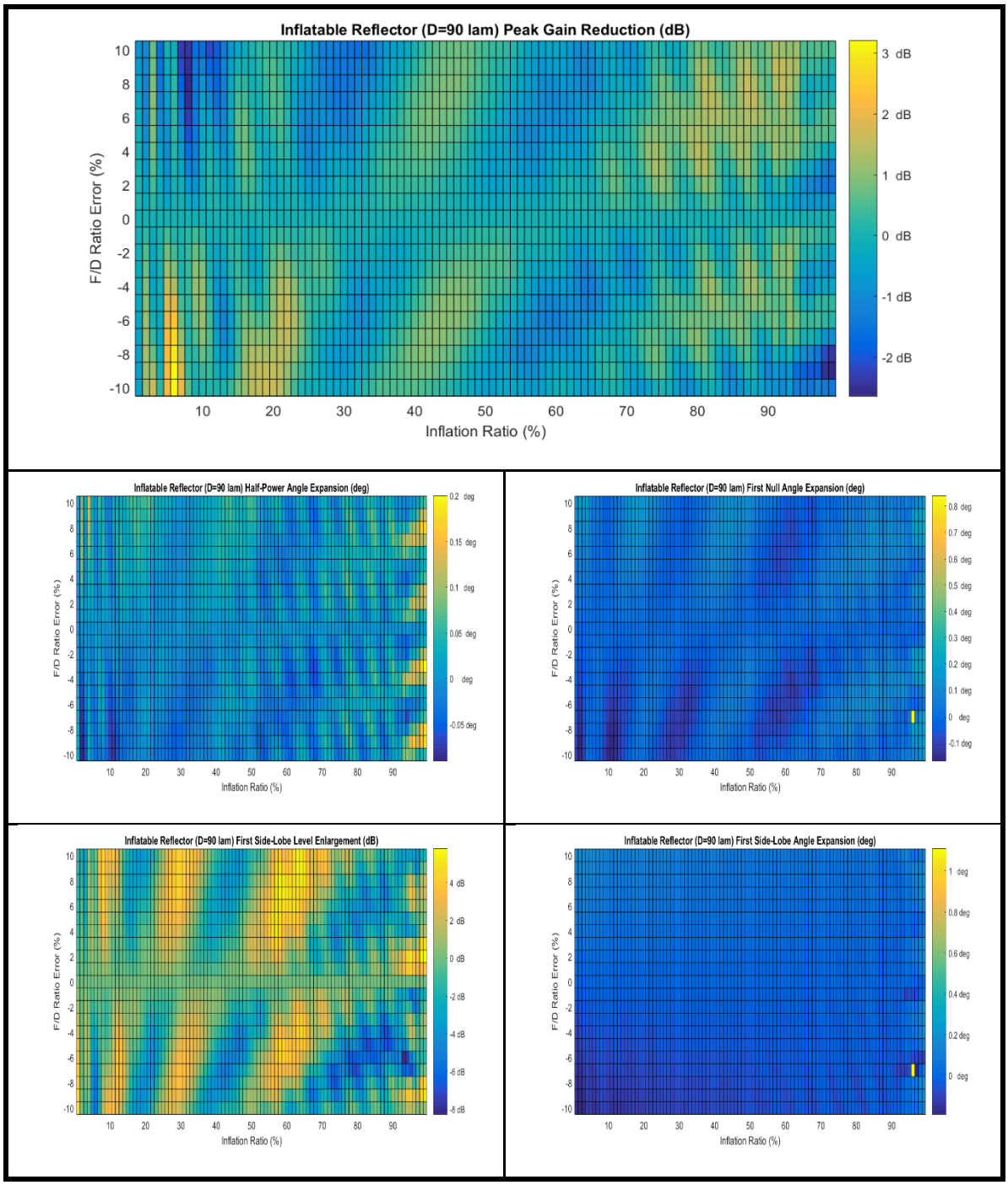

FIGURE 111: Focal Length Variation Comparisons: Diameter = 90 Wavelengths

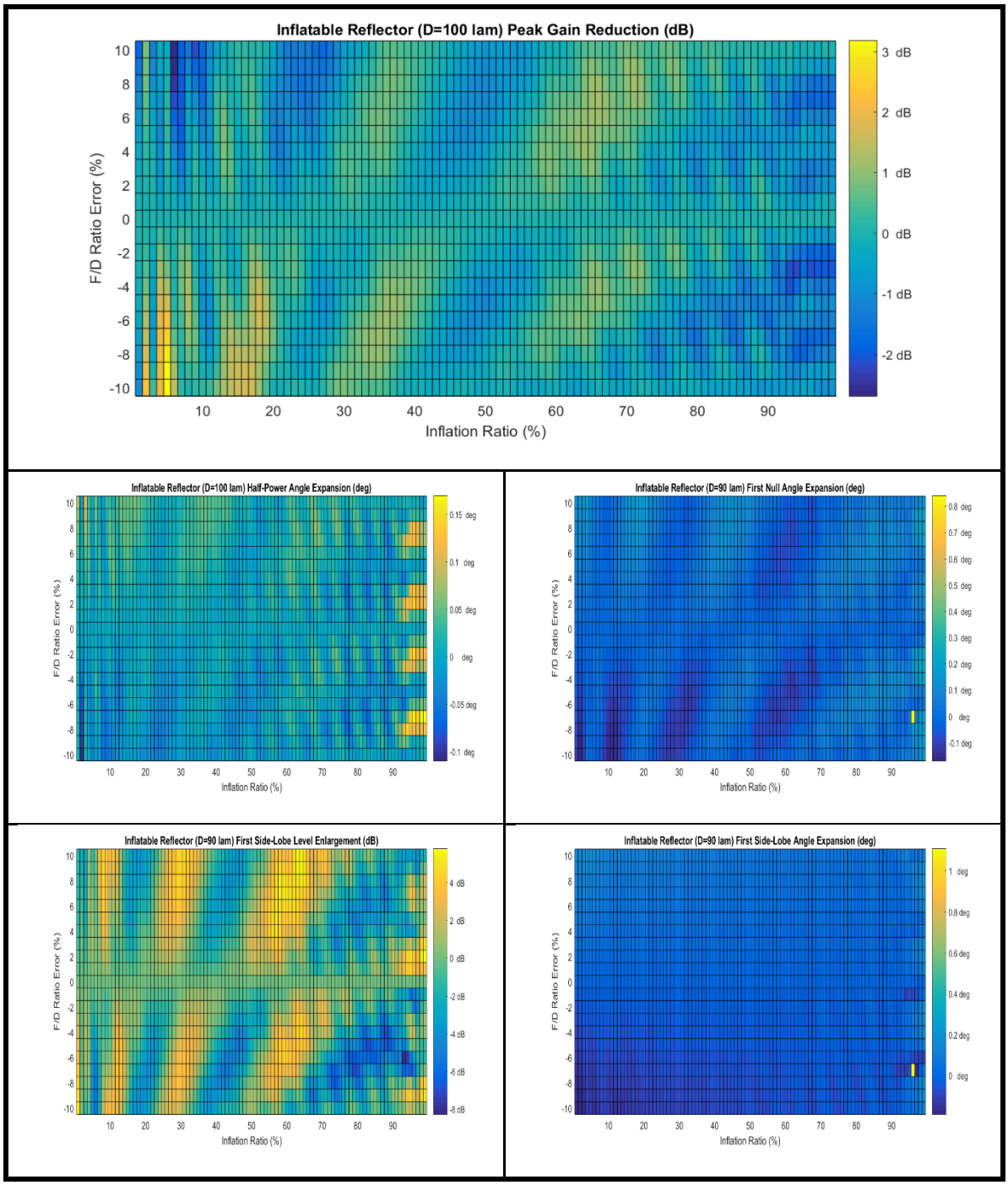

FIGURE 112: Focal Length Variation Comparisons: Diameter = 100 Wavelengths

There are several important observations that can be gathered across the data presented in Figures 104 through 112. The peak gain degradation shows the difference of the focal length variation against the best-fit focal length, and the results show differences

as a non-periodic function of the Inflation Ratio. The peak gain degradations vary as a function of the focal length variation percentage as a function of the antenna diameter. The half-power beamwidth, first null beamwidth, and first side-lobe level degradation variations also vary in terms of antenna size, Inflation Ratio, and focal length variation percentage, but those three terms look to follow common trends in changes. The first side-lobe angle does not have consistent variation as the other RF metrics have, though at some antenna diameters, performance at high Inflation Ratios is noted to have distinct performance offsets.

This is due to the main beam expanding in such a way that the first null is no longer nominally defined due to the poor antenna design, and so the main beam spreads and the side-lobe now identified as the first side-lobe was related to the second side-lobe of the best-fit pattern. Figure 113 illustrates the actual antenna patterns, zoomed into the primary region of interest near the main beam and first side-lobe, for a diameter of 30 wavelengths. In this figure, the Inflation Ratio value of 0.98 is illustrated, using the focal length to diameter ratio errors of −2%, −4%, −6%, −8% and −10% against the optimal focal length to diameter ratio case corresponding to 0% in Figure 105. Only the −4% and −6% cases illustrate the performance cases that are not consistent with the optimal focal length to diameter ratio case.

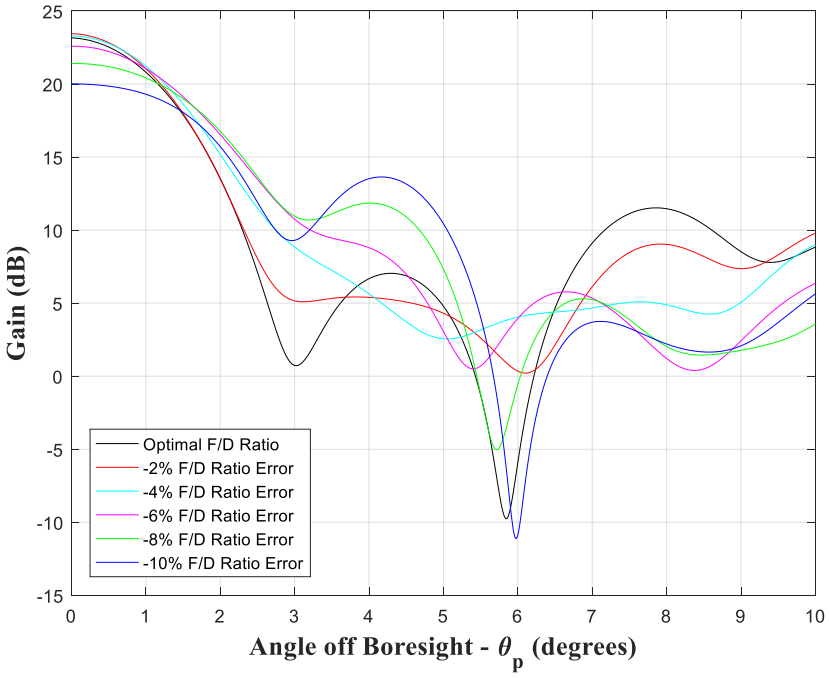

FIGURE 113: Specific Focal Length Variation Comparison at 30 Wavelengths

4.5 RF Performance Comparison Using Common Diameter

Section 4.3 had described three methodologies of comparing the RF performance of the inflatable aperture antenna with the solid parabolic reflector antenna. This section will utilize the common diameter approach, where the solid parabolic reflector antenna was analyzed at an equivalent focal length to diameter ratio to the best-fit value of each Inflation Ratio. The RF performance was varied in the same methodology of diameter from 20 wavelengths to 100 wavelengths in increments of 10 wavelengths, feed taper values of -11dB to 0dB in increments of 1dB and for Inflation Ratio values of 0.01 to 0.99 in increments of 0.01. Figures 114 through 122 illustrate the comparative results,

which are displayed in comparison to the solid parabolic reflector antenna, using the common figure methodology of the previous section.

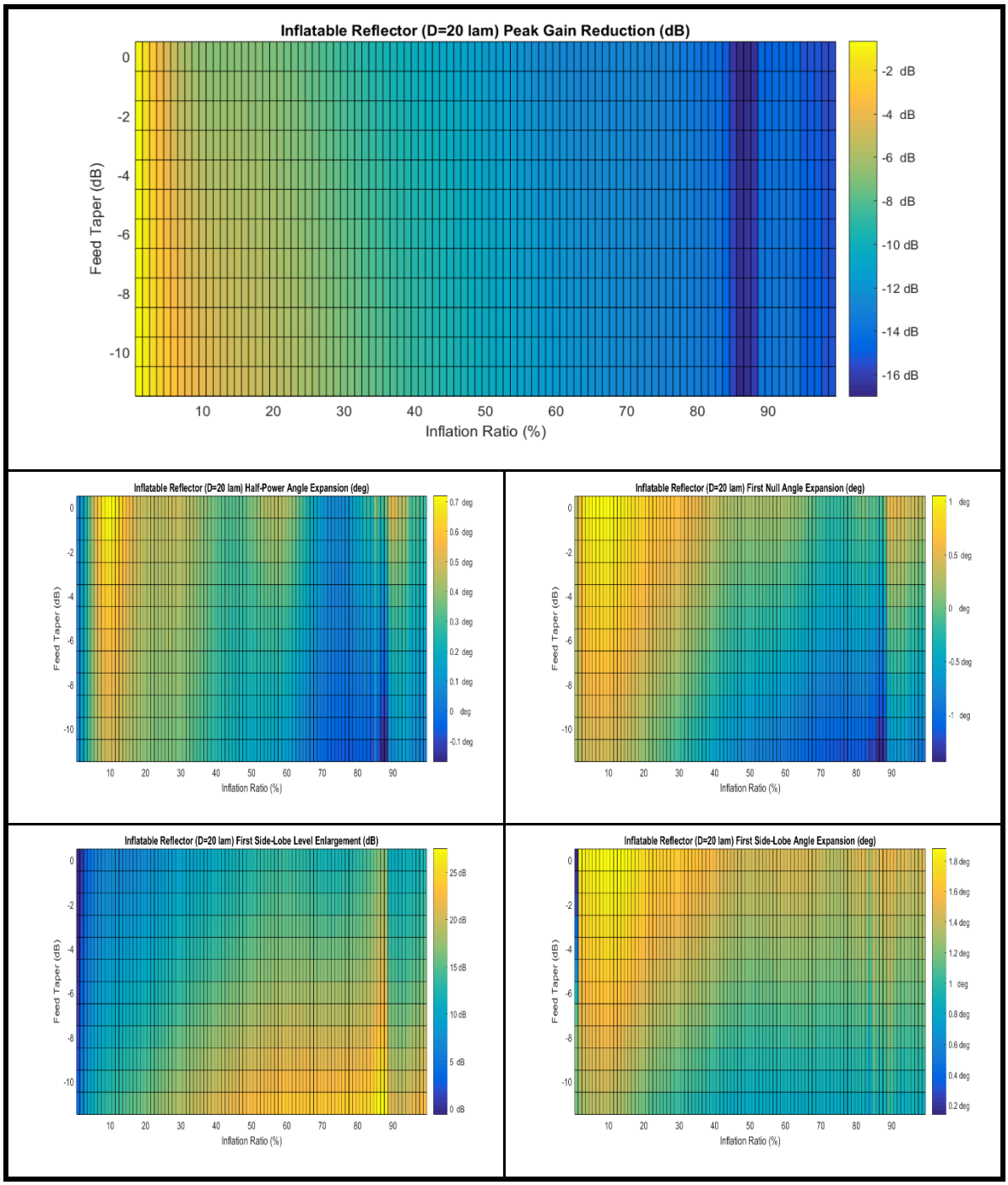

FIGURE 114: Common Diameter Comparisons: Diameter = 20 Wavelengths

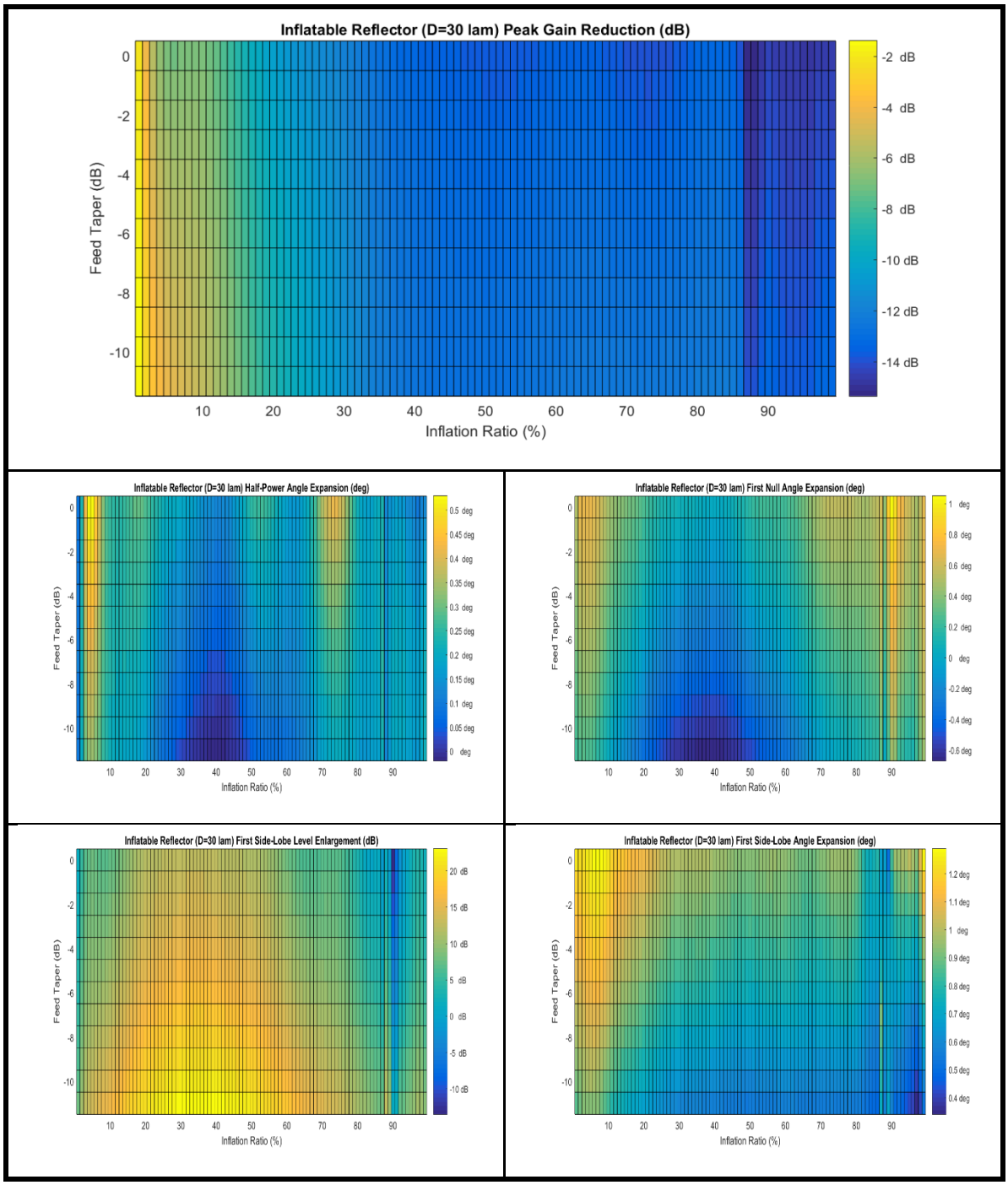

FIGURE 115: Common Diameter Comparisons: Diameter = 30 Wavelengths

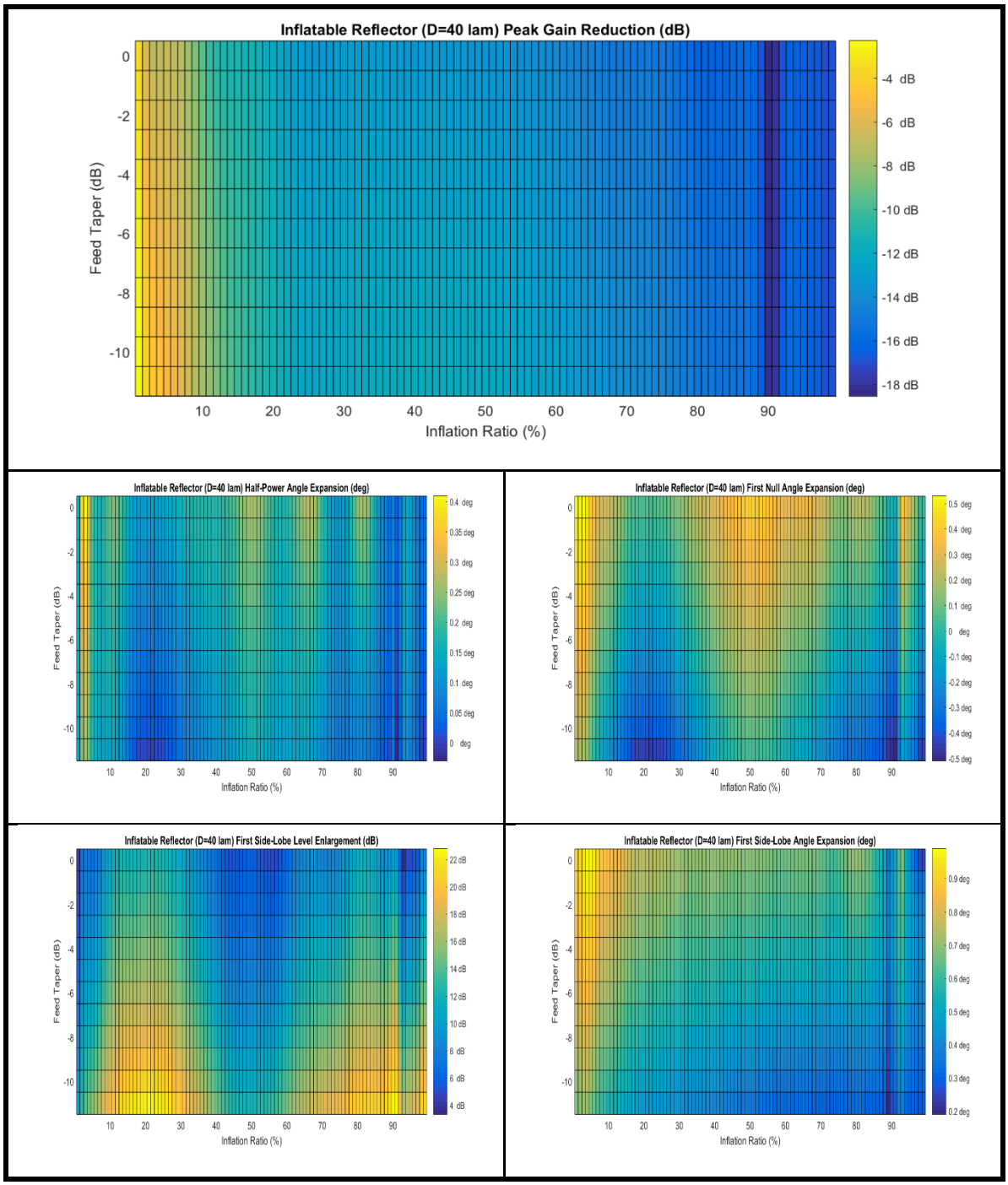

FIGURE 116: Common Diameter Comparisons: Diameter = 40 Wavelengths

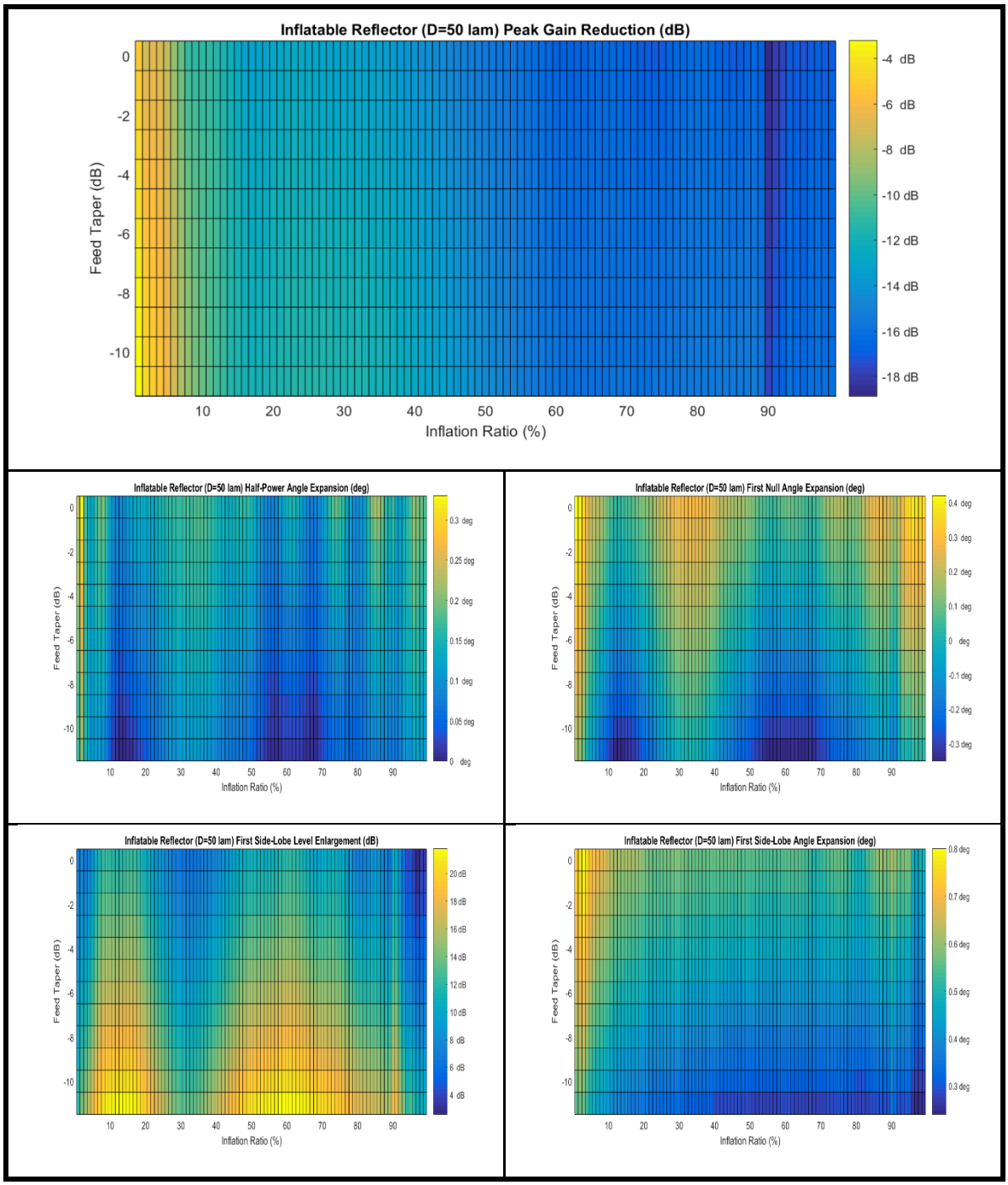

FIGURE 117: Common Diameter Comparisons: Diameter = 50 Wavelengths

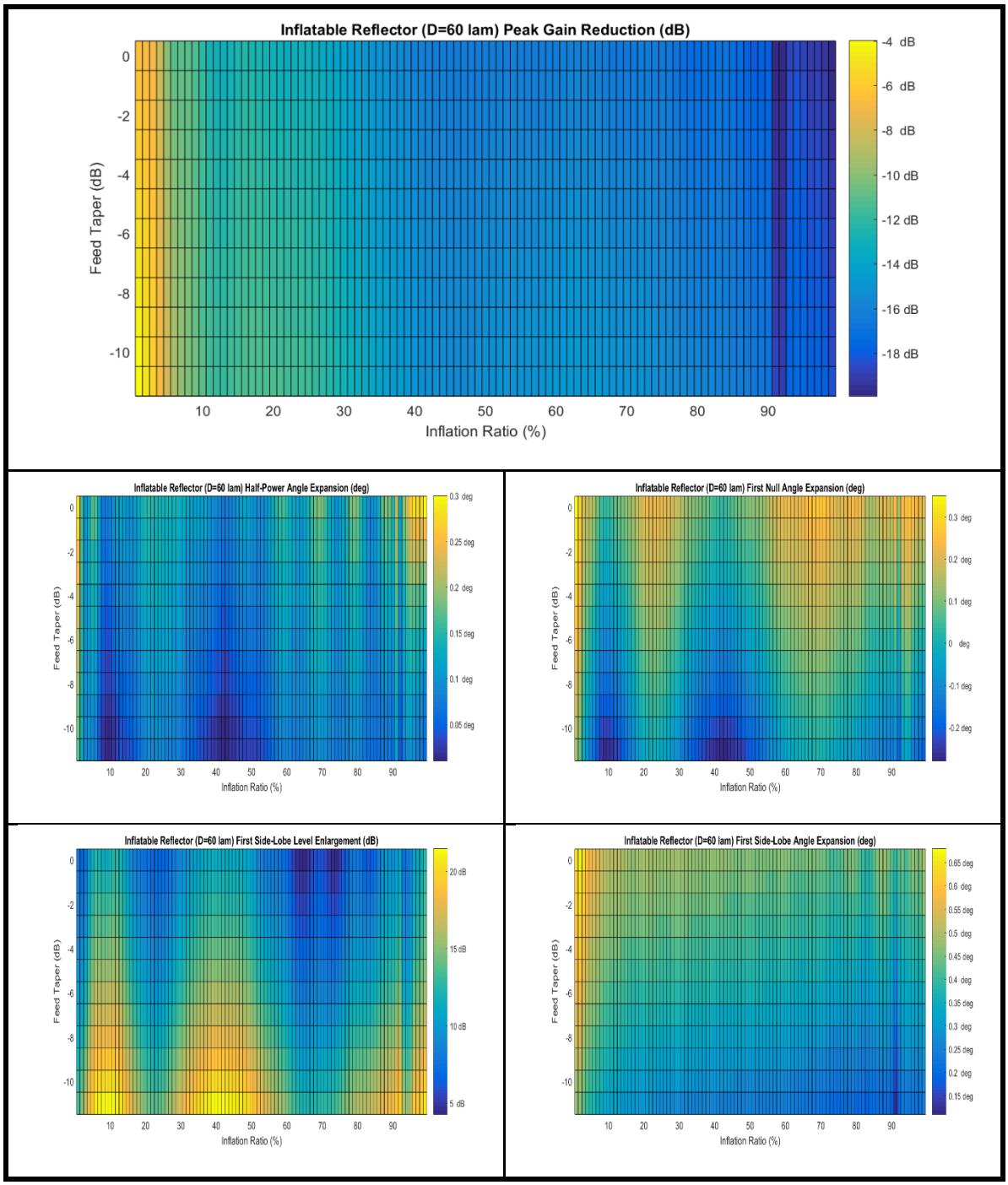

FIGURE 118: Common Diameter Comparisons: Diameter = 60 Wavelengths

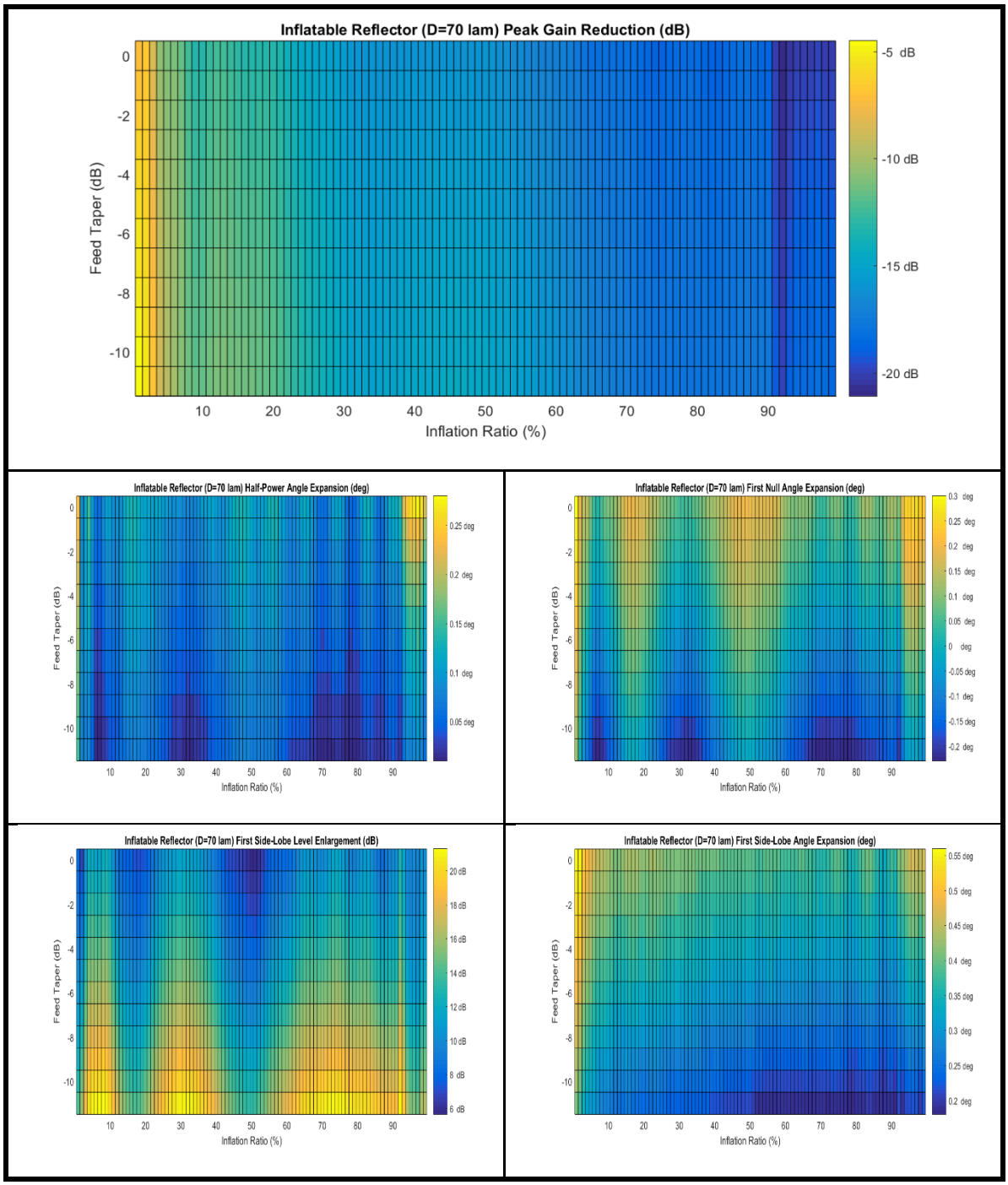

FIGURE 119: Common Diameter Comparisons: Diameter = 70 Wavelengths

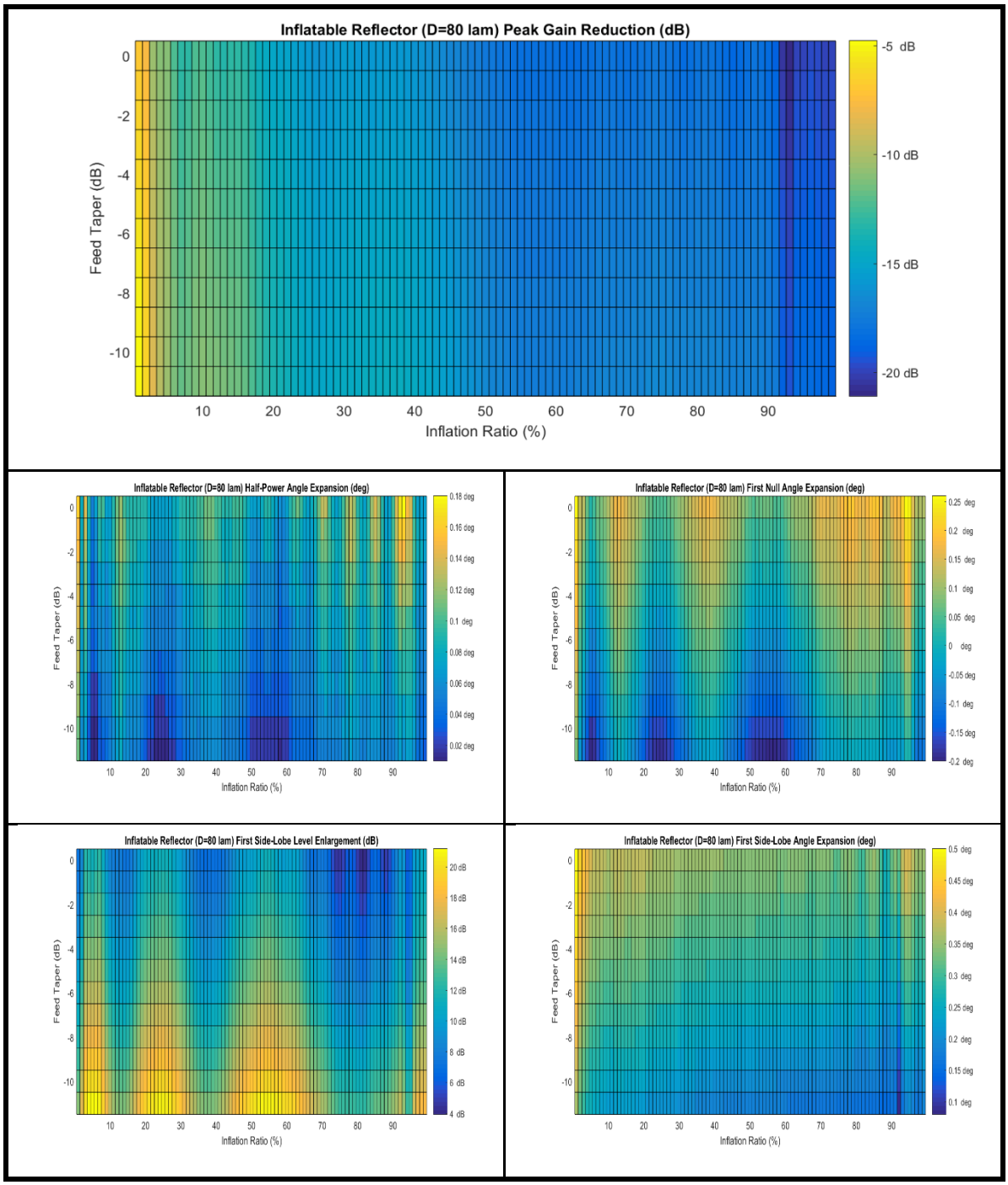

FIGURE 120: Common Diameter Comparisons: Diameter = 80 Wavelengths

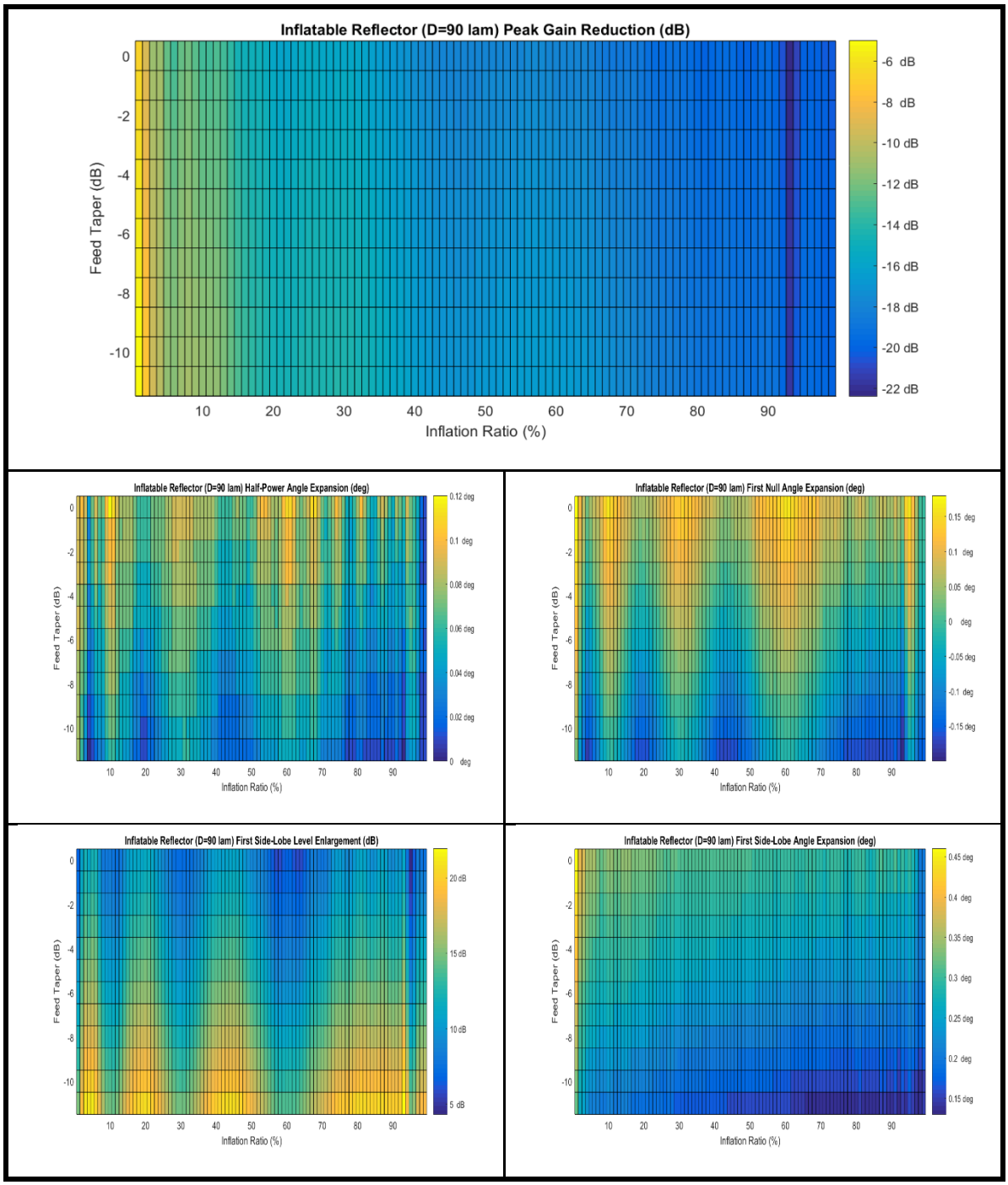

FIGURE 121: Common Diameter Comparisons: Diameter = 90 Wavelengths

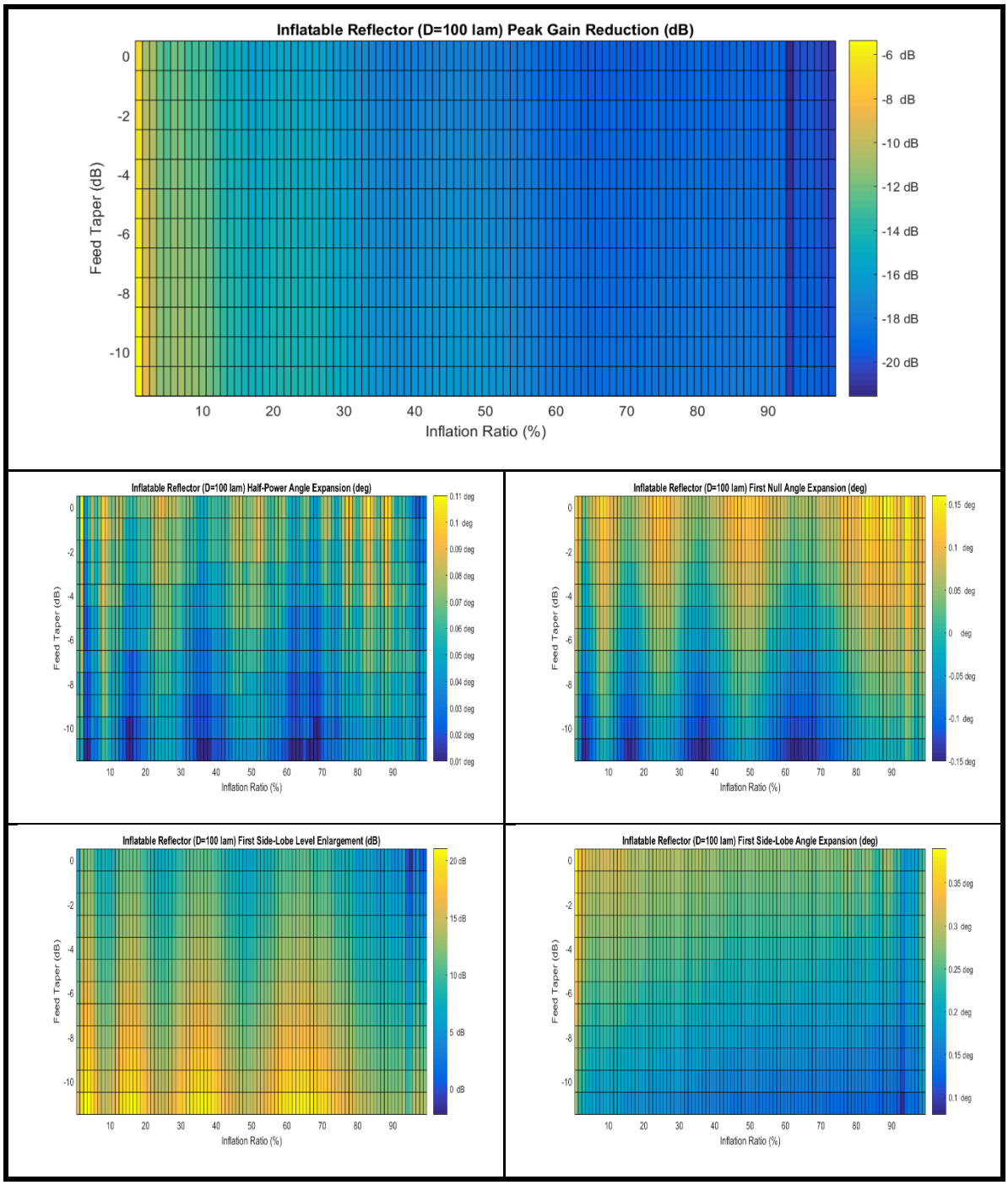

FIGURE 122: Common Diameter Comparisons: Diameter = 100 Wavelengths

There are several important observations that can be gathered across the data presented in Figures 114 through 122. The peak gain degradation shows that the inflatable aperture antenna does not have a larger peak gain value than solid parabolic

reflector antenna. The peak gain degradation does not appear to be correlated to the feed taper at any diameter. That is different for the half-power beamwidth, first null beamwidth, and first side-lobe level degradation metrics, as the comparisons of metrics do vary as a function the Inflation Ratio and feed taper. The half-power beamwidth angles always expand positively, meaning that the inflatable aperture antenna beam is wider, but the first null angle can vary positively or negatively, showing that the main beam's shape is not just wider, but also steeper in the region after the half-power threshold is satisfied. The first side-lobe angle also always expands positively, correlating to the beam being spread wider against the solid parabolic reflector antenna.

4.6 RF Performance Comparison Using Common Depth

Section 4.3 had described three methodologies of comparing the RF performance of the inflatable aperture antenna with the solid parabolic reflector antenna. This section will utilize the common depth approach, where the solid parabolic reflector antenna was analyzed at an equivalent focal length to diameter ratio to the best-fit value of each Inflation Ratio. The RF performance was varied in the same methodology of diameter from 20 wavelengths to 100 wavelengths in increments of 10 wavelengths, feed taper values of -11dB to 0dB in increments of 1dB and for Inflation Ratio values of 0.01 to 0.99 in increments of 0.01. Figures 123 through 131 illustrate the comparative results, which are displayed in comparison to the solid parabolic reflector antenna, using the common figure methodology of the previous section.

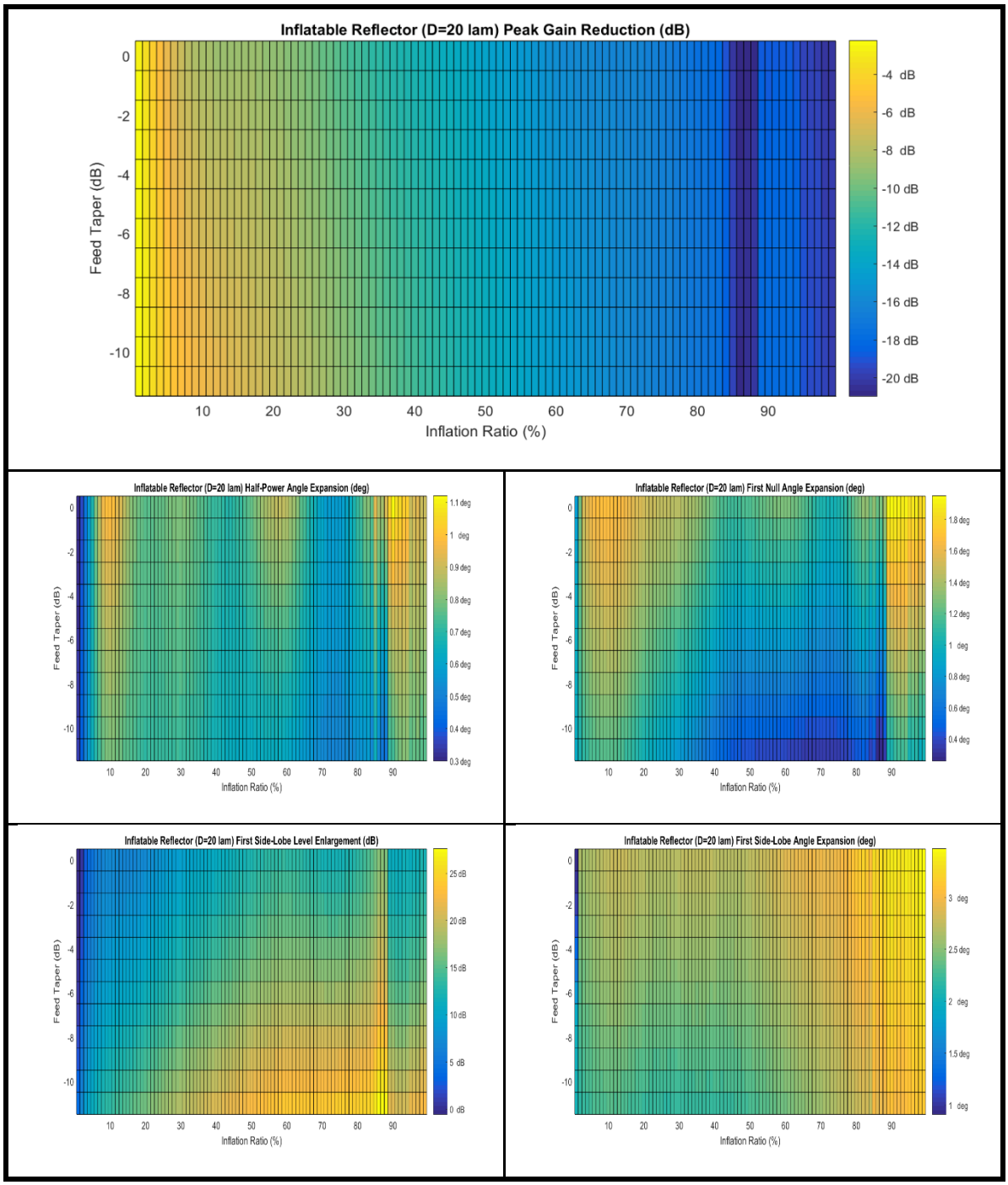

FIGURE 123: Common Depth Comparisons: Diameter = 20 Wavelengths

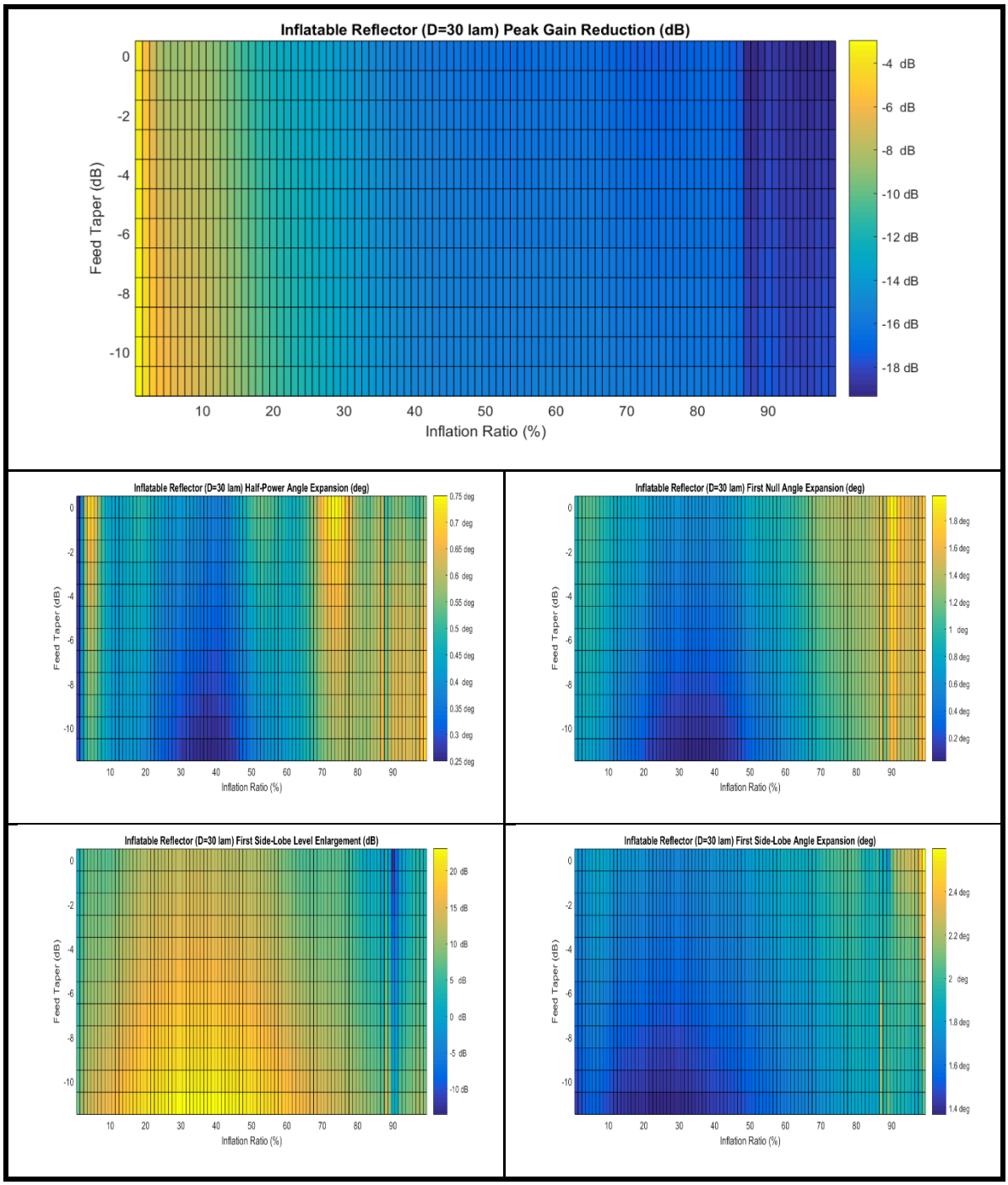

FIGURE 124: Common Depth Comparisons: Diameter = 30 Wavelengths

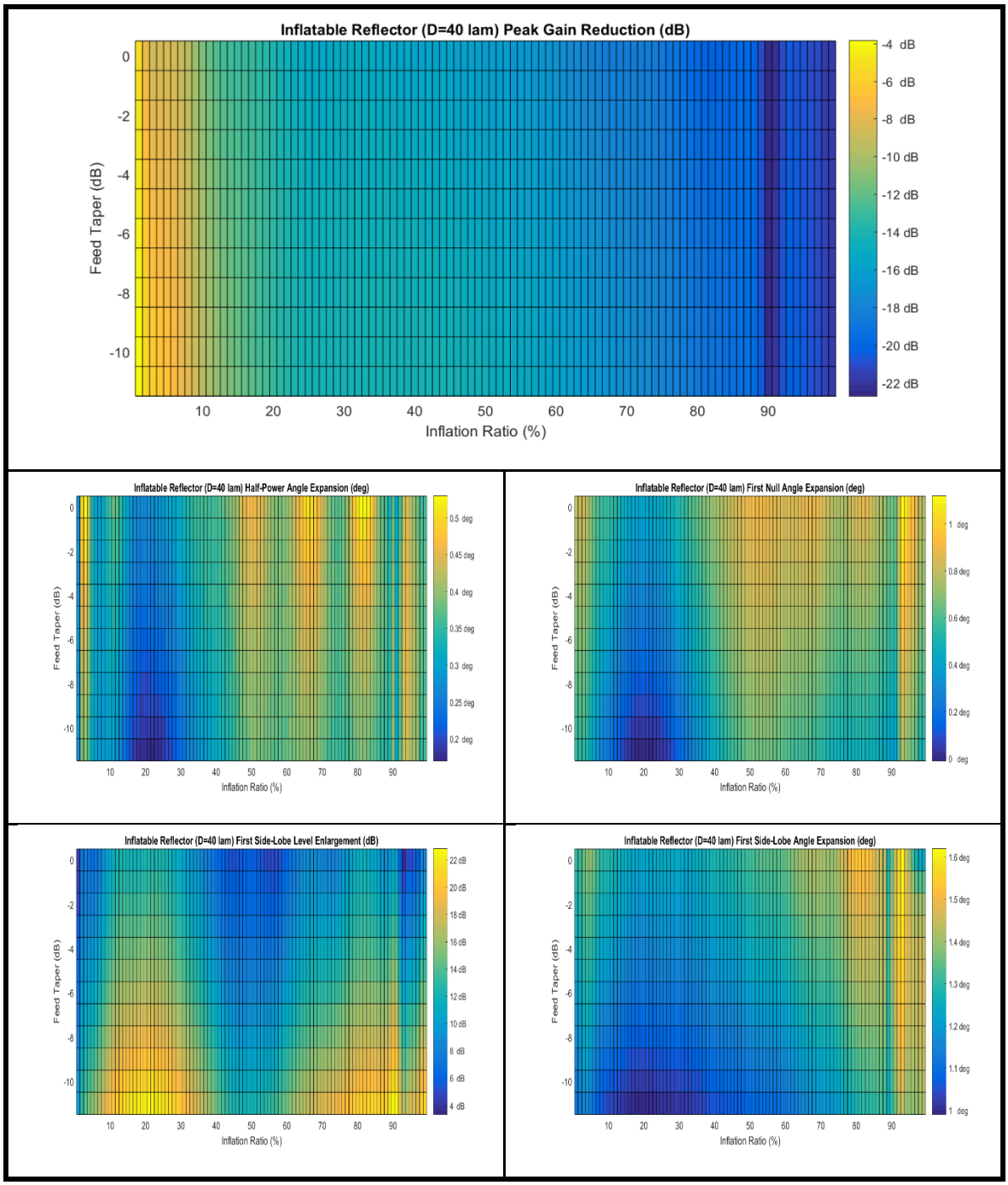

FIGURE 125: Common Depth Comparisons: Diameter = 40 Wavelengths

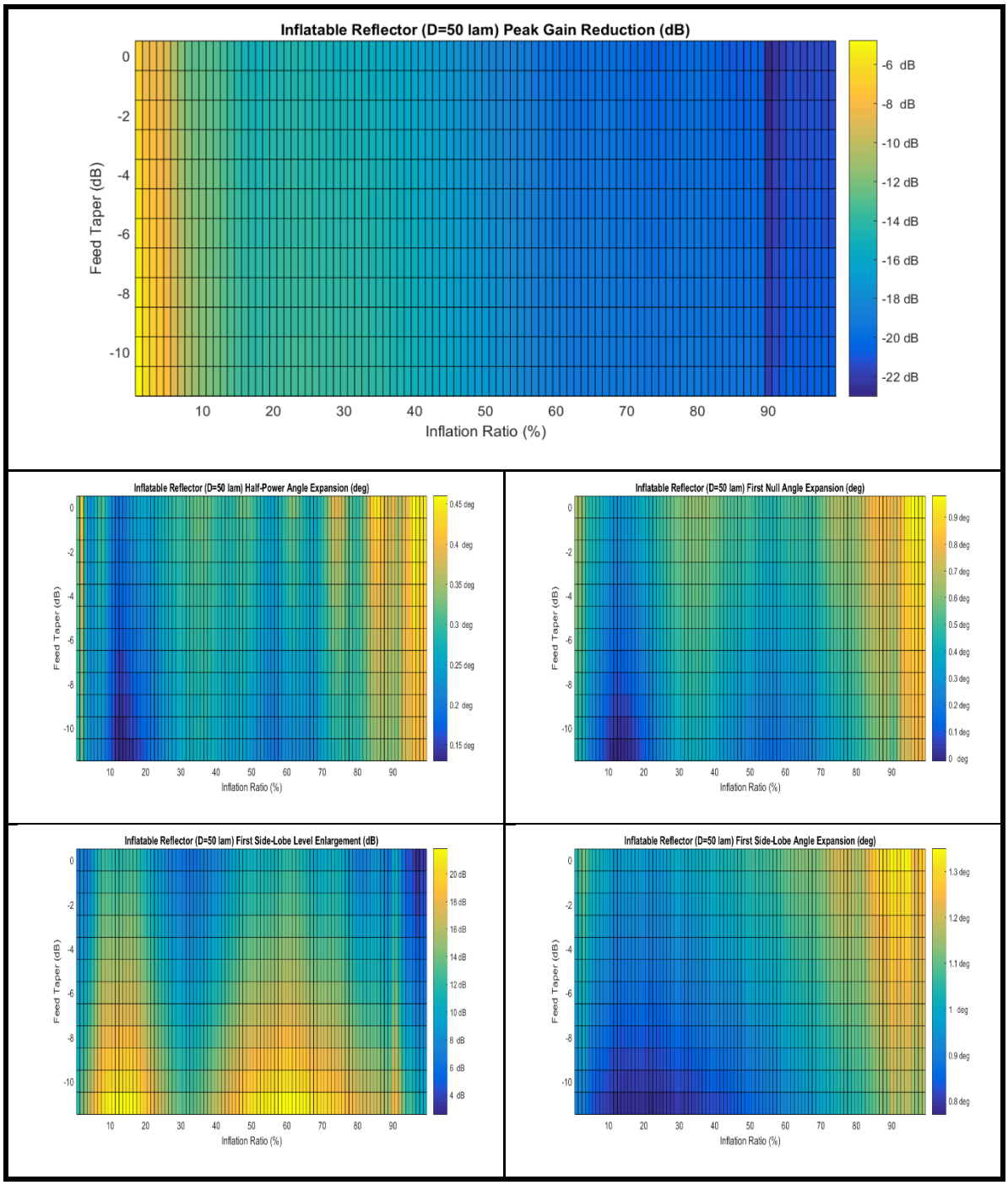

FIGURE 126: Common Depth Comparisons: Diameter = 50 Wavelengths

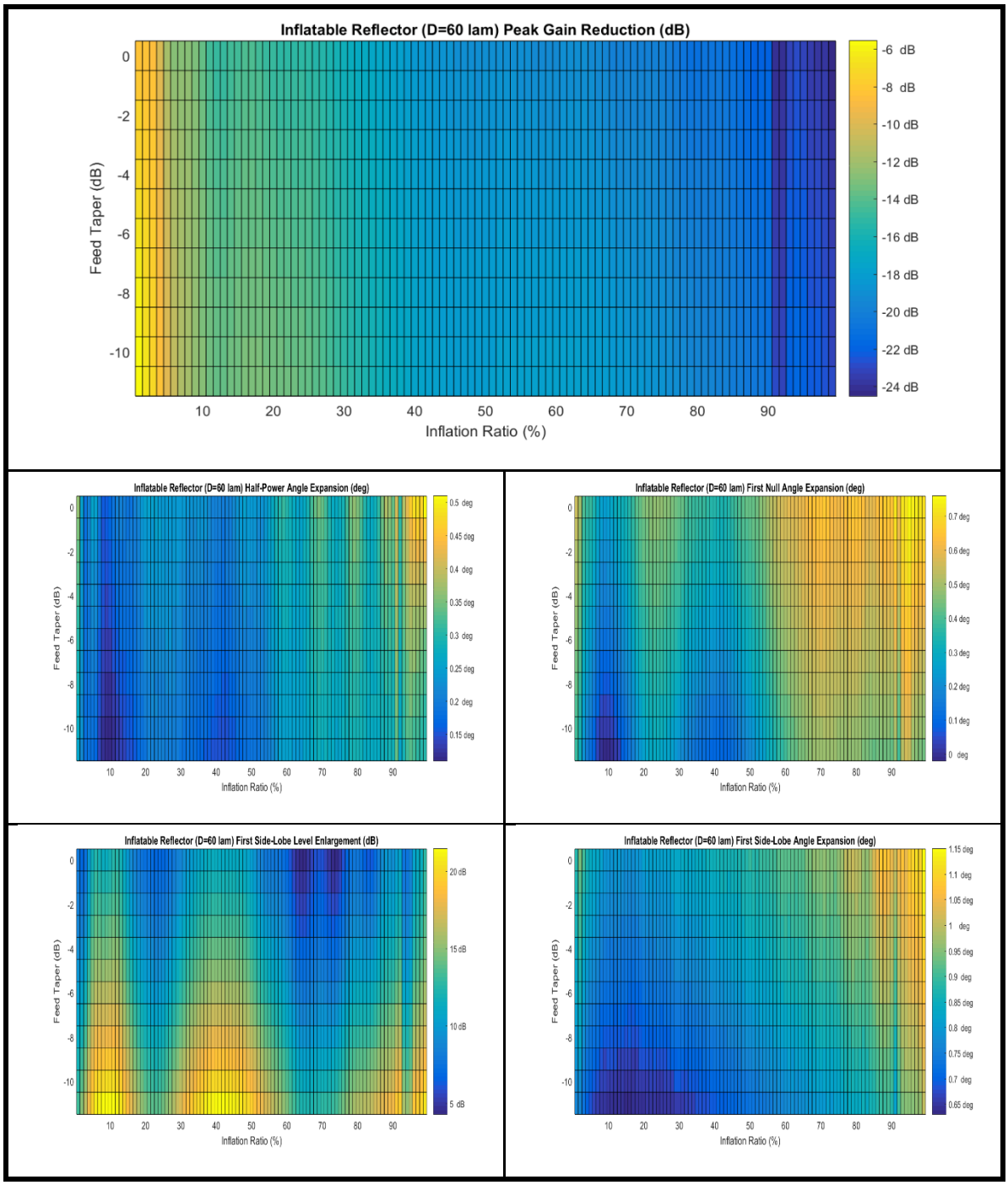

FIGURE 127: Common Depth Comparisons: Diameter = 60 Wavelengths

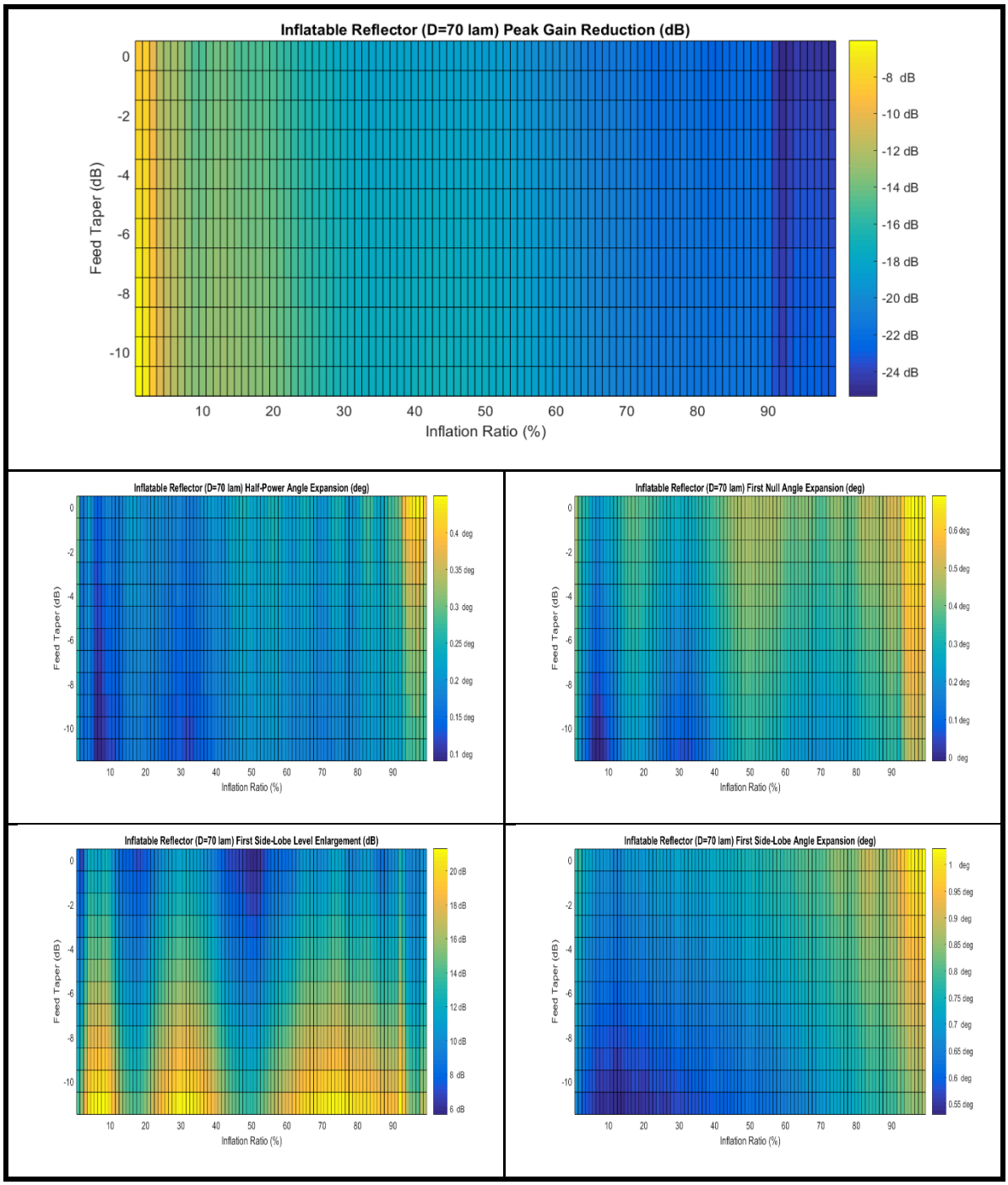

FIGURE 128: Common Depth Comparisons: Diameter = 70 Wavelengths

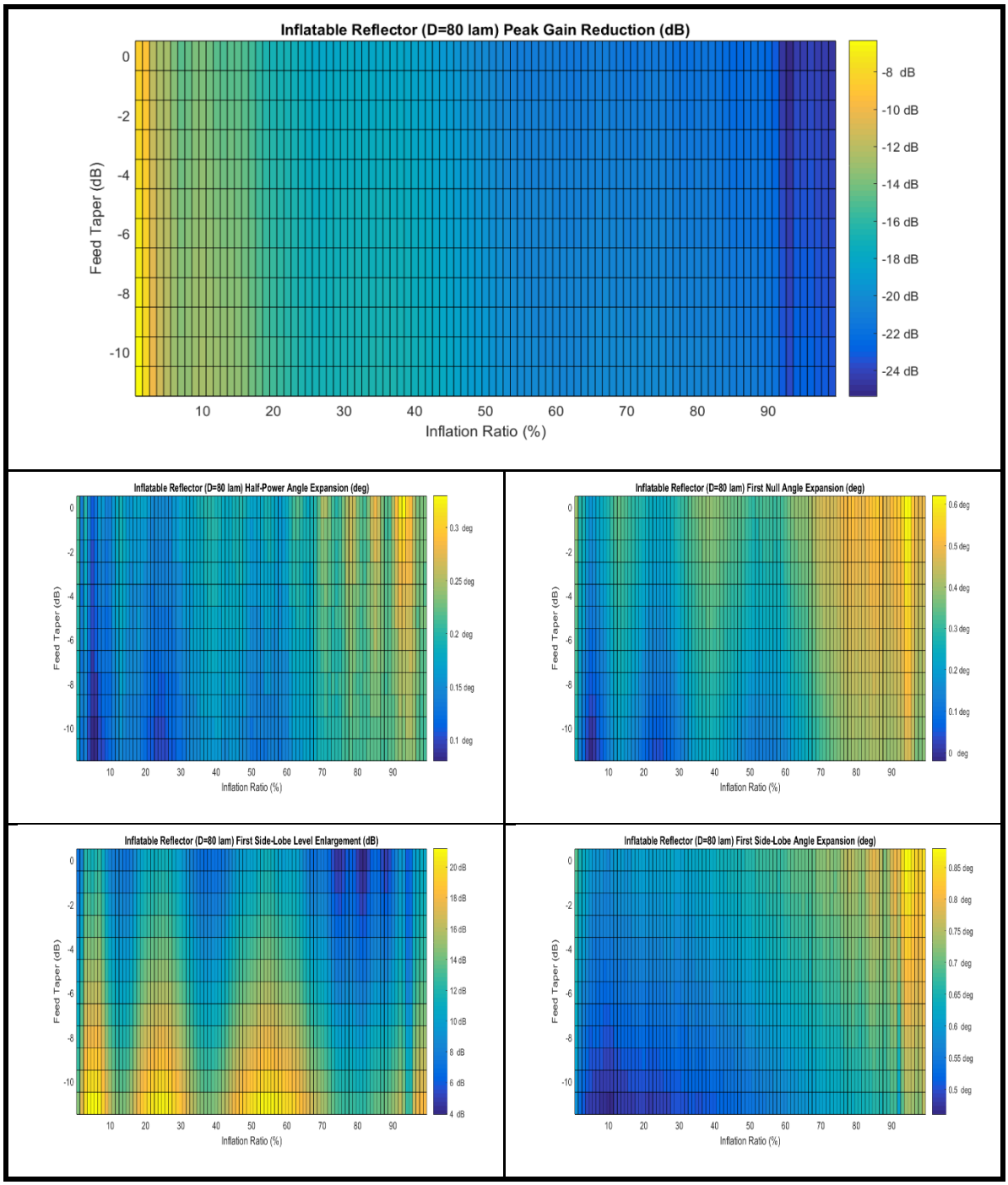

FIGURE 129: Common Depth Comparisons: Diameter = 80 Wavelengths

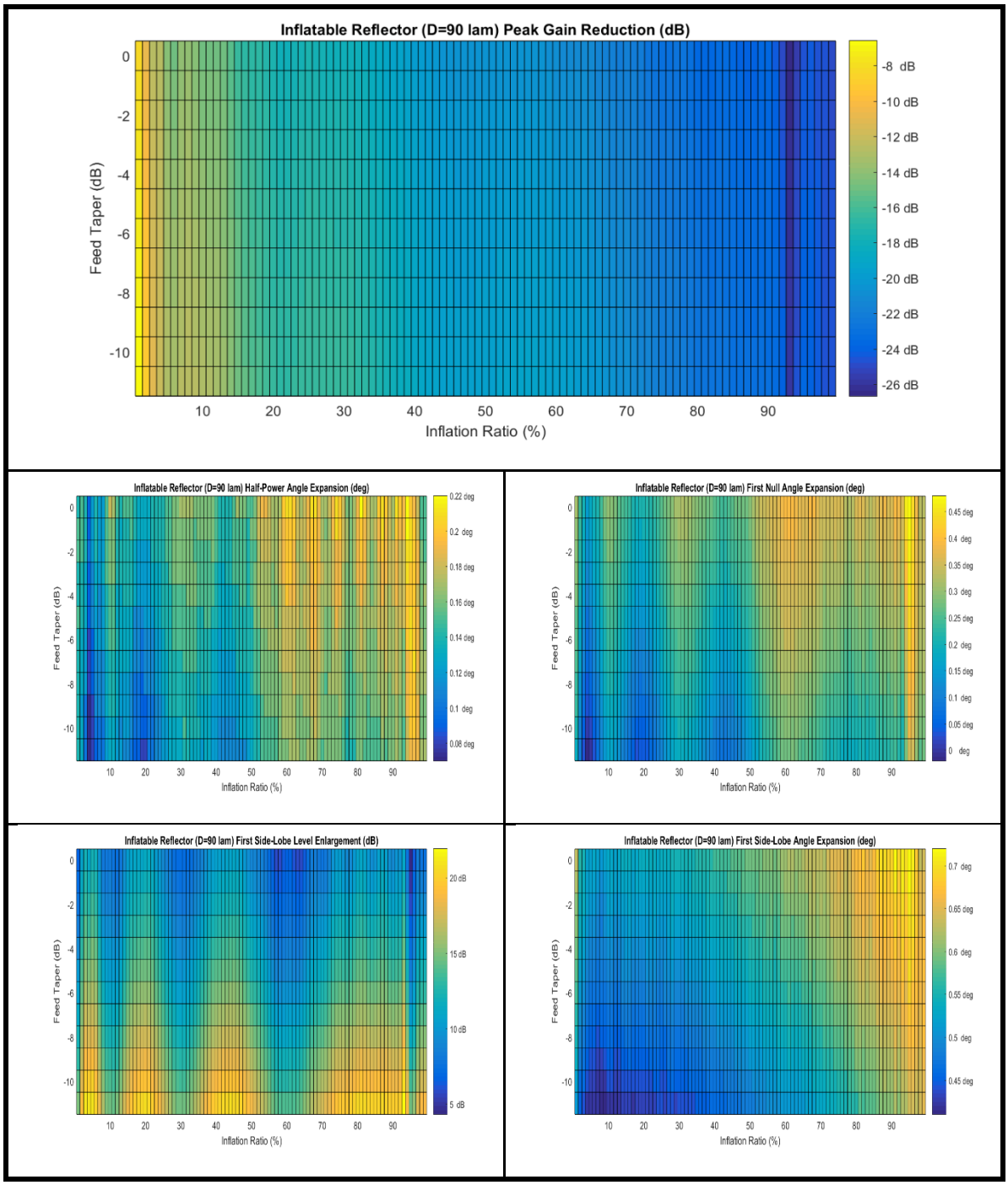

FIGURE 130: Common Depth Comparisons: Diameter = 90 Wavelengths

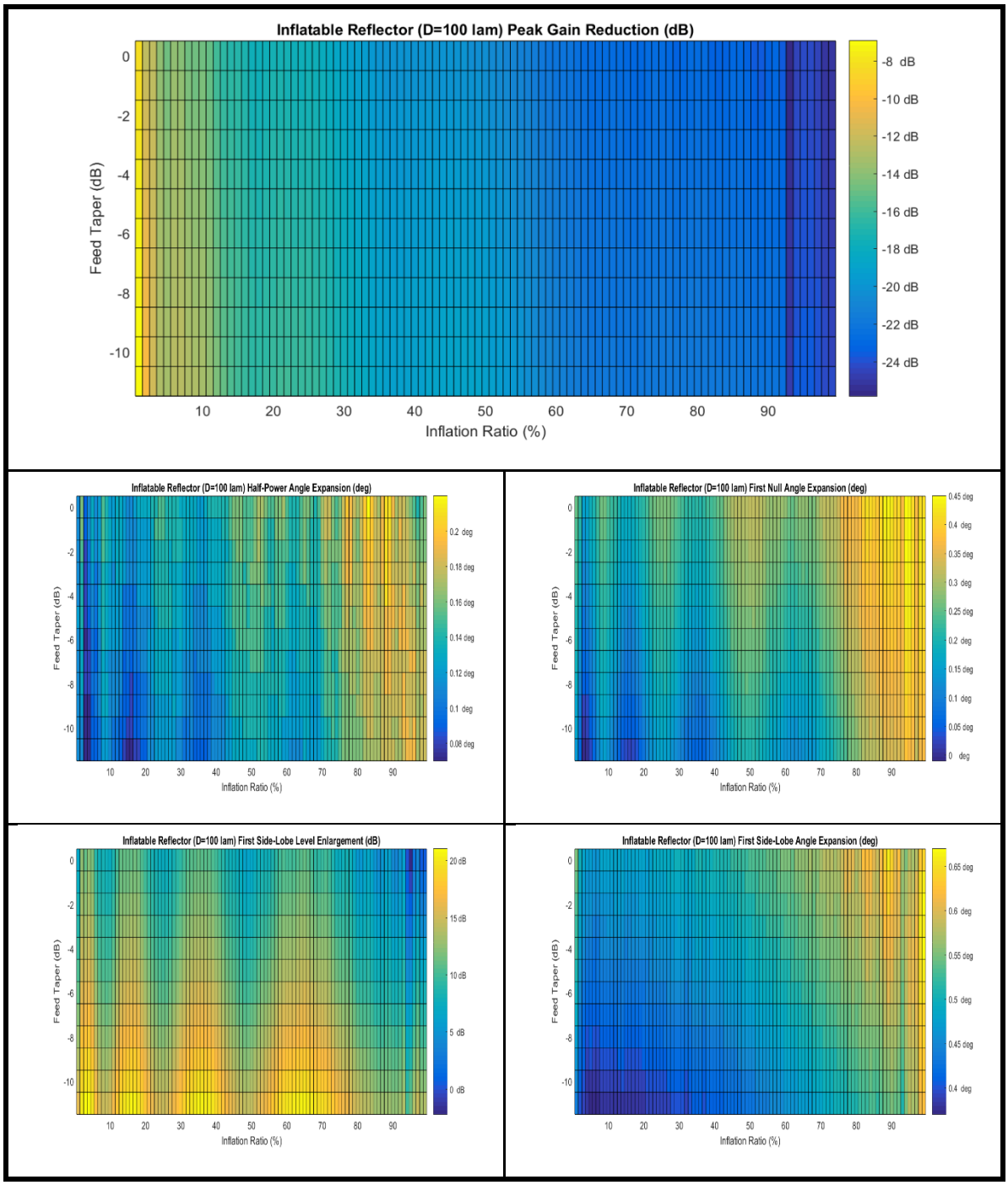

FIGURE 131: Common Depth Comparisons: Diameter = 100 Wavelengths

There are several noted observations that can be gathered across the data presented in Figures 123 through 131. The peak gain degradation shows that the inflatable aperture antenna again does not have a larger peak gain value than solid

parabolic reflector antenna. The peak gain degradation again does not appear to be correlated to the feed taper at any diameter. That is different for the half-power beamwidth, first null beamwidth, and first side-lobe level degradation metrics, as the comparisons of metrics do vary as a function the Inflation Ratio and feed taper. The half-power beamwidth angles, first null angles, and first side-lobe angles typically always expand positively, meaning that the beam is typically expanding consistently. The first side-lobe level degradation comparisons are typically always positive, meaning that the first side-lobe level has larger magnitude than that of the solid parabolic reflector antenna, when using a common depth.

4.7 RF Performance Comparison Using Common Arc Length

Section 4.3 had described three methodologies of comparing the RF performance of the inflatable aperture antenna with the solid parabolic reflector antenna. This section will utilize the common arc length approach, where the solid parabolic reflector antenna was analyzed at an equivalent focal length to diameter ratio to the best-fit value of each Inflation Ratio. The RF performance was varied in the same methodology of diameter from 20 wavelengths to 100 wavelengths in increments of 10 wavelengths, feed taper values of -11dB to 0dB in increments of 1dB and for Inflation Ratio values of 0.01 to 0.99 in increments of 0.01. Figures 132 through 140 illustrate the comparative results, which are displayed in comparison to the solid parabolic reflector antenna, using the common figure methodology of the previous section.

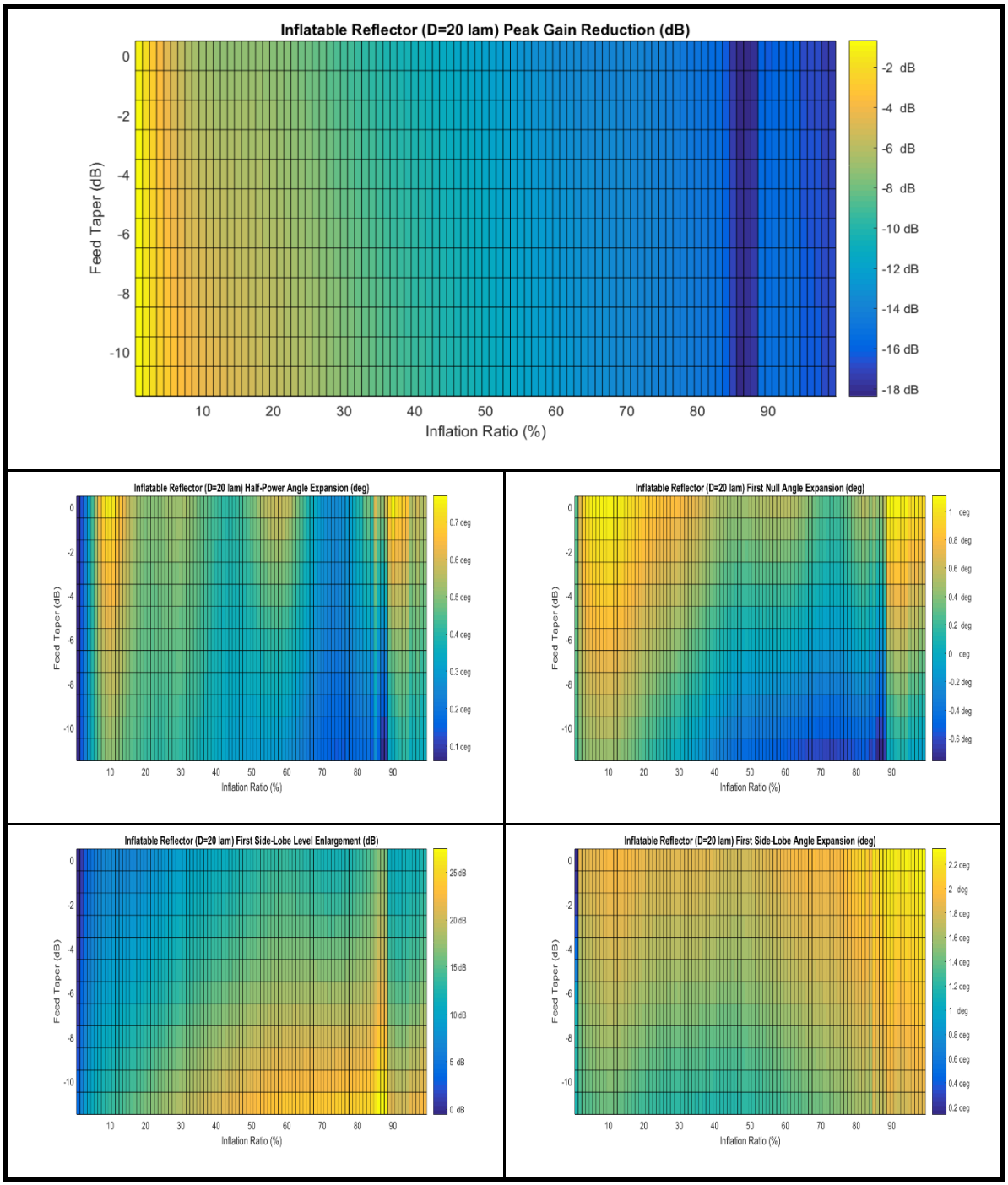

FIGURE 132: Common Arc Length Comparisons: Diameter = 20 Wavelengths

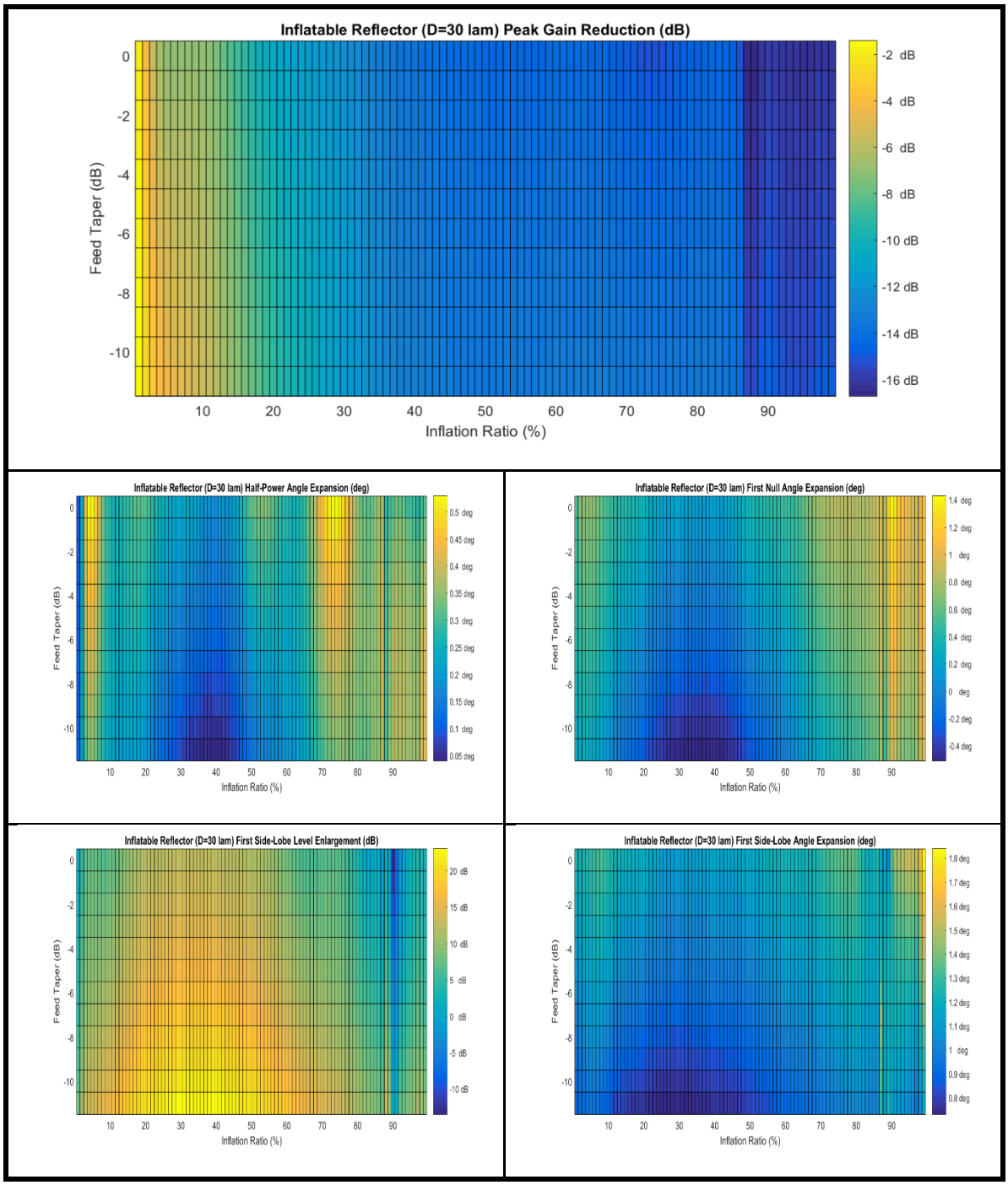

FIGURE 133: Common Arc Length Comparisons: Diameter = 30 Wavelengths

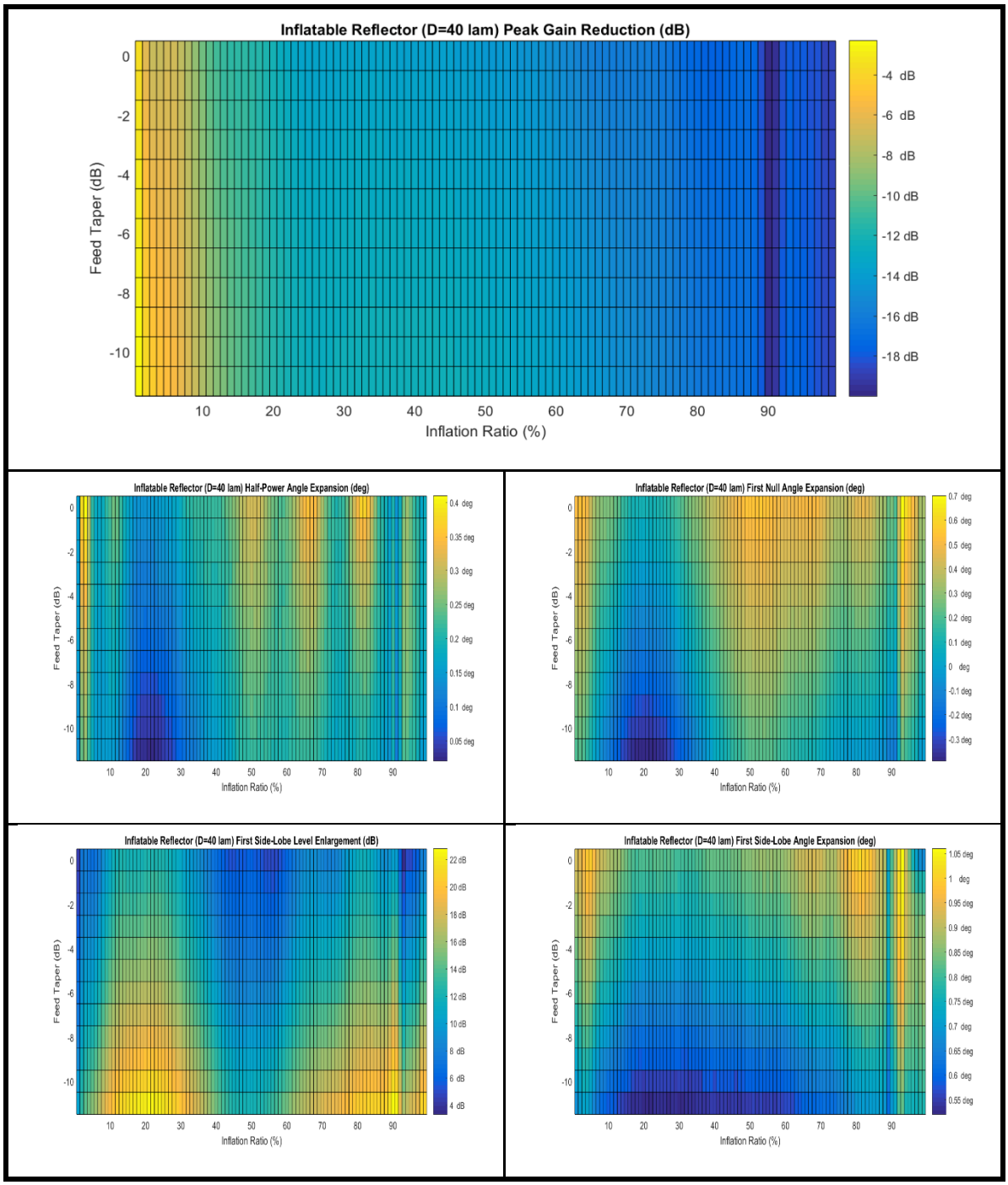

FIGURE 134: Common Arc Length Comparisons: Diameter = 40 Wavelengths

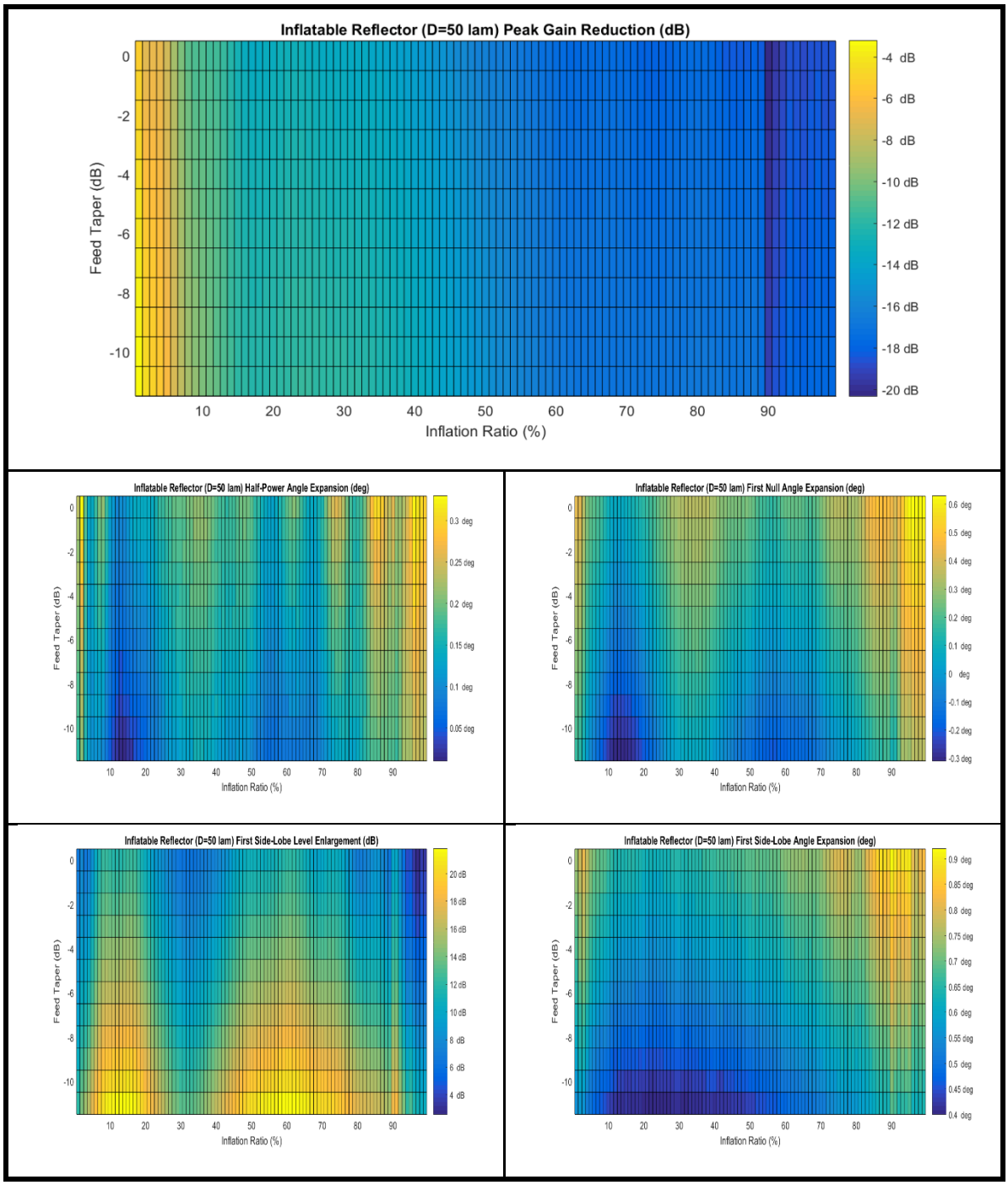

FIGURE 135: Common Arc Length Comparisons: Diameter = 50 Wavelengths

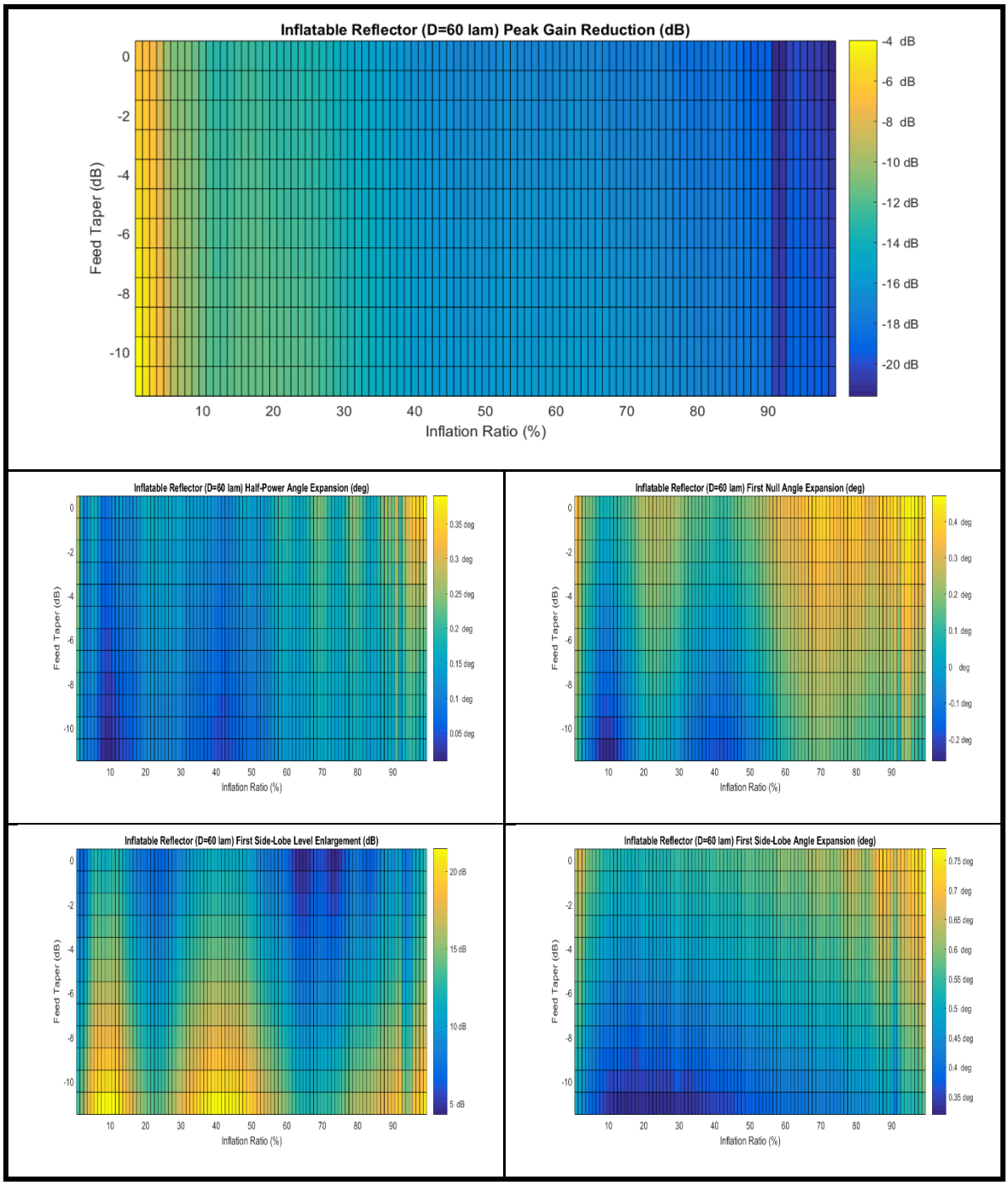

FIGURE 136: Common Arc Length Comparisons: Diameter = 60 Wavelengths

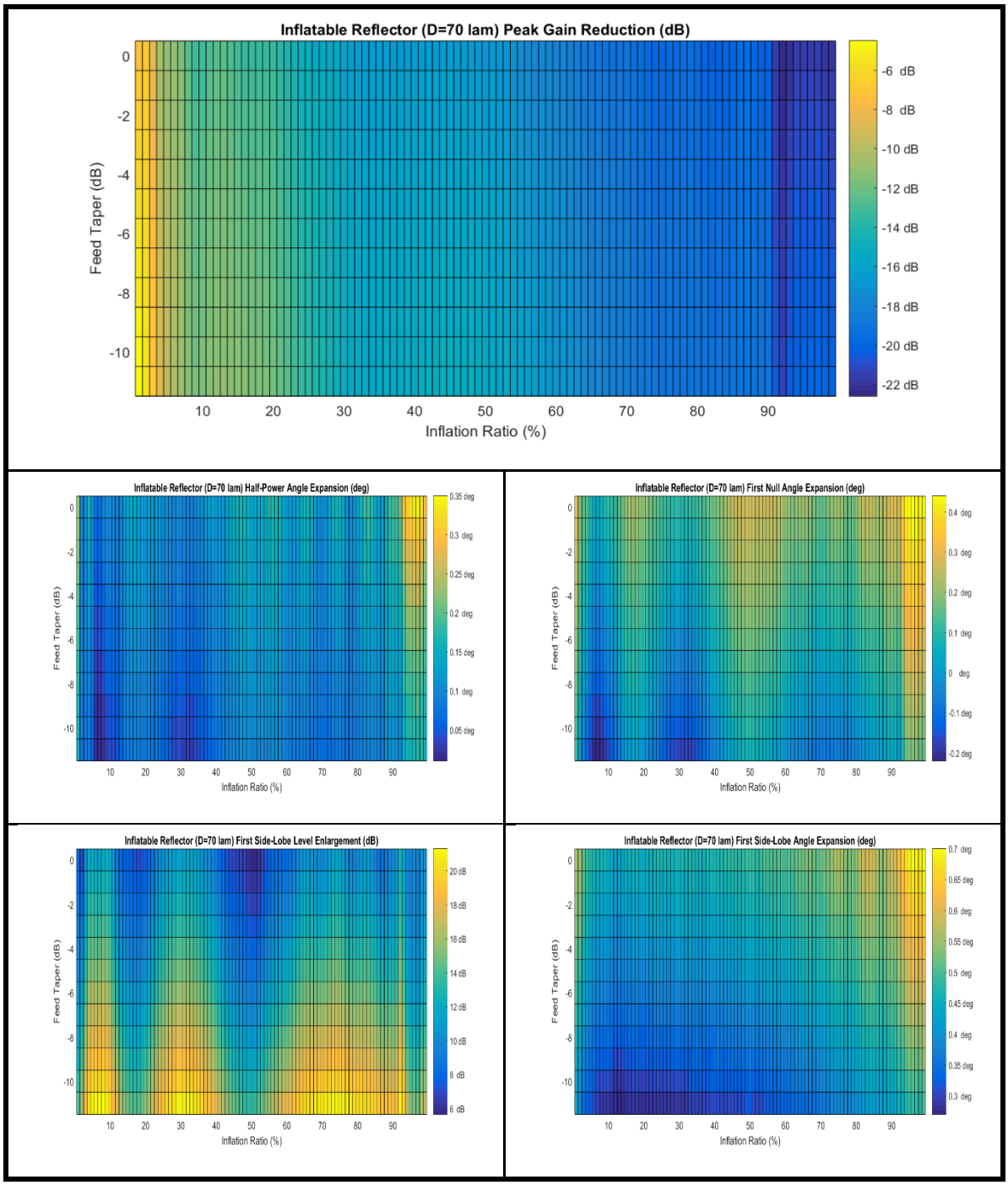

FIGURE 137: Common Arc Length Comparisons: Diameter = 70 Wavelengths

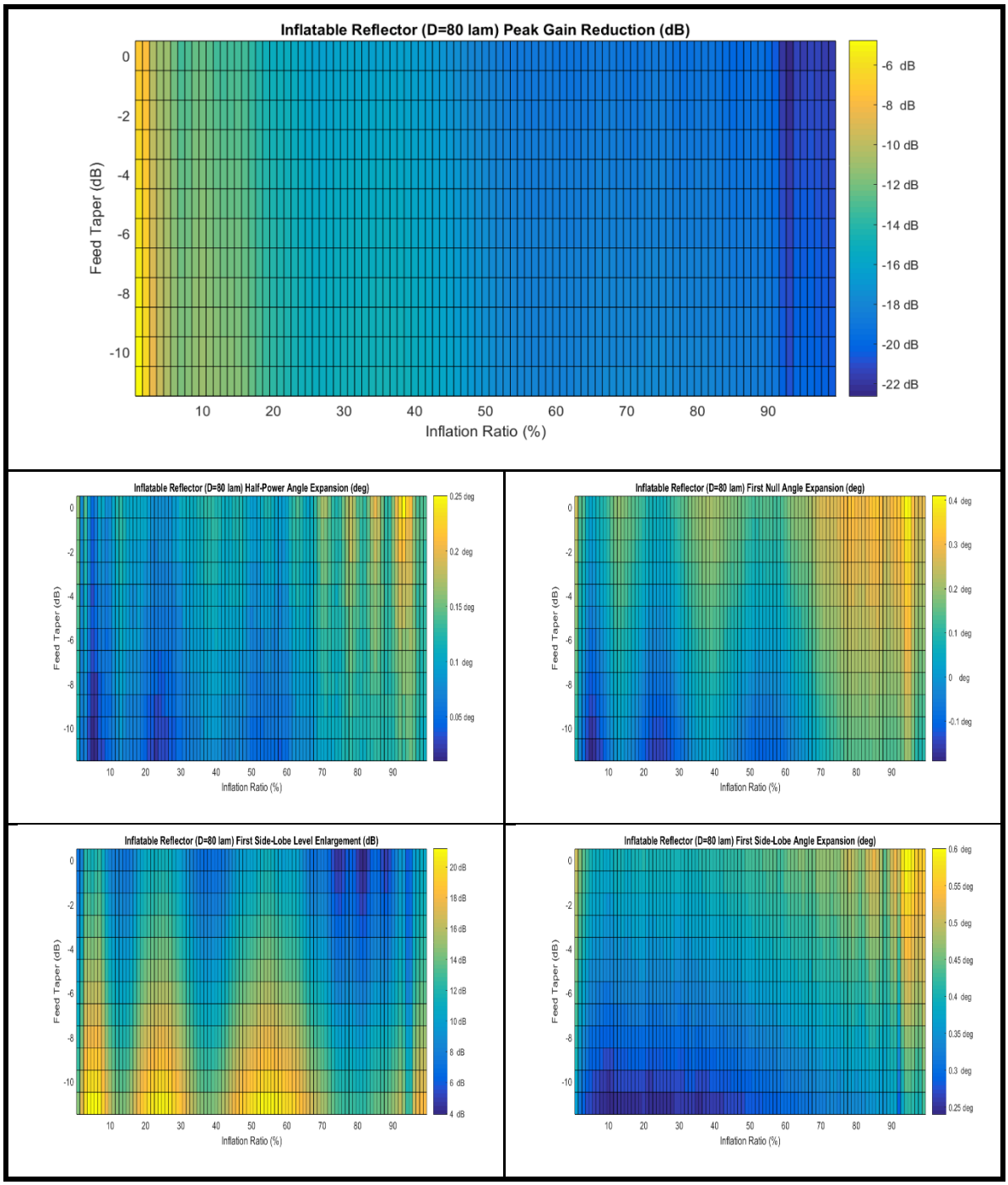

FIGURE 138: Common Arc Length Comparisons: Diameter = 80 Wavelengths

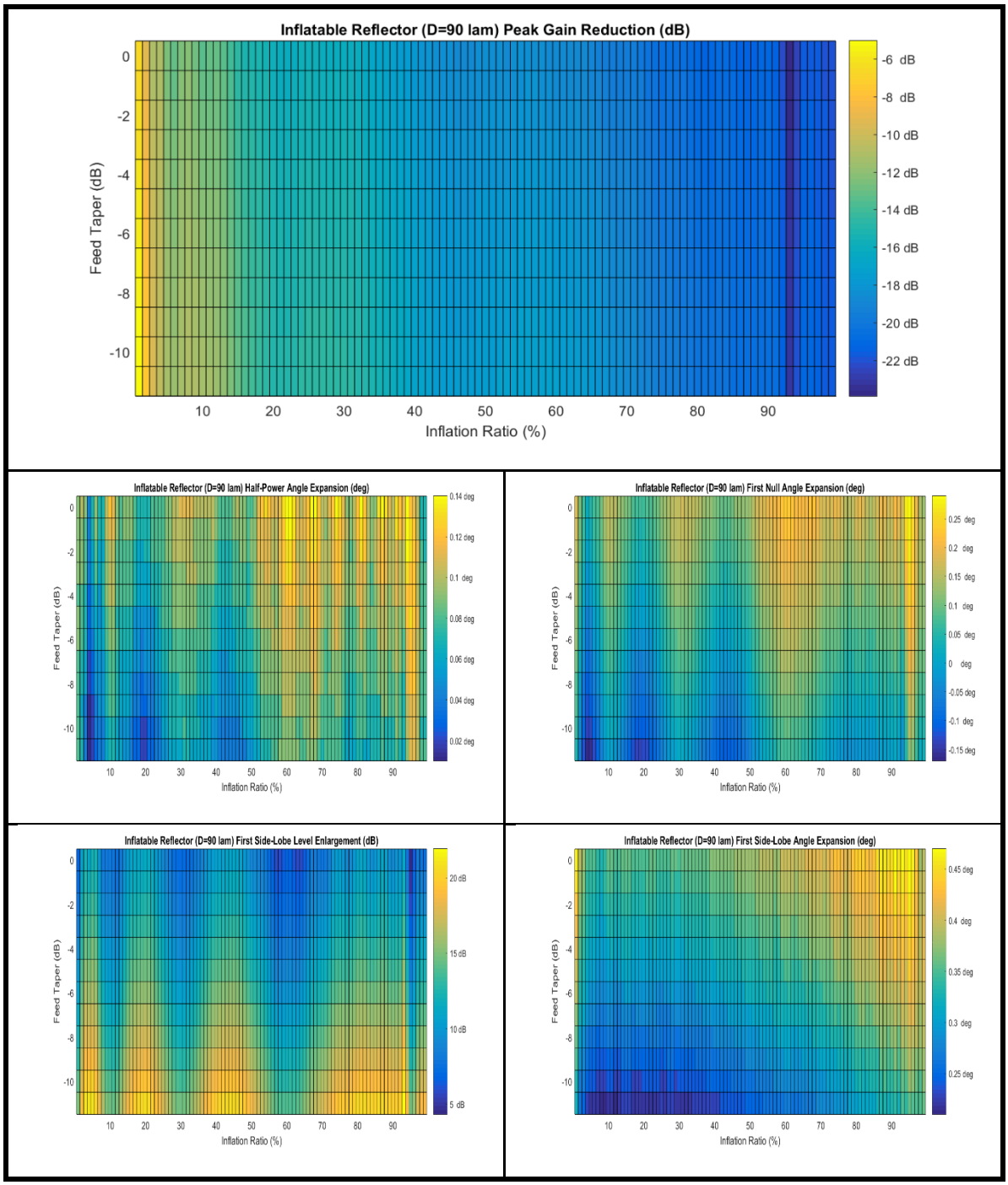

FIGURE 139: Common Arc Length Comparisons: Diameter = 90 Wavelengths

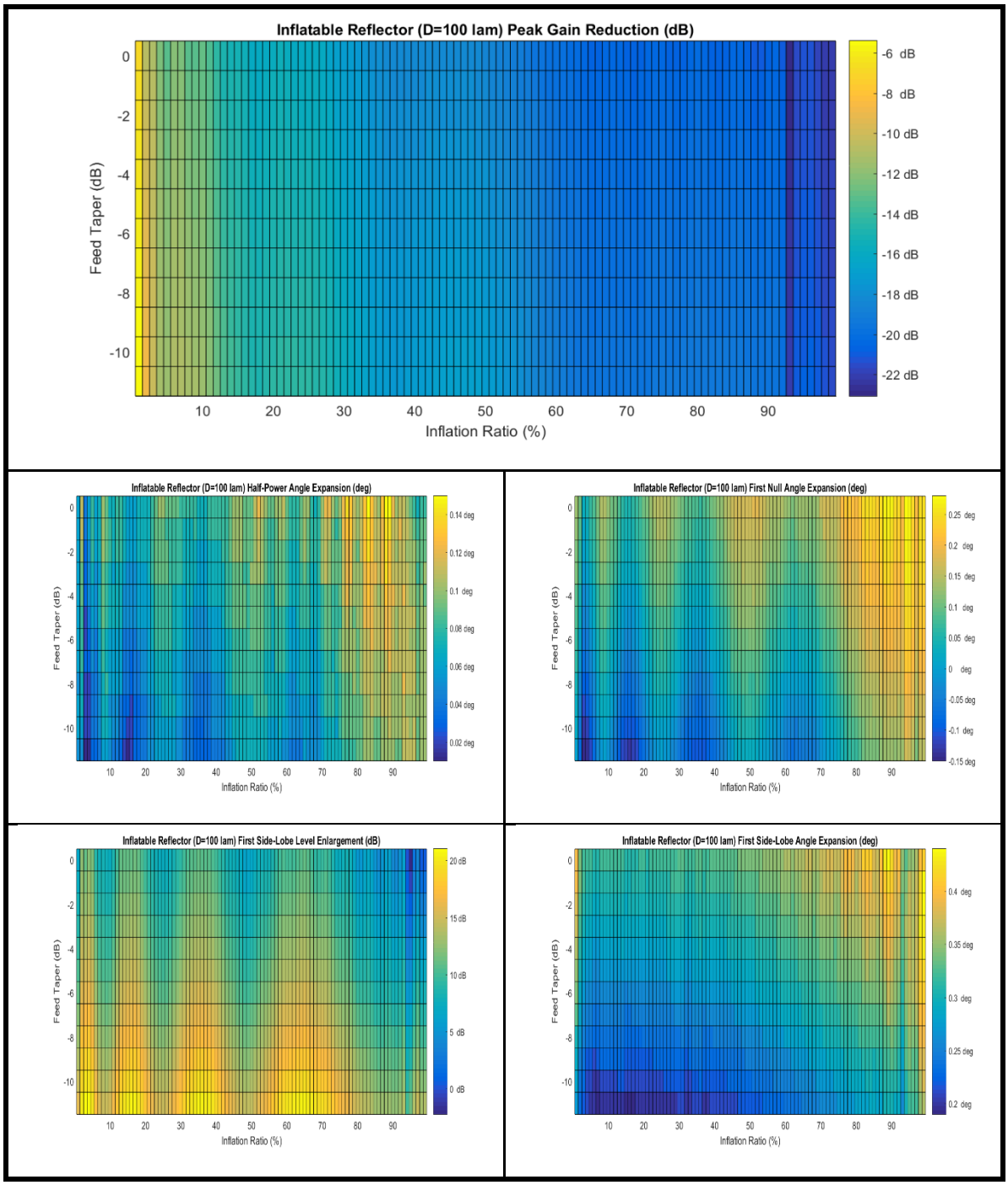

FIGURE 140: Common Arc Length Comparisons: Diameter = 100 Wavelengths

There are several noted observations that can be gathered across the data presented in Figures 132 through 140. The peak gain degradation shows that the inflatable aperture antenna again does not have a larger peak gain value than solid

parabolic reflector antenna. The peak gain degradation appears to have minimal correlation to the feed taper across the diameters tested. However, this is different for the half-power beamwidth, first null beamwidth, and first side-lobe level degradation metrics, as the comparisons of metrics do vary greatly as a function the Inflation Ratio and feed taper. The half-power beamwidth angles and first side-lobe angles typically always expand positively, meaning that the beam is typically expanding consistently. However, first null angles vary both positively, and negatively, meaning that the shape of the main lobe beam can become steeper between the half-power threshold and the first null threshold. The first side-lobe level degradation comparisons are typically always positive, meaning that the first side-lobe level is larger magnitude than that of the solid parabolic reflector antenna, when using this common arc length approach.

4.8 Summary

The author's contributions described a set of metrics to assess the RF performance of antennas, and utilized those metrics to form comparisons of the RF performance between the solid parabolic reflector antenna and an inflatable aperture antenna. These metrics were calculated from the antenna pattern methodologies discussed in Chapter III. Three approaches were utilized to compare the inflatable aperture antenna against the solid parabolic reflector antenna, which involve using common diameters, depths, or arc lengths of the different antenna technologies. The RF performance was assessed at various diameters and feed tapers, across the range of Inflation Ratios of the inflatable aperture antenna using best-fit focal lengths. Additionally, the inflatable aperture antenna

performance was tested against itself when varying the utilized focal length. Insights into the observed performance across each of these test cases were noted after performance plots were shown of the calculated datasets. This effort illustrates that there is no single ideal configuration for an inflatable aperture antenna, but does show that operating the antenna at lower Inflation Ratios can cause the peak gain to have minimal degradation when compared to the solid parabolic reflector antenna.

CHAPTER V

CONCLUSIONS

This chapter will cover the three primary contributions of this work. Additionally, three topics of potential future work to continue to determine the RF performance of inflatable aperture antennas will be discussed.

5.1 Contributions

In this Dissertation, three contributions to the field of antenna technology were introduced. First, the mathematical model of the inflatable aperture antenna surface profile shape was determined from the Calculus of Variations technique. The derivation shows a highly consistent form for the shape of the inflatable aperture antenna to the shape of the Mylar balloon. The primary difference between the two surface profiles is due to the edge of the inflatable antenna having a slope that can vary between zero and negative infinity, where the edge of the Mylar balloon always has a slope of negative infinity. This varying slope creates an offset term in the elliptic integral functions of the

surface profile shape. The shape was validated using an inflatable test article by measuring the surface profile via Laser Radar metrology.

Second, the RF performance model of the inflatable aperture antenna was derived through the use of Physical Optics. The derivation is based on the nominal derivation of a solid parabolic reflector antenna. Primary differences in the physical optics model of the inflatable aperture antenna are based on the inflatable aperture surface profile, the modified surface normal vector of the inflatable aperture antenna, and the modified grid point surface area numerical integration methodology. A common form of the surface normal vector was noted between the inflatable aperture antenna and the solid parabolic reflector antenna. An artifact of the surface profile that causes the surface area calculation to have terms that cannot be separated for calculation simplification is noted.

Finally, simulated RF performance comparisons were made of the inflatable aperture antenna against the solid parabolic reflector antenna. Three approaches were utilized to compare the inflatable aperture antenna against the solid parabolic reflector antenna, which were using common diameters, depths, or arc lengths of the different antenna technologies. The RF performance was assessed at various diameters and feed tapers, across the range of Inflation Ratios of the inflatable aperture antenna using best-fit focal lengths. Additionally, the inflatable aperture antenna performance was tested against itself when varying the utilized focal length. Insights into the observed performance across each of these test cases were noted after performance plots were shown of the calculated datasets. This effort illustrates that there is no one single analysis metric or single ideal configuration for an inflatable aperture antenna, but does show that

operating the antenna at lower Inflation Ratios can cause the peak gain to have minimal degradation when compared to the solid parabolic reflector antenna.

5.2 Future Work

Three topics for potential future work as a continuation of this Dissertation effort are noted next. First, the inflatable aperture antenna could be created using discs molded from a mandrel, where that mandrel is based on a specific targeted Inflation Ratio. Once the inflatable aperture were formed and inflated based on the use of the mandrel, one should be able to note that wrinkles do not appear when the targeted diameter is maintained. Second, the inflatable aperture antenna created from the mandrel should be used to perform RF antenna testing in an anechoic chamber using different feed taper profiles. This testing would be useful to validate the RF performance model capability derived in this Dissertation effort. Finally, the RF performance modeling should be extended to consider the use of a phased array antenna feed. A phased array antenna feed could allow for pre- or post-compensation of the signal reflected off the inflatable surface, or could be used to negate regions of the inflatable antenna surface near the rim which diverge away more from the ideal parabolic shape. Assuming that the compensation through the use of a phased array feed simulates to show promising results, RF performance testing considered as the second future work should be extended to test with the phased array feed that can compensate for the inflatable aperture antenna surface profile shape.

BIBLIOGRAPHY

[1] Acosta, R. and Lee, R., "Case Study of Sample Spacing in Planar Near-Field Measurement of High Gain Antennas," NASA TM-86872, Sep. 1984.

[2] Balanis, C., *Antenna Theory Analysis and Design*, New York, John Wiley & Sons, 1982.

[3] Bao, V., "Nonconstant Correlation Interval in Antenna Tolerance Theory," *IEEE Transactions on Antennas and Propagation*, pp. 118-119, Jan. 1970.

[4] Bao, X., Bar-Cohen, Y., Chang, Z., Sherrit, S., and Badescu, M., "Wirelessly Controllable Inflated Electroactive Polymer (EAP) Reflectors," *SPIE Structures Conference, San Diego, CA*, vol. 5759-52, Mar. 2005.

[5] Bracewell, R., "Tolerance Theory of Large Antennas," *IRE Transactions on Antennas and Propagation*, pp. 49-58, 1961.

[6] Cheng, D., "Effect of Arbitrary Phase Errors on the Gain and Beamwidth Characteristics of Radiation Pattern," IRE *Transactions – Antennas and Propagation*, pp. 145-147, 1955.

[7] Cherrette, A. and Lee, S., "Detection of Reflector Surface Error from Near-Field Data: Effect of Edge Diffracted Field," NASA TM-89920, Jun. 1987.

[8] Coleman, M., "Surface Accuracy Analysis and Mathematical Modeling of Deployable Large Aperture Elastic Antenna Reflectors," Doctoral Dissertation, The George Washington University, Aug. 2010.

[9] Collin, R., *Antennas and Radiowave Propagation*, New York, McGraw-Hill Book Company, 1985.

[10] Collin, R. and Zucker, F., *Antenna Theory Part 1*, New York, McGraw-Hill Book Company, 1969.

[11] Colliver, C., "Extended Antenna Tolerance Theory and its Application to Satellite Antennas," Doctoral Dissertation, University of Dayton, Dec. 1997.

[12] Diaz, L., Milligan, T., *Antenna Engineering Using Physical Optics: Practical CAD Techniques and Software,* Boston, Artech House, 1996.

[13] Freeland, R., Bilyeu, G., and Veal, G., "Validation of a Unique Concept for a Low-Cost Lightweight Space-Deployable Antenna Structure," *IAF-93-I.1.204*.

[14] Freeland, R., Bilyeu, G., Veal, G., Steiner, M., and Carson, D., "Large Inflatable Deployable Antenna Flight Experiment Results," *IAF-97-1.3.01*.

[15] Gasper, J., Sreekantamurthy, T., Mann, T., Behun, V., Romanofsky, R., Lambert, K., and Pearson, J., "Test and Analysis of an Inflatable Parabolic Dish Antenna," *47th AIAA Structures, Structural Dynamics, and Materials Conference, May 2006*.

[16] Gelfand, I. and Fomin, S., *Calculus of Variations,* Prentice-Hall, Inc., 1963.

[17] Hoferer, R. and Rahmat-Samii, Y., "RF Characterization of an Inflatable Parabolic Torus Reflector Antenna for Space-Borne Applications," *IEEE Transactions on Antennas and Propagation*, vol. 46, no. 10, pp. 1449-1457, Oct. 1998.

[18] Jansma, P., "Open! Open! Open! Galileo High Gain Antenna Anomaly Workarounds," *2011 IEEE Aerospace Conference, Mar. 2011*.

[19] Jenkins, C., Kalanovic, V., Padmanabhan, K., and Faisal, S., "Intelligent Shape Control for Precision Membrane Antennae and Reflectors in Space," *Smart Material Structures*, vol. 8, pp. 857-867, 1999.

[20] Marker, D. and Jenkins, C., "Surface Precision of Optical Membranes with Curvature," *Optics Express*, vol. 1, no. 11, pp. 324-331, Nov. 1997.

[21] Mladenov, I., "New Geometrical Applications of the Elliptic Integrals: The Mylar Balloon," *Journal of Nonlinear Mathematics and Physics*, vol. 11, pp. 55-65, 2004.

[22] Mladenov, I., Oprea, J., "On some deformations on the Mylar balloon," *Proceedings of the XV International Workshop on Geometry and Physics*, vol. 11, pp. 310-315, Sep. 2006.

[23] Mladenov, I., Oprea, J., "The Mylar balloon: New viewpoints and generalizations," *Proceedings of the Eighth International Conference on Geometry, Integrability, and Quantization*, pp. 246-263, Jun. 2006.

[24] Mladenov, I., Oprea, J., "The Mylar balloon revisited," *The American Mathematical Monthly*, vol. 110, no. 9, pp. 761-784, Nov. 2003.

[25] Olver, F., Lozier, D., Boisvert, R., and Clark, C., *NIST Handbook of Mathematical Functions*, Cambridge, Cambridge University Press, 2010.

[26] Oprea, J., *Differential Geometry and its Applications*, Pearson Education, Inc., 2007.

[27] Paulsen, W., "What is the Shape of a Mylar Balloon?," *The American Mathematical Monthly*, vol. 101, no. 10, pp. 953-958, Dec. 1994.

[28] Pearson, J., "Inflatable Membrane Antennas," NASA TR 05-1088, Mar. 2005.

[29] Pearson, J., "Phase III Inflatable Membrane Antennas," NASA TR 04-1052, Feb. 2004.

[30] Pearson, J. and Romanofsky, R., "Thin Film Antenna Development and Optimization," *47th AIAA Structures, Structural Dynamics, and Materials Conference, May 2006*.

[31] Rahmat-Samii, Y., "An Efficient Computational Method for Characterizing the Effects of Random Surface Errors on the Average Power Pattern of Reflectors," *IEEE Transactions on Antennas and Propagation,* vol. AP-31, no. 1, pp. 92-98, Jan. 1983.

[32] Rahmat-Samii, Y., "Useful Coordinate Transformations for Antenna Applications," *IEEE Transactions on Antennas and Propagation,* vol. AP-27, no. 4, pp. 571-574, Jul. 1979.

[33] Romanofsky, R., Bibyk, I., Welch, B., and Lambert, K., "The Potential for Gossamer Deployable Antenna Systems in Ka-Band Exploration and Science Communications Architectures," *12th Ka-Band and Broadband Communications Conference, September 2006*.

[34] Ruze, J., "Antenna Tolerance Theory – A Review," *Proceedings of the IEEE,* vol. 54, no. 4, pp. 633-640, Apr. 1966.

[35] Ruze, J., "The Effect of Aperture Errors on the Antenna Radiation Pattern," *Supplemento al Nuovo Cimento,* vol. 9, no. 3, pp. 364-380, 1952.

[36] Tan, H., Bai, X., and Lin, G., "Surface Accuracy Measurement and Analysis of an Inflatable Antenna by Photogrammetry," *IEEE Cross Strait Quad-Regional Radio Science and Wireless Technology Conference, May 2011*.

[37] Welch, B., "Application of the Ruze Equation for Inflatable Aperture Antennas," Master's Thesis, Cleveland State University, Dec. 2006.

[38] Welch, B., “Derivation of Surface Shape for Inflatable Large Aperture Antennas,” *Mathematical Methods in the Applied Sciences,* pp. 1-16, 2019, https://doi.org/10.1002/mma.5791.

[39] Williams, W., “High Capacity Communications from Martian Distances,” NASA TM-2006-214415, Mar. 2006.